REACTIONS OF $Na_2SO_4(l)$ AND $CoSO_4-Na_2SO_4(l)$ WITH

$SO_3(g)$ AND $Al_2O_3(s)$, 900 - 1250 K

by

RAYMOND KAM-FAI LAM

B.S. Mechanical Eng., University of Hawaii at Manoa
(1981)

M.S. Mechanical Eng., University of Hawaii at Manoa
(1983)

Submitted to the Department of
Materials Science and Engineering
in partial fulfillment of the requirements
for the degree of

DOCTOR OF SCIENCE

IN METALLURGY

at the

MASSACHUSETTS INSTITUTE OF TECHNOLOGY

May 1988

© Massachusetts Institute of Technology 1988

Signature Redacted

Signature of Author......................................
Department of Materials Science and Engineering
April 29, 1988

Signature Redacted

Certified by..
John F. Elliott
Thesis Supervisor

Signature Redacted

Accepted by.................................
John B. Vander Sande
Chairman, Departmental Committee on Graduate Students

- 1 -

REACTIONS OF $Na_2SO_4(l)$ AND $CoSO_4$-$Na_2SO_4(l)$ WITH $SO_3(g)$ AND $Al_2O_3(s)$, 900 - 1250 K

by

RAYMOND KAM-FAI LAM

ABSTRACT

Physical chemistry of the reactions of sodium sulfate liquid and cobalt sulfate-sodium sulfate liquid with sulfur trioxide gas and aluminum oxide solid has been studied at 900 K to 1250 K. These reactions are recognized to be the chemical processes which are responsible for acclerated corrosion attacks (hot corrosion) to gas turbine materials at elevated temperatures. Two types of experimental techniques are employed with either platinum or alumina crucibles at a controlled partial pressure of sulfur trioxide: (1) thermogravimetric analysis (TGA) which measures the solubility of sulfur trioxide gas in the sulfate melt; and (2) electromotive force (EMF) measurement which monitors the activity of sodium oxide in the sulfate by employing the following electrochemical cell:

Pt, $O_2(g)$		Na^+		Pt, $O_2(g)$, $SO_2(g)$
Na_2O-$WO_3(l)$		fused silica		$Na_2SO_4(l)$ or $CoSO_4$-$Na_2SO_4(l)$
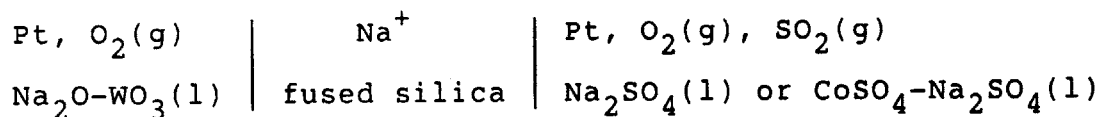
The solubility of aluminum oxide solid in the sulfate is determined by analyzing samples extracted from equilibrated melts.

The solubility of sulfur trioxide is observed to increase with an increase in partial pressure of sulfur trioxide, a decrease in temperature, and a decrease in cobalt sulfate concentration in the sulfate liquid. More than 95 percent of the dissolved sulfur trioxide reacts with aluminum oxide to form aluminum sulfate at log partial pressure of sulfur trioxide > -4.5. The dissolved aluminum has no effect on the activity of sodium oxide.

The solution rate of sulfur trioxide gas in molten sulfate ,which is controlled by liquid phase mass transfer, is much faster than the dissolution rate of aluminum oxide

solid, which is controlled by chemical reaction.

The thermodynamic properties of the sodium sulfate-sodium pyrosulfate system have been fully explored. The solution behaves in such a way that the activities of the two components equal to the mole fractions of the respective species. The phase diagram and a stability diagram are determined. The partial pressures of sulfur trioxide in equilibrium with pure sodium pyrosulfate and pure sodium sulfate are evaluated at 1160 K and 1200 K.

The acidic fluxing by sodium sulfate on aluminum oxide has been determined. The equilibrium solubility of aluminum oxide in molten sodium sulfate varies from 8016 to 0.37 ppm of dissolved aluminum at log partial pressure of sulfur trioxde = -1.5 to -4.5. The solubility of aluminum oxide disagrees entirely with the two results reported by other researchers. Basic fluxing is not possible to be measured by the EMF cell because the reaction between solid electrolyte and sulfate melt at log a_{Na_2O} > -12 at 1200 K.

The thermodynamic properties of the cobalt sulfate-sodium sulfate system have also been evaluated. The activities of cobalt sulfate and sodium sulfate exhibit negative deviations from ideality. The activity of sodium oxide is observed to decrease with an increase in the partial pressure of sulfur trioxide and with an increse in cobalt sulfate concentration. Isoactivity lines of sulfur trioxide on the phase diagram and the stability diagram are determined. The accuracy of the phase diagram of cobalt sulfate-sodium sulfate is questionable.

Finally, the implications of this investigation on the sodium sulfate induced hot corrosion and the ways to prevent corrosion attacks at elevated temperatures are discussed.

Thesis Supervisor: John F. Elliott
Title: Professor of Metallurgy

TABLE OF CONTENTS

LIST OF ILLUSTRATIONS AND FIGURES

LIST OF TABLES

ACKNOWLEDGEMENTS

I express my deepest gratitudes to my parents, Kwok-Chuen Lam and Sook-Yee Tong, for their many encouragements and sacrifices to fulfill my dreams. I am indebted to my beloved wife, Juliana, for her unceasing love

and support even at times of trial and tribulation. Above all, I thank God for His abundent blessings and love.

A   surface area in cm^2.

a_i activity of species i.

c_i concentration of species i in $mole \cdot cm^{-3}$.

c_b^g concentration of SO_3 in bulk gas $mole \cdot cm^{-3}$.

c_i^g concentration of SO_3 at the gas/liquid interface in $mole \cdot cm^{-3}$.

c_b^l concentration of SO_3 in bulk liquid $mole \cdot cm^{-3}$.

c_i^l concentration of SO_3 at the gas/liquid interface in $mole \cdot cm^{-3}$.

C_p heat capacity.

D_g gas phase diffusion coefficient in $cm^2 \cdot sec^{-1}$.

D_l liquid phase diffusion coefficient in $cm^2 \cdot sec^{-1}$.

E   cell potential in volt.

F   Faraday's constant.

ΔG_r^o standard Gibbs free energy of reaction.

$\Delta G_f^o(i)$ standard Gibbs free energy of formation of species i.

ΔG_m molar Gibbs free energy of melting.

G^M integral Gibbs free energy of mixing.

G^{ID} integral Gibbs free energy of ideal mixing.

G^{EX} excess Gibbs free energy of mixing.

G_i^M partial molar Gibbs free energy of mixing of species i.

(g)   gas phase.

H_i^M partial molar enthalpy of mixing of species i.

$\Delta H_{m,i}$ molar enthalpy of melting of species i.

$\Delta H_f^o(i)$	standard enthalpy of formation of species i.
J_i	flux of species i in $mole \cdot cm^{-2} \cdot sec^{-1}$.
K	equilibrium constant.
K'	apparent equilibrium constant.
k_{c1}	first-order chemical reaction rate constant.
k_{c2}	second-order chemical reaction rate constant.
k_g	gas phase mass transfer coefficient in $cm \cdot sec^{-1}$.
k_l	liquid phase mass transfer coefficient in $cm \cdot sec^{-1}$.
(l)	liquid phase.
M_i	molecular weight of species i.
m	slope of curve.
n_i	mole of species i.
P_i	partial pressure of species i in atmosphere.
R	universal gas constant.
$\Delta S_{m,i}$	molar entropy of melting of species i.
$\Delta S_f^o(i)$	standard entropy of formation of species i.
(s)	solid phase.
T	temperature in Kelvin.
T_f	final temperature in Kelvin.
T_i	initial temperature in Kelvin.
$T_{m,i}$	melting temperature of species i in Kelvin.
t	time in second.
V	volume of melt in cm^3.
W_0	weight of melt at beginning in gram.
W_e	weight of melt at equilibrium in gram.
W_t	weight of melt at time t in gram.
X_i	mole fraction of species i.

ω thermal diffusivity.

λ bulk density.

ρ thermal conductivity.

γ_i activity coefficient of species i.

α_i α function of species i.

δ_g gas boundary layer thickness in cm.

δ_l liquid boundary layer thickness in cm.

CHAPTER ONE

INTRODUCTION

The accelerated corrosion of gas turbine materials, such as cobalt-base and nickel-base superalloys, and ceramics due to the presence of the liquid phase of condensed salts at elevated temperature is commonly known as hot corrosion or sulfidation if the molten salts are sulfates. The corrosion destroys the surface protective layer of oxide of alumina (Al_2O_3) or chromia (Cr_2O_3) and then attacks the material itself. The attack causes frequent replacement of the parts [79], unnecessary disruption of daily operations [80], and even total shut-down of a power generating plant or an aircraft engine [81].

Sodium sulfate has been recognized to be the principal precursor to this type of rapid degradation of materials. Deposition of molten sodium sulfate is the result of salt ingested into the engine and sulfur from the combustion of fuel. The molten phase of $CoSO_4$-Na_2SO_4 mixtures was also determined to be detrimental to turbine vanes and blades made up of cobalt-base superalloys and protective coatings such as CoCrAlY at temperatures in the range of 900-1100 K. This type of attack known as Low Temperature Hot Corrosion (LTHC) is attributed to the presence of a low-melting sulfate eutectic at temperatures below the melting point of sodium sulfate (1157 K). The formation of $CoSO_4$-Na_2SO_4 liquids results from the deposit of sodium sulfate and

subsequent sulfation reactions on the cobalt oxide scales that are formed after the protective oxide layer of alumina or/and chromia has been dissolved and the Co-base superalloy has been oxidized.

Reports of investigations on hot corrosion are numerous in the literature. To understand the corrosion mechanism, most of the articles on hot corrosion treat the morphology of corrosion products. However, studies on the basic physico-chemical processes that determine the nature and rates of the corrosion processes are of paramount importance [82]. The goal of the research reported here is thus directed to an understanding of the physical chemistry of phases that are involved in the sulfate-induced corrosion process at elevated temperatures.

The objectives of the investigation focus on: (1) the thermodynamic properties of sodium sulfate and mixtures of Co-Na sulfates; (2) the effect of the partial pressure of sulfur trioxide on the solubility of that gas in the melts of sodium sulfate and in the mixtures of Co-Na sulfates; (3) the solubility of alumina in molten sodium sulfate and in mixtures of Co-Na sulfates; and (4) other phases coexisting with the liquid phase in the $CoSO_4$-Na_2SO_4 system. The experimental program consists of electrochemical measurements and thermogravimetric studies. The compositions of melts are determined with a DC plasma arc elemental emission spectrometer and the transformation of phases are studied by differential thermal analysis.

Optical microscopy, scanning electron microscopy (SEM), and energy dispersive X-Ray spectroscopy (EDX) are conducted to examine solidified samples.

CHAPTER TWO

LITERATURE SURVEY

This chapter can be classified into two main topics: (1) a general background of hot corrosion which includes the hypothesis of acidic-basic fluxing; and (2) a review of the literature on the experimental technique of electrochemical measurements employed in sulfate systems, the solubilities of oxides and sulfur trioxide in sodium sulfate, and the $CoSO_4$-Na_2SO_4 molten salt system.

2.1 Hot Corrosion

For more than thirty years, hot corrosion [1,2,3,4] has been observed and examined in the hot section of land-base power generating plants, boilers, marine engines, and aircraft engines. The first incidence of hot corrosion in an aircraft engine installed in a patrol boat application was reported in 1959 [5]. With the use of low chromium high-strength superalloys and the increase in engine temperature, the problem became of importance in aircraft gas turbines, particularly those operating near the sea. Sodium sulfate was found to be the most important corroding medium as early as in 1945 by Reid et al. [6] and later by many others [7,8,9,10]. DeCrescente and Bornstein [18] have shown that a sodium sulfate vapor-air mixture was innocuous to nickel-base superalloys. Catastrophic attack on high temperature alloys required the presence of a molten phase

composed principally of sodium sulfate on the surface of an engine or boiler parts [11].

Formation of sodium sulfate in a gas turbine is enhanced by the impurities of fuel, and the ingestion of salt [12,13,14]. Impurities in gas turbine fuel [15] typically are at the level of 1.2 weight percent of sulfur, 0.85 ppm of sodium plus potassium, 1.97 ppm vanadium, 0.38 ppm calcium, 0.02 ppm lead, and 0.26 ppm of magnesium. Whereas, there is less than 0.4 percent of sulfur in the JP-5 aviation-turbine fuel [16]. Sodium sulfate not only is directly ingested as part of a sea salt which has as much as 11 weight percent of sodium sulfate [17], but DeCrescente and Bornstein [18] also pointed out that sodium sulfate could be formed by reactions with sodium chloride in the presence of oxygen and an excess of sulfur. Kohl et al. [19] demonstrated that the deposition of Na_2SO_4 from conversion of NaCl could be completed in a residence time of 2.2 milliseconds inside a gas turbine.

Most of the studies on hot corrosion have been directed to developing an understanding of the morphology of corrosion products on coupons of metals which have been exposed to sodium sulfate, and examining the damaged parts of turbine and boiler parts. The attack is characterized by a mixed oxide-metal layer just below the thick, porous external scale, and still below this is a row of metal sulfide particles which often has the approximate formula M_2S_3 where M is mainly chromium, but it can also be Ni, Co,

Al, Ti, and the refractory metals. The metal surface is highly irregular, with detached particles of metal within the oxide layer and deep penetration of oxides into the metal [20]. This type of attack is known as Sulfidation or Type 1 Hot Corrosion [21]. The reaction shows a high dependence on temperature. There is little attack below 1073 K, then the rate increases with temperature to a maximum at 1173-1223 K, and falls rapidly above 1273 K.

A second form of attack was detected in the early 1970's as a result of operating gas turbines in a marine environment at temperatures low enough to avoid Type 1 Hot Corrosion. This type of attack usually appears as deep pits, with a relatively smooth metal surface at the bottom of the pits. There is little or no sulfide phases within the metal beneath the pits, although sulfur is often contained in the corrosion products within the pits. This type of attack has its maximum in the range 979-1005 K and is absent below 922 K and above 1033 K; this is called Low Temperature Hot Corrosion or Type 2 Hot Corrosion. Both cobalt sulfate and sodium sulfate have been identified in the salt near the corroding surface. The formation of a liquid phase of a Co-Na sulfate mixture can be achieved by the following sulfation reactions of the oxides:

$$Na_2O(s) + SO_2(g) + 1/2\ O_2 = [Na_2SO_4] \qquad (2-1)$$

$$CoO(s) + SO_2(g) + 1/2\ O_2(g) = [CoSO_4] \qquad (2-2)$$

$$1/3\ Co_3O_4(s) + SO_2(g) + 1/2\ O_2(g)$$
$$= [CoSO_4] + 1/6\ O_2(g) \qquad (2-3)$$
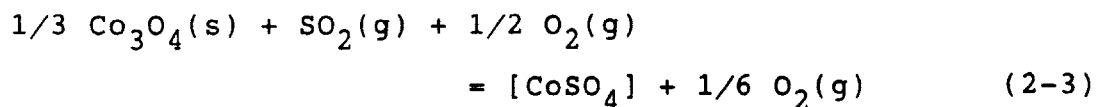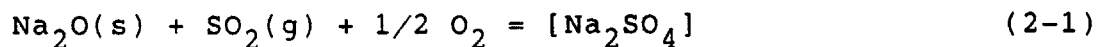
where brackets indicate that the species is in solution, and (s) and (g) denote a solid and a gas phase, respectively.

The formation of the sulfate mixture was observed by Shores and Luthra [22] as pure sodium sulfate gradually changed to mixtures of $CoSO_4-Na_2SO_4$ in their experiments. Luthra and Shores [23] further performed thermodynamic calculations to show that liquid $CoSO_4-Na_2SO_4$ could form on the surface of cobalt based superalloys at moderate SO_3 levels in the gas.

2.2 Acidic-Basic Fluxing Hypothesis

Many models [26-30] have been proposed to explain the mechanism of hot corrosion. These models were reviewed by Kawakami, Goto and Rapp [31]. Among them the model of acidic-basic fluxing, which was proposed by Bornstein and DeCrescente [32] and was later extended by Goebel, Pettit et al. [33-36], is most generally accepted for sodium sulfate-induced hot corrosion. This model states that the corrosion process is basically controlled by the acidic or basic condition of the molten salt.

The basicity of a molten salt can be expressed as the concentration of oxygen ion, O^{2-}, or the activity of the basic oxide in the melt. Acidic fluxing occurs when the concentration of oxygen ion is low. The general acidic reaction of oxide dissolution is expressed as

$$MO(s) = [M^{2+}] + [O^{2-}] \tag{2-4}$$

where $[M^{2+}]$ is a metal cation in the melt. In the case of attack on alumina coatings, the acidic reaction is written as

$$Al_2O_3(s) + 3SO_3(g) = [Al_2(SO_4)_3] \tag{2-5}$$

or

$$Al_2O_3(s) + 3Na_2SO_4(l) = [Al_2(SO_4)_3] + 3[Na_2O] \tag{2-6}$$
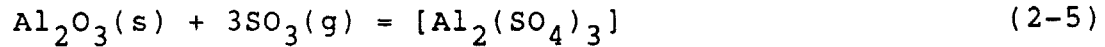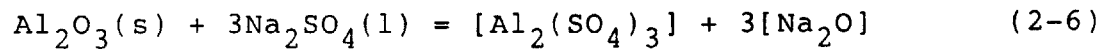
where brackets indicate that the species is in solution, and (s), (g), and (l) denote that the phase is solid, gas, and liquid, respectively. Basic fluxing occurs when the concentration of oxygen ion is high. The general basic reaction is

$$MO(s) + [O^{2-}] = [MO_2^{2-}] \tag{2-7}$$
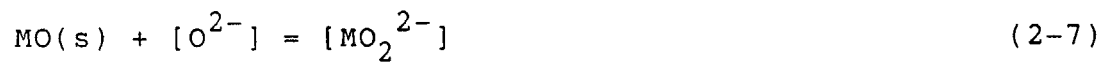
In the case of alumina, the reaction is

$$Al_2O_3(s) + [Na_2O] = 2[NaAlO_2] \tag{2-8}$$

or

$$Al_2O_3(s) + Na_2SO_4(l) = 2[NaAlO_2] + SO_3(g) \tag{2-9}$$
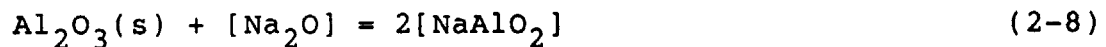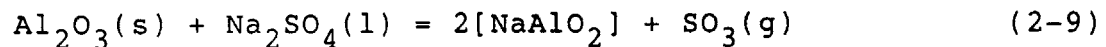
It is necessary to fix the partial pressure of $SO_2(g)$ and $O_2(g)$ to establish the activity of sodium oxide in sodium sulfate. Alternatively, the activity of sodium oxide in the liquid sulfate is determined by the partial pressure

of $SO_3(g)$ according to the reaction

$$Na_2SO_4(l) = [Na_2O] + SO_3(g) \qquad (2-10)$$

Therefore, the concentration of oxygen ions or the activity of the basic oxide plays an important role in the dissolution process of alumina protective coatings.

2.3 Solubility of Oxides in Moten Salts

Superalloys derive their oxidation resistance by the formation of a thin, adherent and self-healing oxide scale composed primarily of alumina (Al_2O_3) and/or chromia (Cr_2O_3) [49,50]. It is now well known that protective oxide scales can be dissolved in the presence of liquid Na_2SO_4, as Bornstein [51] showed in 1967 that nickel and chromium oxides can be dissolved in sodium sulfate.

Liang and Elliott [38] in 1967 reported a few results on the solubilities of Cr_2O_3 and Al_2O_3 in Na_2SO_4 in terms of the basicity of the melt at 1200 K. Other studies on the solubility measurements of Cr_2O_3 [39,47], Al_2O_3 [39,40,45], Co_3O_4 [41], CoO [42], NiO [41,42], Y_2O_3 [43], Fe_2O_3 [44,46], Fe_3O_4 [46], SiO_2 [48], and CeO_2 [95] in molten sodium sulfate or molten NaCl are also available in the literature. The solubility of metal oxides in molten sulfates is governed by the acidic and basic fluxing reactions of (2-4) and (2-7), respectively. Rapp and co-workers

[39,41,44,45,46,48] demonstrated that the solubility of a number of oxides in molten sodium sulfate is related to the basicity which is the activity of Na_2O, or, alternatively, the partial pressure of SO_3. In acidic fluxing, the solubility of the oxide, measured as the concentration of the metal cation, decreases as the partial pressure of SO_3 in the gas phase in equilibrium with the melt decreases. The solubility of the metal oxide reaches a minimum value and increases apparently in the more basic melts as the equilibrium concentration for the oxy-anion, described by the basic fluxing reaction, increases. Therefore, the plot of solubility of oxides versus basicity shows a curve with a V-shape as it is shown in Figure 2.1 by Jose, Gupta, and Rapp [45]. The slopes of the curve are governed by the acidic and basic fluxing reactions if the dissolution of alumina obeys the Temkin ideal ionic solution model. The acidic fluxing reaction of alumina, reaction (2-5), can be written as

$$Al_2O_3(s) + 3SO_3(g) = 2[Al^{3+}] + 3[SO_4^{2-}] \qquad (2-11)$$
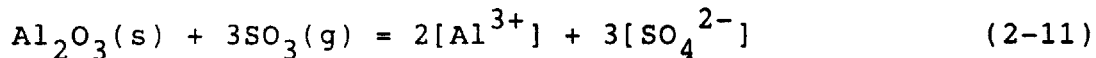
the slope in the log-log plot of concentration of oxide versus partial pressure of SO_3 is given by

$$\partial \log a_{Al^{3+}} / \partial \log P_{SO_3} = 3/2 \qquad (2-12)$$

For the basic fluxing reaction, reaction (2-9), can be expressed as
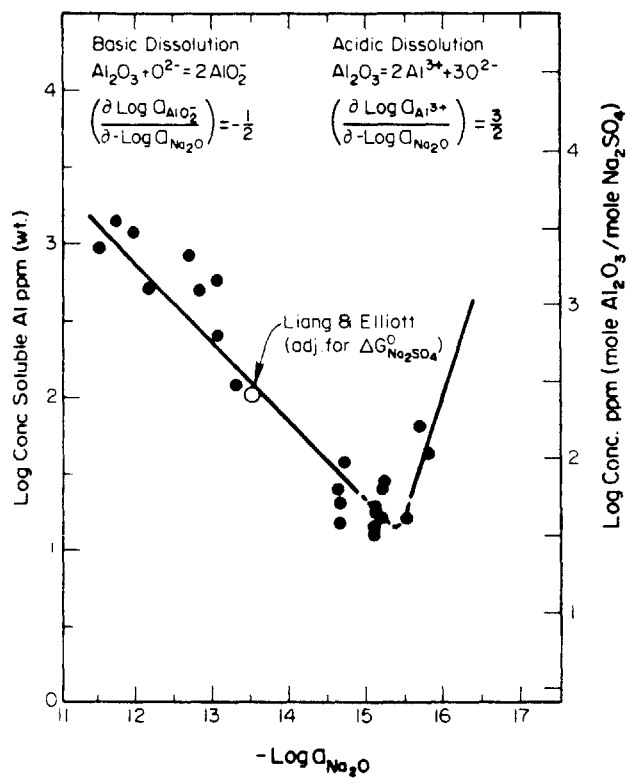
Figure 2.1 - Acidic-basic fluxing of Al_2O_3 by Na_2SO_4 at 1200 K [45].

$$Al_2O_3(s) + Na_2SO_4(l) = 2Na^+ + 2Al^{3+} + 4O^{2-} + SO_3(g) \quad (2-13)$$
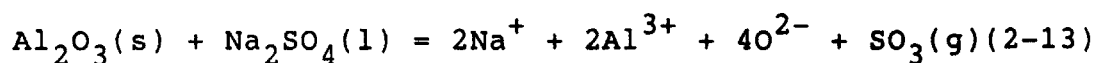
and the slope in the solubility plot is given by

$$\partial \log a_{Al^{3+}} / \partial \log P_{SO_3} = -1/2 \qquad (2-14)$$

Conflicting results on the solubility of alumina in molten sodium sulfate at 1200 K have been reported by Stroud and Rapp in 1978 [39]; Jose, Gupta, and Rapp in 1985 [45]; and Elliott, Yurek, McNallan, and Minh [40]. Stroud and Rapp [39] employed an eletrochemical cell made of a solid electrolyte of mullite to monitor the activity of Na_2O in molten Na_2SO_4, and the solubility of alumina was determined by atomic absorption analysis. Jose, Gupta, and Rapp [45] used a complicated electrochemical cell made of two solid electrolyte reference electrodes -- a sodium sensor and an oxygen probe, and a working electrode of platinum wire to monitor the activity of Na_2O and to electrochemically change the melt basicity. The sodium sensor was made of mullite as the solid electrolyte, while the oxygen probe was CaO-stabilized zirconia. The aluminum concentration in the salt was again determined by atomic absorption spectroscopy. Elliott et al. [40] made use of a rotating rod to react alumina with molten Na_2SO_4 under a known partial pressure of SO_3. Equilibrated samples were analyzed by atomic absorption spectroscopy to determine the solubility of Al_2O_3 as aluminum sulfate.

2.4 Electrochemical Measurements

To determine the acid-base equilibrium in sulfate melts, many electrochemical measurements were reported in the literature. Flood et al. [52,53] employed a porous plug to provide a salt bridge as an electrolyte. A more convenient EMF experiment employs a solid material as the ionic medium. The solid electrolytes can be divided into Na^+ and O^{2-} ionic membranes. Examples of the sodium cation membrane are borosilicate glass [54-56], porcelain [57], quartz glass [58], mullite [33,60-64], and beta-alumina [37,65-69]; whereas zirconia [59] is an oxygen anion membrane.

Several studies [70-74] have demonstrated reversible electrochemical measurements of oxygen and Na_2O (or SO_3) activities in liquid sulfates. Bornstein, DeCrescente et al. [61,62] and Shores et al. [63,64] made use of an Ag/Ag^+ reference electrode with mullite as the solid electrolyte to investigate the acid-base bebavior of sodium sulfate. The cell is represented by

$$Ag,Na_2SO_4\text{-}Ag_2SO_4 \quad \left| \begin{array}{c} Na^+ \\ \\ mullite \end{array} \right| \quad Na_2SO_4,O_2,SO_3,Pt(or\ Au)$$
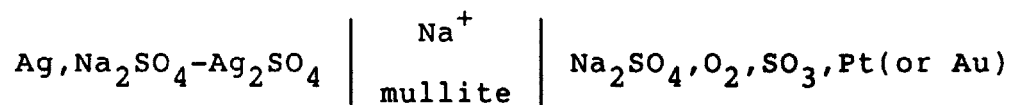
The measurement of the various investigators, however, cannot be compared directly because a standard electrode was not used. Electrochemical measurements with a beta-alumina solid electrolyte in conjunction with a platinum electrode responding to the sodium oxide activity in Na_2SO_4 have been

used by Liang and Elliott [37,66] to determine the Na_2O activity in molten sodium sulfate. The electrochemical cell can be described as

$$W,WS_2,Na_2S \quad \left| \begin{array}{c} Na^+ \\ \text{beta-alumina} \end{array} \right| \quad Na_2SO_4(l),SO_2,O_2,Pt$$
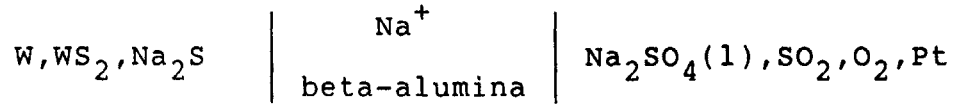
Nevertheless, the stability of the beta-alumina solid electrolyte may be jeopardized in the presence of melts with low activity of sodium oxide [75].

Stroud and Rapp [39] employed mullite as the solid electrolyte to measure the activity of sodium oxide at 1200 K in the following galvanic cell:

$$\begin{array}{c} Na_2SO_4(l),O_2(g),Pt \\ (Na_2O) \text{ anode} \end{array} \quad \left| \begin{array}{c} Na^+ \\ \text{Mullite} \end{array} \right| \quad \begin{array}{c} Na_2SO_4(l),SO_2(g),O_2(g),Pt \\ (Na_2O) \text{ cathode} \end{array}$$
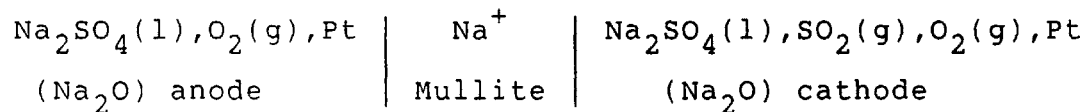
Jose, Gupta, and Rapp [45], however, noted that the EMF measurements of Stroud and Rapp [39] were probably faulty because of reactions of Na_2SO_4 with platinum in the sodium sulfate melts.

In 1985 Jose, Gupta and Rapp [45] used not only mullite as a sodium ion probe but also CaO-stablized zirconia as a oxygen probe to determine the activity of Na_2O in Na_2SO_4 at 1200 K. The sodium ion probe is represented by the cell [41]:

$$\begin{array}{c} Au,O_2,SO_3,Na_2SO_4 \\ \text{Working electrode} \end{array} \quad \left| \begin{array}{c} Na^+ \\ \text{Mullite} \end{array} \right| \quad \begin{array}{c} Na_2SO_4-10m/o\ Ag_2SO_3,Ag/Pt \\ \text{Reference electrode} \end{array}$$
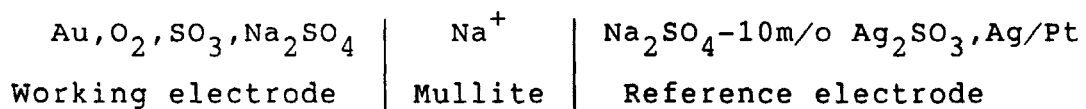
The oxygen probe is depicted by the following cell:

$$\text{air}, P_{O_2}=0.21, \text{Pt} \quad \bigg| \quad (O^{2-}) \quad \bigg| \quad Na_2SO_4, O_2, SO_3, Au/Pt$$

Working electrode $\quad\big|\quad$ ZrO_2(3.5w/o CaO) $\quad\big|\quad$ Reference electrode
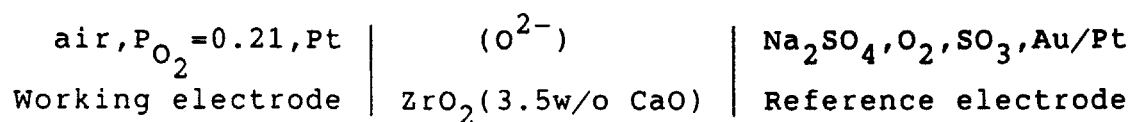
Mullite may, nevertheless, be attacked in the presence of basic melt, since Brown, Bornstein, and DeCrecente [61] observed with their EMF cell, in which the solid electrolyte was mullite, that stable potentials were never achieved after additions of Li_2O. Gupta and Rapp [41] indicated that their cell potentials showed a slight drift with time, presumably resulting from a slight attack of the mullite, zirconia, and alumina refractories. Silver in the sodium probe was found by Watt, Andresen, and Rapp [76] to have diffused through the solid electrolyte of mullite and contaminated the sodium sulfate. Watt, Andresen, and Rapp [76] also indicated that the oxygen probe with zirconia as the solid electrolyte failed to measure the correct oxygen pressure.

Recently, fused silica has successfully been applied by Mittal and Elliott [77,78] as a solid electrolyte for Na^+ ion transfer in V_2O_5-Na_2O and Na_2SO_4 melts. It was shown that clear-fused silica (GE214) has performed satisfactorily as a sodium-ion electrolyte, and it can be employed for open-circuit measurements below an activity of sodium oxide of 10^{-13} and in the temperature range of 1050-1210 K.

2.5 Solubility of Sulfur Trioxide in Sodium Sulfate

Several investigations [83-86] on the solubility of SO_3 in Na_2SO_4 have been reported primarily at low temperatures. The equilibrium reaction between sulfur trioxide and sodium sulfate produces sodium pyrosulfate according to

$$Na_2SO_4(s,l) + SO_3(g) = Na_2S_2O_7(s,l) \qquad (2-15)$$
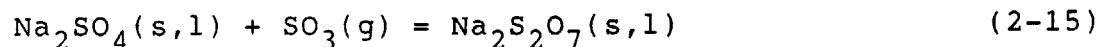
The equilibrium constant, K, is expressed as

$$K = a_{Na_2S_2O_7} / (a_{Na_2SO_4} \cdot P_{SO_3}) \qquad (2-16)$$

The apparent equilibrium constant, K', written in terms of mole fraction, X, is defined as

$$K' = X_{Na_2S_2O_7} / (X_{Na_2SO_4} \cdot P_{SO_3}) \qquad (2-17)$$

Flood and Forland in 1947 [83] conducted experiments by means of a simple gravimetric method. Samples were weighed before and after exposure to SO_3 gas in the temperature range of 828 K (555°C) to 928 K (655°C). The changes in standard Gibbs free energy and standard enthalpy for the decomposition reaction of $Na_2S_2O_7$, or the reverse of reaction (2-15), were determined to be 20.0 Kcal/mole and 30.5 Kcal/mole, respectively. The method of visual determination was employed by Coats, Dear, and Penfold [84] to investigate the effects of the partial pressure of SO_3 and temperature on the formation of the liquid phase

- 33 -

containing pyrosulfate in the system of $Na_2SO_4-SO_3$. A portion of the phase diagram of the $Na_2SO_4-Na_2S_2O_7$ system was determined for compositions ranging from 100 to 85 mole percent of $Na_2S_2O_7$. The system of $Na_2SO_4-Na_2S_2O_7$ was later investigated by Kostin, Pluzhnikov, and Ketov with a thermogravimetric apparatus at temperatures ranging from 743 K (470°C) to 853 K (580°C). The apparent equilibrium constant, K' was found to be

$$Log\ K' = -7.27 + (7500/T) \qquad\qquad (2-18)$$

Ingraham and Hotz [86] conducted static pressure measurements to study the equilibrium between Na_2SO_4 and $Na_2S_2O_7$ in the presence of SO_3 in the temperature range 747.6 K to 946.0 K. The standard Gibbs free energy change, $\Delta G°$, of the reaction (2-15) was -22,840 + 23.09 T (cal/mole). Recently, Lin [87] employed a thermogravimetric apparatus to measure the solubility of SO_3 in pure Na_2SO_4 at 1160 K, 1200 K, 1224 K, and 1250 K and the results are depicted in Figure 2.2.

Lin [87] and Mittal [88] found that the solubilities of oxygen and sulfur dioxide in molten sodium sulfate were below the detection level of the thermogravimetric apparatus employed. Andresen [89] found very small solubilities of sulfur dioxide and oxygen in molten sodium sulfate. Under the equilibrium gas mixture with partial pressures of SO_3, SO_2, and O_2 ,respectively, being 0.0869, 0.6087, and 0.3043 atm at 1200 K, the concentrations of O_2 and SO_2 in Na_2SO_4
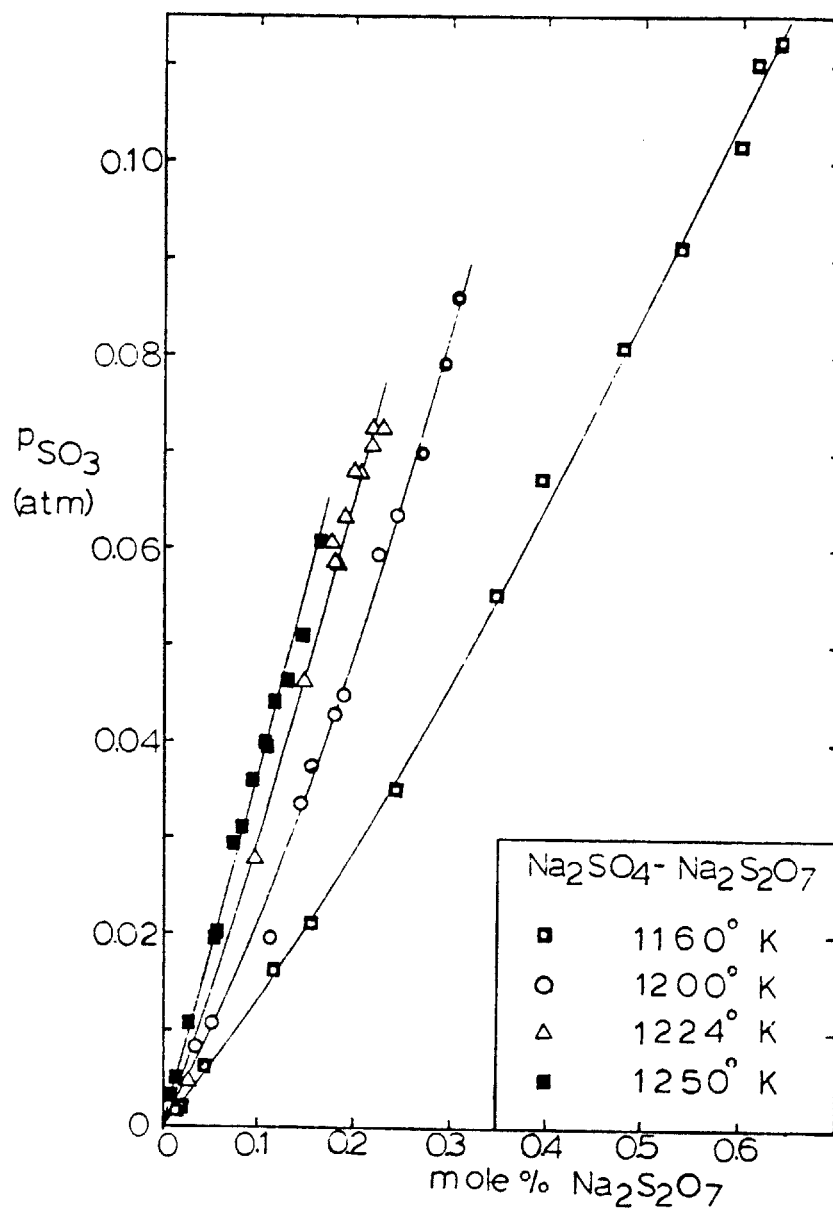
Figure 2.2 - Solubility of SO_3 in Na_2SO_4 at 1160, 1200, 1224, and 1250 K [87].

were determined to be 0.065 ppm and 0.89 ppm on a molar basis, respectively. Yurek and Deeter [90] confirmed that molten sodium sulfate remains virtually stoichiometric in the presence of equilibrium gas mixtures of SO_3, SO_2, and O_2 for P_{SO_3} in the range of 10^{-9} to 10^{-1} atm at 1200 K and 1250 K, since the density and surface tension of sodium sulfate remain independent of partial pressures of SO_3 (or SO_2 and O_2). Thus, the amounts of pyrosulfate ($S_2O_7^{2-}$), peroxide (O_2^{2-}) and superoxide (O^-) anions are present, if any, in small quantities.

2.6 Cobalt Sulfate-Sodium Sulfate System

The phase diagram of $CoSO_4$-Na_2SO_4 was investigated by Calcagni and Marotta in 1913 [24] by the method of cooling curves with visual readings. Isotherms were identified at 698 K (425°C) and at 848 K (575°C), and an eutectic transformation was found at 50 weight percent (52.17 mole percent) of Na_2SO_4. The compound of $3Na_2SO_4 \cdot CoSO_4$ was also identified. Later in 1956, Bolshakov and Fedorov [25] reported a detailed phase diagram of $CoSO_4$-Na_2SO_4 system by means of thermal analysis and visual-polythermal method. The phase diagram reported in the literature is shown in Figure 2.3; however, the eutectic reaction at 565°C violates the Gibbs phase rule. A homogenous liquid phase was shown to extend to as low as 838 K (565°C) where the eutectic transformation took place at 49 weight percent of cobalt sulfate. Three solid compounds, $Na_2SO_4 \cdot 3CoSO_4$, $Na_2SO_4 \cdot CoSO_4$
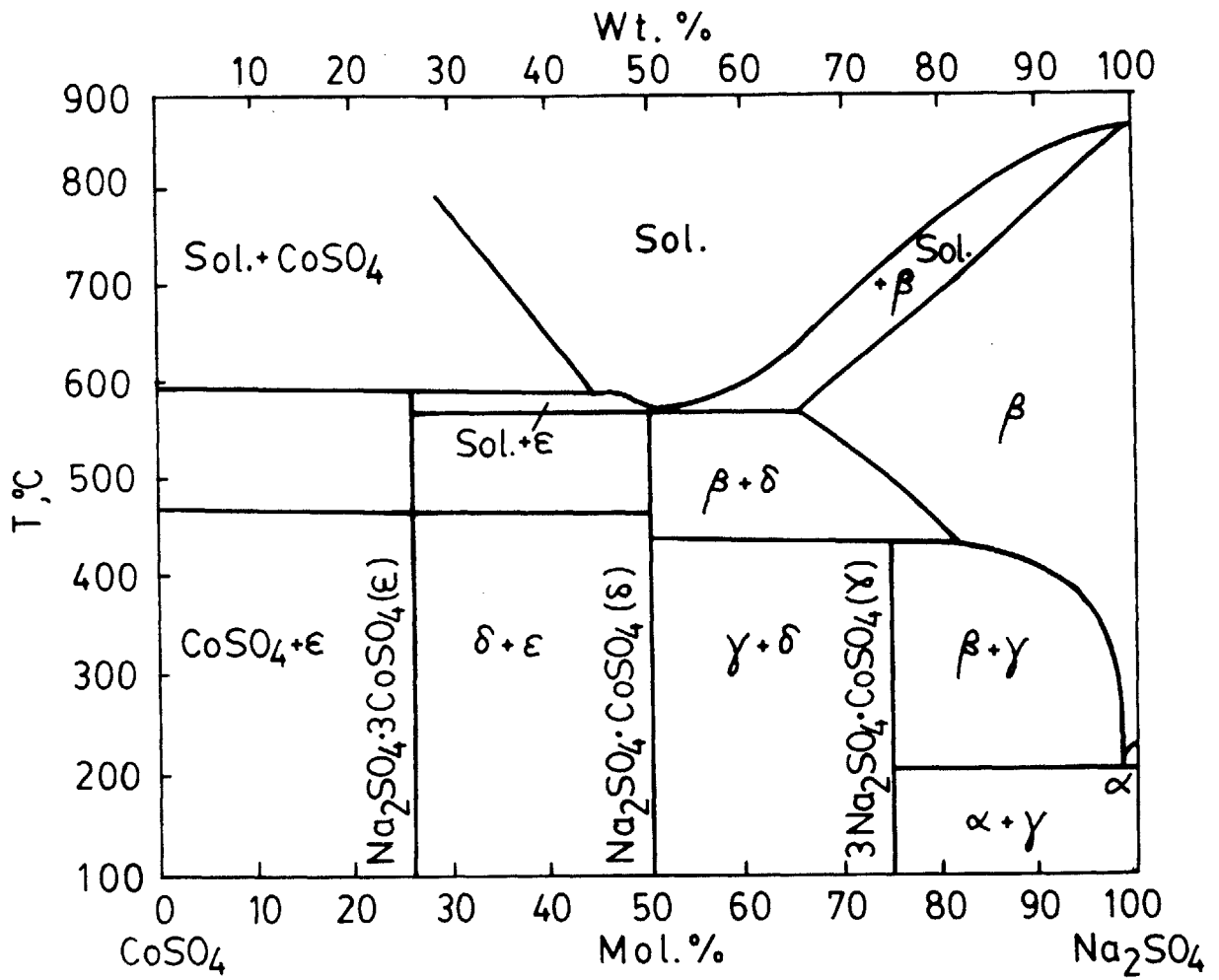
Figure 2.3 - Phase diagram of the $CoSO_4$-Na_2SO_4 system [25].

and $3Na_2SO_4 \cdot CoSO_4$, were noted in the system.

The thermodynamic properties of $CoSO_4$-Na_2SO_4 system in relation to Low Temperature Hot Corrosion have been estimated by two groups of researchers in the literature. Luthra and Shores [22,23,26,27,92] have estimated the minimum partial pressures of SO_3 to stabilize the liquid phase of $CoSO_4$-Na_2SO_4 in equilibrium with Co_3O_4 or CoO as a function of temperature and isobars of SO_3. Since there was no direct measurement in the literature on the activity of $CoSO_4$ in the liquid or solid solution of $CoSO_4$ and Na_2SO_4, their analysis was based on the phase diagram of $CoSO_4$-Na_2SO_4, and the assumption that the melt is a regular solution consisting of molecular species of Na_2SO_4 and $CoSO_4$.

Misra, Whittle, and Worrell [91], however, treated the molten salt as a random ionic solution as described by the Temkin model. The mole fraction of $CoSO_4$ was measured by weighing mixtures of Na_2SO_4-Co_3O_4 before and after reaction with the gas mixture with known partial pressure of SO_3. Their experiments did show that at high solute concentrations, the simple regular solution model may not be a very good approximation. Their analysis also estimated the minimum partial pressure of SO_3 to form a $CoSO_4$-Na_2SO_4 liquid in equilibrium with Co_3O_4 and CoO by using the estimated entropy of fusion for $CoSO_4$ of 3 cal K^{-1} g ion^{-1}.

CHAPTER THREE

OUTLINE AND PLAN OF WORK

Because of the lack of agreement of the reports on the solubility of solid Al_2O_3 in molten Na_2SO_4 in the literature, and the nonexistence of the thermodynamic properties of $CoSO_4-Na_2SO_4$ system in relation to the Low Temperature Hot Corrosion, this study is initiated to understand the physico-chemical behavior of liquid Na_2SO_4 and molten $CoSO_4-Na_2SO_4$ in the presence of SO_3 gas and Al_2O_3 solid at elevated temperatures.

The research program can be divided into two categories: (1) investigations into pure Na_2SO_4 melts; and (2) investigations into $CoSO_4-Na_2SO_4$ melts. Equilibrium and kinetic studies are undertaken to measure the solubility of $SO_3(g)$ and $Al_2O_3(s)$ in the molten salts, the activity of Na_2O in the melts, the rates of solution of $Al_2O_3(s)$ and $SO_3(g)$ in the melts.

A thermogravimetric apparatus (TGA) is employed to determine the solubility of sulfur trioxide and alumina in molten sulfates and the rate of absorption or desorption of SO_3 gas by the melt. An electrochemical (EMF) cell employing a solid electrolyte of clear fused silica is used to measure the activity of sodium oxide. A DC plasma arc elemental emission spectrometer is utilized to determine the composition of samples of melts taken from the EMF experiments. Differential thermal analysis, optical microscopy, electronic scanning microscopy, and energy

dispersive X-ray spectrometry are employed to identify phases present in the melts.

The plan of work is as follows:

(1) Measurement of the equilibrium solubility of $SO_3(g)$ in molten Na_2SO_4 at 1160 K, 1200 K, 1224 K, and 1250 K by the thermogravimetric analysis, and evaluation of the thermodynamic properties of the $Na_2S_2O_7-Na_2SO_4$ system.

(2) Determination of the activity of Na_2O in molten Na_2SO_4 from 1160 to 1250 K by the electrochemical technique, and evaluation of the thermodynamic properties of Na_2SO_4.

(3) Kinetic study of the absorption and desorption of $SO_3(g)$ in and from molten Na_2SO_4 in the temperature range of 1160 to 1250 K.

(4) Measurement of the equilibrium solubility of $Al_2O_3(s)$ in liquid Na_2SO_4 (i) by the thermogravimetric analysis at 1160 and 1200 K, (ii) by equilibrations in the EMF experiments with simultaneous monitoring of the activity of Na_2O at 1200 K. The aluminum concentration in the melt is determined by DC plasma arc elemental emission spectroscopy.

(5) Kinetic study of the solution of $Al_2O_3(s)$ in molten Na_2SO_4 by equilibrating the melt with pure $Al_2O_3(s)$. The aluminum concentration in the melt is measured by DC plasma arc elemental emission spectroscopy at 1200 K.

(6) Measurement of the equilibrium solubility of $SO_3(g)$ in liquid $CoSO_4-Na_2SO_4$ by the thermogravimetric analysis at 1100 K.

(7) Determination of the activity of Na_2O in liquid $CoSO_4-Na_2SO_4$ by the electrochemical method at 900 K to 1250 K, and evaluation of the thermodynamic properties of the $CoSO_4-Na_2SO_4$ system.

(8) Measurement of the equilibrium solubility of $Al_2O_3(s)$ in molten $CoSO_4-Na_2SO_4$ by the thermogravimetric analysis. The concentration of aluminum is determined by atomic absorption techniques.

(9) Identification of phases in the system of $CoSO_4-Na_2SO_4$ by differential thermal analysis, scanning electron microscopy, and energy dispersive X-ray spectroscopy.

(10) Implications of this study on the Na_2SO_4-induced hot corrosion.

CHAPTER FOUR

EXPERIMENTAL APPARATUS AND PROCEDURE

Two experimental techniques are employed in the study:
(1) thermogravimetric analysis (TGA), and (2) electromotive
force (EMF) measurements in which the equilibrated melt is
sampled for chemical analysis. Chemical analysis by plasma
arc elemental emission spectrometry and phase identification
by differential thermal analysis (DTA) are also performed on
samples taken during the EMF experiments.

4.1 Thermogravimetric Analysis (TGA)

The molten sulfate phase contained in either a platinum
or an alumina crucible is equilibrated with various partial
pressures of $SO_3(g)$ at temperatures ranging from 1100 to
1250 K. To obtain the desired partial pressure of $SO_3(g)$ at
the reaction temperature, a mixture of gases of
predetermined composition is prepared with pre-purified
argon, oxygen, and sulfur dioxide gases. A stream of this
gas mixture is introduced over the melt at a rate of 100 to
120 ml(STP) per minute. The total pressure of the
equilibrated gas mixture is one atm. Step changes in the
partial pressure of $SO_3(g)$ are made periodically at each
temperature by changing the partial pressures of O_2 and SO_2
appropriately, and for each step, the weight of the melt and
crucible are recorded continuously until no further weight
change is detected.

4.1.1 TGA Experimental Apparatus

The experimental apparatus shown in Figure 4.1 consists of: (1) a gas train which purifies the reaction gases, controls the gas pressures, and measures the gas flows of argon, oxygen, and sulfur dioxide; (2) a Kanthal resistance furnace; (3) a Leed and Northrup temperature controller (model Electromax III); (4) an Ainsworth thermobalance (model RV) with its Ainsworth recording unit (model No. Bristol AU-1); and (5) a reactor in which melt samples are exposed to the gas stream.

The gas train is made primarily of Pyrex glass to handle the three gases -- O_2, SO_2, and Ar. The sources and purities of materials employed in this study are listed in Appendix A. All gases are dried before entering individual capillary flowmeters. Oxygen and argon are respectively purified in magnesium perchlorate and ascarite columns; sulfur dioxide is passed through a column containing phosphorus pentoxide. The flowmeters indicate gas flowrates by means of the pressure difference across a capillary tube through which the gas flows. The gas flowrate is controlled by regulating the pressure in the system by a bleeder installed before the flowmeter. The DC 550 silicone oil is the fluid employed in the adjustable bleeders and the flowmeters. The oxygen and sulfur dioxide are mixed in a chamber filled with glass beads before they are introduced into the reactor. The argon gas is delivered directly to purge the upper chamber of the reactor after it passes
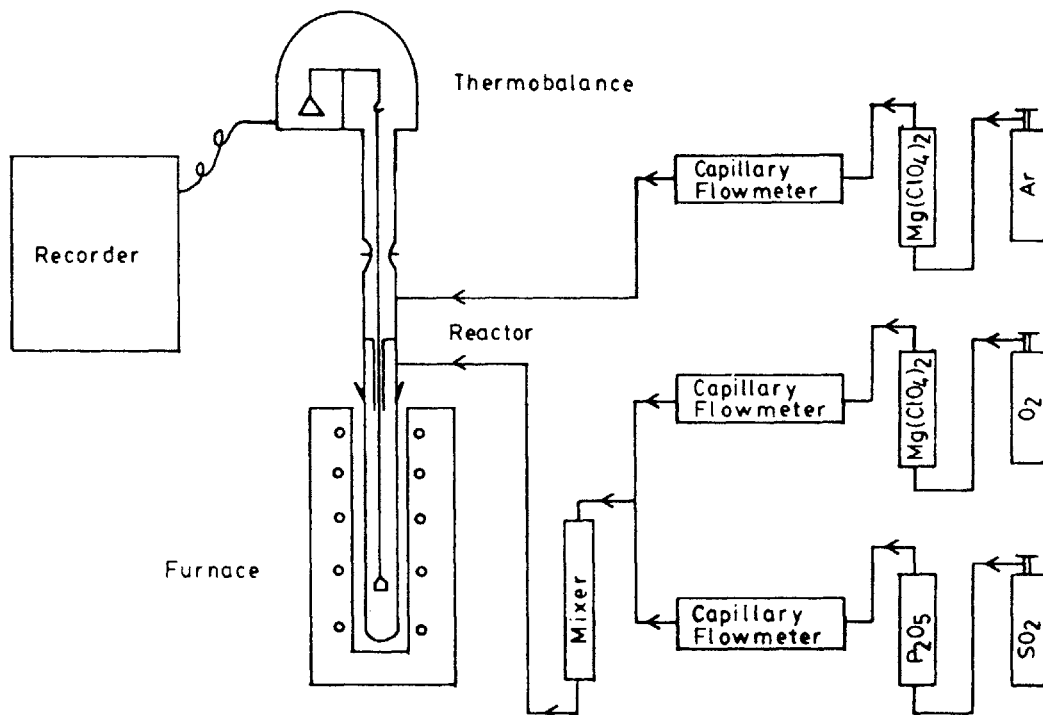
Figure 4.1 - Apparatus of thermogravimetric analysis.

through the flowmeter. All the flowmeters are calibrated with a 100 ml soap bubble column for gas flowrates exceeding 30 cc/min, and with a 5 ml soap bubble column for gas flowrates equal to and less than 30 cc/min. Every few runs and each time a gas cylinder is replaced, the calibrations are checked; all measured flowrates agree to within 2 percent.

A vertical tube furnace is the high-temperature heat source (350 mm height, 170 mm diameter) heated by a Kanthal Fe-Cr-Al-Co resistance wire wound around a mullite tube (51 mm O.D., 45 mm I.D., 350 mm length). Ceramic bricks and high-temperature ceramic fibers are placed around the mullite tube to form a 59 mm thick insulation layer. The furnace is situated on a laboratory jack which can adjust the vertical position of the furnace. A control thermocouple of Pt/Pt-10%Rh sheathed with double-bore alumina beads (3.2 mm O.D., 1.0 mm I.D.) is placed in the mullite furnace tube and its tip is located at 90 mm above the bottom of the furnace. The thermocouple employed for temperature control feeds signals to a temperature controller. The temperature profile of the TGA furnace has been determined to note that a constant temperature hot zone of 50 mm long is located 70 mm above the bottom of the furnace. The temperature of the furnace is controlled to within ±1 degree Kelvin of the desired temperature with the PID temperature controller.

The thermobalance is a semi-microbalance equipped with an automatic weight-changing mechanism on its balance arm. The maximum allowable weight change is 400 mg. The weight change interval for each addition or subtraction is 10 mg. The sensitivity of the thermobalance reading is limited to ± 0.1 mg because of a small disturbance of the crucible arising from convective currents in the reaction chamber. The weight of the crucible is continuously recorded with a wide-strip chart recording unit.

The reactor shown in Figure 4.2 is composed of two parts. The top half, constructed of Pyrex glass, is attached to the enclosure of the thermobalance and the bottom half, made of clear quartz, encloses the reaction crucible. They are joined together with a ball/socket ground joint (size 65/40). The lengths of the top and bottom half are respectively 320 mm and 275 mm, the outer diameter is 38 mm. The reactor also has three clear quartz tubulations; one of which has its lower end closed and contains the thermocouple for sensing the temperature of the molten salt, a second with an opened lower end delivers the reaction gas stream to a point 20 mm above the melt surface, and a third which is centrally located and through which passes the platinum suspension wire for the crucible.

A stream of argon flowing at a rate of 30 ml(STP)/min in the upper chamber keeps the reaction gases away from the thermobalance. This gas flow is insurance against the possibility of destroying the balance by the reaction gas.
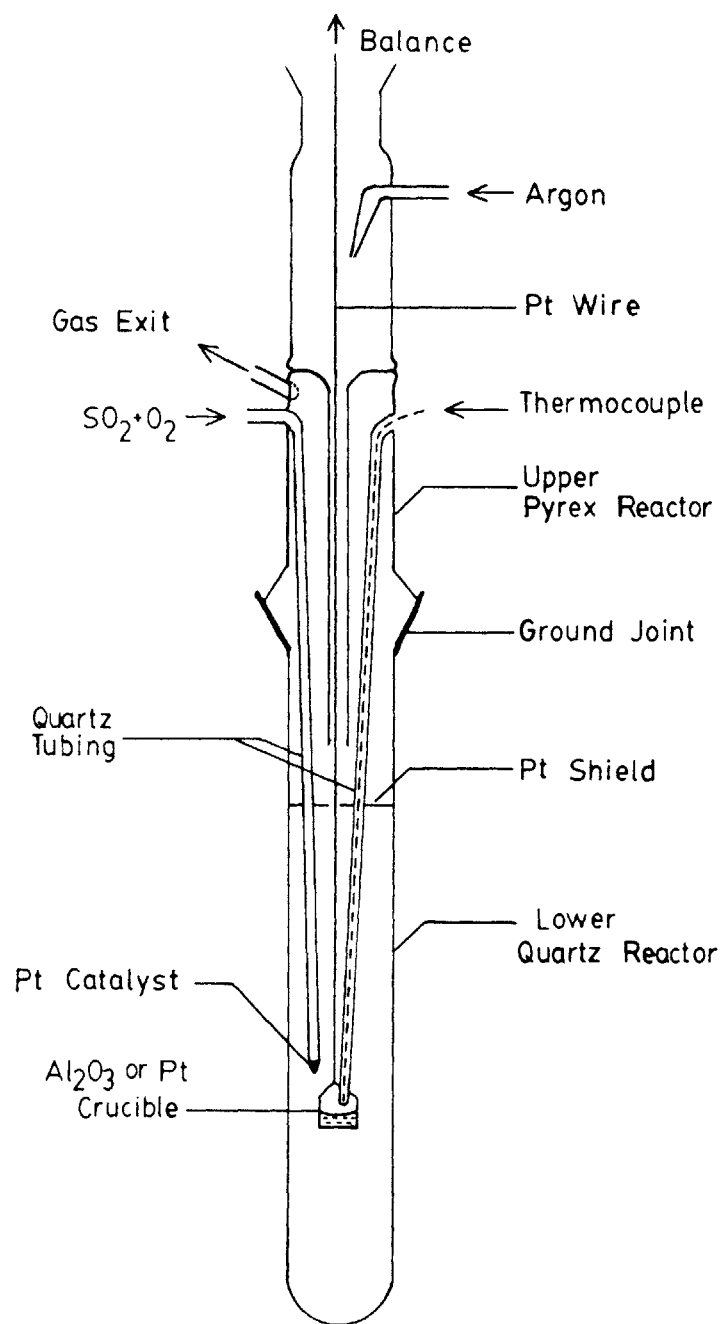
Figure 4.2 - Reactor of thermogravimetric analysis.

It passes down along the suspension wire into the lower chamber of the reaction tube and then out the exit port. This flow also prevents condensation of vapors from the reaction chamber on the suspension wire. A cylindrical alumina crucible (Coors, Cat. CN-10, nominally 99.8% Al_2O_3, 22 mm O.D., 19 mm I.D., and 17.5 mm height) or a cylindrical platinum crucible (24 mm O.D., 16 mm height, and 0.3 mm thickness) is suspended to the thermobalance with the platinum suspension wire (0.254 mm diameter, 1.3381 gm weight, CP grade). This wire passes through the central quartz tube (9 mm O.D., 180 mm length). The gas mixture of SO_2 and O_2 or SO_2, O_2 and Ar with a total flowrate of 100 to 120 ml(STP)/min is introduced into the reaction chamber through a 6 mm O.D. quartz tube extending down to 20 mm above the rim of the crucible that is suspended from the balance arm. A platinum gauze shaped into a basket is fitted over the end of the gas inlet tube. It acts as a catalyst to assure that the reaction to form SO_3:

$$SO_2(g) + 1/2\ O_2(g) = SO_3(g) \qquad\qquad (4\text{-}1)$$

reaches equilibrium as the gas mixture passes into the reactor. A platinum shield (30 mm diameter) is placed at approximately 100 mm above the crucible to reduce the effects of gas convection and the radiation heat loss from the hot zone of the furnace, and to prevent the dilution of the reaction gas by the argon. A gas outlet is located at the lower chamber of the upper reactor.

A Pt/Pt-10%Rh (Type S) thermocouple outfitted with an ice-cold water junction is positioned in the closed-end quartz tubulation (6 mm O.D.) within the reactor with its tip positioned 10 mm above the melt surface. The thermocouple is calibrated in air against the melting point of gold. The calibration is performed according to the wire method (see Appendix C) employing a gold wire 0.254 mm diameter by 10 mm length. The heating rate of 0.5 K per minute is employed in the calibration. The melting point of gold is measured to be 1334 K (1061°C); however, the actual melting is recorded to be 1337.4 K (1064.4°C) [96]. A correction of 3.4 K is added to the temperatures measured by the thermocouple to obtain accurate temperature readings. Temperature readings are measured with a Leed and Northrups potentiometer (model No. 298861) and a Fluke digital multimeter (model No. 8050A). It is estimated that the temperature of the melt in crucible is known to within ± 1.5 K.

4.1.2 TGA Experimental Procedure

At the start of the TGA experiment, materials are prepared before they are charged to either a platinum or an alumina crucible. The platinum crucible is employed only in experiments with pure sodium sulfate; the alumina crucibles are used with pure Na_2SO_4 melts as well as $CoSO_4-Na_2SO_4$ melts. Sodium sulfate (J.T.Baker, anhydrous, analytical reagent grade) is further purified to remove any possible

moisture in the salt. The sodium sulfate contained in a pre-weighed silica crucible is weighed on an Ainsworth analytical balance (Type 10V) which is calibrated to 0.1 mg precision; it is then placed and sealed in a low-temperature Pyrex tube furnace. The dehydration process of heating to 723 K (450°C) under a vacuum of -100 kilopascals maintained by a rotary vacuum pump (W.M.Welch; model Duo-Seal) is carried out for at least two days. Upon completion of the drying process, the sodium sulfate placed in a weighing bottle is weighed again and stored in a sealed container within a desiccator for future use. The percentage of weight loss of the sodium sulfate ranging from 0.0052 to 0.044 is determined after the drying process. The results of drying sodium sulfate are listed in Table 4-1. The platinum or alumina crucible is weighed before two grams of Na_2SO_4 are placed in the crucible. Weighing is performed again after the sulfate is added. The sodium sulfate contained in the crucible is, thus, ready for the TGA experiment on pure sodium sulfate only.

In TGA experiments on sulfate mixtures of cobalt and sodium, the $CoSO_4$-Na_2SO_4 melt is prepared by removing the water from the cobaltous sulfate, $CoSO_4 \cdot 7H_2O$ (MCB, crystal, reagent grade), and adding the purified Na_2SO_4 to the cobalt sulfate. The $CoSO_4 \cdot 7H_2O$ contained in an alumina crucible is weighed on the analytical balance after the weight of the crucible has been determined. The cobaltous sulfate is then heated up to 723 K (450°C) in air for at least 5 hours in a vertical tube furnace to get rid of the water molecules. At

TABLE 4-1

Drying of Sodium Sulfate
at 450°C under vacuum at -100 kilopascal

Date	Duration day	Original Wt gram	Final Wt gram	% Wt. Loss
01/19/84	4	18.2466	18.2385	0.044
08/26/84	2	47.7726	47.7619	0.022
03/23/85	4	13.5161	13.5105	0.041
06/26/85	2	9.5760	9.5738	0.023
10/18/85	6	7.6878	7.6848	0.039
02/03/86	2	27.0424	27.0410	0.0052
03/26/86	47	30.2630	30.2578	0.017
07/17/86	4	35.9281	35.9247	0.0095*
10/10/86	19	35.5049	35.5019	0.0084
10/29/86	6	35.6186	35.6124	0.017*
11/20/86	11	32.2555	32.2517	0.012
12/02/86	53	29.1485	29.1469	0.0055
03/06/87	11	28.5600	28.5572	0.0098

* No weight change is detected after a repeated drying.

the end of the drying period, the alumina crucible with its content is transferred to a pre-weighed weighing bottle and air-cooled. Until the bottle reaches room temperature, weighing is conducted again. The measured final weight of $CoSO_4$ is checked against the theoretical weight calculated from stoichiometry to ensure complete dehydration. The results of the drying of $CoSO_4 \cdot 7H_2O$ are presented in Table 4-2. The ratio of the theoretical weight of $CoSO_4$ to the actual weight ranged from 0.9605 to 0.9905; the drying period varies from 5 to 24 hours. The cobaltous sulfate may not have seven molecules of water per mole of cobaltous sulfate. Sadakane, Kawakani, and Goto [93] confirmed by X-ray diffration that complete dehydration is achieved by heating the $CoSO_4 \cdot 7H_2O$ to 673 K – 723 K (400°C – 450°C) in air for 5 hours. A pre-determined quantity of the purified Na_2SO_4 is added to the $CoSO_4$ contained in the alumina crucible inside a glove bag filled with argon gas. Weighing bottles and glove bags are utilized to prevent the sulfates from absorbing moisture in air during the preparation process. The total weight of the sulfate mixture is approximately equal to two grams. The alumina crucible with its content of sulfates is placed in a weighing bottle and weighed again to find out the exact weight of the sodium sulfate added. The sulfate mixture contained in the crucible is, therefore, ready for the TGA experiment.

TABLE 4-2

Drying of $CoSO_4 \cdot 7H_2O$

at 450°C in air

Date	Time hour	$CoSO_4 \cdot 7H_2O$ original Wt gram	Actual final Wt gram	Theoret. final Wt gram	$\dfrac{Wt\ CoSO_4,th}{Wt\ CoSO_4,ac}$
10/21/83	5 days	21.5152	11.9825	11.8678	0.9904
11/28/83	18	6.1235	3.4615	3.3777	0.9758
12/02/83	5	4.4572	2.5119	2.4586	0.9788
12/28/83	5	1.2422	0.7024	0.6852	0.9755
01/05/84	5	0.7774	0.4393	0.4288	0.9761
02/03/84	6	1.1553	0.6536	0.6373	0.9751
03/01/84	7	1.5644	0.8890	0.8629	0.9706
04/03/84	18.25	1.8906	1.0750	1.0424	0.9696
06/11/84	6	0.7768	0.4461	0.4285	0.9605
01/26/85	6	1.8927	1.0818	1.0436	0.9647
10/07/86	16.2	18.9558	10.5976	10.4519	0.9863
11/04/86	17.3	19.0941	10.6295	10.5281	0.9905
12/01/86	23	9.7201	5.4161	5.3595	0.9895
02/02/87	23	28.1470	15.6762	15.5197	0.9900
03/02/87	24	14.5201	8.0927	8.0061	0.9893
03/17/87	14	32.5618	18.1445	17.9540	0.9895
03/25/87	24	32.5718	18.1571	17.9595	0.9890
03/31/87	11	9.7217	5.4163	5.3829	0.9897
04/06/87	17	23.6767	13.197	13.0549	0.9892

where   Wt $CoSO_4$,th = theoretical final weight
      Wt $CoSO_4$,ac = actual final weight

Upon completion of the material preparation, the thermobalance and the recording unit is calibrated with a 10 mg standard weight. The upper half of the reactor is then sparingly covered with vacuum grease at the ball/socket ground joint and attached to the thermobalance with a clamp. The platinum suspension wire is secured to an arm of the thermobalance after it is carefully passed through the balance and the reactor. This wire is aligned with great care in the reactor to ensure it is free hanging. The alignment can be facilitated by employing a small radioactive unit to get rid of the static electricity created on the reactor surface. The crucible with two grams of sulfate is attached to the suspension wire when the wire is free from touching the central tubulation of the reactor. The lower half of the reactor is then clamped to the upper half, and the resistance furnace is raised up to the point that the crucible is located in the hot zone 70 mm above the bottom of the furnace. Several layers of high-temperature alumina silica ceramic fibers (Kaowool by Babcock and Wilcox) are laid on top of the furnace around the reactor to reduce heat loss to the atmosphere. The system is therefore fully assembled; the reactor is then flushed with argon introduced in the upper half of the reactor. The crucible and its contents are weighed continuously as the system is brought up to the selected temperature and the gas is changed to the ratio of pressures of O_2 to SO_2 required for the experiment. When the preselected temperature is reached, the weight measurement is monitored continuously by

the wide-strip chart recorder during absorption or desorption of sulfur trioxide gas until weight change is less than the detection limit of ± 0.1 mg for at least two hours. Equilibrium between the gas and melt is thus assumed to have been reached. Subsequently, the temperature or gas composition, or both, is altered in steps for additional measurements to be made. At the end of the experiment with the reaction gases flowing, the furnace and the lower portion of the reactor chamber are lowered to expose the melt to a draft of air from a fan. In this way the melt is cooled quickly such that the temperature is reduced to below 500 K within 5 minutes.

Chemical analysis is used to investigate the amount of alumina dissolved in the molten sulfate. Samples are obtained by drilling the solidified melt with a clean 1/4 in. steel drill. On a number of experiments, samples are taken from the upper, middle, and lower levels in the melts to check for possible segregation of aluminum. The concentrations of aluminum in the salt are determined by the atomic absorption method. No segregation of aluminum is detected within the limit of precision of ± 0.01 weight percent in the analytical procedure.

4.1.3 Thermobalance Corrections

To ensure the validity and accuracy of the experimental results, the issues of (1) buoyancy and gas impingement effects, (2) solubility of oxygen and sulfur dioxide in the sodium sulfate, and (3) internal equilibrium of the reaction gases are determined before experimental results are analyzed.

4.1.3.1 Buoyancy and Gas Impingement Effects

The buoyancy effect is caused by a change in gas density from altering the temperature and from changing the gas composition. The gas impingement effect arises when moving gas molecules bombard against the crucible and the melt; thus, flowing gases exert an additional pulling force, and the effect increases with temperature. Control experiments are undertaken to determine the buoyancy and gas impingement effects on platinum and alumina crucibles containing an alumina rod which is of the same volume of the sulfate melt. Weight changes are recorded under different gas compositions and at each preselected temperature. The gas impingement effect is obtained by subtracting the buoyancy force calculated from the Archemede's Principle from the measured weight change. Therefore, necessary corrections on the order of 1 to 2 mg are to be applied to the experimental results.

4.1.3.2 Solubility of Oxygen and Sulfur Dioxide

Lin [87], Mittal [88], Andresen [89], and Yurek and Deeter [90] all found a very small solubility of oxygen and sulfur dioxide in molten sodium sulfate; as it has been shown in Section 2.5. The absorption/desorption of sulfur dioxide and oxygen by the sulfate melt is checked again by observing the weight of the sample while changing the partial pressures of SO_2 and O_2 in the gas and, at the same time, maintaining a constant partial pressure of SO_3. The fact that no weight change is recorded within the precision limit of ± 0.1 mg indicates that only sulfur trioxide is responsible for the weight increase or decrease, respectively, during gas absorption or desorption process.

4.1.3.3 Equilibrium of the Reaction Gases

The chemical equilibrium among reaction gases of oxygen, sulfur dioxide, and sulfur trioxide is verified by two types of tests to ensure that partial pressures of sulfur trioxide can be calculated from the thermodynamic data of reaction (4-1). The first test is conducted by changing the total flowrate of the inlet gases at a constant ratio of SO_2 to O_2, thus, maintaining a constant partial pressure of SO_3 in the reactor. The results show that no weight change is detected within the precision limit of the thermobalance. In the second test, the reaction gases are changed from O_2-rich regime to SO_2-rich regime at a constant

temperature as the partial pressure of SO_3 is increasing, going through a maximum, and decreasing. The maximum weight increase is shown to correspond to the peak in the partial pressure of SO_3. The two tests prove that equilibrium in the gaseous phase is well established in the TGA reactor.

4.2 Electromotive Force (EMF) Measurements

During the EMF measurements, activities of sodium oxide in either the pure sodium sulfate or the cobalt-sodium sulfate and temperatures of the melt are measured respectively with an electrochemical cell and a Pt/Pt-10%Rh thermocouple. Samples are also extracted periodically to study the aluminum concentration in the molten Na_2SO_4 and the phase relationship in the $CoSO_4-Na_2SO_4$ system during equilibration experiments.

4.2.1 Principles of The Electrochemical Cell

The electrochemical measurements provide a means of measuring the electromotive force (EMF) of a cell and, thus, determining the activity of sodium oxide in the molten sulfates. The following EMF cell is utilized for the experiment:

| Pt, O_2(g) | Na^+ | Pt, O_2(g), SO_2(g) |
| Na_2O-WO_3(l) | fused silica | Na_2SO_4(l) or $CoSO_4-Na_2SO_4$(l) |
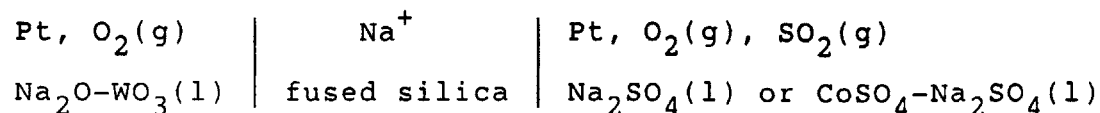
The activity of sodium oxide in the Na_2O-WO_3 melt has been determined by Lin and Elliott [68]. The anodic reaction occurring in the Na_2O-WO_3 reference melt is:

$$(Na_2O)_r = 1/2\ O_2(g)_r + 2Na^+ + 2e^- \qquad (4-2)$$
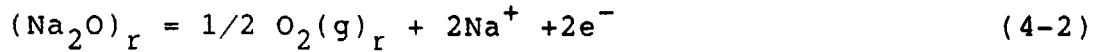
where the subscript r signifies that the species belongs to the reference melt. The cathodic reaction occurring in the sulfate working melt is:

$$1/2\ O_2(g)_w + 2Na^+ + 2e^- = (Na_2O)_w \qquad (4-3)$$
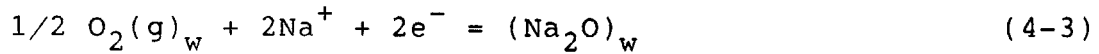
where the subscript w signifies that the species belongs to the working melt. By summing reactions (4-2) and (4-3) the overall reaction is:

$$(Na_2O)_r + 1/2\ O_2(g)_w = (Na_2O)_w + 1/2\ O_2(g)_r \qquad (4-4)$$
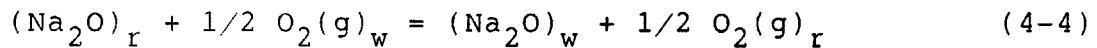
The corresponding Nernst equation with E(0) being zero in a concentration cell is written as:

$$E = -(RT/2F)\ \ln[(a_{Na_2O,w} \cdot P_{O_2,r}^{1/2})/(a_{Na_2O,r} \cdot P_{O_2,w}^{1/2})] \qquad (4-5)$$

where E is the cell potential; R is the universal gas constant; F is the Faraday's constant (96,487 coul/mole); T is the cell temperature in Kelvin; a_i is the activity of the species i; and P_{O_2} is the partial pressure of oxygen which is related to P_{SO_3} by the equilibrium reaction (4-1). This

- 59 -

can be further arranged to

$$\log a_{Na_2O,w} =$$

$$\log a_{Na_2O,r} - (1/2)\log(P_{O_2,r}/P_{O_2,w})-(2FE/2.303RT) \quad (4-6)$$

Hence, the activity of sodium oxide in the sulfate cathode melt can be calculated by knowing the cell potential. The standard states for sodium oxide and oxygen are pure liquid Na_2O and pure O_2 gas at 1 atm pressure.

4.2.2 EMF Cell

A schematic diagram of the electrochemical cell is shown in Figure 4.3. Pure sodium sulfate or mixtures of $CoSO_4$ and Na_2SO_4 is employed as the working melt in this study. The working melt of sulfate is contained in either a conical alumina crucible (Coors; cat. CC-50, 99.8% Al_2O_3, 53 mm height, 45 mm top O.D., 36 mm bottom O.D., 2.1 mm thickness) or a conical platinum crucible (30 mm height, 45 mm top O.D., 30 mm bottom O.D., 0.2 mm thickness). Thirty particles of tabular alumina (ALCOA; T-61, 99.5+% Al_2O_3, 0.06% SiO_2, 0.06% Fe_2O_4, 0.10% Na_2O, 6 to 8 mesh) are also charged to the pure sodium sulfate during Al_2O_3 solubility study to enhance the rate of equilibration. The crucible is in turn placed in another outer conical alumina crucible (47 mm height, 47 mm top O.D., 27 mm bottom O.D., 1.4 mm thickness) in the furnace. The sulfate melt is contained in the inner crucible; the outer crucible protects the furnace
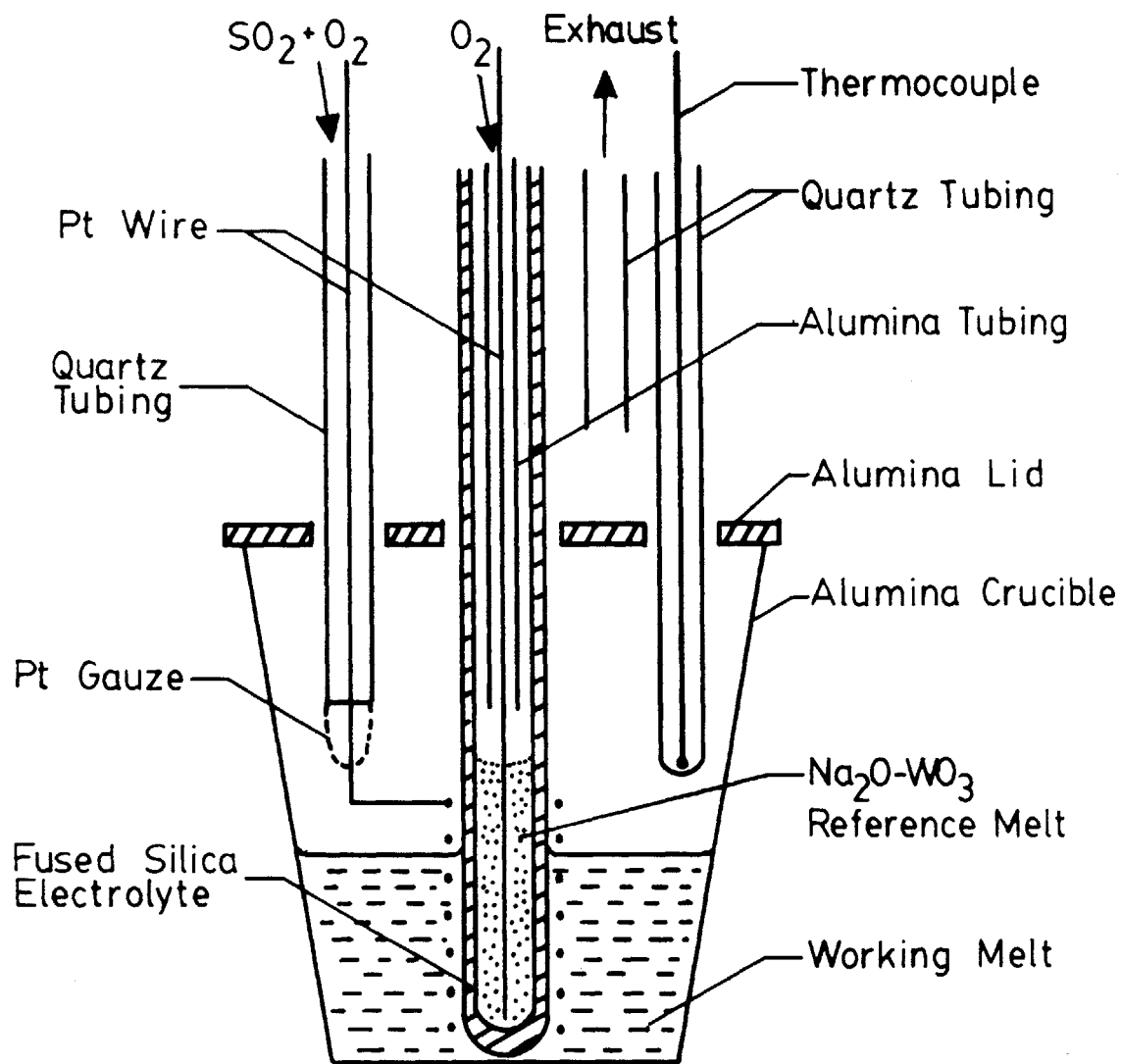
Figure 4.3 - Electrochemical cell.

tube from attack by the melt in the case of inner crucible failure. The outer crucible is attached with two platinum wires; it serves as a basket to transfer the melt in and out of the furnace tube. The outer and the inner crucibles are situated on top of bubble alumina 60 mm above the bottom of the furnace tube. A sintered alumina plate with four ports to admit a solid electrolyte, a thermocouple with its protective quartz tube, a sampling quartz tube, a gas inlet quartz tube, and a gas exhaust quartz tube covers the crucible. Either the thermocouple or the sampling tube is placed in the furnace at any point of time during the experiment.

The solid electrolyte is a clear quartz tube (General Electric 214, 4 mm I.D., 6 mm O.D., 609 mm length) that is closed at the lower end with a flame torch. This quartz tube, which contains approximately 0.9 gm of the sodium tungstate reference melt and a platinum lead wire (0.5 mm diameter, CP grade), is dipped into the sulfate working melt during EMF measurements. The lead wire is sheathed in a round single-bore alumina tube (McDanel; 99.8% Al_2O_3, 1.6 mm I.D., 2.4 mm O.D., 609 mm length), and it acts as the negative electrode or the anode. The lower end of the platinum lead wire is in contact with the reference melt, while the protective single-bore alumina tube is placed 10 mm above the reference melt. Oxygen for the reference electrode is passed at a rate of approximately 10 ml per minute and at a total pressure of one atmosphere down the interior of the protective alumina tube and up the annulus

between the alumina tube and the electrolyte tube. The
system is arranged so that the electrolyte tube can be
dipped in the sulfate melt to the bottom of the crucible or
it can be withdrawn such that its tip is approximately 10 mm
above the surface of the sulfate melt.

A Pt/Pt-10%Rh thermocouple is constructed of two lead
wires passing into a round double-bore alumina tube
(McDanel; 99.8% Al_2O_3, 3.2 mm O.D., 1.0 mm I.D., 762 mm
length), and a bead is made on the lower end of the wires
with a flame torch. The thermocouple is then sheathed in a
protective closed-lower-end quartz tube (4 mm I.D., 6 mm
O.D.), and its tip is extended to approximately 10 mm above
the surface of the working melt. The thermocouple outfitted
with an ice-cold water junction is calibrated against the
melting point of gold by the wire method. A correction of
5.5 K is added to the temperature measured by the
thermocouple to obtain the actual temperature of the melt.

The sampling tube is a clear quartz tube (4 mm I.D., 6
mm O.D.) and it is connected to a syringe by a 889 mm long
flexible tygon tube. A piece of platinum gauze of 52 mech
placed at the tip of the tube acts as a filter to prevent
solid phases from being sucked up during sampling in
experiments with pure sodium sulfate. The gauze is
positioned inside the tube and is fixed in place by a
platinum wire (0.254 mm diameter, CP grade) running along
the length of the tube. The tube is employed to extract
samples of 1 to 2 gm from the sulfate melts after the

thermocouple has been withdrawn from the furnace, since the sampling tube and the thermocouple are using the same port in the brass head of the furnace.

The gas inlet tube (4 mm I.D., 6 mm O.D., 609 mm length) which is made of clear quartz extends to approximately 10 mm above the surface of the working melt, and it also carries the connecting platinum lead wire (0.5 mm diameter, CP grade) for the sulfate melt. This wire is the positive electrode or the cathode, and it passes through the platinum gauze cap fitted over the end of the gas inlet tube. · Ten turns of it are wound around the tip of the electolyte tube. The platinum gauze is placed at the end of the gas inlet tube to ensure internal gas equilibrium.

The gas exit tube is a quartz tube (4 mm I.D., 6 mm O.D., 609 mm length), and its tip is extended 10 mm above the cover plate of the crucible. The exhaust gases pass through the exit tube, then through a condensation trap constructed of a 500 ml Pyrex filter flask before it is vented to a hood.

The EMF cell is housed in a mullite furnace tube (McDanel MV 30 grade; 57 mm O.D., 51 mm I.D., 508 mm length). This tube is closed on the lower end; a water cooled brass head is attached to the top of the tube. The head consists of an upper plate and a lower plate. The two plates are held together by means of four screws and they are sealed together by means of a rubber O-ring. The lower plate is secured to the mullite tube. The upper plate is

- 64 -

equipped with four gas tight fittings (Cajon Untra-Torr;
6.35 mm I.D., 9.53 mm O.D.) through which passes the
electrolyte tube, the gas inlet tube, the gas outlet tube,
the thermocouple tube, and the sampling tube. Either the
thermocouple tube or the sampling tube is placed in the cell
at any point in time. The mullite tube is in turn mounted
in a vertical tube furnace (Lindbery 1773 K single-zone tube
furnace, model No. 54233) which is heated by 8 pieces of
silicon carbide hot rods (Kanthal; XL, 406 mm overall
length, 127 mm heating zone, 12.7 mm diameter), and the
temperature of which is controlled by an electronic
controller (Leeds and Northrup 6261 Electromax). A constant
temperature zone with a length of 100 mm is determined to be
located at 60 mm above the bottom of the mullite furnace
tube. A total of two electrochemical experiments are set
up, the second electrochemical cell is constructed in the
identical manner as the one described, except the
temperature of the furnace is controlled by a Eurotherm
controller (model No. 810) incorporated in a Lindberg
control console (model No. 59545).

The gas train for the EMF measurements is essentially
the same as that for the TGA apparatus described earlier.
Pure sulfur dioxide and oxygen are employed to produce
equilibrium partial pressures of sulfur trioxide greater
than 0.008 atm. Below this SO_3 pressure, equilibrium
partial pressures of sulfur trioxide are generated by
reacting oxygen with 4.9%, 0.93%, or 119 ppm SO_2-Ar gas
mixture.

The entire EMF experimental apparatus is incorporated with a Cyborg ISAAC data-acquisition and control system and an Apple II+ computer for temperature and EMF measurements and temperature control. A schematic diagram of the computer peripherals used for measurement and control of the EMF experiment is shown in Figure 4.4. The ISAAC system consists of a main board, 41A expansion box, which is connected to the Apple II+ computer by an ISAAC/Apple interface card installed in slot No. 4 of the Apple. The 41A expansion box provides interface slots to three modules: (1) I-100 analog/digital (A/D) converter modules; (2) I-120 binary input/output (I/O) module; and (3) I-130 preamp interface modules installed in slot Nos. 0, 1, and 2 of the 41A main board, respectively. The I-140 remote preamp system is connected between the I-130 module and the thermocouple.

The potential of the electrochemical cell is measured with the I-100 A/D converter module. The A/D converter is capable of 12 bit resolution over a nominal conversion time of 25 microseconds and a channel acquisition time of 100 microseconds. The input impedance is 10^8 ohms and the input range is setted at ± 2500 mv. The module is operated in the true differential mode with an accuracy of $\pm$ 0.05% of the full scale or ± 2.5 mv for each sampling. An experimental point is an average of 1000 samplings; thus, the accuracy of each EMF measurement amounts to ± 0.079 mv.
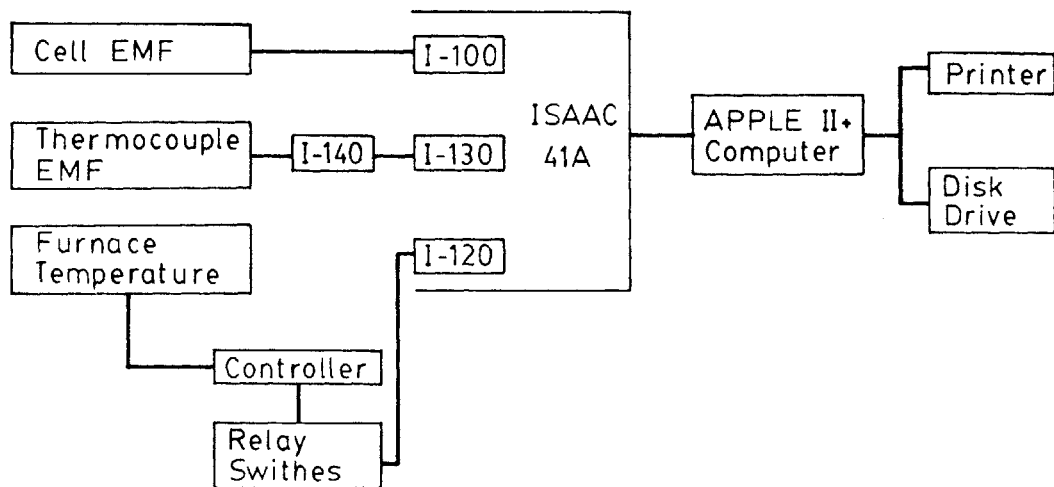
Figure 4.4 - Computer peripherals used for measurement and control of the EMF experiment.

The potential of the thermocouple is measured with the I-130 preamp interface module and the I-140 remote preamp system. The I-130 provides channel selection, analog/digital conversion, and programmable cold-junction compensation functions; the I-140 supplies input protection, and accurate and low drift amplification for a variety of low level signals. The input impedance is 1.8 x 10^5 ohms and the input range is $\pm$100 mv. The I-130 module is capable of 12 bit resolution with a convertion delay of 2.5 milliseconds. Both I-130 and I-140 are configurated to be compatible with type S thermocouples. The two modules possess an accuracy of $\pm$0.3% full scale or $\pm$0.3 mv for each sampling. An experimental point is an average of 1000 sampling; therefore, the accuracy of each temperature measurement equals to $\pm$0.009 mv or $\pm$1 K.

Computer control of the furnace temperature is acheived by connecting the modified Electromax temperature controller and the ISAAC system with the I-120 binary I/O module. Signals from two channels are used to control a 5 volt DC motor which is mechanically connected to the temperature setting of the Electromax furnace controller. The temperature setting of the Electromax controller is programmed to be within $\pm$10 K of the selected temperature.

The computer software of the computer system is enhanced by the language "Labsoft" provided by the ISAAC system. The "Labsoft" is an extension of the "Applesoft" language of the Apple II+ computer. Programs are written

using both of these languages to control and change the temperature of the EMF cell and measure cell potential and temperture. Several programs have been written to obtain measurements of cell potential and temperature from either one or two experiments carried out at the same time. A program used to run equilibrium measurements with two EMF cells is included in Appendix D.

The system is arranged so that readings of cell potential and temperature can be taken simultaneously at periods from 30 seconds to 15 minutes. Each set of measurements is printed out by a dot-matrix printer (IBM Proprinter) and is stored simultaneously in a floppy disk. The temperature of the furnace is programmed to change automatically after the potential and temperature of the cell are constant within ± 0.5 mv and ± 1 K, respectively, over a set period of time, usually 30 minutes. At such time, equilibrium is assumed to be attained. Therefore, measurements are obtained from the cell around the clock. The type S thermocouple is calibrated against the gold point, and, including the uncertainty associated with digitizing the potential, the temperature of the cell is known to within ± 1.5 K of the true value.

The outputs of the cell is sampled for a period of 25 microseconds every 10 milliseconds for a total of 1,000 measurements to obtain an experimental point. The rate of sampling is essentially 100 samplings per second. The average of this set of measurements is recorded as the

potential of the cell for the point. Set of readings are taken at intervals from 30 seconds to 15 minutes. During the equilibration experiments the interval of 5 minutes is employed, each EMF point is compared with the point taken 30 minutes ago. If the two values agree within ± 0.5 mv for 6 measurements (30 minutes), the cell potential is assumed to have reached equilibrium. The temperature is sampled and compared in the same manner as the cell potential. If the cell temperature remains constant within ± 1 K for 30 minutes, the criterion for equilibrium in the temperature is assumed to be reached. The final cell equilibrium is assumed to be attained when both EMF and temperature readings satisfy simultaneously their respective criterion for 30 minutes.

Periodically, the recorded potentials of the cell and the thermocouple are checked with a high-impedance pH meter (Beckman model Phi 71), a null potentiometer (Leeds and Northrup model 298861), and a digital multimeter (Fluke model 8050A). This is to test the reliability of the measurements. Measurements with the pH meter, the potentiometer, and the digital multimeter agree with the recorded potential within one or two millivolts. After some experience with the recording system, and because of this agreement, it is concluded that the computer driven measuring and recording system give satisfactory results. The EMF experiment is constructed in such a way that two electrochemical cells are connected to the ISAAC system; thus, two EMF experiments are able to be conducted

simultaneously.

4.2.3 EMF Experimental Procedures

The reference melt of sodium tungstate is prepared
according to the method given by DeYoung [94]. The
preparation procedure of the sodium tungstate melt is
included in Appendix B. Either sodium sulfate or a mixture
of cobalt sulfate and sodium sulfate is employed as the
working melt. The sodium sulfate is prepared according to
the same procedure described in the TGA experiment. It is
purified at 723 K (450°C) under vacuum for at least five
days. Thirty grams of the purified sodium sulfate are
placed in either a platinum or an aluminum crucible for EMF
experiments on pure sodium sulfate. During the
equilibration experiments using pure sodium sulfate and
alumina crucibles, thirty particles of alumina of sizes
ranging from 6 to 8 meshes are also charged to the crucible.

To prepare mixtures of Co-Na sulfates, precautions are
taken in handling the cobalt sulfate by using weighing
bottles and a glove bag because of the hygroscopic nature of
$CoSO_4$. A pre-determined amount of cobaltous sulfate,
$CoSO_4 \cdot 7H_2O$, contained in a silica crucible is heated to
723 K (450°C) in air in a vertical tube furnace for at least
two days to remove the water molecules. Upon completion of
the dehydration period, the material is placed immediately
in a pre-weighed weighing bottle to be air-cooled to room

temperature before weighing. The weight of the cobaltous sulfate after drying is checked against the weight of cobalt sulfate calculated from stoichiometry to ensure complete dehydration. The changes in weight during the drying process of $CoSO_4 \cdot 7H_2O$ are presented in Table 4-2. The cobalt sulfate is later transferred to an alumina crucible in a glove bag filled with argon gas. Finally, a selected weight of the purified sodium sulfate is added, inside the glove bag, to the alumina crucible to create a mixture of Co-Na sulfates of pre-specified compositions. During the preparation, every container with its content is weighed before and after material transfer to determine the actual amount of sulfate that has been added. Only alumina crucibles are utilized for the experiments with Co-Na sulfate mixtures. A total weight of 30 gm of the sulfate mixture is employed for the EMF experiments with $CoSO_4-Na_2SO_4$.

The solid electrolyte is fabricated by closing off one end of a clear fused quartz tube (GE214) with a flame torch. Two small elongated pieces of quartz tubes (approximately 10 mm length, 1 mm diameter) are attached with a flame torch to the outer surface of the electrolyte at a distance of 50 mm away from the tip of the closed end. The two elongated tubes extending out from the electrolyte provide support to the alumina cover plate of the crucible. The reference melt of sodium tungstate with a weight of 0.9 grams are charged to the electrolyte tube.

After the working and reference melts have been placed in their respective containers, the electrochemical cell is ready to be assembled together. The solid electrolyte, the thermocouple with its protective quartz tube, the gas inlet tube, and the gas exhaust tube are passed through the four gas-tight fittings located at the water-cooled brass head. The positive electrode platinum wire accompanied with the platinum gauze cap is then installed in the gas inlet tube; the end of the wire is wound around the tip of the electolyte tube. The negative electrode lead wire sheathed in an alumina tube is inserted into the electrolyte tube.

The next step is to put the cell together in the mullite furnace tube. The alumina or platinum crucible containing the sulfate melt is placed in the furnace tube, before the brass head with the four tubes is lowered on the furnace at the temperature of 800 K. The furnace tube is subsequently sealed and flushed completely with the reaction gas of SO_2 and O_2 or SO_2-Ar and O_2, while the furnace is heated gradually to the selected temperature. Oxygen is allowed to pass to the reference melt at a rate of approximately 10 ml per minute at a total pressure of one atm. After the working melt has been maintained for a few hours at the selected temperature, the equilibration between the working and the reference melts begins when the electrolyte is dipped into the working melt.

Before the EMF measurements are started, the cell is allowed to equilibrate overnight. Cell potential and temperature readings are taken at a set period of time ranging from 30 seconds to 15 minutes. The experiment is carried out under the conditions that either the temperature or the partial pressure of SO_3 is varied in steps. The system is programmed in such a way that when the cell equilibrium criteria have been satified, the temperature of the furnace is changed automatically to within 10 K of the pre-selected temperature. Thus, measurements at different temperatures at a constant ratio of inlet O_2 to SO_2 can be obtained around the clock. To gether EMF data at different partial pressures of SO_3 at a constant temperature, the flowrates of the reaction gases are altered manually by setting the bleeders of the flowmeter at selected levels; however, measurements are taken automatically by the computerized data acquisition system.

Samples of the sulfate melt are taken periodically to examine the aluminum concentration in the melt. Prior to sampling, a quartz tube (GE214, 4 mm I.D., 6 mm O.D.) is connected to a syringe with a flexible tygon tube. A piece of platinum gauze of 52 mesh is placed at the tip of the sampling quartz tube to prevent picking up of any solid particles. The quartz tube is inserted through the water cooled brass plates and down into the melt after the thermocouple has been withdrawn. A sample weighing approximately one gram is drawn into the sampling tube with the aid of the syringe, the tube with sample is then removed

rapidly from the system and allowed to cool to room temperature in air. The samples are subsequently dissolved in deionized water. The dissolved samples are analyzed for the aluminum content with a D.C. plasma arc elemental emission spectrometer (Beckman SpectraSpan V Direct Current Plasma Emission Sequential Spectrometer) by comparing against standard solutions made up of dissolved pure aluminum and sodium sulfate.

During the studies on pure sodium sulfate, granular sodium peroxide, Na_2O_2, is added to the melt on several occasions to increase the activity of sodium oxide, Na_2O, in molten Na_2SO_4. The sodium peroxide is dehydrated before it is employed in the experiment. A batch of sodium peroxide weighing approximately 5 grams is placed in a vertical tube furnace, and is heated to 423 K (150°C) under a vacuum of -100 kilopacals for 19 hours. Upon completion of the drying period, the sealed furnace tube and its content is put in a glove box filled with argon gas. The dehydrated sodium peroxide is weighed and stored in a gas-tight container for future use inside the glove box.

When sodium peroxide is employed in the molten sodium sulfate, a portion of the purfied sodium peroxide is taken from the gas-tight container and placed in a special addition device inside a glove bag filled with argon gas. The weight of the sodium peroxide employed in the EMF experiment ranges from 7 to 81 mg. The special addition device, shown in Figure 4.5, consists of a Pyrex glass tube

glass tubing

clamp

tygon tubing

glass tubing

Na_2O_2 powder

tygon tubing

clamp
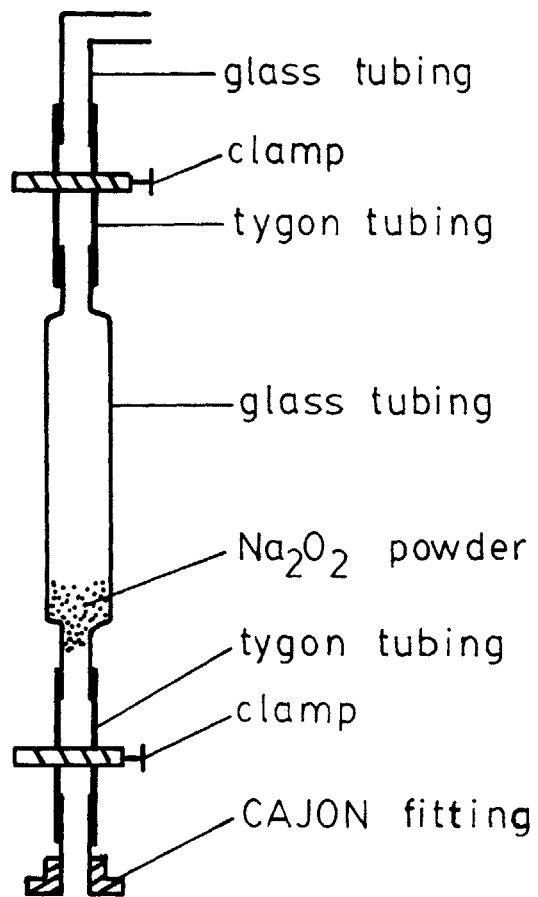
CAJON fitting

Figure 4.5 - Sodium peroxide addition device.

(11.5 mm O.D., 7 mm I.D., 110 mm length), two 65 mm long
tygon tubes, an Ultra-Torr Cajon fitting, a glass tube with
a 90° angle, and two clamps. The glass tube with a 90°
angle is attached to the top of the Pyrex glass tube with a
tygon tube; on the other end, the fitting is joined to the
bottom of the Pyrex glass tube with another tygon tube. The
two clamps are used to create a gas tight atmosphere in the
Pyrex glass tube by closing down the two tygon tubes located
at the two ends. The glass tube with a 90° angle acts as a
joint for an oxygen inlet tube; thus, the oxygen gas can be
utilized to purge the Pyrex tube and facilitate droppings of
the sodium peroxide into the furnace.

Prior to the Na_2O_2 addition, a quartz tube (GE214, 6 mm
O.D., 4 mm I.D., 609 mm length) is connected to the addition
device containing sodium peroxide at the Cajon fitting.
After the thermocouple has been removed from the furnace,
the quartz tube is passed through the water-cooled brass
head and extends to about 10 mm above the surface of the
melt. The sodium peroxide is released to the melt by
untightening the lower clamp of the addition device. In
several cases, oxygen is purged from the top of the addition
device to push all the sodium peroxide into the furnace.
After the addition, the quartz tube with the addition device
is removed and the thermocouple is put back in place. The
addition device is weighed before and after the Na_2O_2
release to determine the actual weight of the sodium
peroxide added to the sulfate melt. During the addition
process, the cell potential is measured every 15 seconds to

monitor the change in the activity of sodium oxide in sodium sulfate.

At the end of the experiment, the cell assembly is withdrawn from the mullite tube and quenched with a draft of air from a fan. The tip of the electrolyte is sectioned and inspected for attack by either the reference or the working melt. Even after an electrolyte is used for over 100 hours, no erosion internally or externally is observed. After the experiment with Na_2SO_4 or Co-Na sulfates, the alumina crucible is noted to be attacked most severely at the gas/liquid interface, a distinct band of concave area is observed. However, no attack is found in the platinum crucible after experiment with pure Na_2SO_4. Each run is started with all new cell materials except for the platinum wires and thermocouple.

4.3 Supporting Experiments

A number of experimental techniques are employed to analyze samples taken from molten melts equilibrated under a selected experimental condition. Chemical analysis employing a DC plasma arc elemental emission spectrometer and differential thermal analysis (DTA) are carried out solely by the author as part of the experimental program to determine the concentration of aluminum in sulfate melts and to find out possible phase transformations in the Co-Na sulfate system, respectively. The two analyses will be

described in detail in the following sections. Other sample analysis techniques including atomic absorption spectrometry, optical microscopy, scanning electron microscopy (SEM), and energy dispersive of X-ray spectrometry (EDX) are also performed at facilities available at M.I.T.

4.3.1 Chemical Analysis by Plasma Emission Spectrometry

Two methods are employed to measure the concentration of aluminum in sodium sulfate. Atomic absorption spectrometry is employed for TGA samples at high concentrations of aluminum. This method is somewhat uncertain at concentrations below approximately 10 ppm. Most of the analyses, particularly those below 10 ppm, are made with a DC plasma arc elemental emission spectrometer (Beckman, model SpectraSpan V). Care is taken to avoid problems with matrix effects. Frequent standardization measurements are performed in a series of determinations, and each standard solution contains a concentration of sodium sulfate equivalent to that in the unknown solution. For aluminum concentrations below 5 ppm, more concentrated solutions are employed to avoid the restriction set by the detection limit of the instrument (i.e. 0.002 mg/l Al in the solution). The analysis with the DC plasma arc elemental emission spectrometer will be described in detail in the following sections.

4.3.1.1 The Spectrometer

The direct-current plasma arc elemental emission spectrometer (Beckman, model SpectraSpan V DC Plasma Single Channel) features a high-energy DC plasma excitation source and a high resolution Echelle grating. Liquid samples are converted to aerosol form and introduced into the excitation region.

The spectrometer has a three-electrode excitation source where the argon plasma is sustained by two DC arc path discharging from the tungsten cathode to the two graphite anodes. The ceramic sleeves which surround the electrodes are made of alumina. During operation, argon gas flows through the sleeves and around the electrodes. The fluid sample, introduced via a peristatic pump and nebulizer, enters the plasma as an aerosol through the wide orifice sample introduction tube. Argon serves as the carrier gas for the sample. The excitation region, or area of observation, is located below the plasma continum where there is a very high signal to background ratio.

The Echelle grating and prism in the optics module separate the emitted light into its component wavelengths and create a two-dimensional spectral pattern. This compact spectrum permits access to wavelengths from 190 nm to 800 nm. The ultra high performance Echelle grating resolves these lines 5 to 10 times better than conventional monochromators. A resolution of 0.0019 nm in the UV is permited by the grating.

The intensity of the emitted light at predetermined wavelengths is proportional to the concentration of the element unique to these wavelengths. For quantitative analysis, optical cassettes are used to extract information from the spectrum. The cassettes serve as masking devices, allowing one or more selected wavelengths to pass to a detector module. One or more photomultiplier tubes in the detector convert the light energy to a proportional electric current. Based on front panel switch settings, the resulting currents are converted to a voltage and amplified. The computer then uses a calibration curve to convert the measured voltage to a value representing the actual concentration of that element. This conversion curve is developed by measuring two known concentrations of that element prior to the test and, assuming a linear relationship between measured voltage and element concentration, interpolating the measured voltage and determining a measured concentration. Results are outputed in digital form to a dot matrix printer.

4.3.1.2 Chemical Analysis Procedure

To conduct chemical analysis with the DC plasma arc elemental emission spectrometer, the following operations are carried out: (1) changing anodes, cathodes, and sleeves; (2) aligning electrodes and sample introduction tube; (3) igniting and adjusting the plasma -- adjust sleeve and nebulizer flow; (4) optimizing viewing zone; (5) peaking

in an emission line; (6) setting analytical parameters --
set integration time and repeats; (7) establishing
calibration curve -- input high standard and low standard;
(8) running a sample and evaluating the data; and (9)
updating/recalibrating standard curve. The specific
procedures are included in Appendix E.

The chemical analysis requires a lot of standard
solutions to be made before actual analysis is performed.
Two primary standard solutions are prepared for sodium and
aluminum. These standards are later used to prepare working
standard solutions for actual chemical analysis. The types
of standard solutions that have been employed in this study
are listed in Appendix F.

The sodium primary standard solution is prepared by
dissolving anhydrous sodium sulfate in deionized water. The
Na_2SO_4 is heated at 450°C under vacuum for at least two days
to ensure complete dehydration before it is utilized.
Sodium sulfate of 61.7841 g is added to a beaker containing
400 ml of deionized water. The beaker with its content is
warmed up on top of a hot plate until dissolution of sodium
sulfate is complete. A plastic bottle is weighed with a
digital balance (Sartorius, model 1518) before the solution
is transferred to the bottle. The solution in the plastic
bottle is further diluted with deionized water to obtain a
solution with a total weight of one kilogram. The process
of dilution is taking place on top of the digital balance,
thus instantaneous weight measurements is recorded. The

concentration of the sodium standard is determined to be 19.9995 g Na/kg solution.

The aluminum primary standard is created by dissolving approximately one gram of high purity aluminum pellets in deionized water. The pre-determined aluminum pellets are placed in a beaker before 50 ml of concentrated HCl is added. The beaker with its content is heated up on top of a hot plate until dissolution of aluminum is complete. The solution is then diluted with deionized water to achieve an one-kilogram solution on top of the digital balance. The aluminum primary standard of 0.9998 g Al/kg solution is stored in a plastic bottle for preparations of working standard solutions.

Two methods of preparation of working standards from the primary standard solutions have been employed during the course of study -- dilution by volume and dilution by weight. During the investigation on the effects of sample matrix, working standards are prepared by diluting the solutions to a total volume of one liter in a volumetric flask. Testing solutions are also diluted by volume during the investigation. During actual sample analysis, sample dilution to an uniform level of sodium in background and the unit of concentration expressed in parts per million (ppm) by weight are desired, the working standard solutions are therefore made by diluting with deionized water to a total weight of one kilogram during actual sample analysis. Unknown samples taken from EMF experiments are also diluted
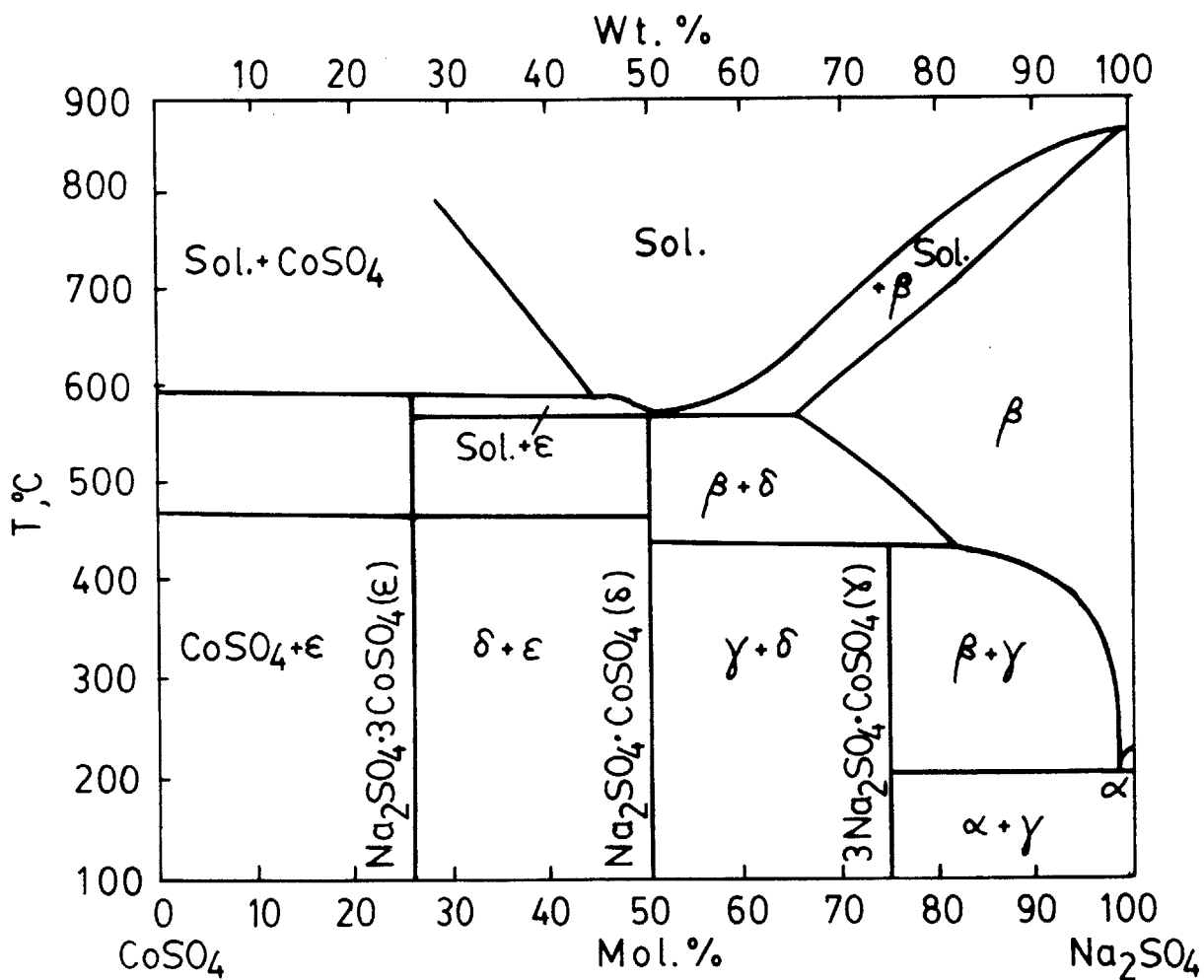
Figure 2.3 – Phase diagram of the $CoSO_4$–Na_2SO_4 system [25].
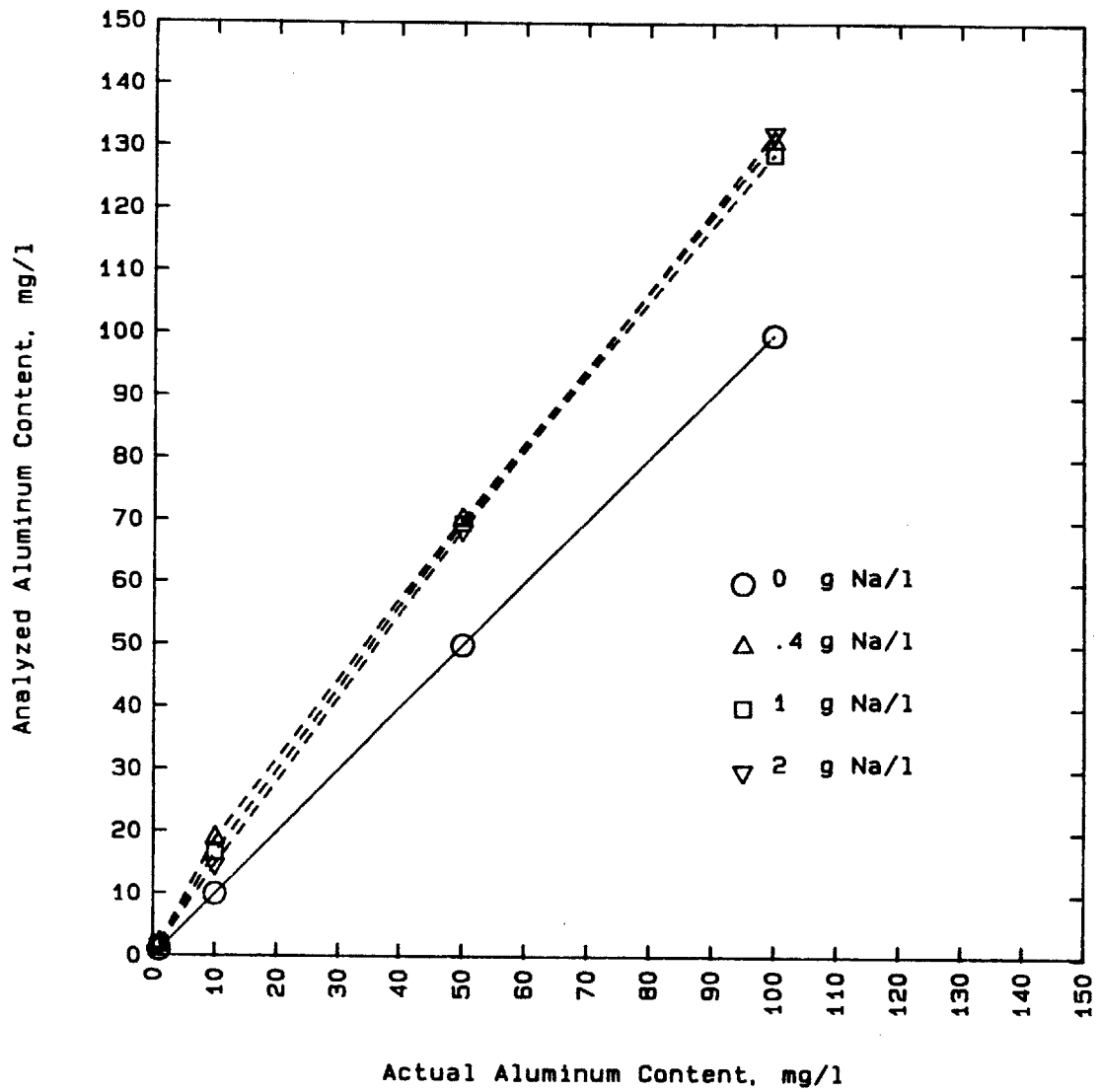
Figure 4.6 - Effects of sodium on aluminum standards, pure aluminum solutions as standards.

standards, respectively. The results of the test are shown in Figure 4.7. The sodium in the background is again observed to be important in the chemical analysis. The analysis on testing solutions with sodium in the background shows a much accurate result than on pure aluminum testing solutions. It is therefore concluded that accurate chemical analysis is to be conducted by comparing unknown samples and standard solutions containing identical amount of Na_2SO_4 in the background. The samples and standards are decided to be diluted with deionized water to maintain one gram of sodium in the background in all the sample analysis.

Samples taken with a quartz tube (6 mm O.D.) from the EMF experiment are to be dissolved in deionized water. The portion of the quartz tube containing the solidifed sample is cut off with a glass tubing cutter, and it is then weighed. The tube and its content are placed in a beaker filled with approximately 50 ml of deionized water. When the dissolution of sample is complete, the quartz tube is rinsed with sprays of deionized water above the beaker. The weight of the clean quartz tube is recorded to determine the weight of sample dissolved and the amount of dilution. The content of the beaker is subsequently transfered to a pre-weighted plastic bottle for further dilution. The unknown sample is diluted by weight to the concentration of one gram of sodium in the background on a digital balance. Chemical analysis is later performed with the spectrometer to determine the aluminum concentration. The most intense wavelength of aluminum of 396.152 nm with a detection limit
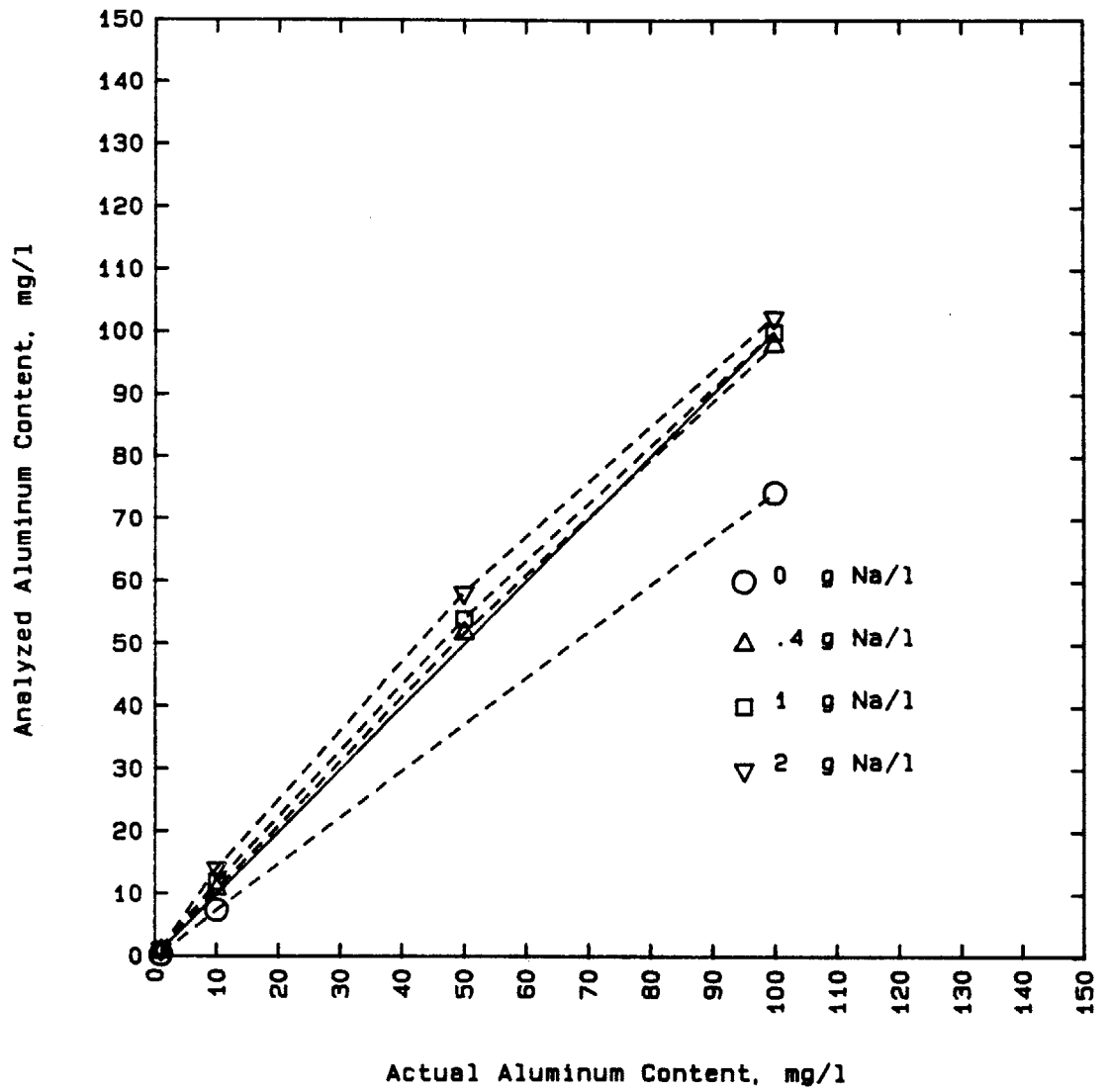
Figure 4.7 - Effects of sodium on aluminum standards, Al solutions with 1 g Na/l as standards.

of 0.002 mg/l is employed during the analysis.

4.3.2 Differential Thermal Analysis (DTA)

During the investigation into the system of $CoSO_4-Na_2SO_4$, the electrochemical measurements are not in agreement with the phase diagram in the literature shown in Figure 2.3. Further investigation into the possibility that another phase might exist in the liquid field of the phase diagram is proceeded. The differential thermal analysis is therefore employed to identify possible phase transformation and to detect transformation temperature.

4.3.2.1 DTA Apparatus

The differertial thermal analysis apparatus depicted in Figure 4.8 consists of a DTA analyzer (Perkin-Elmer DTA 1700 High Temperature Differential Thermal Analyzer), a control module (Perkin-Elmer System 7/4 Microprecessor Controller), and a X-Y recorder (Perkin-Elmer $X-Y_1-Y_2$ recorder). The DTA analyzer includes a high temperature furnace and the cell base for the furnace. The system measures the differential temperature changes between sample and reference materials, in the range between ambient and 1500°C, due to phase transformation and chemical reaction such as sample decomposition. The temperature of the furnace can be programmed to raise and lower at a linear rate. The

SYSTEM 7/4 CONTROL MODULE

SYSTEM 4

FURNACE

DTA 17CC DIFFERENTIAL
THERMAL ANALYZER

X-Y1-Y2 RECORDER
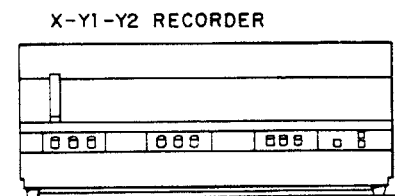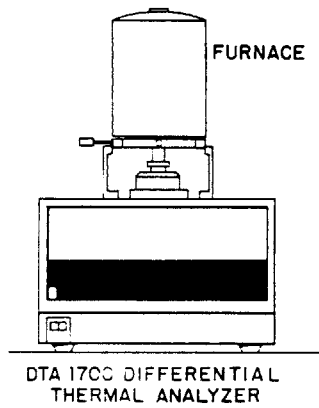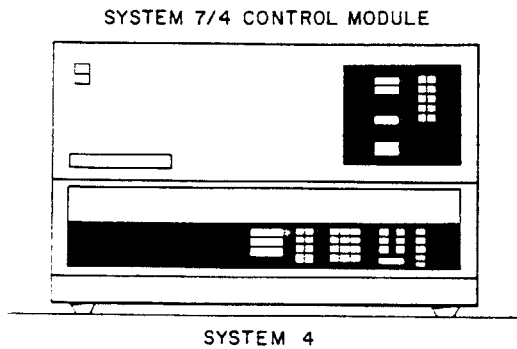
Figure 4.8 - Apparatus of differential thermal analysis.

temperature through which the sample is being heated is displayed as the X (abscissa) value on the X-Y recorder; the differential temperature (ΔT) appears as the Y (ordinate) value.

Two thermocouples constructed of platinum and platinum/10% rhodium are used to monitor the temperatures of both the sample material and the reference material (see Figure 4.9). The thermocouples are sheathed in an alumina protective tube (1.6 mm O.D., 160 mm length) and wired together to measure the differential temperature, ΔT, which represents the temperature derived from subtracting the reference temperature from the sample temperature. The sample is placed in a 100 mm^3 cylindrical alumina liner which is, in turn, placed in a platinum cup (5.1 mm O.D., 4.7 mm I.D., 4.5 mm height). The whole assembly is then placed on top of the sample thermocouple. The reference material of alumina powder is mounted in the same way as the sample on top of the reference thermocouple. A closed-one-end cylindrical alumina tube (19 mm O.D., 15.2 mm I.D., 192 mm length) is placed over the cups to ensure even heating of both the sample and reference materials. An alumina purge tube (2.5 mm O.D., 1.7 mm I.D., 290 mm length), located between the sample and reference cups, permits purging the sample area; the purge gas removes effluents and provides an uniform sample environment. The cylindrical alumina tube is surrounded by a furnace (139.5 mm O.D., 145 mm height) located on top of the DTA analyzer module. The furnace position around the sample is adjusted
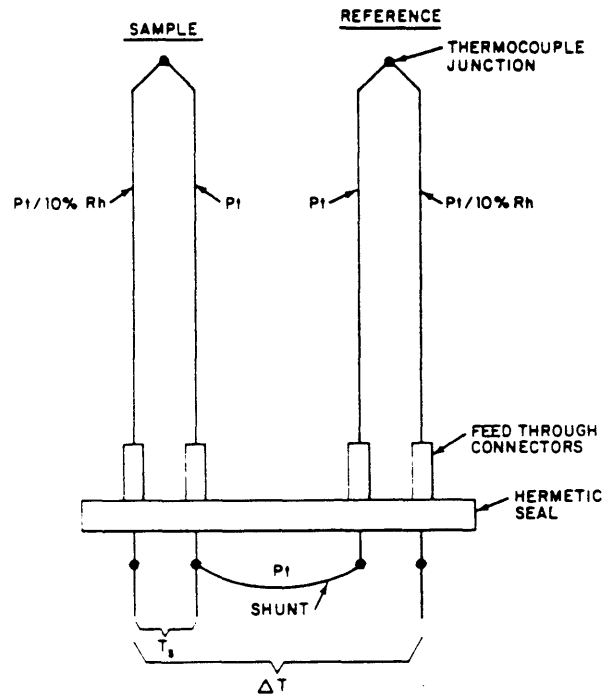
Figure 4.9 - DTA thermocouple construction.

by two vernier screws to obtain optimum baseline performance. The furnace can be cooled at a selected rate by passing air through the cavity surrounding it.

The control module monitors the differential temperature, the furnace temperature, and the sample temperature. It then generates a signal which is sent to the analyzer module furnace to aid in maintaining accurate furnace temperature control. The control module is also the programming source for the analyser. Program parameters, such as minimum temperature, maximum temperature, heating rate, cooling rate, differential temperature range, and temperature output range, are selected with a keyboard. The differential temperature signal from the sample and reference thermocouples is transmitted from the analyzer module to the control module, where it is linearized and transmitted to the X-Y recorder.

4.3.2.2 DTA Experimental Procedure

Thermocouple calibrations against both the melting points of silver and gold are performed before actual temperature measurements are carried out with the DTA apparatus. A quantity of 31.8 mg of silver powder (Bradford Scientific, 99.95 % pure) of 400 mesh is weighed and placed in a 60 mm^3 alumina liner. The reference material of 20 mg aluminum oxide powder is also weighed and placed in another alumina liner of the same size. A small quantity of alumina

powder, approximately 1 to 2 mg, is laid in the two platinum cups around the tip of the thermocouples to ensure efficient heat conduction before the liners are placed in the cups. The whole assembly of liners, cups, and thermocouples is enclosed by the cylindrical alumina tube and then surrounded by the furnace. The argon gas is turned on to purge the reaction chamber at a rate of approximately 20 cc/min. The calibration experiment is started by rapidly heating the silver powder from room temperature to 900°C at a rate of 50°C per minute. Above that temperature, the heating rate of 2°C/min is employed to increase furnace temperature until melting (960.9°C) at which an endothermic peak is displayed on the recorder. The temperature corresponding to the initial break in the slope of the curve denotes the melting point of silver. Only the heating curve is focused on to determine the melting points of silver, since the melting point is depressed by the activation energy to nucleate and grow during solidification in cooling. The temperature recorded by the DTA system is determined to register 9.9°C less than the actual temperature.

A similar calibration test is performed with gold. A piece of gold wire (0.254 mm O.D.) weighing 42.3 mg is employed to check against the melting point of gold at 1064.4°C. The same calibration procedures are repeated for gold; and the result shows that the temperature registered by the DTA apparatus is recorded 10.1°C below the actual temperture. With the results from the two calibration experiments, it is established that a correction factor of

10°C is added to the temperature measured by the DTA apparatus to obtain the actual temperature.

The two thermocouples are also checked if they are the matched pair before actual temperature measurements are taken and when they are replaced. Two calibrations are performed with gold according to the same procedures described above. The first calibration is conducted when the two thermocouples are situated in their original positions; the same calibration procedures are repeated after the thermocouples have interchanged their positions. The testings reveal that the two thermocouples agree with each other within 1°C of the measured temperature.

At the start of the differential thermal analysis, two 100 mm^3 alumina liners are weighed on a digital analytical balance (Mettler, model AE163). The reference melt of alumina weighing 44 mg is placed in one of the alumina liner. The sample of $CoSO_4-Na_2SO_4$ taken from the EMF experiments is weighed and put into the other alumina liner. The weights of the Co-Na sulfate range from 26.8 to 72.6 mg. The two alumina liners are placed in their respective cups, and the assembly of liners, cups, and thermocouples is then enclosed by the cylindrical alumina tube. The furnace is also put in place surrounding the alumina tube. Since a static atmosphere is decided in the reaction chamber to maintain a partial pressure of SO_3 over the sample, no purging gas of argon is in use.

The DTA experiment is then ready to be carried out. The minimum temperature, maximum temperature, heating rate, cooling rate, differential temperature range, and temperature output range are inputed with the keybroard into the control module. The heating rates ranging from 1 to 50°C per minute have been employed in the study; however, at temperatures above 500°C, slow heating rates ranging from 1 to 10°C per minute are used to investigate possible phase transformations. After a piece of chart paper has been placed on the recorder and aligned with a recording pen, the sample and the reference material are heated from room temperature to as high as 990°C. Repeated cycles of heating and cooling of the sample are carried out in each run to investigate the effect of various heating rates on the recorded temperatures. At the end of a run, the furnace is cooled rapidly down to room temperature at a rate of approximate 40°C per minute by passing compressed air in the cavity surrounding the furnace. The sample and the reference material are removed from the cups when the cooling process is complete. The DTA experiment is started again with new sample and liners, because the $CoSO_4-Na_2SO_4$ melt fuse with the alumina liner making liner cleaning a difficult task.

4.3.3 Other Sample Analysis Techniques

Apart from the chemical analysis by DC plasma-arc elemental emission spectriscopy and differential thermal analysis, samples taken from melts equlibrated under controlled partial pressures of SO_3 are also analysed by scanning electron microscopy (SEM), and energy dispersive analysis of X-ray spectroscopy (EDX) at the facilities available at M.I.T. Detailed discussion on the methods of these techniques will not be presented in this report.

CHAPTER FIVE

RESULTS AND CALCULATIONS

The experimental results are divided into three categories: (1) solubility of sulfur trioxide (gas) in molten sodium sulfate; (2) solubility of alumina (solid) in molten sodium sulfate; and (3) cobalt sulfate-sodium sulfate system. The TGA and EMF experimental results are included in all of the three sections. Additional results of the chemical analysis by DC plasma-arc elemental emission spectroscopy and differential thermal analysis are presented in the second and third section, respectively. Other results of phase identification techniques, such as scanning electron microscopy (SEM) and energy dispersive analysis of X-ray spectroscopy (EDX), are also included in the third section.

5.1 Solubility of Sulfur Trioxide in Sodium Sulfate

In this section, the equilibrium solubility of SO_3 in molten Na_2SO_4 and the thermodynamic calculations based on the system of $Na_2S_2O_7$-Na_2SO_4 are presented first. The thermodynamic properties of Na_2SO_4, performance of fused silica solid electrolyte at basic condition, and kinetics of absorption/desorption of SO_3(gas) into/from liquid Na_2SO_4 are later shown.

5.1.1 Sodium Pyrosulfate - Sodium Sulfate System

Thermogravimetric analysis of sodium sulfate under a controlled atmosphere of SO_3 at temperatures above the melting point of sodium sulfate (1157 K) has been performed. The equilibrium solubility of SO_3 in molten Na_2SO_4 contained in a platinum crucible at 1160 K, 1200 K, 1224 K, and 1250 K are shown in Figure 5.1. The experimental data are tabulated in Appendix G. The solubility of SO_3 is expressed in terms of the mole fraction of sodium pyrosulfate, $X_{Na_2S_2O_7}$, in Na_2SO_4 according the reaction

$$Na_2SO_4(l) + SO_3(g) = Na_2S_2O_7(l) \qquad (5-1)$$
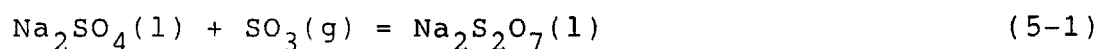
The reaction may be written in terms of the ionic structure of the molten salt as:

$$SO_4^{2-} + SO_3 = S_2O_7^{2-} \qquad (5-1A)$$

The solubility of SO_3 in molten Na_2SO_4 contained in platinum crucibles is found to be very small in this study. The maximum amount of sodium pyrosulfate formed from the reaction between SO_3 and Na_2SO_4 is 0.0654 mole fraction of $Na_2S_2O_7$ under the partial pressure of SO_3 of 0.115 atm. at 1160 K. The solubility of SO_3 in Na_2SO_4 is determined to increase in a non-linear fashion with an increase in the partial pressure of SO_3 and with a decrease in the temperature.
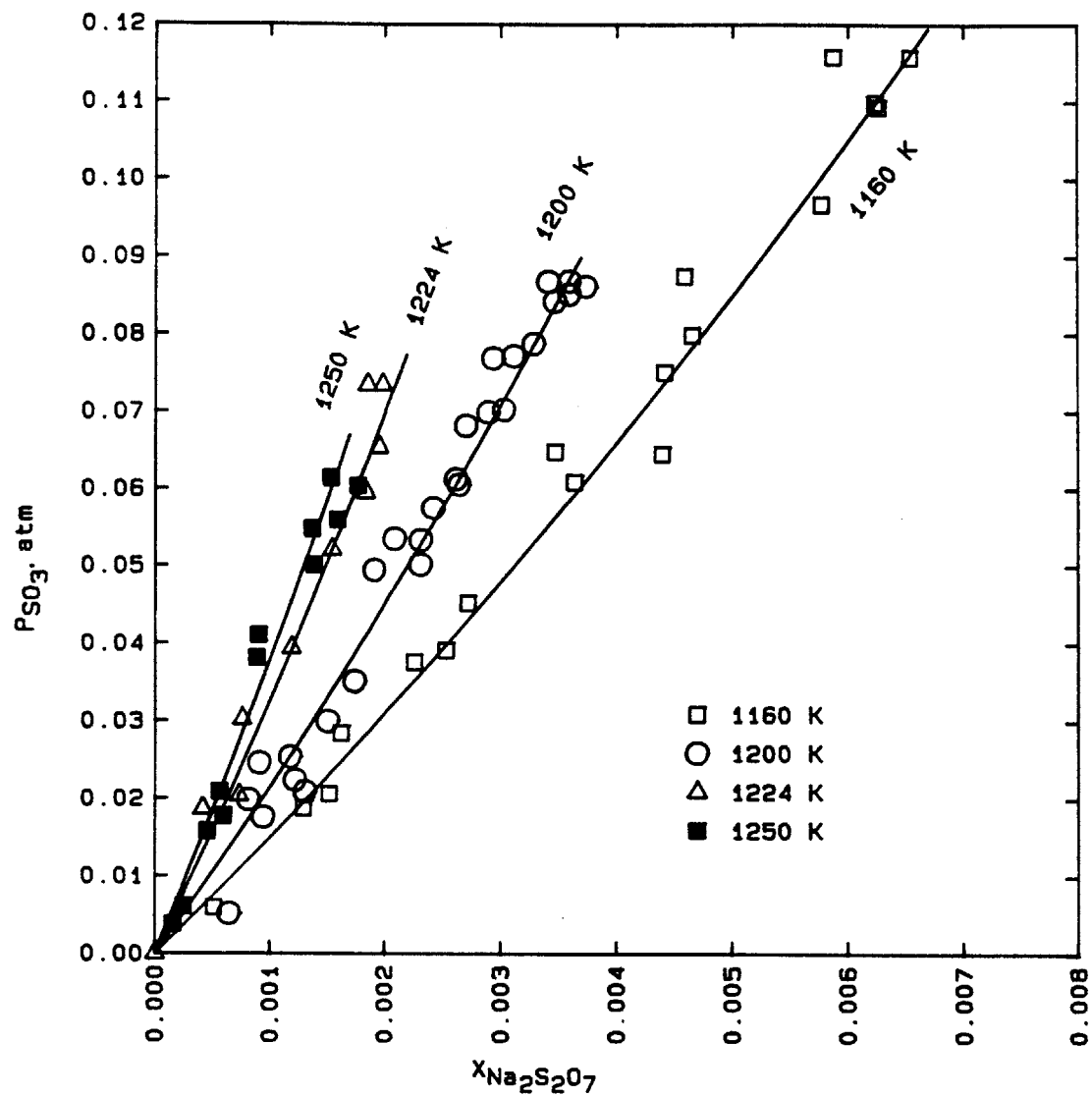
Figure 5.1 - Equilibrium solubility of SO_3 in Na_2SO_4 at 1160 K, 1200 K, 1224 K, and 1250 K.

The following thermodynamic analysis of the system $Na_2S_2O_7$-Na_2SO_4 is based upon the experimental results of the equilibrium solubility of SO_3 in Na_2SO_4 in this study shown in Figure 5.1 and the works by Flood and Forland [83]; Coats, Dear, and Penfold [84]; Kostin, Pluzhnikov, and Ketov [85]; and Ingraham and Hotz [86]. The results of Ingraham and Hotz [86] are, nevertheless, treated with much less weight than those of the other investigators. The decomposition reaction of sodium pyrosulfate, or the reverse reaction of (5-1), below the melting pointing of sodium sulfate is reported by other researchers in the literature; however, the data are valid for this analysis.

In accordance to the chemical reaction of (5-1), the apparent equilibrium constant, K', expressed in terms of mole fraction of species i, X_i, and partial pressure of species i, P_i, is described as:

$$\log K' = \log \left(X_{Na_2S_2O_7(l)} \, / \, X_{Na_2SO_4(l)} \right) - \log P_{SO_3} \quad (5-2)$$

Figure 5.2 shows that the apparent equilibrium constants, K', are essentially independent of melt composition at a constant temperature. The log K' at 1160 K, 1200 K, 1224 K, and 1250 K are determined to be -1.22, -1.38, -1.52, and -1.61, respectively. According to Topping [114], the standard deviations of log K' are 0.056, 0.10, 0.074, and 0.11, at 1160 K, 1200 K, 1224 K, and 1250 K, respectively. Figure 5.3 compares the TGA experimental data with the SO_3 solubility calculated from the constant log K' at the four
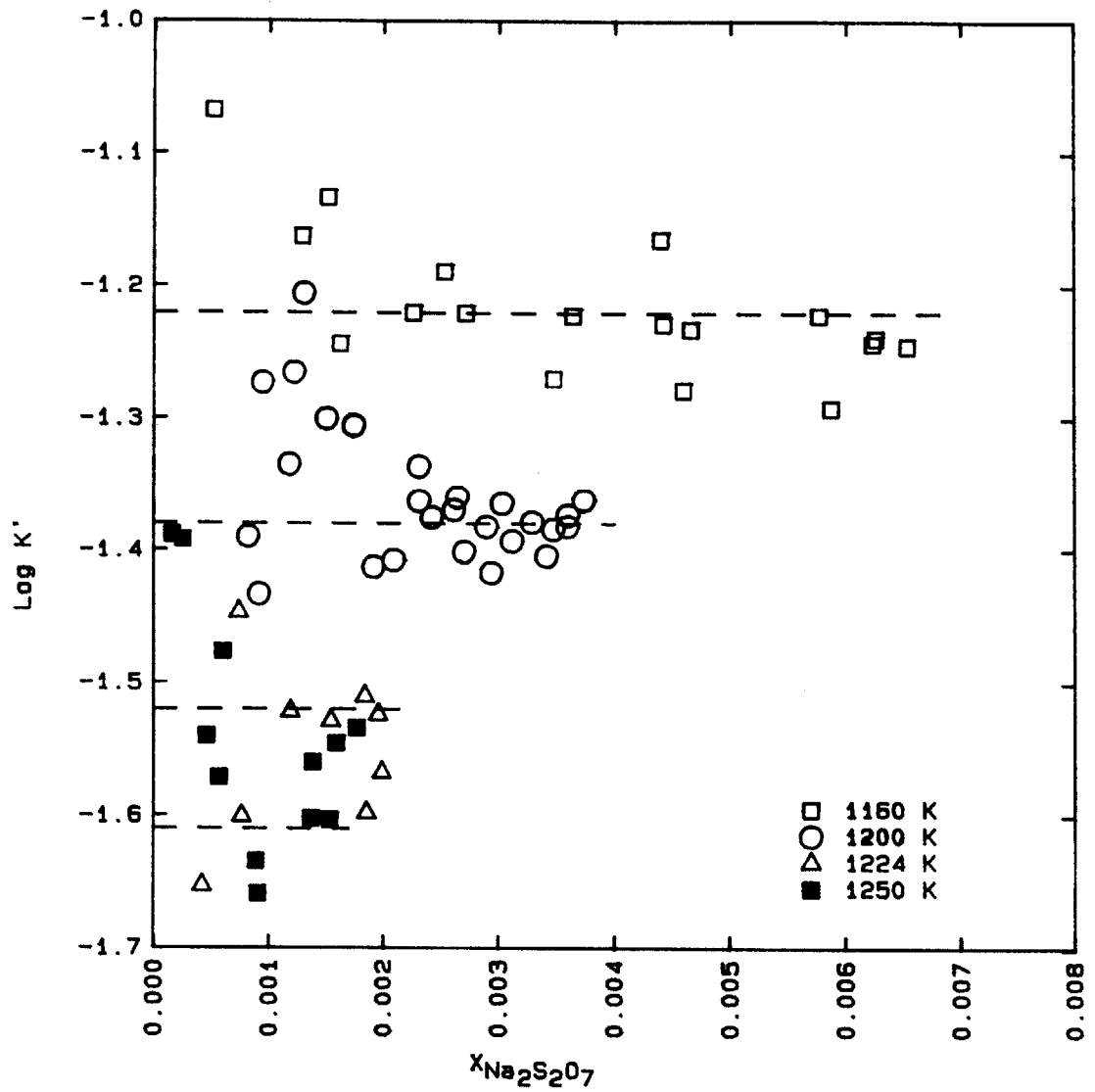
Figure 5.2 - Composition independence of apparent
equilibrium constants at 1160 K, 1200 K, 1224 K,
and 1250 K.
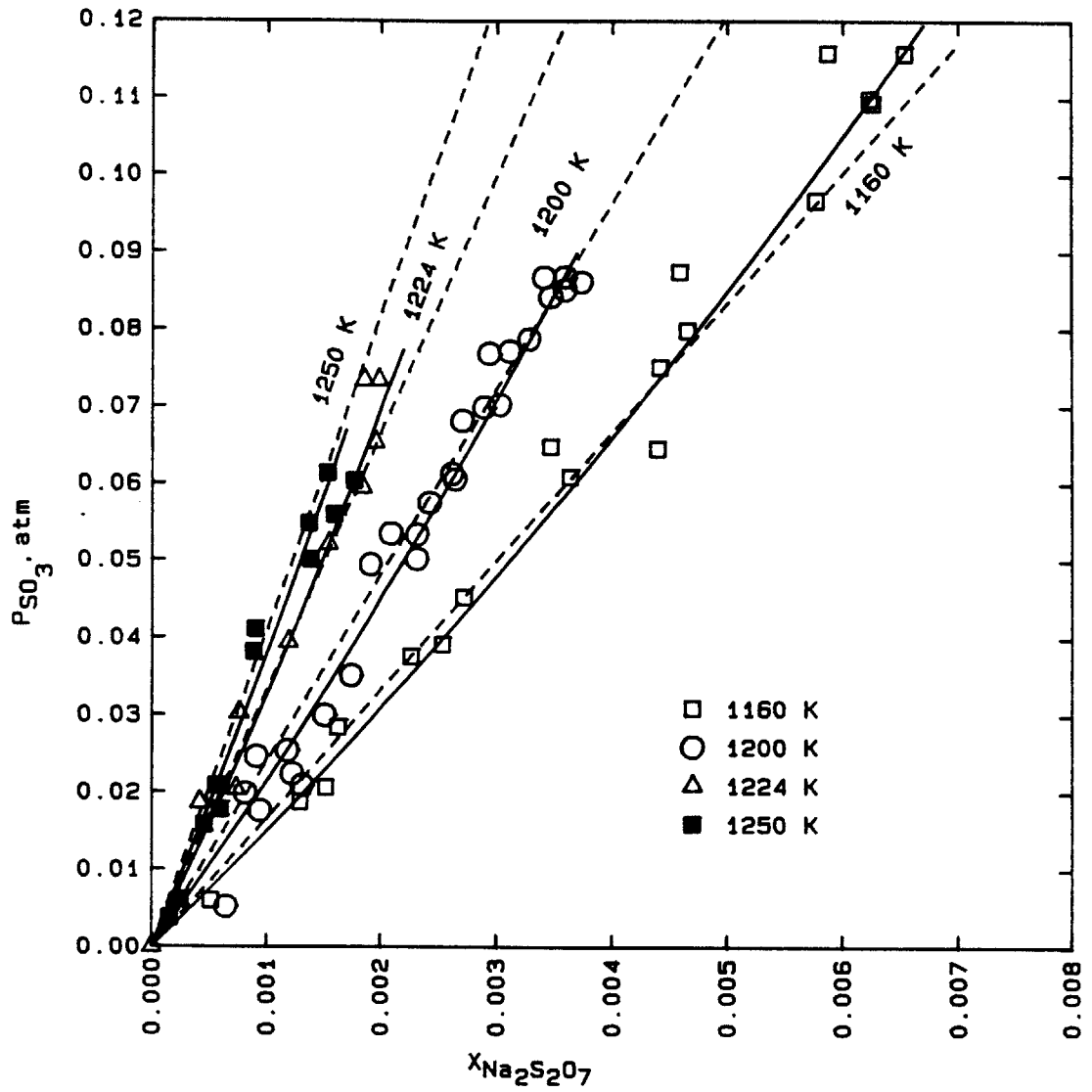
Figure 5.3 - Comparison of sulfur trioxide solubility with results calculated from the apparent K.

temperatures. It is found that the log K' value at a given temperature provides a very good representation of the experimental data for that temperature.

The solubility results of this study described by the log K' at the four temperatures and the data of Flood et al. [83], Kostin et al. [85], and Coats et al. [84] are presented in Figure 5.4. Having weighed the data of Kostin et al. [85] much less than the others, the linear relationship noted among all of the data is

$$\log K' = -(8.055 \pm 0.066) + (7946 \pm 53)/T \qquad (5-3)$$

The standard deviation of log K' and the correlation coefficient are determined to be ± 0.058 and 0.9995, respectively. The standard Gibbs free energy of reaction, $\Delta G°$, is related to the equilibrium constant, K, by:

$$\Delta G° = -2.303 \ RT \log K \qquad (5-4)$$

where R is the universal gas constant, and T is the temperature in Kelvin. With the solution model of ideal mixing, log K equals to log K', the linear relationship (5-3) is transformed to:

$$\Delta G°_{5-1} = -36364 + 36.86 \ T \ [cal/mole] \qquad (5-5)$$

Log K' = -8.055 + 7946/T

☐ This Study

△ Flood et al. [83]

■ Kostin et al. [85]

○ Coats et al. [84]

Log K'

1/Temperature, 1/K (X 1E+04)
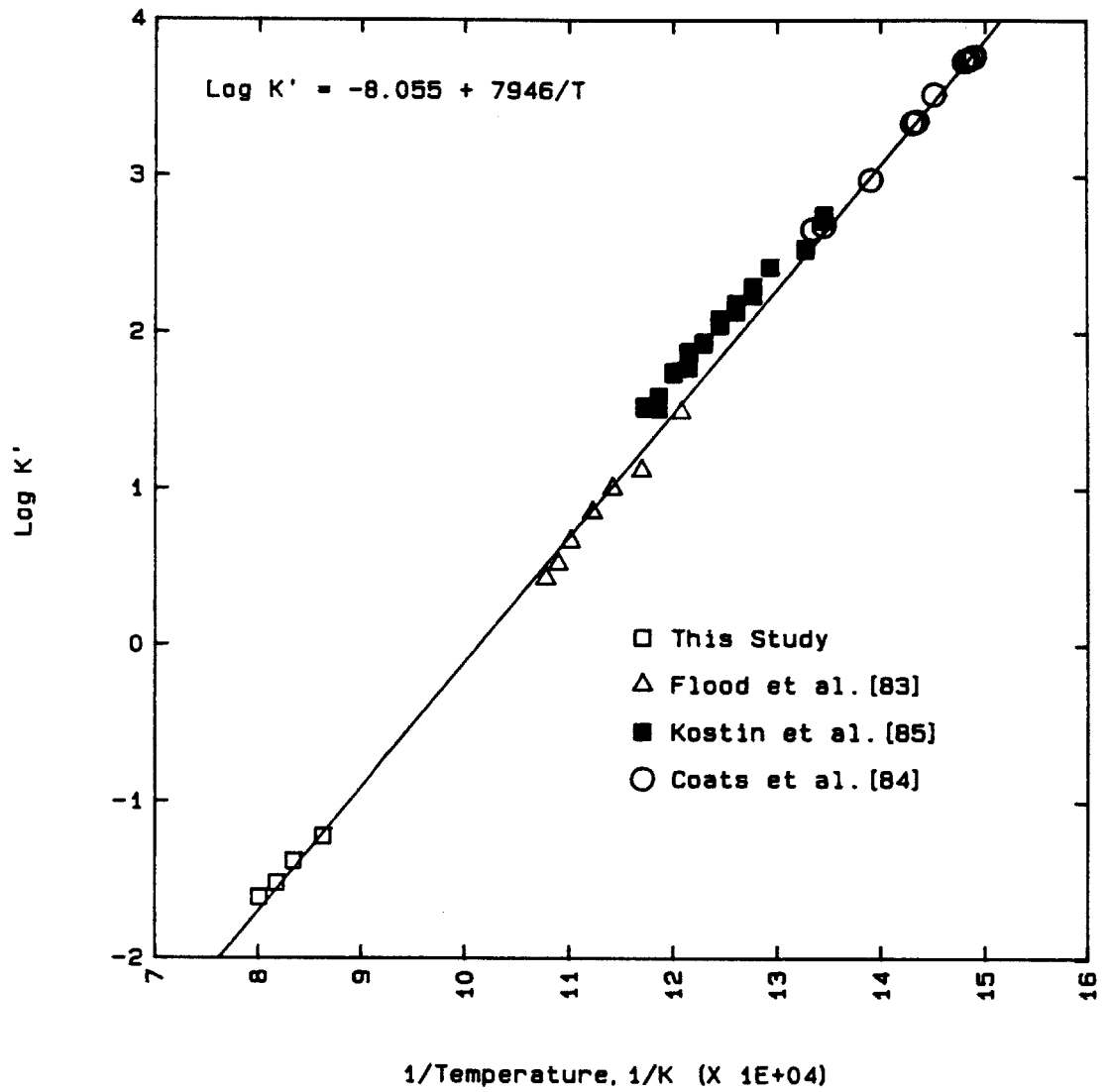
Figure 5.4 - Comparison of SO_3 solubility in Na_2SO_4.

With the knowledge of the enthalpy of reaction, $\Delta H°$, of reaction (5-1) being -36364 cal/mole, the results in the literature are extrapolated to a common isothermal of 1160 K by means of the Gibbs-Helmholtz equation:

$$[\partial(\Delta G°/T) \; / \; \partial(1/T) = \Delta H°] \; \text{const. composition} \qquad (5-6)$$

The Gibbs-Helmholtz equation can be further written in terms of the species of SO_3 as:

$$[\partial(\log P_{SO_3})/\partial(1/T) = \Delta H°/2.303 \; R]_{\text{const. composition}} \qquad (5-7)$$

or at a constant ratio of mole fraction of $Na_2S_2O_7$ to Na_2SO_4, the equation becomes:

$$\log P_{SO_3,T_f} - \log P_{SO_3,T_i}$$

$$= (\Delta H°/2.303 \; R) \cdot (1/T_f - 1/T_i) \qquad (5-8)$$

where P_{SO_3} is the partial pressure of SO_3, T_f is the final temperature of 1160 K, T_i is the initial temperature, and P_{SO_3,T_f} and P_{SO_3,T_i} are the partial pressures of SO_3 at the final temperature and at the initial temperature, respectively. The results of the other investigators [83-85] extrapolated to 1160 K are listed in Appendix H.

The equilibrium constant, K, in terms of the activity of species i, a_i, is written as:

$$\log K = \log (a_{Na_2S_2O_7(l)} / a_{Na_2SO_4(l)}) - \log P_{SO_3} \qquad (5\text{-}9)$$

By means of the relationships that $a_i = \gamma_i \cdot X_i$ and $\alpha_i = \ln \gamma_i / (1-X_i)^2$, where γ_i and α_i are respectively the activity coefficient and α function of the ith species, the apparent equilibrium constant, K', is then related to the equilibrium constant, K, by:

$$\log K' = \log K - \log (\gamma_{Na_2S_2O_7} / \gamma_{Na_2SO_4}) \qquad (5\text{-}10)$$

or

$$\log K' = \log K - (\alpha/2.303) \cdot (X^2_{Na_2SO_4} - X^2_{Na_2S_2O_7}) \qquad (5\text{-}11)$$

The data of this study at 1160 K and those of other investigators are presented in the plot of log K' versus $X^2_{Na_2SO_4} - X^2_{Na_2S_2O_7}$ in Figure 5.5. It is apparent that all of the data at 1160 K are best represented by a horizontal line at log K' = -1.22. The α function is zero; thus, the system does not follow the regular solution model. With the additional fact that a single log K' is sufficent to describe all of the TGA experimental data at a constant temperature, the activities of Na_2SO_4 and $Na_2S_2O_7$ are basically equal to their respective mole fractions. The system of $Na_2S_2O_7$-Na_2SO_4 is therefore determined to obey the ideal solution model at compositons between $Na_2S_2O_7$ and
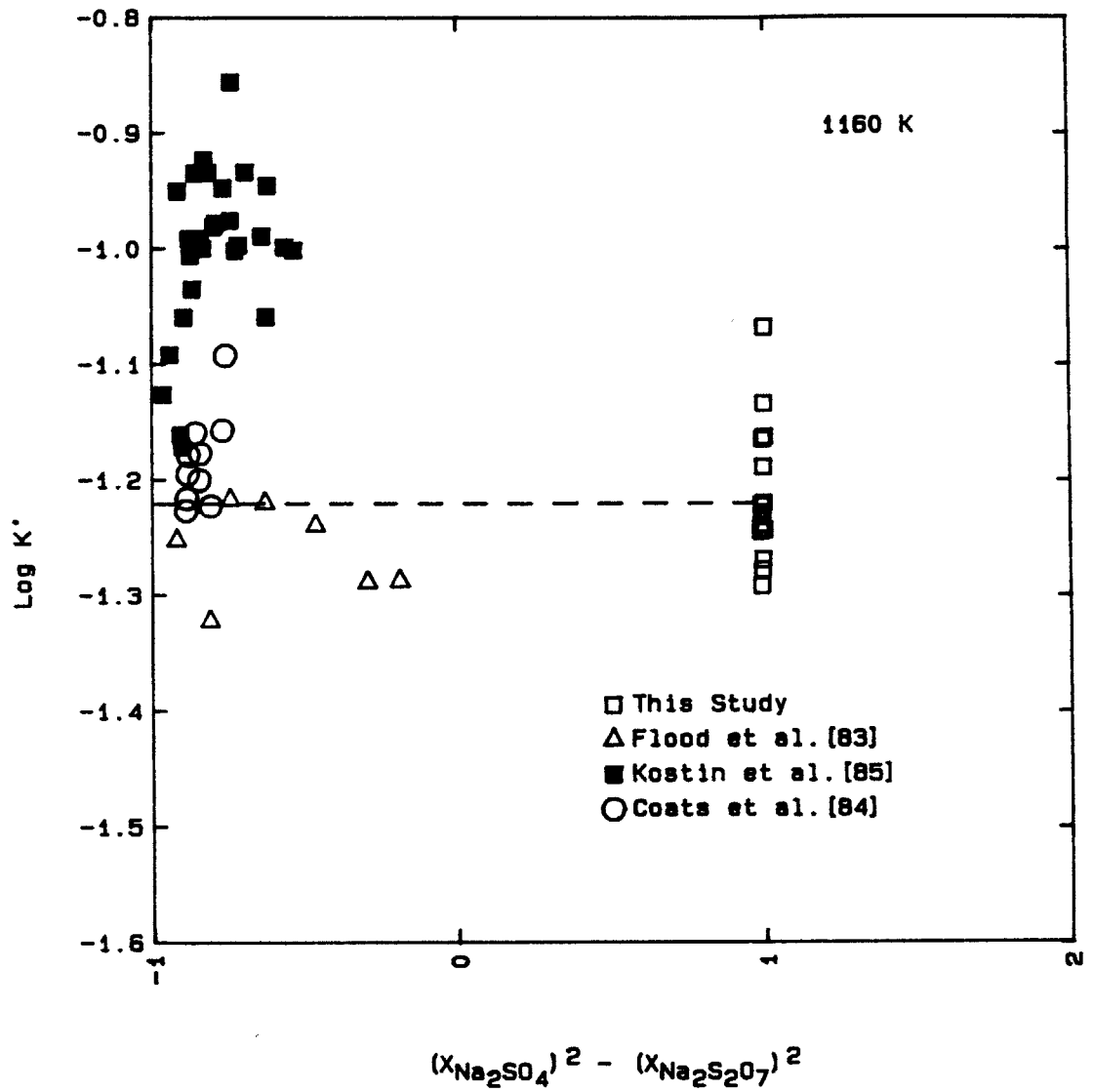
Figure 5.5 - Comparison of apparent equilibrium constants across composition range at 1160 K.

Na_2SO_4.

The phase diagram of the system of $Na_2S_2O_7$-Na_2SO_4 is fully explored with the thermodynamic properties determined from this study. A partial phase diagram with mole fraction of Na_2SO_4 ranging from 0 to 0.11 has been described by Coats et al. [84] to consist of four regions: $Na_2S_2O_7(s)$ + $Na_2SO_4(s)$; liquid + $Na_2S_2O_7(s)$; liquid + $Na_2SO_4(s)$; and liquid. In this study, the liquidus line on the Na_2SO_4-rich side of the phase diagram is completely determined by the method of freezing point lowering.

With the assumption that the solution is athermal down to 670 K, the partial molar enthalpy of mixing of Na_2SO_4 and that of $Na_2S_2O_7$ are thus zero, or the activity coefficients of Na_2SO_4 and $Na_2S_2O_7$ are independent of temperature. The activities of Na_2SO_4 and $Na_2S_2O_7$ at 1160 K are therefore valid down to 670 K.

The method of freezing point lowering is based on the reaction

$$Na_2SO_4(s) = Na_2SO_4(l) \qquad (5-12)$$

The molar Gibbs free energy of melting, ΔG_m, can be represented by the following expressions:

$$\Delta G_m = - RT \ln (a_{Na_2SO_4(l)} / a_{Na_2SO_4(s)}) \qquad (5-13)$$

The ΔG_m is calculated from the difference in the standard

Gibbs free energies of formation of $Na_2SO_4(l)$ and $Na_2SO_4(s)$:

$$\Delta G_m = \Delta G_f^o(Na_2SO_4(l)) - \Delta G_f^o(Na_2SO_4(s)) \qquad (5-14)$$

The values of the standard Gibbs free energy of formation of Na_2SO_4 liquid and those of the Na_2SO_4 crystal I solid, which is the stable phase at 514 to 1157 K, are obtained from the JANAF Tables [104]. The Gibbs free energy of formation and the melting properties of sodium sulfate are listed in Table 5-1. Since the solid Na_2SO_4 is taken as the standard state, the activity of Na_2SO_4 with respect to solid is therefore one. The equation (5-13) is reduced to:

$$\Delta G_m = - RT \ln a_{Na_2SO_4(l)} \qquad (5-15)$$

For an ideal solution, the expression can be rearranged to be:

$$X_{Na_2SO_4(l)} = Exp \left(- \Delta G_m/RT\right) \qquad (5-16)$$

The liquidus line is thus given by equation (5-16). The standard Gibbs free energy of melting employed in the calculations are shown in Figure 5.6. Values greater than those given in the JANAF Tables [104] are utilized at temperatures below 900 K; thus, the phase boundary determined by Coats et al. [84] is satified.

Table 5-1

Gibbs Free Energy of Formation and Melting Properties of Sodium Sulfate

taken from JANAF [104]; Data published on June 30, 1978

T	$\Delta G_f^o(Na_2SO_4(l))$	$\Delta G_f^o(Na_2SO_4(s))$[*]
K	Kcal/mole	Kcal/mole
600	−271.352	−274.194
700	−262.439	−264.778
800	glass transition	−256.639
900	−244.614	−245.936
1000	−234.564	−235.364
1100	−224.639	−224.924

* Data of Crystal I solid are employed. The Crystal I solid is the stable phase from 514 to 1157 K.

T	ΔG_m	ΔH_m	ΔS_m
K	Kcal/mole	Kcal/mole	cal/mole·K
600	2.842	5.859	5.028
700	2.339	5.859	5.028
800	/	/	/
900	1.322	6.013	5.212
1000	0.800	6.012	5.212
1100	0.285	5.857	5.065
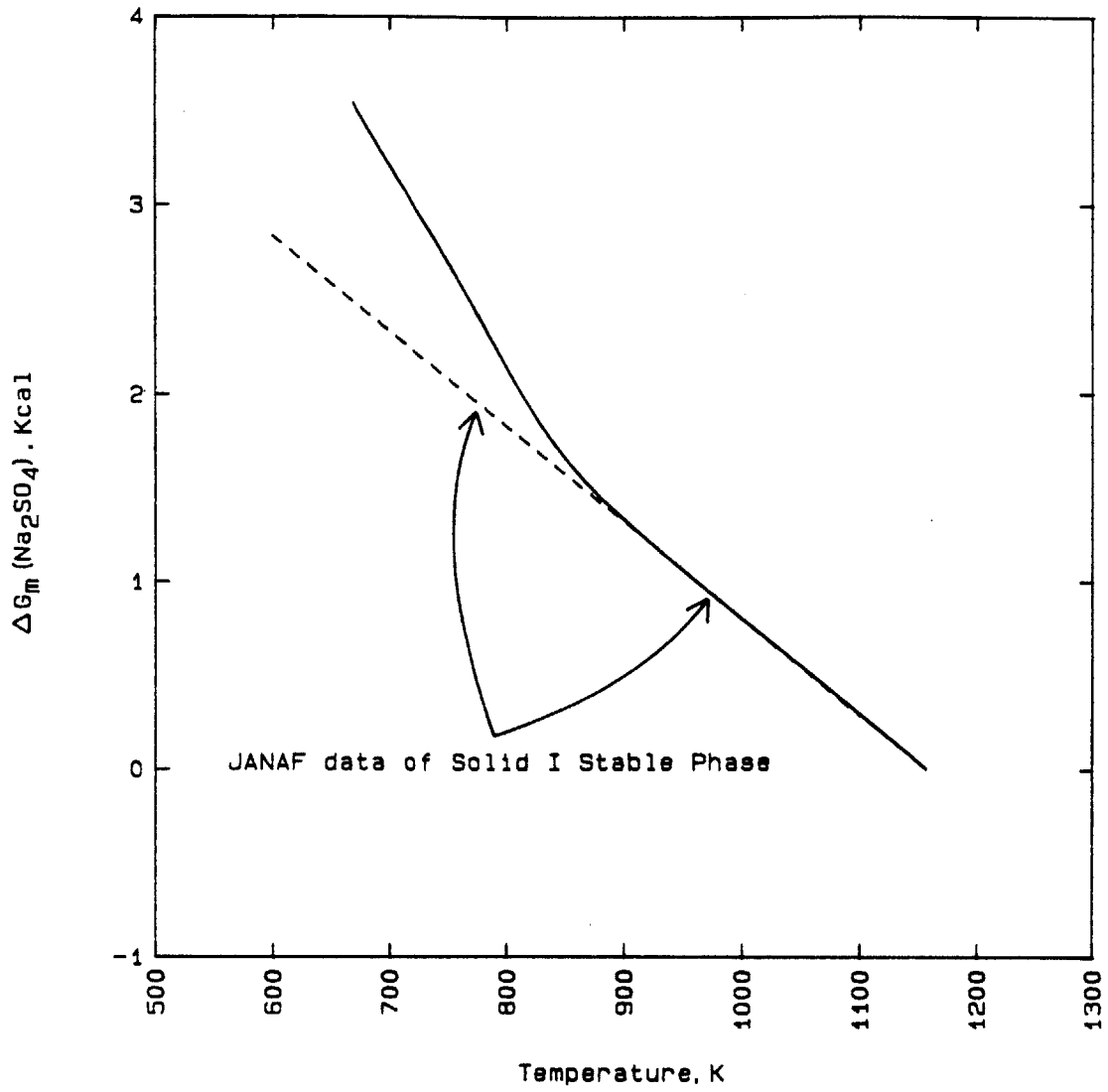
Figure 5.6 - Free energy of melting of sodium sulfate
employed in the analysis.

Lines of constant pressure of SO_3 on the phase diagram for ideal solution behavior are calculated by substituting the log K' in equation (5-3) by the expression (5-2). The final relationship becomes:

$$T = \frac{7946}{\log (X_{Na_2S_2O_7} / X_{Na_2SO_4}) - \log P_{SO_3} + 8.055} \qquad (5-17)$$

A partial phase diagram and an isobar of $\log P_{SO_3} = -2.2$ are compared with those determined by Coats et al. [84] in Figure 5.7.

The entire phase diagram of the $Na_2S_2O_7$-Na_2SO_4 system with isoactivity lines of SO_3 in terms of $\log P_{SO_3}$ ranging from -2.5 to 4.0 is presented in Figure 5.8. The SO_3 isobars of $\log P_{SO_3}$ less than 0.5 intersect the liquidus line twice, it is therefore proposed that a slight solid solubility of Na_2SO_4 in $Na_2S_2O_7$ or a β phase exists in the system to eliminate any violation of the laws of thermodynamics. A maximum partial pressure of SO_3 in the two-phase region of liquid+β is thus noted.

In the β phase, the change in the partial pressure of SO_3 as a function of temperature is governed by the Gibbs-Helmholtz equation (5-6) for the reaction:

$$Na_2SO_4(s) + SO_3(g) = Na_2S_2O_7(s) \qquad (5-18)$$
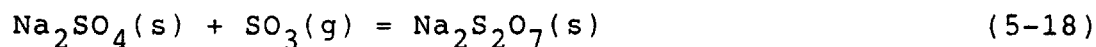
The standard Gibbs free energy of melting of $Na_2S_2O_7$ is estimated from the phase diagram reported by Coats, Dear,
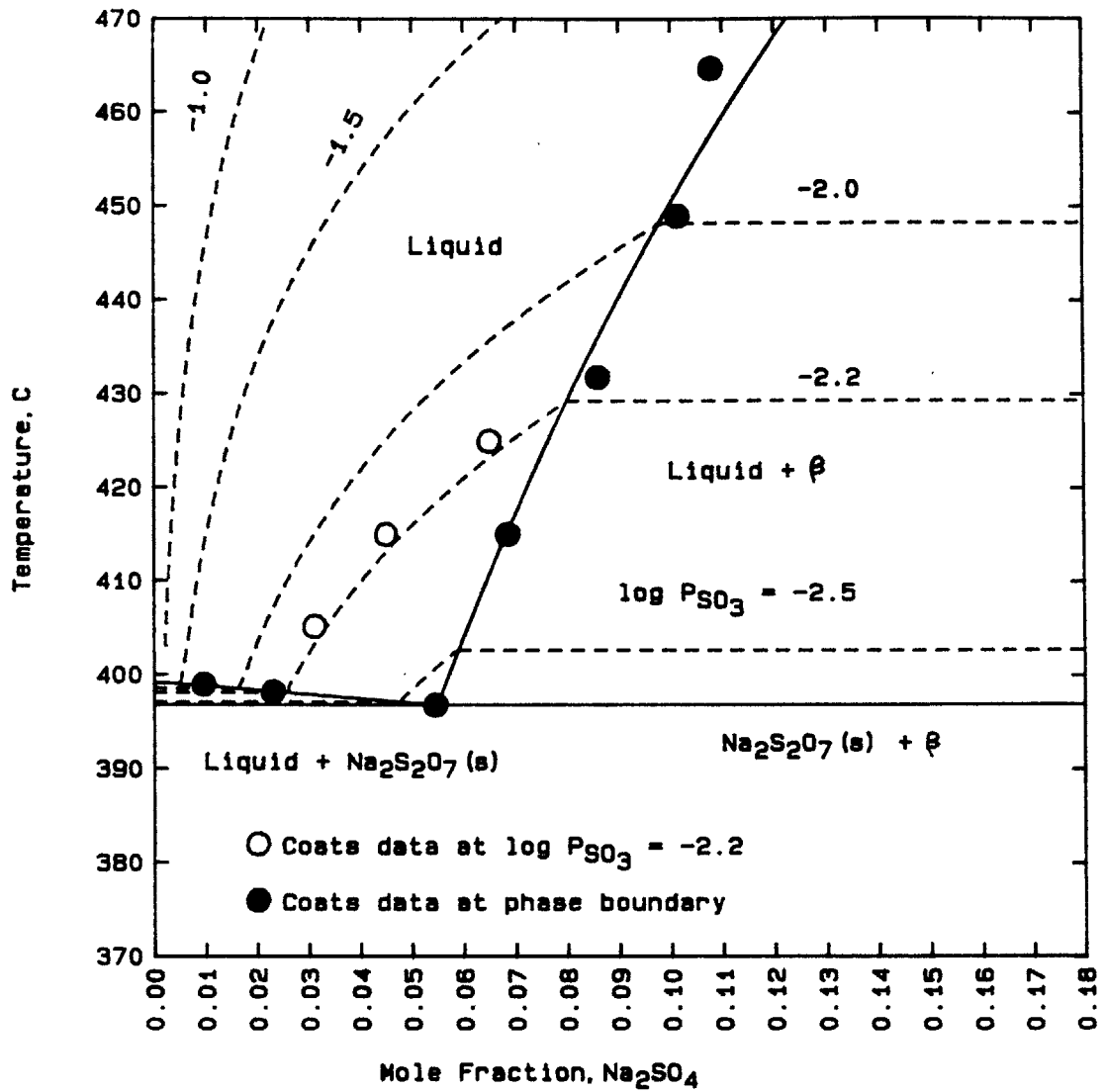
Figure 5.7 — Comparison of phase boundaries and isobars of SO_3 with those of Coats et al.[84].
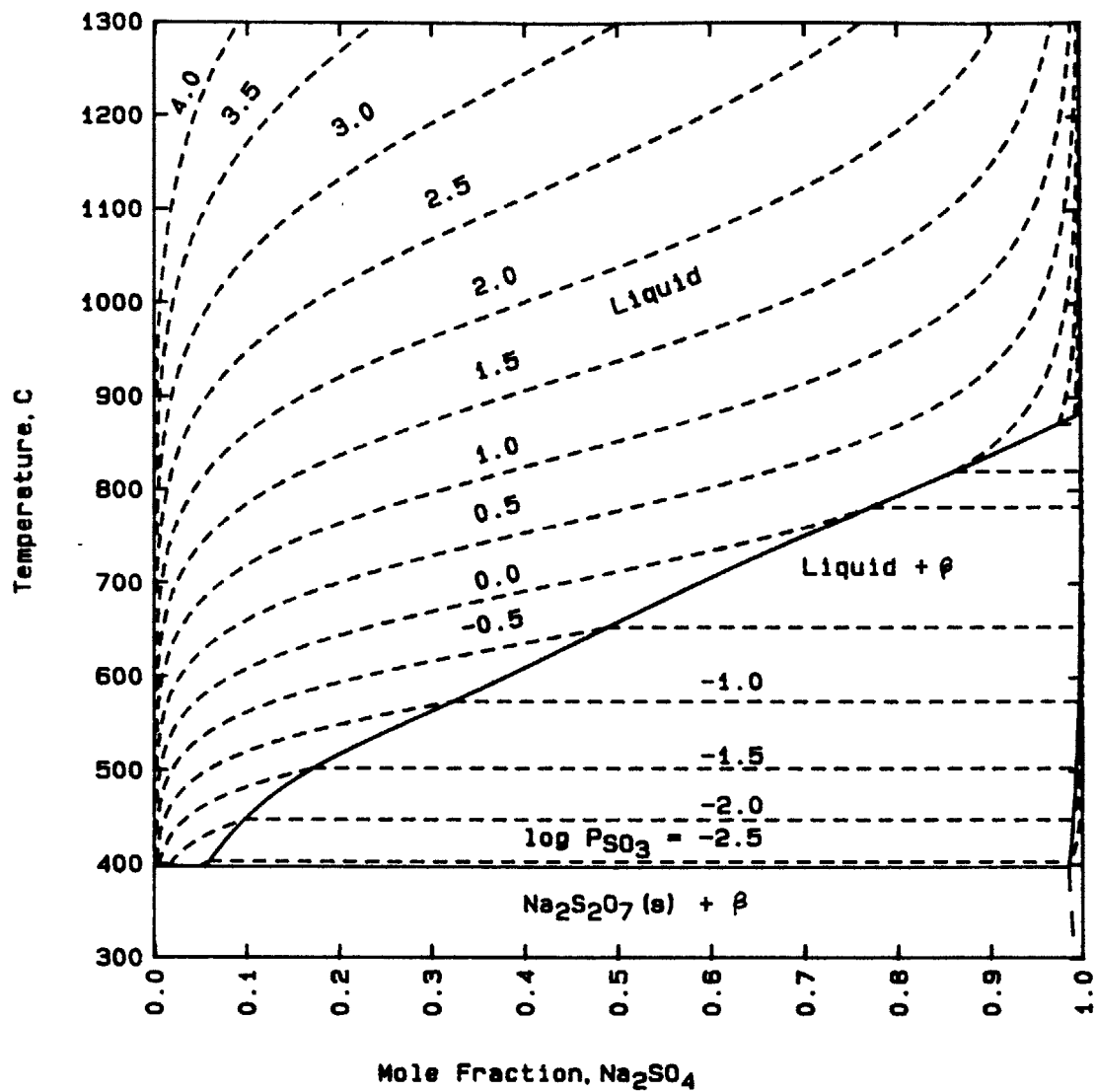
Figure 5.8 - Phase diagram of sodium pyrosulfate - sodium sulfate system with isobars of SO_3 in log (P_{SO_3}, atm).

and Penfold [84] according to the equilibrium:

$$Na_2S_2O_7(s) = Na_2S_2O_7(l) \qquad (5-19)$$

The estimated molar Gibbs free energy of melting is:

$$\Delta G_{m,Na_2S_2O_7} = 672.28 - 0.03380 \ T \ [cal/mol] \qquad (5-20)$$

The molar Gibbs free energy of melting of Na_2SO_4 is reported in the JANAF Tables [104] in the range of 600 K to 1200 K as:

$$\Delta G_{m,Na_2SO_4} = 5906.83 - 5.102 \ T \ [cal/mol] \qquad (5-21)$$

Thus, the standard Gibbs free energy of the reaction (5-18) equals:

$$\Delta G^o_{5-18} = \Delta G^o_{5-1} + \Delta G_{m,Na_2SO_4} - \Delta G_{m,Na_2S_2O_7} \qquad (5-22)$$

or

$$\Delta G^o_{5-18} = -31129.46 + 31.79 \ T \ [cal/mol] \qquad (5-23)$$

With the heat of the reaction being -31129.46 cal/mol, the partial pressure of SO_3 is extrapolated from an arbitrary point (log $X_{Na_2S_2O_7}$ = -4.0, log P_{SO_3} = -0.5) at the melting point of Na_2SO_4 (1157 K) to lower temperatures by means of the Gibbs-Helmholtz equation.

To determine the change in partial pressure of SO_3 at a constant temperature, the equilibrium constant K of the equilibrium (5-18), with mole fraction of Na_2SO_4 being approximately one, is employed as:

$$\log K = \log X_{Na_2S_2O_7} + \log \gamma_{Na_2S_2O_7} - \log P_{SO_3} \qquad (5-24)$$

or

$$\log K - \log \gamma_{Na_2S_2O_7} = \log X_{Na_2S_2O_7} - \log P_{SO_3} \qquad (5-25)$$

With the assumption that the activity coefficient of $Na_2S_2O_7$ is constant at a given temperature, the left hand side of equation (5-25) is represented by a constant, M, as:

$$M = \log X_{Na_2S_2O_7} - \log P_{SO_3} \qquad (5-26)$$

The constant, M, can be evaluated at each temperature from the points determined by the Gibbs-Helmholtz equation. The change in partial pressure of SO_3 at a constant temperature can then be calculated with the same equation (5-26) for a given mole fraction of $Na_2S_2O_7$. Figure 5.9 depicts the behavior of the isoactivity lines of SO_3 in the β region for $\log P_{SO_3}$ ranging from -2.5 to 0.0. The estimated boundaries of the β phase are governed by the intersections of the isobars in SO_3 of the liquid+β phase and those in the β phase. The solidus line in the $Na_2S_2O_7$-Na_2SO_4 phase diagram is shown in Figure 5.10.
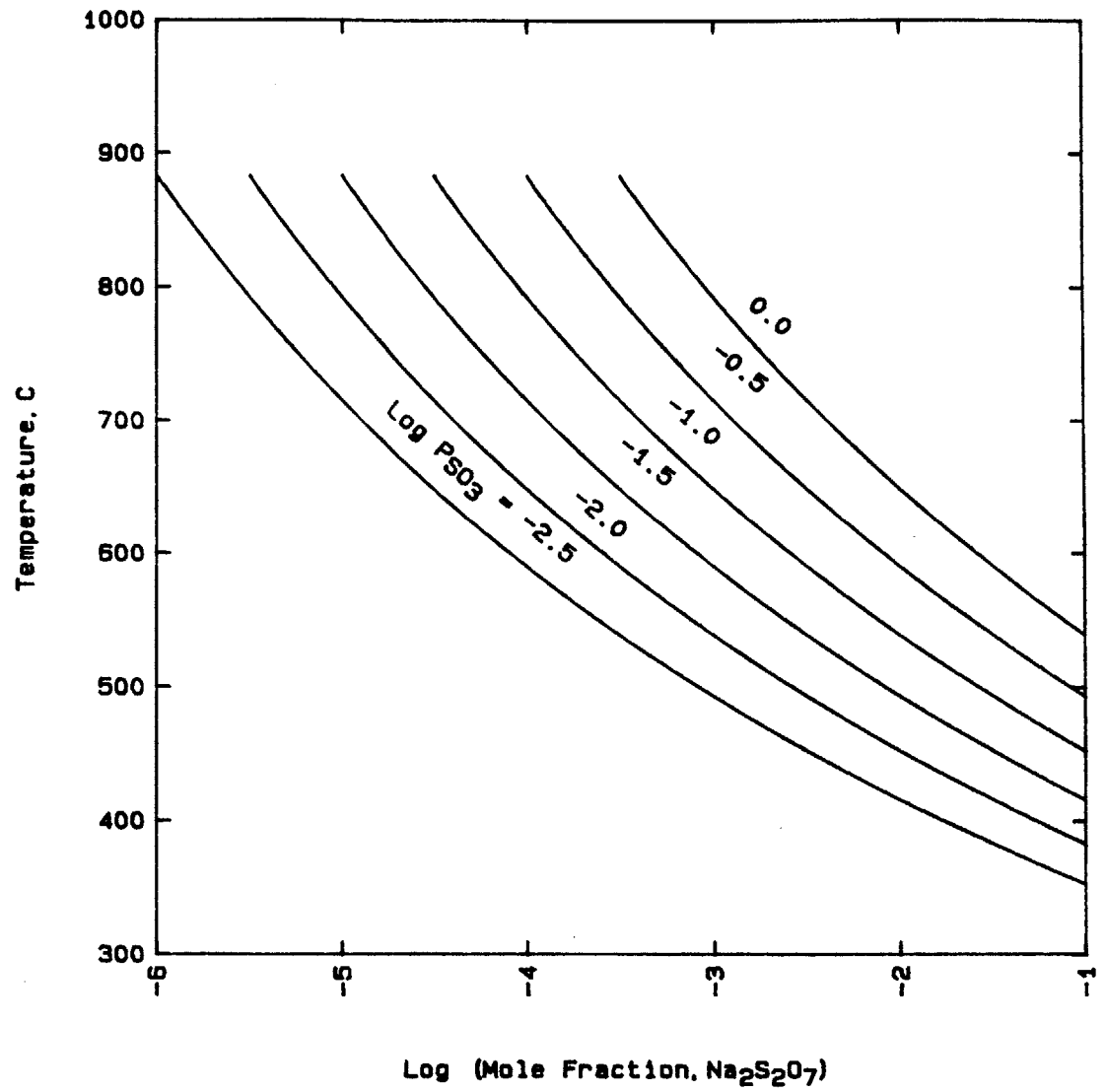
Figure 5.9 - Behavior of isobars of SO_3 in β phase field.
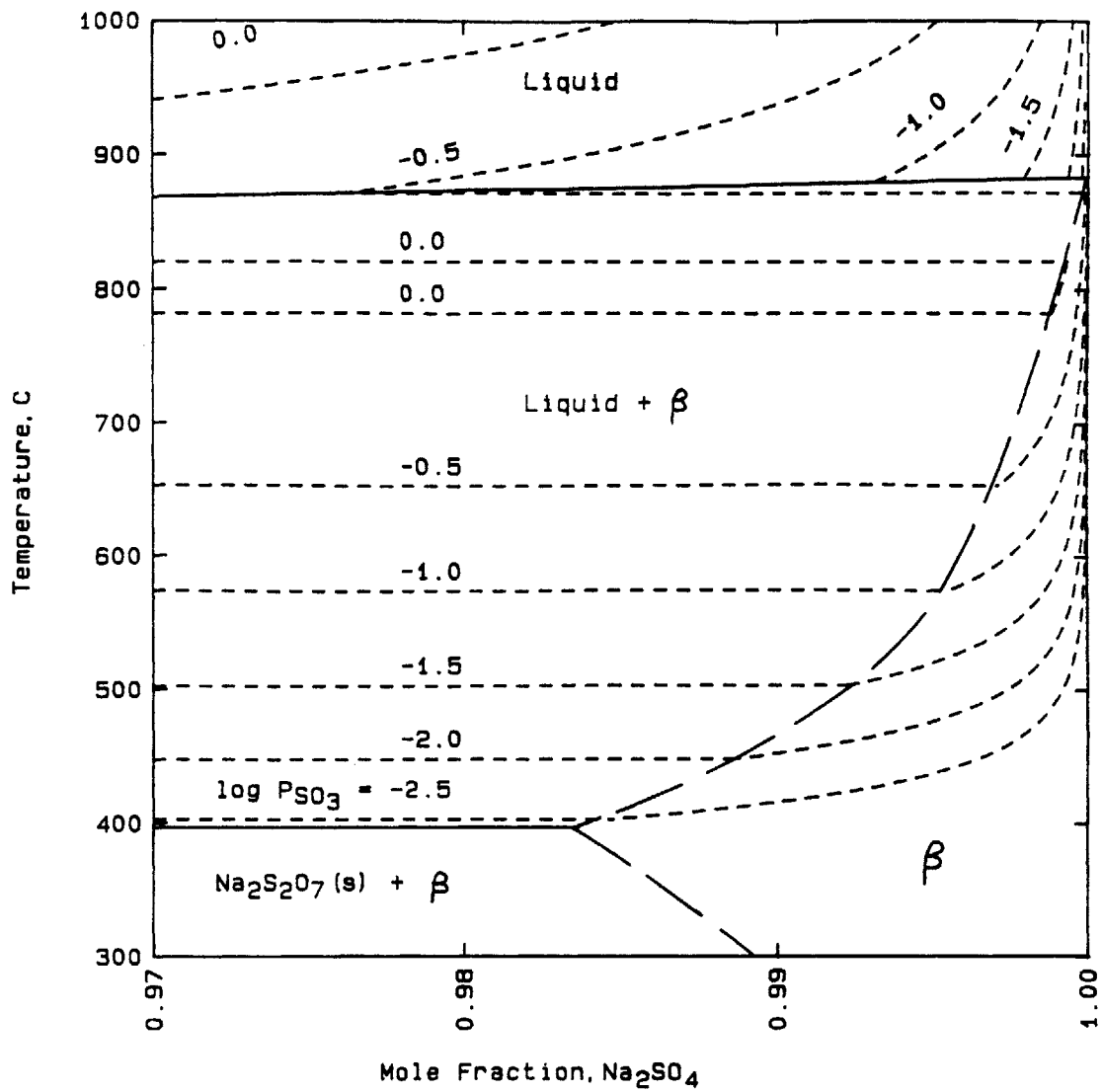
Figure 5.10 - Phase boundary of β phase with isobars of SO_3 in log (P_{SO_3}, atm).

A stability diagram in terms of temperature and log P_{SO_3} showing the stable regions of the solid Na_2SO_4, the solid $Na_2S_2O_7$, and the liquid phase is illustrated in Figure 5.11. The experimental data reported by Coats, Dear, and Penfold [84] are also included for comparison.

To determine the partial pressures of SO_3 in equilibrium with pure $Na_2S_2O_7$ and pure Na_2SO_4, the integral Gibbs free energy of mixing, G^M, in the binary system of SO_3-Na_2O is calculated in the composition range between $Na_2S_2O_7$ and Na_2SO_4. The reference state are $SO_3(g)$ and $Na_2O(1)$ at one atmosphere. The equilibrium partial pressure of SO_3 over a certain melt composition is given by the intersection of the SO_3 y-axis and a tangent to the curve of the integral Gibbs free energy of mixing at the given composition. There are two ways of calculating the integral Gibbs free energy of mixing: (1) analytical method which gives the exact solution; however, solutions at the two limiting compositions of $Na_2S_2O_7$ and Na_2SO_4 are undefined. (2) numerical integration of the Gibbs-Duhem equation which tends to inherit numerical errors; however, solutions at the limiting compositions can be obtained. Therefore, both methods of calculation are employed to determine the G^M curve at all compositions between $Na_2S_2O_7$ and Na_2SO_4 inclusive.

The partial Gibbs free energy of mixing of Na_2SO_4 ($G^M_{Na_2SO_4}$) and that of $Na_2S_2O_7$ ($G^M_{Na_2S_2O_7}$) are respectively calculated based on the following two equilibriums:
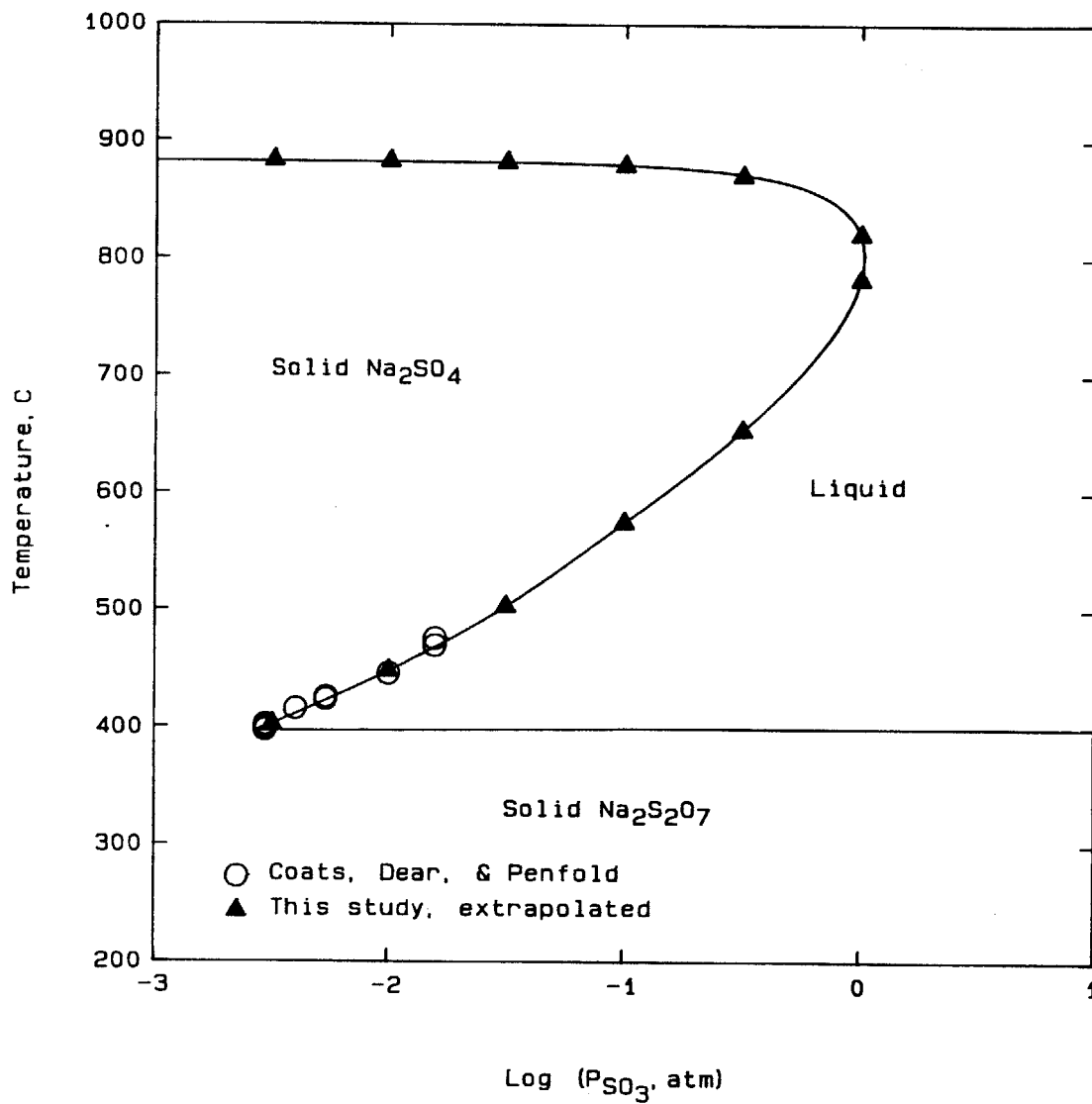
Figure 5.11 - Phase stability diagram of $Na_2S_2O_7-Na_2SO_4$ system.

$$Na_2O(l) + SO_3(g) = Na_2SO_4(l) \qquad \text{(5-27)}$$

and

$$Na_2O(l) + 2SO_3(g) = Na_2S_2O_7(l) \qquad \text{(5-28)}$$
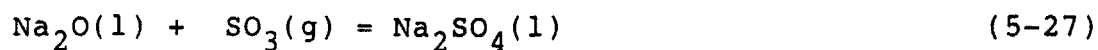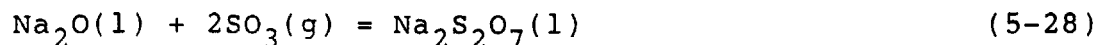
The Gibbs free energy of reaction (5-27), ΔG°_{5-27}, has been determined in this study to be $-120080 + 21.38\ T$ [cal/mol] (a detailed discussion of the result is presented in section 5.1.3). The equilibrium (5-28) can be derived from reactions (5-27) and (5-1) as follows:

$$Na_2O(l) + SO_3(g) = Na_2SO_4(l) \qquad \text{(5-27)}$$
$$+)\ Na_2SO_4(l) + SO_3(g) = Na_2S_2O_7(l) \qquad \text{(5-1)}$$

$$Na_2O(l) + 2SO_3(g) = Na_2S_2O_7(l) \qquad \text{(5-28)}$$
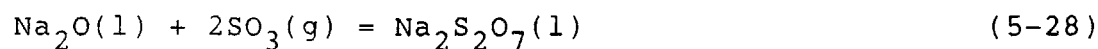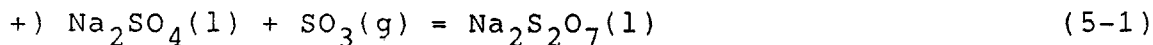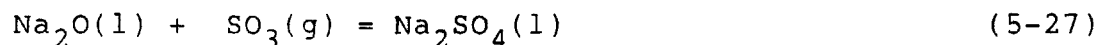
The Gibbs free energy of reaction (5-28) which is the summation of ΔG°_{5-27} and ΔG°_{5-1} equals :

$$\Delta G^\circ_{5-28} = -156444 + 58.24\ T\ \text{[cal/mol]} \qquad \text{(5-29)}$$

For a system of one mole, the Gibbs free energy of mixing at the two limiting compositions of Na_2SO_4 and $Na_2S_2O_7$ are:

$$G^M_{Na_2SO_4} = 1/2\ \Delta G^\circ_{5-27} = -60040 + 10.69T\ \text{[cal/mol]} \qquad \text{(5-30)}$$

and

$$G^M_{Na_2S_2O_7} = 1/3\ \Delta G^\circ_{5-28} = -52148 + 19.41T\ \text{[cal/mol]} \qquad \text{(5-31)}$$

The analytical method focuses on the equilibriums of (5-1) and (5-27) with the melt being an ideal solution. The equilibrium constants of the two equilibriums are expressed as:

$$\log K_{5-1} = \log (X_{Na_2S_2O_7}/X_{Na_2SO_4}) - \log P_{SO_3} \qquad (5\text{-}32)$$

$$\log K_{5-27} = \log (X_{Na_2SO_4}/a_{Na_2O}) - \log P_{SO_3} \qquad (5\text{-}33)$$

The relationship between mole fraction of Na_2SO_4 in the $Na_2S_2O_7$-Na_2SO_4 system and that of Na_2O in the SO_3-Na_2O system is:

$$X_{Na_2SO_4} = 6 X_{Na_2O} - 2 \qquad (5\text{-}34)$$

The integral Gibbs free energy of mixing is given by:

$$G^M = 2.303RT (X_{SO_3} \log P_{SO_3} + X_{Na_2O} \log a_{Na_2O}) \qquad (5\text{-}35)$$

The analytical solution is then evaluated by solving the four equations (5-32) to (5-35) simultaneously at a given temperature.

The numerical method is focused on the following integration of the Gibbs-Duhem equation:

$$\left. \log a_{Na_2O} \right|_{X_{Na_2O}=X_{Na_2O}} - \left. \log a_{Na_2O} \right|_{X_{Na_2O}=0.5}$$

$$= - \int_{\log P_{SO_3} \text{ at } X_{Na_2O}=0.5}^{\log P_{SO_3} \text{ at } X_{Na_2O}=X_{Na_2O}} (X_{SO_3}/X_{Na_2O}) \, d \log P_{SO_3} \qquad (5-36)$$

The $\log P_{SO_3}$ is governed by equation (5-32), and the relation of mole fraction of Na_2SO_4 to that of Na_2O is given by equation (5-34).

The lower limit of integration is governed by the behavior of the G^M function as it approaches $X_{Na_2O} = 0.5$. The integral Gibbs free energy of mixing is determined to reach its minimum at Na_2SO_4. Figures 5.12 and 5.13 show the tangent to the G^M curve at Na_2SO_4 is a horizontal line at 1160 K and 1200 K, respectively. The TGA experimental data in terms of G^M are calculated according to equation (5-35) and the thermodynamic properties of Na_2SO_4 obtained in this study shown in Figure 5.18. The TGA data at 1160 K and 1200 K are compared with the G^M curve determined by the analytical method in Figure 5.12 and 5.13, respectively. The minimum $\log P_{SO_3}$ are equal to -8.59 and -8.97 at 1200 K and 1600 K, respectively, at the limiting composition of Na_2SO_4. The integration of the Gibbs-Duhem equation at 1200 K thus begins at $\log P_{SO_3} = -8.59$ as it is shown in Figure 5.14.
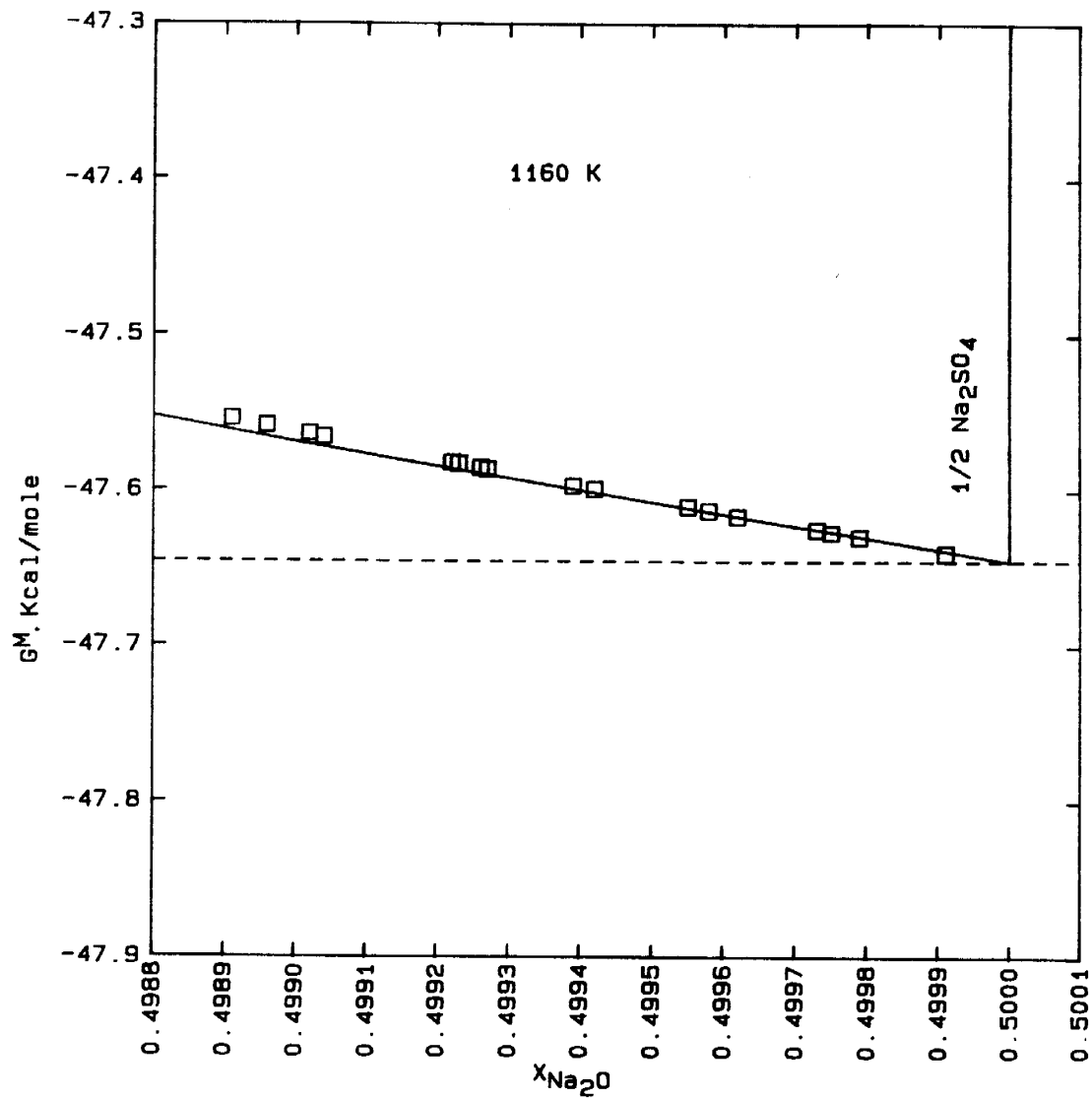
Figure 5.12 - Comparison of integral free energy of mixing at 1160 K.
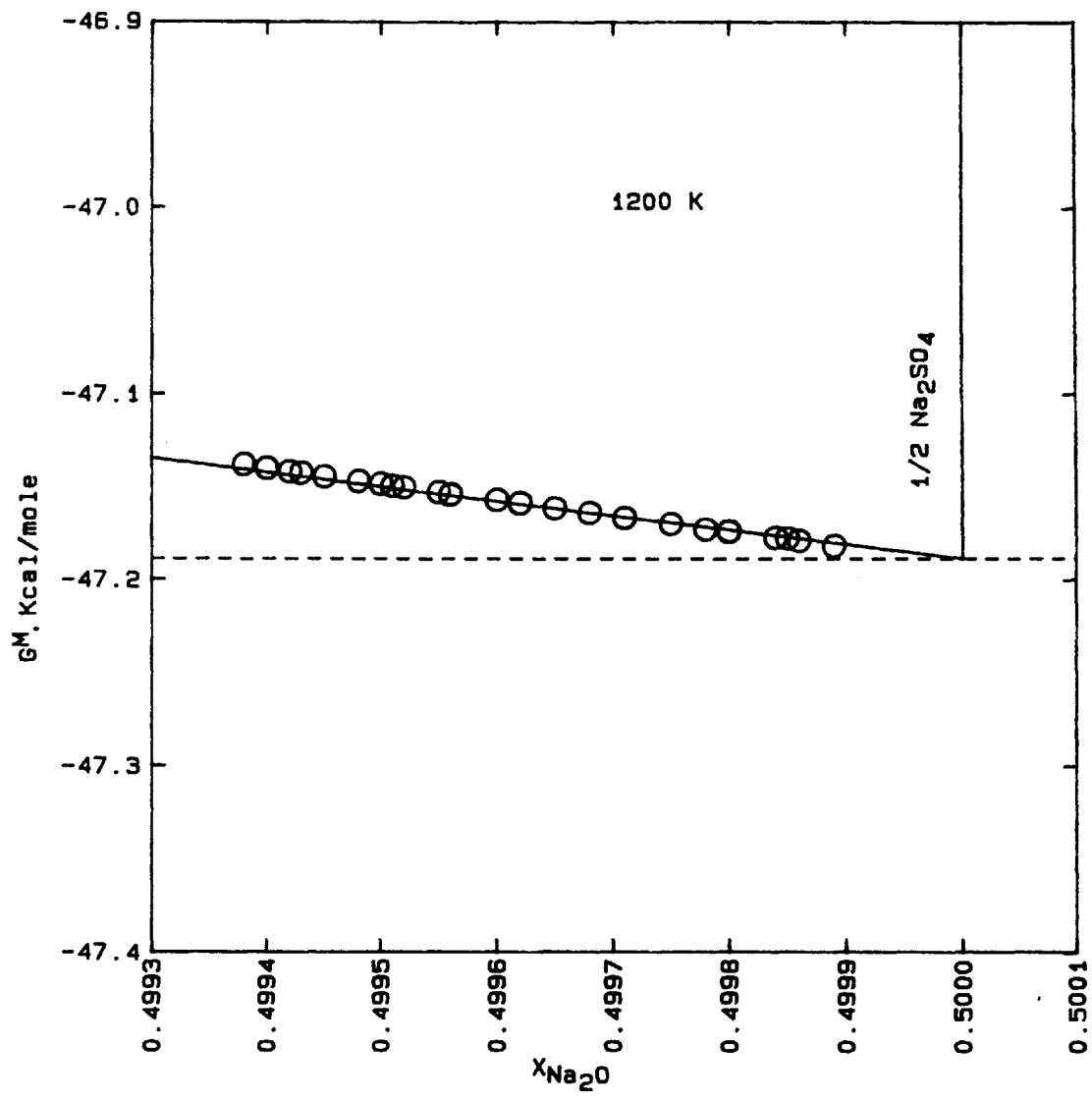
Figure 5.13 – Comparison of integral free energy of mixing at 1200 K.
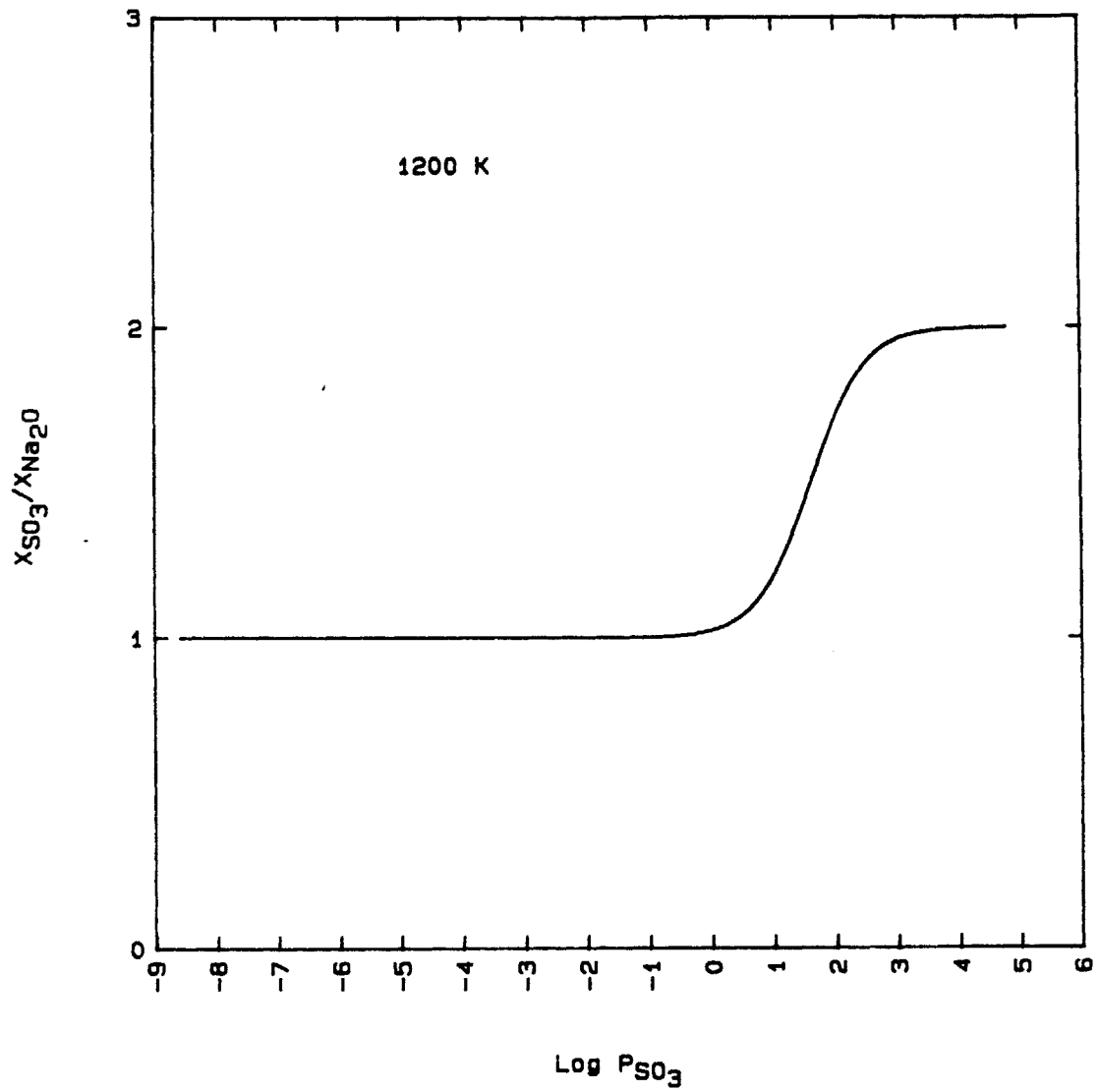
Figure 5.14 - Gibbs-Duhem integration for the activity of Na_2O at 1200 K.

The upper limit of integration is determined by integrating the Gibbs-Duhem equation (5-36) from a known point, X^*, at log P_{SO_3} greater than 4.0 determined by the analytical method to an unknown log P_{SO_3} at $X_{SO_3}/X_{Na_2O} = 2$ where the curve of X_{SO_3}/X_{Na_2O} versus log P_{SO_3} is essentially horizontal in this range; and, simultaneously, by satifying the following criteria at $Na_2S_2O_7$:

$$G^M_{Na_2S_2O_7} = 2.303RT \ (1/3 \ \log \ a_{Na_2O} + 2/3 \ \log \ P_{SO_3}) \quad (5-37)$$

The area under the curve when log $P_{SO_3} > 4.0$ in Figure 5.14 is approximated by:

$$area = (X_{SO_3}/X_{Na_2O})_{midpoint} \ x \ \Delta \log \ P_{SO_3} \quad (5-38)$$

where $(X_{SO_3}/X_{Na_2O})_{midpoint}$ is the average height of the trapezoid. The slope at composition X^* and the slope between X^* and $X_{Na_2O} = 1/3$ are also calculated so that the slope of the G^M curve is increasingly negative as the composition approaches the $X_{Na_2O} = 1/3$. The value of log P_{SO_3} at $Na_2O_2O_7$ ($X_{Na_2O} = 1/3$) must have the largest value between $X_{Na_2O} = 1/2$ and $1/3$, and it must monotonically increase in value as the limiting composition is approached. Since the G^M curve must be slightly concaved upward, intercepts on the Y-axis at $X_{Na_2O} = 0.0$ and tangents to the G^M curve are increasingly at higher values as $Na_2S_2O_7$ is approached. Therefore, the maximum value of log P_{SO_3} extrapolated from a known point X^* is selected to be the

partial pressure of SO_3 in equilibrium with pure $Na_2S_2O_7$.
The equilibrium conditions at $Na_2S_2O_7$ are found to be log
P_{SO_3} = 4.7895 and log a_{Na_2O} = -25.3333 at 1200 K, and log
P_{SO_3} = 4.1997 and log a_{Na_2O} = -25.1470 at 1160 K. Figures
5.15 and 5.16 depict the G^M curve and the tangents at the
two limiting compositions at 1200 K and 1160 K,
respectively.

Figure 5.17 shows the change of partial pressures of
SO_3 in equilibrium with $Na_2SO_4(l)$ and $Na_2S_2O_7(l)$ at a
constant temperature of 1160 K. The partial pressures of
SO_3 in equilibrium with the two limiting compositions of
$Na_2S_2O_7$ and Na_2SO_4 are finite. Therefore, the change of
equilibrium log P_{SO_3} across the composition range from
$Na_2S_2O_7$ to Na_2SO_4 varies from 4.1997 to -8.97 at 1160 K.

5.1.2 Thermodynamic Properties of Sodium Sulfate

Electrochemical experiments employing a platinum
crucible are conducted to investigate the thermodynamic
properties of pure sodium sulfate. The relationship between
the activity of sodium oxide in the sodium sulfate and the
partial pressure of SO_3 maintained over the melt will be
described. The EMF measurements by the solid electrolyte of
clear fused silica are later compared with results of other
investigators in the literature.
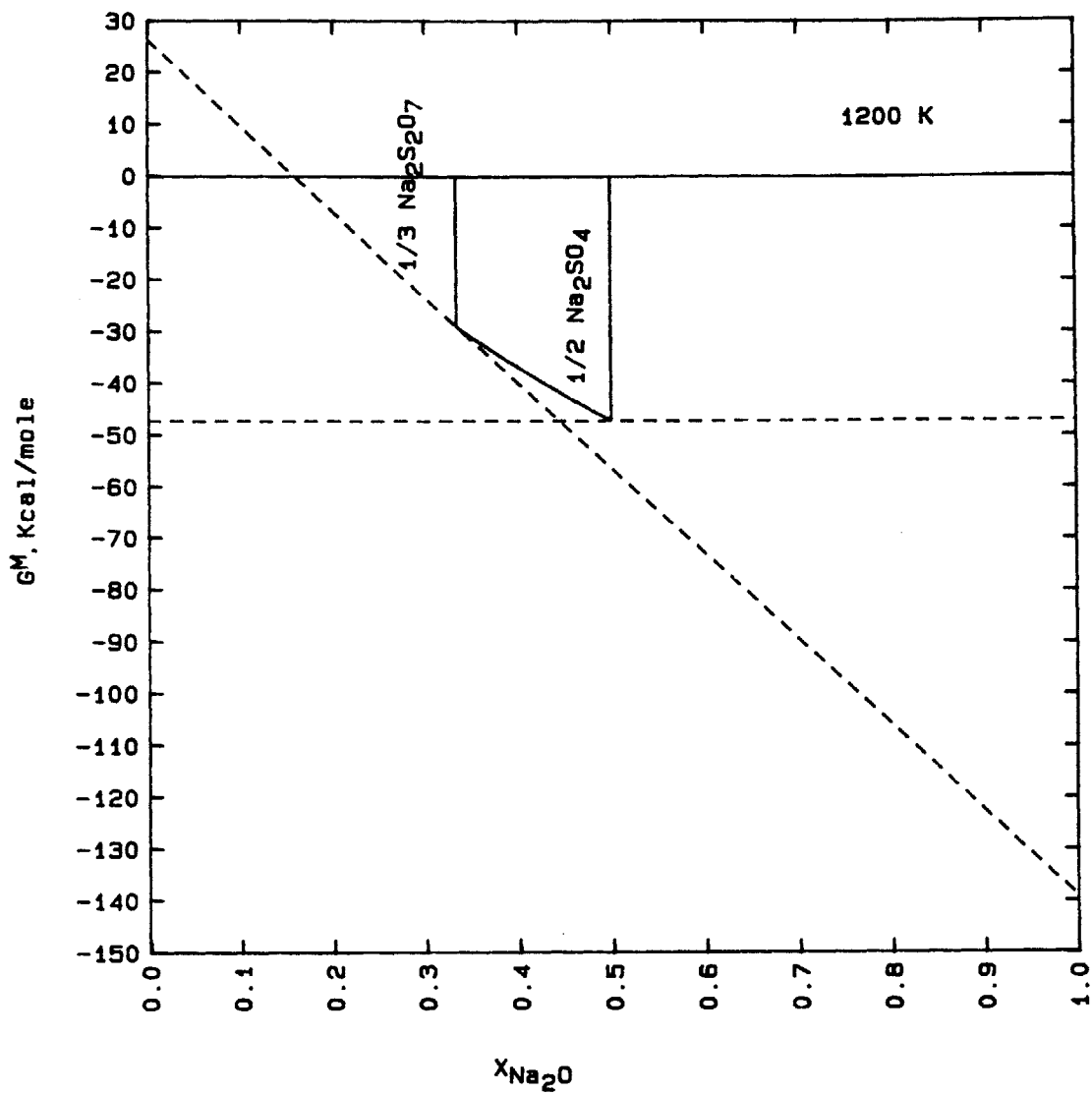
Figure 5.15 - Integral free energy of mixing of sodium pyrosulfate and sodium sulfate, and tangents at limiting compositions at 1200 K.
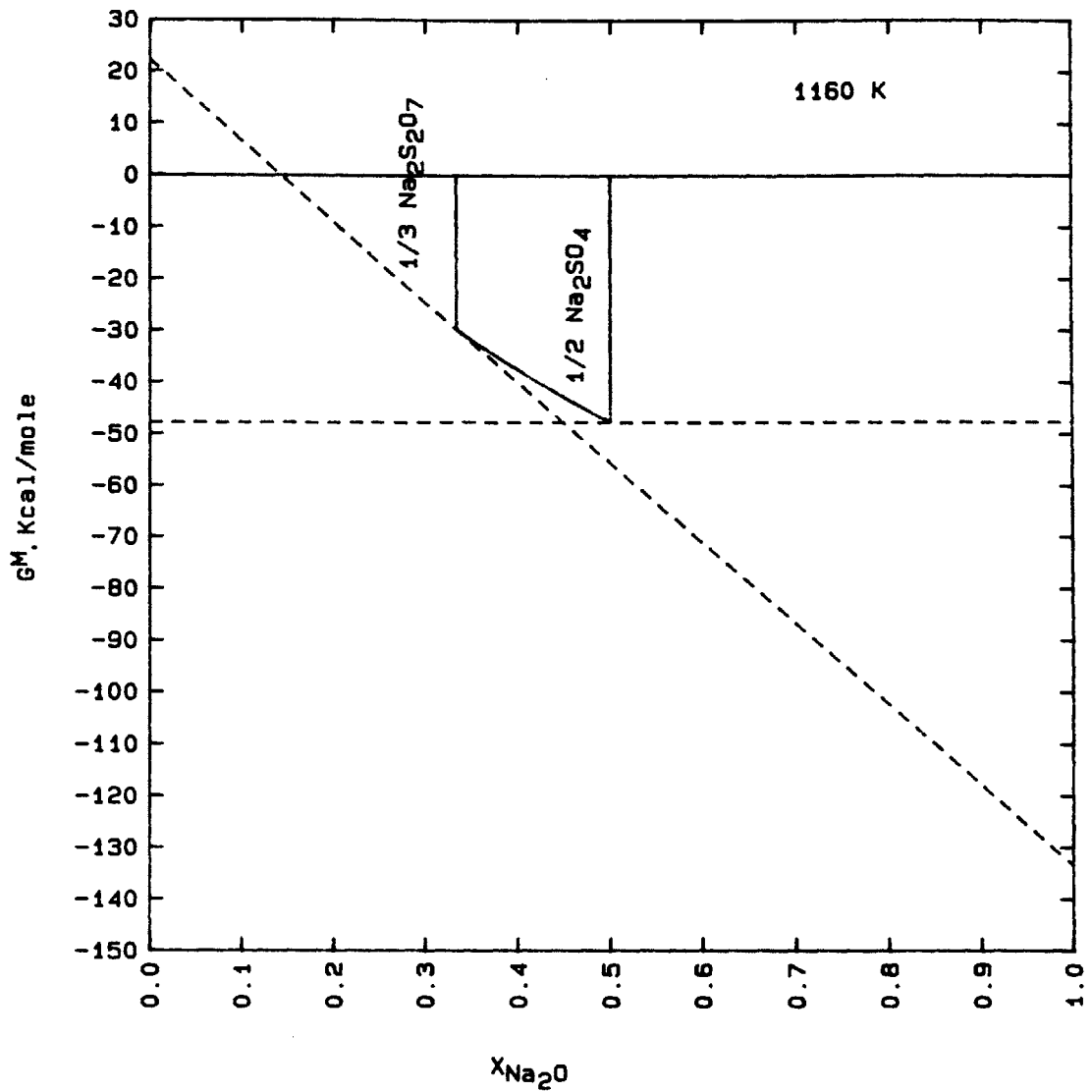
Figure 5.16 - Integral free energy of mixing of sodium pyrosulfate and sodium sulfate, and tangents at limiting compositions at 1160 K.
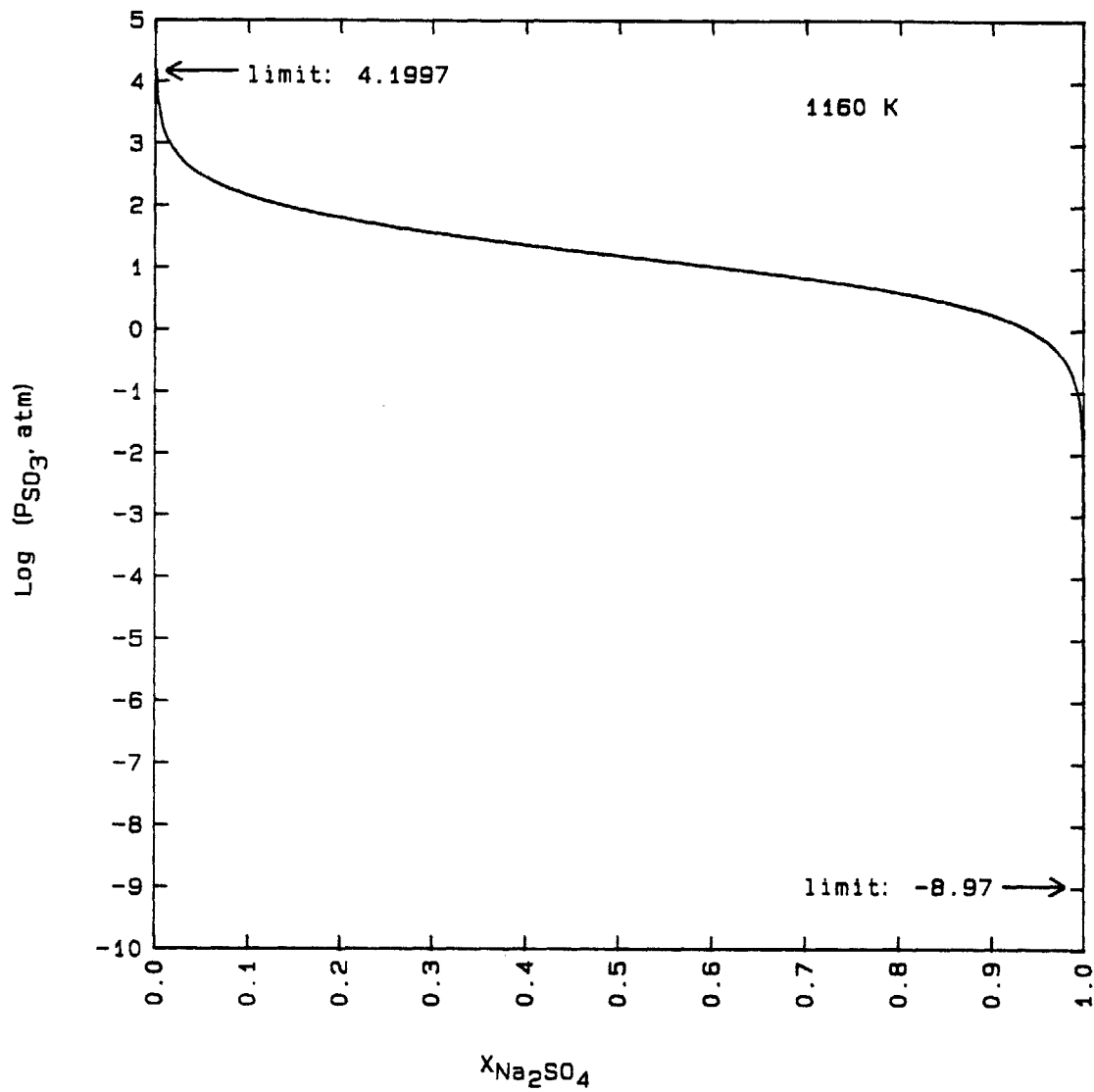
Figure 5.17 - Pressure of sulfer trioxide across composition range at 1160 K.

The thermodynamic properties of sodium sulfate are based on the chemical reaction between liquid sodium oxide and sulfur trioxide gas to form liquid sodium sulfate. Liquid sodium is taken as the standard state. The chemical reaction is:

$$Na_2O(l) + SO_3(g) = Na_2SO_4(l) \qquad (5-39)$$
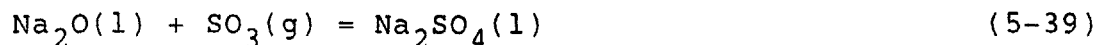
The equilibrium constant, K_{5-39}, is written as

$$K_{5-39} = a_{Na_2SO_4(l)} / (a_{Na_2O(l)} \cdot P_{SO_3}) \qquad (5-40)$$

or

$$\log K_{5-39} = \log a_{Na_2SO_4(l)} - \log a_{Na_2O(l)} - \log P_{SO_3} \qquad (5-41)$$

Since the activity of Na_2SO_4 in pure sodium sulfate is one, the $\log K_{5-39}$ is reduced to

$$\log K_{5-39} = - \log a_{Na_2O(l)} - \log P_{SO_3} \qquad (5-42)$$

or

$$\log a_{Na_2O(l)} = -\log K_{5-39} - \log P_{SO_3} \qquad (5-43)$$

Figure 5.18 illustrates the relationships between $\log a_{Na_2O}$ and $\log P_{SO_3}$ in platinum crucibles at 1160 K, 1200 K, 1224 K, and 1250 K. The experimental data are listed in Appendix J. The least-square equations with the standard deviations and coefficients of correlation are shown in Table 5-2. Figure 5.19 illustrates the relationship between
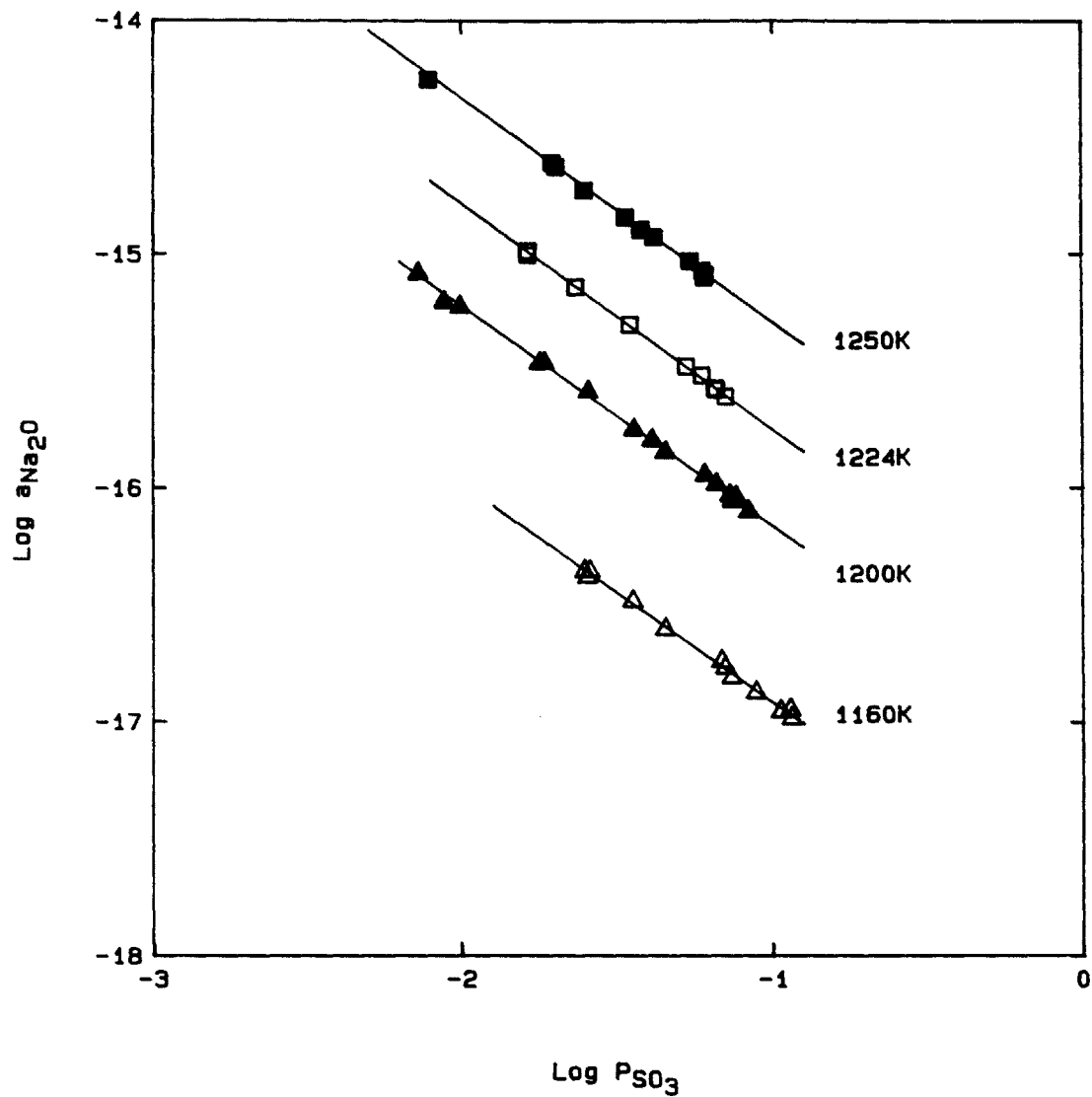
Figure 5.18 - SO$_3$ pressure dependence of activity of Na$_2$O in Na$_2$SO$_4$ contained in Pt crucibles at 1160 K, 1200 K, 1224 K, and 1250 K.
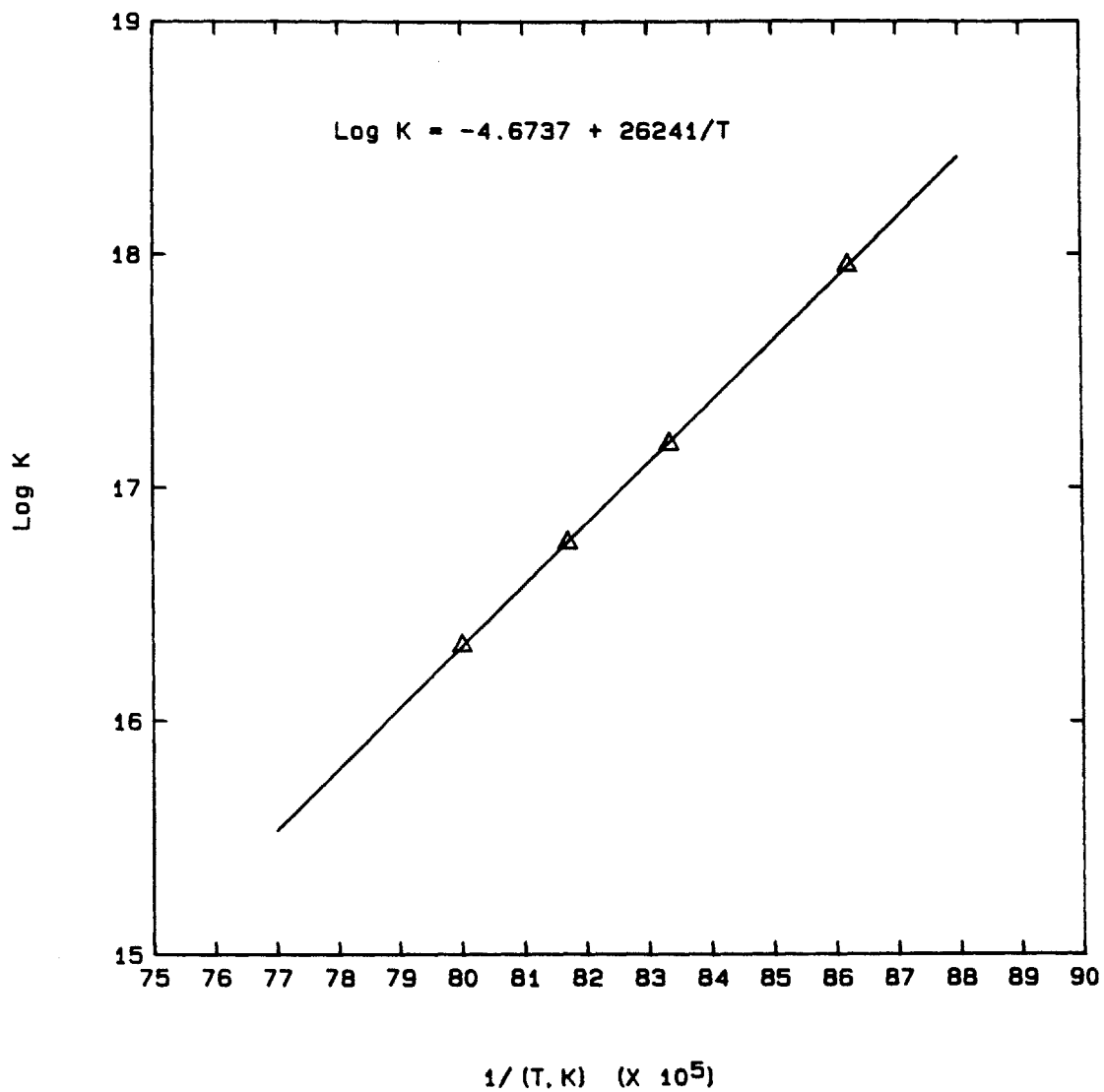
Figure 5.19 - Temperature dependence of equilibrium constant for the reaction to form $Na_2SO_4(l)$.

Table 5-2

Relationships Between Sodium Oxide and Sulfur Trioxide in Sodium Sulfate

$$\log a_{Na_2O(l)} = - \log K - c \cdot \log P_{SO_3}$$

T,K	log K	c	$S(\log a_{Na_2O})$	γ
1160	17.952±0.023	1.0±0.018	0.0158	0.998
1200	17.187±0.015*	1.0±0.010	0.0140	0.9992
1224	16.762±0.012	1.0±0.008	0.0071	0.9996
1250	16.324±0.014	1.0±0.009	0.0087	0.9995

* log K = 17.02 at 1200 K from data of JANAF Tables [104].

where $S(\log a_{Na_2O})$ is the standard deviation of $\log a_{Na_2O}$

γ is the correlation coefficient

the equilibrium constant K and temperature of the
equilibrium among $Na_2O(l)$, $SO_3(g)$, and $Na_2SO_4(l)$ in equation
(5-39). The relationship is:

$$\log K_{5-39} = -4.6737 \pm 0.1244 + (26241 \pm 150)/T \qquad (5-44)$$

The standard deviation of $\log K_{5-39}$ and the coefficient of
correlation are 0.00687 and 0.99996, respectively. The
standard Gibbs free energy of reaction (5-39) becomes:

$$\Delta G^{\circ}_{5-39} = -(120,080 \pm 686) + (21.39 \pm 0.57) \, T \, [cal/mol] \quad (5-45)$$

The standard Gibbs free energy of formation of sodium
sulfate is calculated from the EMF measurements based on
sodium(liquid) as the standard state. It also serves as a
means of testing the reliability of the data measured by the
fused silica solid electrolyte by comparing values in the
literature. The standard Gibbs free energy of reaction
(5-39) is written as:

$$\Delta G^{\circ}_r = \Delta G^{\circ}_f(Na_2SO_4(l)) - \Delta G^{\circ}_f(Na_2O(l)) - \Delta G^{\circ}_f(SO_3(g)) \qquad (5-46)$$

and it can also be expressed as:

$$\Delta G^{\circ}_r = - RT \ln K_{5-39} \qquad (5-47)$$

Having substituted ΔG°_r in equation (5-46) with the
expression in equation (5-47), the equation for unit

activity of Na_2SO_4 is further arranged to become:

$$\Delta G_f^o(Na_2SO_4(l)) = \Delta G_f^o(Na_2O(l)) + \Delta G_f^o(SO_3(g))$$

$$+ 2.303 \ RT \ \log \ (a_{Na_2O(l)} \cdot P_{SO_3}) \quad (5\text{-}48)$$

The $\Delta G_f^o(Na_2O(l))$ and $\Delta G_f^o(SO_3(g))$ are taken from the JANAF Tables [104]. Because the boiling point of sodium is registered at 1176.9 K; above this temperature, the $\Delta G_f^o(Na_2O(l))$ is adjusted to the standard state of sodium as liquid. The change of standard state is accomplished by subtracting the standard Gibbs free energy of condensation of sodium from the standard Gibbs free energy of formation of sodium oxide. The chemical reactions are manipulated as follows:

$$2Na(g) + 1/2 \ O_2(g) = Na_2O(l) \quad (5\text{-}49)$$

$$-) \qquad 2Na(g) = 2Na(l) \quad (5\text{-}50)$$

_____

$$2Na(l) + 1/2 \ O_2(g) = Na_2O(l) \quad (5\text{-}51)$$
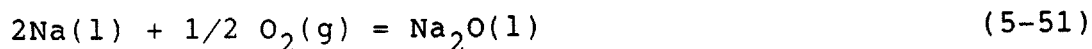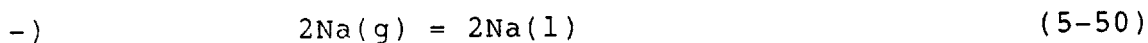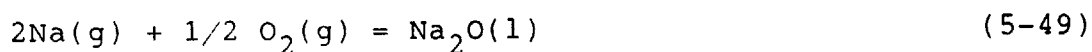
Thus, the standard Gibbs free energy of formation with respect to sodium(liquid) as standard state is

$$\Delta G_f^o(Na_2O(l)) = \Delta G_{5\text{-}49}^o - 2(\Delta G_{5\text{-}50}^o) \quad (5\text{-}52)$$

The activity of $Na_2O(l)$ and partial pressure of SO_3 are provided by the EMF and flowrate measurements, respectively.

The activities of sodium oxide at two constant flow ratios of O_2/SO_2 of 19.526 and 0.6327 using platinum crucibles are shown in Figure 5.20. The standard Gibbs free energy of formation of Na_2SO_4 calculated from the two set of data are compared with the results of the JANAF Tables [104], Mittal [88], and Liang & Elliott [66] in Figure 5.21. The standard Gibbs free energy of formation of Na_2SO_4 determined by this study using platinum crucibles is:

$$\Delta G_f^o(Na_2SO_4(l)) = -314.172 \pm 1.452$$
$$+ (0.08195 \pm 0.00120) \ T \ [Kcal/mole] \ (5-53)$$

The standard deviation of $\Delta G_f^o(Na_2SO_4(l))$ and the correlation coefficient are 0.1137 and 0.998, respectively. In addition to platinum crucibles, alumina crucibles are also employed to investigate the thermodynamic properties of sodium sulfate in the presence of solid Al_2O_3. Five equilibrium EMF runs are conducted at the inlet O_2/SO_2 ratios of 3.58, 5.02, 22.7, 24.2, and 25.5 with alumina crucibles. The activities of sodium oxide at various O_2/SO_2 ratios are shown in Figure 5.22. The experimental results are listed in Appendix K. The standard Gibbs free energy of formation of Na_2SO_4 determined by this study using alumina crucibles is:

$$\Delta G_f^o(Na_2SO_4(l)) = -304.135 \pm 4.655$$
$$+ (0.07359 \pm 0.00381) \ T \ [Kcal/mole] \ (5-54)$$

- 138 -
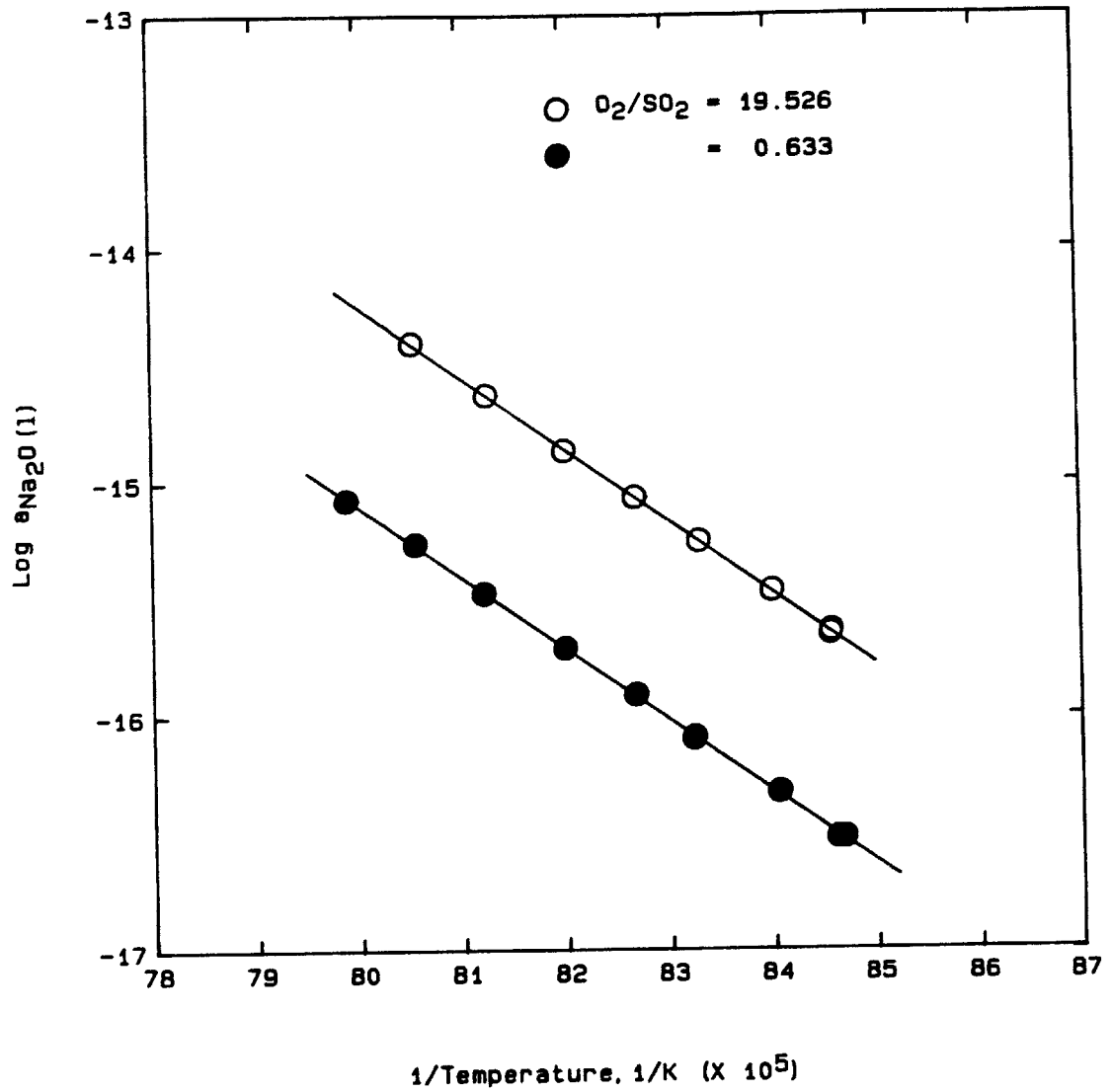
Figure 5.20 - Activity of sodium oxide in sodium sulfate contained in platinum crucibles equilibrated at two inlet gas ratios.
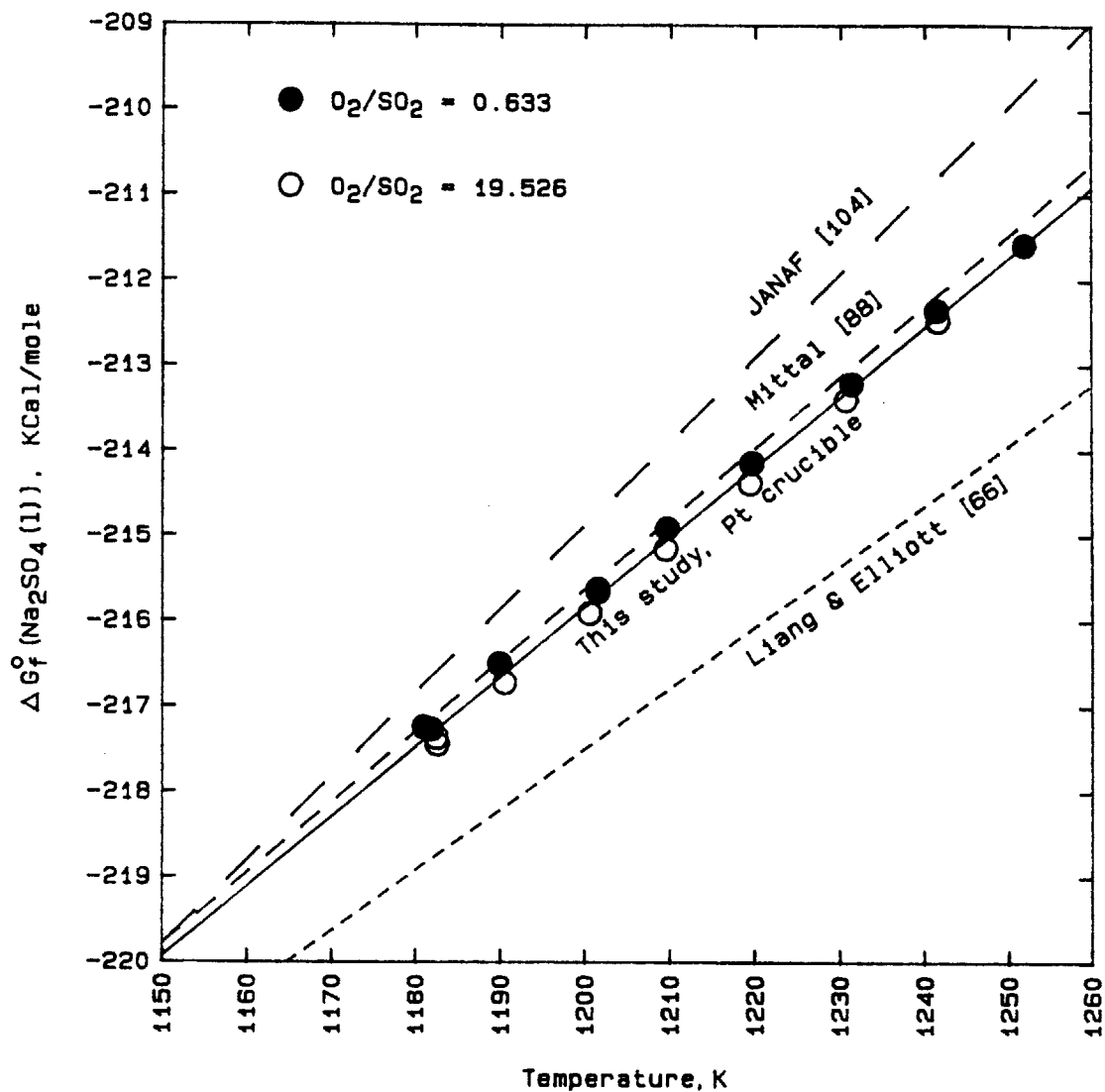
Figure 5.21 – Comparison of standard free energy of formation of Na_2SO_4 contained in platinum crucibles, Na(liquid) as the standard state (equation 5-48).
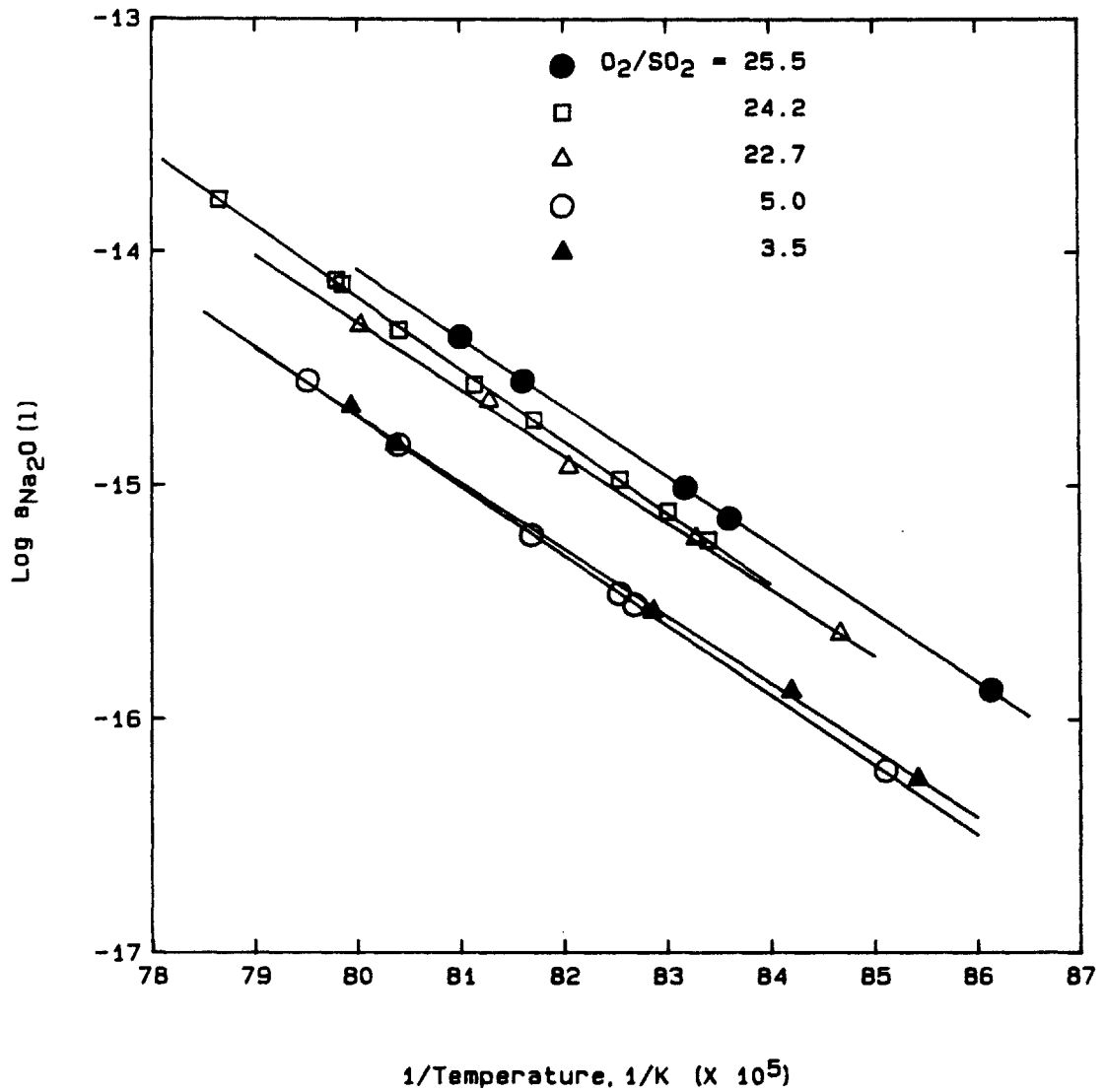
Figure 5.22 - Activity of sodium oxide in sodium sulfate contained in alumina crucibles at five inlet gas ratios.

The standard deviation of $\Delta G_f^o(Na_2SO_4(1))$ and the correlation coefficient are 0.5796 and 0.964, respectively. The $\Delta G_f^o(Na_2SO_4(1))$ are compared with those results of the JANAF Tables [104], Mittal [88], and Liang & Elliott [66] in Figure 5.23. The Gibbs free energies of formation of sodium sulfate from various sources are listed in Table 5-3 for comparison.

5.1.3 Performance of Fused Silica Solid Electrolyte at Basic Conditions

The behavior of the electrochemical cell with fused silica solid electrolyte in the presence of high activity of sodium oxide in sodium sulfate melts is investigated by adding granular sodium peroxide (Na_2O_2) to the sodium sulfate working melt under a pure oxygen atmosphere.

With the use of a platinum crucible, three batches of granular Na_2O_2 are added sequentially to a Na_2SO_4 melt at 1200 K under an atmosphere of oxygen after the melt has been equilibrated under a partial pressure of SO_3 of 0.0851 atm. The change in cell potential with time is depicted in Figure 5.24. A rapid decrease in potential, which indicates a sharp increase in the activity of sodium oxide, is recorded instantaneously after granular Na_2O_2 are dropped. With the additions of 7, 9, and 6 mg of Na_2O_2, the corresponding minimum potentials of -958.7910, -744.9616, and -166.0554 mv are recorded. The activities of Na_2O at the minimums are
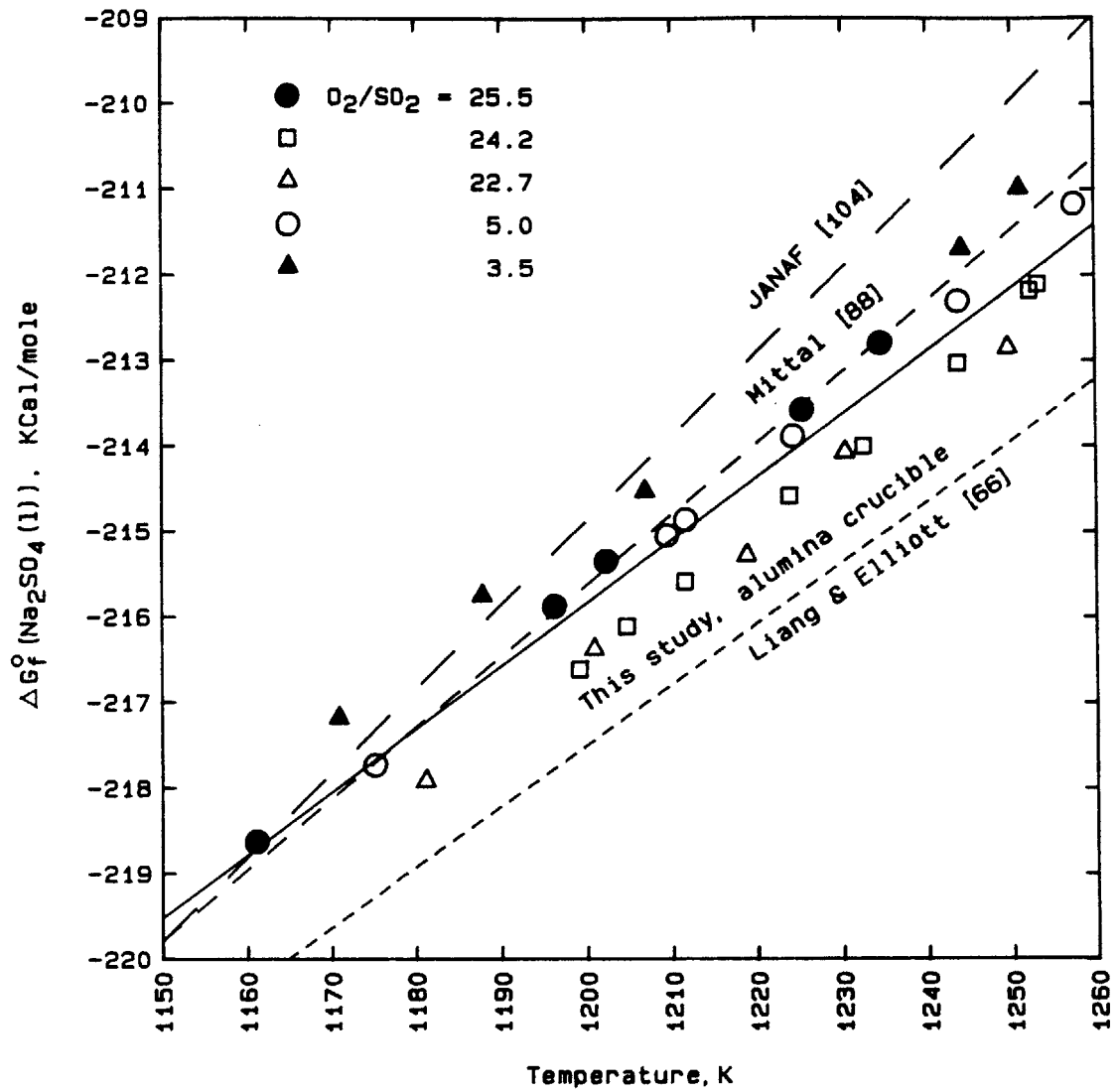
Figure 5.23 – Comparison of standard free energy of
formation of Na_2SO_4 contained in alumina crucibles,
Na(liquid) as standard state.
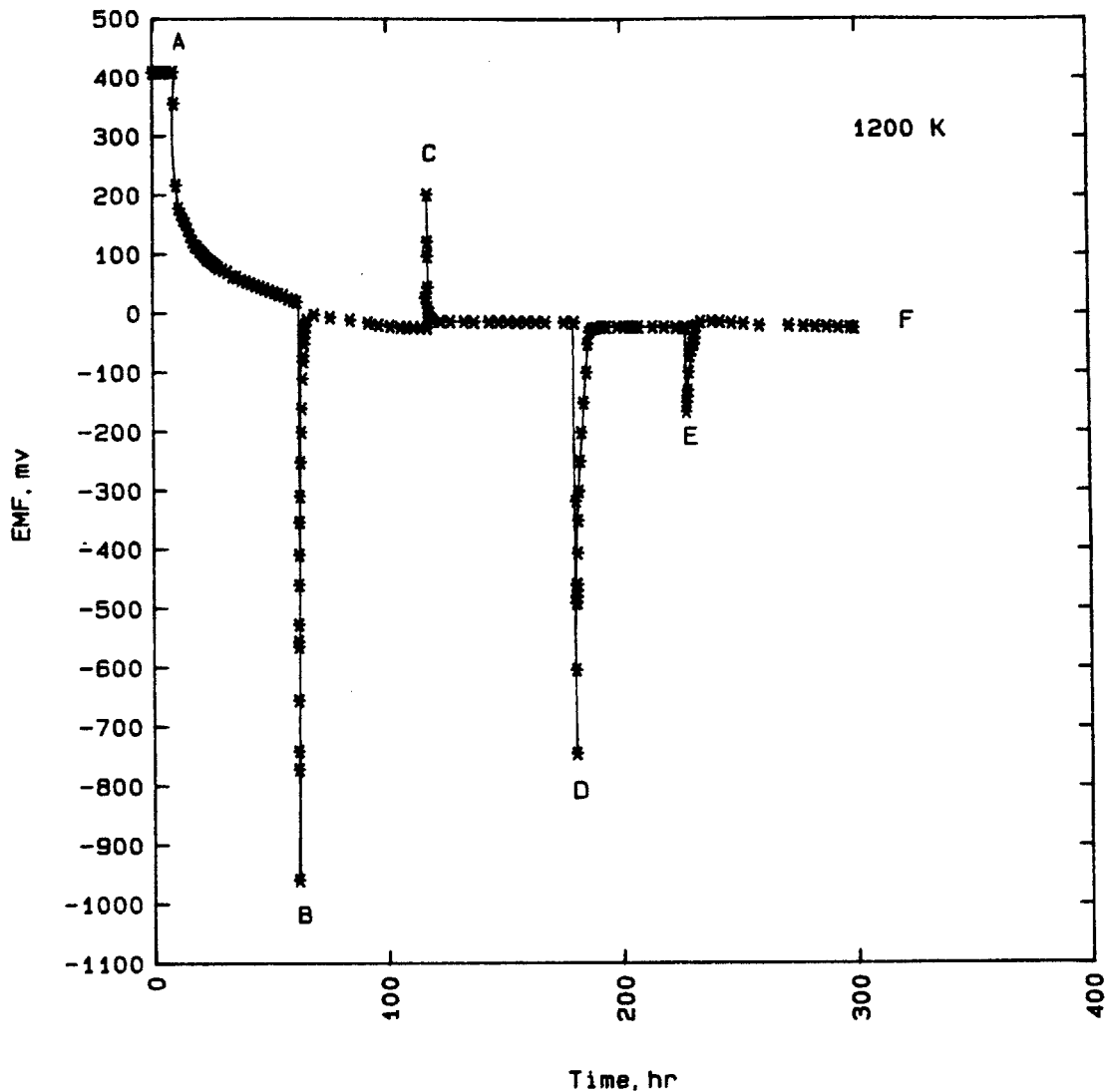
Figure 5.24 - Response of cell potential of sodium sulfate contained in a platinum crucible to Na_2O_2 addition under O_2 atmosphere at 1200 K. A: switching gas atmosphere from P_{SO_3} = 0.0851 to pure O_2; B: adding 7 mg of Na_2O_2, log a_{Na_2O} = -4.39; C: replacing exhaust tubing; D: adding 9 mg of Na_2O_2, log a_{Na_2O} = -6.19; E: adding 6 mg of Na_2O_2, log a_{Na_2O} = -11.05; F: equilibrium log a_{Na_2O} = -12.25.

Table 5-3

<u>Comparison of</u>
<u>Gibbs Free Energy Of Formation of Sodium Sulfate</u>

$$\Delta G_f^o(Na_2SO_4(l)) = \Delta H_f^o - \Delta S_f^o \cdot T$$

Source	solid electrolyte	crucible	ΔH_f^o, Kcal/mole	ΔS_f^o, Kcal/K·mole	1200 K ΔG_f^o, Kcal/mole
This study	clear fused silica	platinum	-314.172	-0.08195	-215.83
This study	clear fused silica	alumina	-304.135	-0.07359	-215.82
Mittal [88]	clear fused silica	platinum	-315.262	-0.08303	-215.63
Liang & Elliott [66]	beta-alumina	platinum	-302.837	-0.07112	-217.49
JANAF [104]	/	/	-332.734	-0.09822	-214.87

Standard state: 1 atm pressure; pure Na(l), $S_2(g)$, and $O_2(g)$.

equal to -4.396, -6.192, and -11.054 of log a_{Na_2O}, respectively. However, the cell potential always returns back to a value of -23.6 mv or log $a_{Na_2O} = -12.25$ within 10 hours. The increase in cell potential at 117 hours is recorded after the exhaust tubing has been replaced, but the EMF decreases back to -14.947 mv which corresponds to log $a_{Na_2O} = -12.32$. The activity of Na_2O maintains at a constant value regardless of the type of disturbance under pure O_2 atmosphere. Therefore, activities of Na_2O higher than $10^{-12.25}$ in Na_2SO_4 contained in a platinum crucible at 1200 K are not possible with the employment of solid electrolyte of fused silica.

With the use of an alumina crucible, batches of granular Na_2O_2 are added and samples are extracted during equilibration of Na_2SO_4 under pure oxygen at 1200 K, after the melt has been equilibrated under a partial pressure of SO_3 of 0.00225 atm for 12.5 hours. Two batches of Na_2O_2 of 9 mg and 10 mg are added during the transient stage of potential decay. The cell potential decreases instantaneously, and it exhibits a rapid return to the course of decay within an hour. The change in EMF is shown in Figure 5.25. The melt is thus acidic enough to neutralize the basic oxide in a short period of time.

More Na_2O_2 additions and samplings are performed as the liquid Na_2SO_4 comes to equilibrium in oxygen atmosphere. The effects on the cell potential is included in Figure 5.26. A batch of 8 mg Na_2O_2 is dropped at 95 hour or the
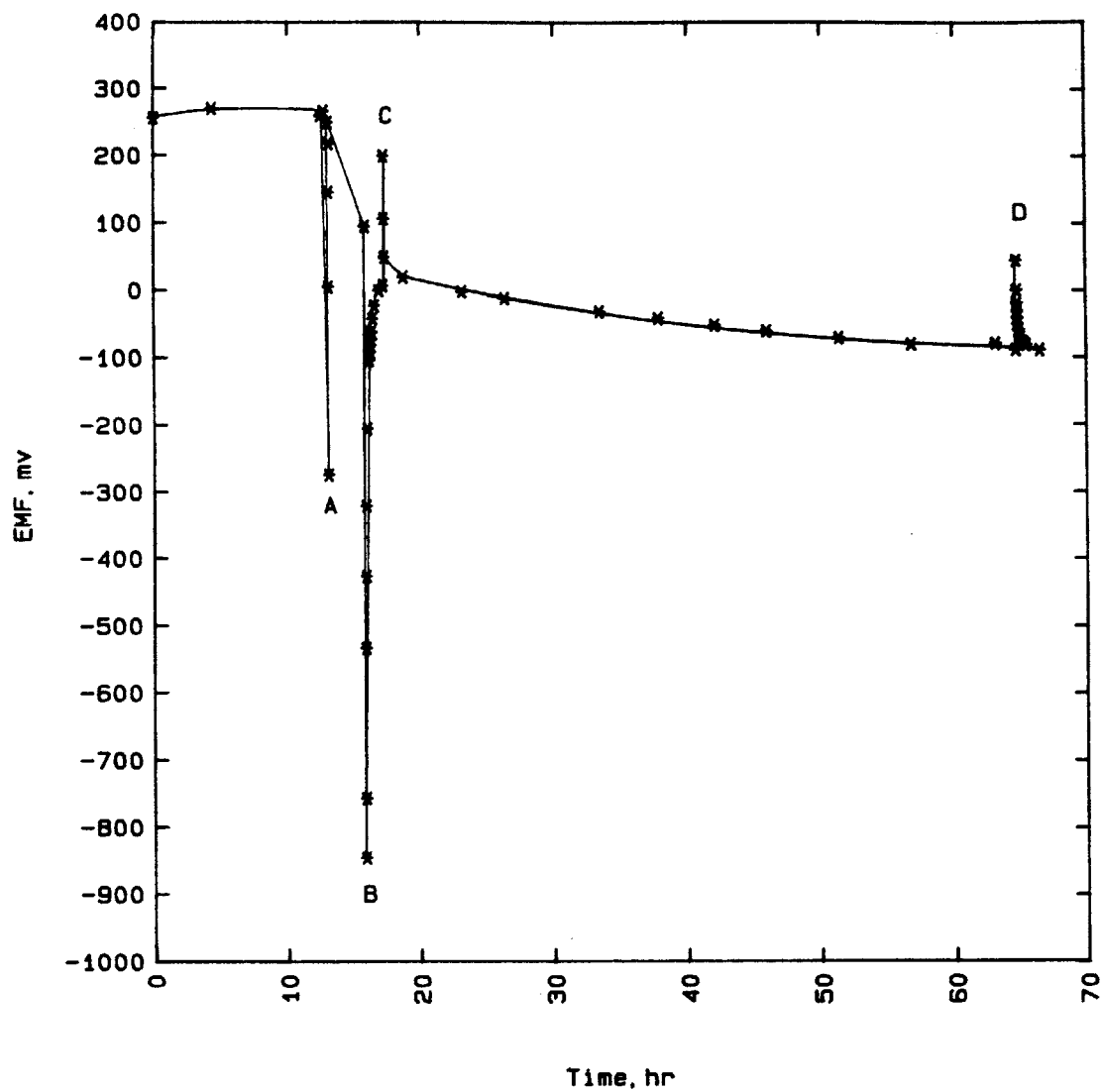
Figure 5.25 – Response of cell potential of sodium sulfate contained in an alumina crucible to Na_2O_2 addition under O_2 atmosphere at 1200 K. A: Switching gas atmosphere from P_{SO_3} = 0.0022 atm to pure O_2, and adding 9 mg of Na_2O_2; B: adding 10 mg of Na_2O_2; C: sampling; D: sampling.
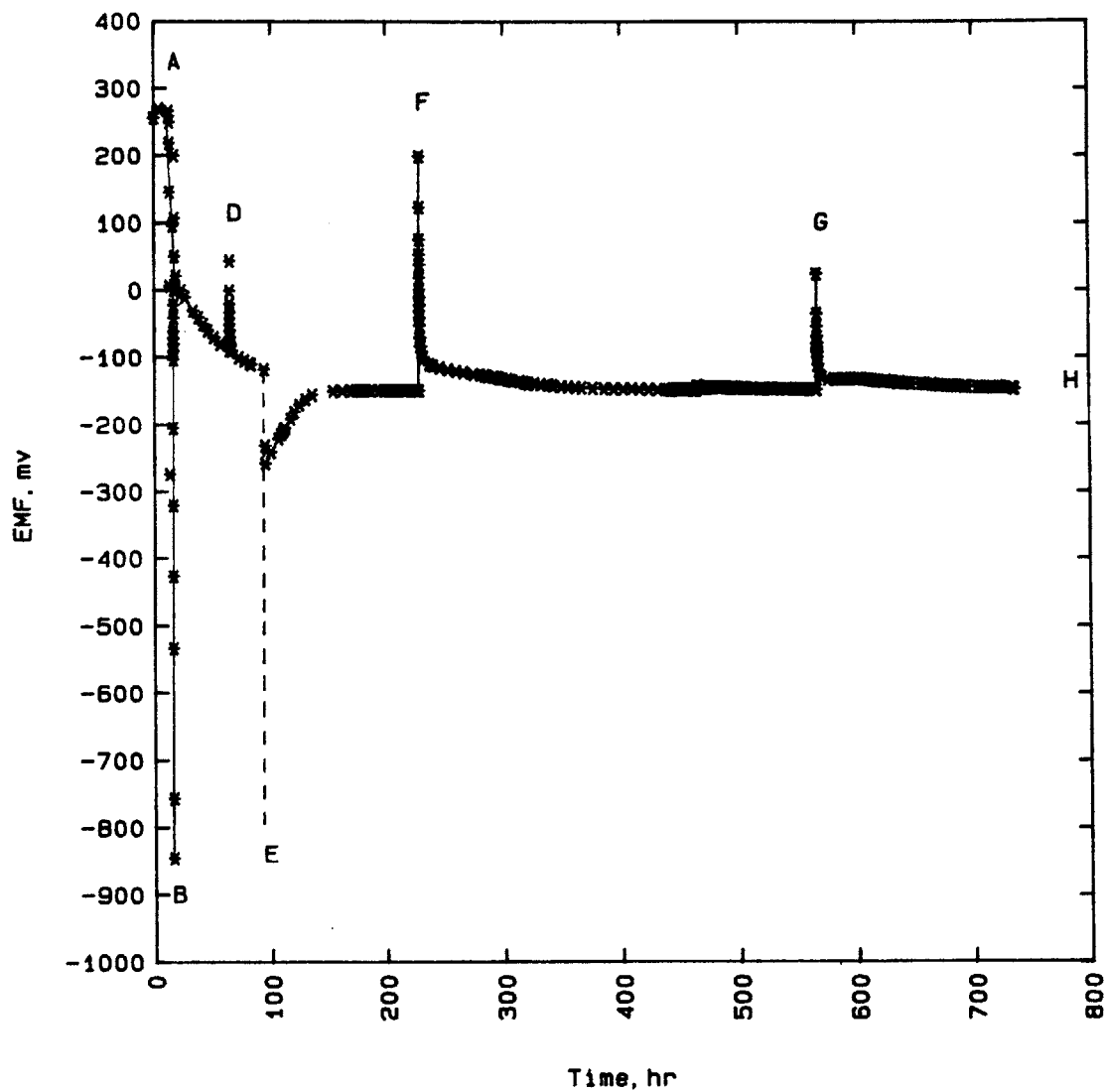
Figure 5.26 – Response of cell potential of sodium sulfate contained in an alumina crucible to Na_2O_2 addition under O_2 atmosphere at 1200 K. A: Switching gas atmosphere from P_{SO_3} = 0.0022 atm to pure O_2, and adding 9 mg of Na_2O_2; B: adding 10 mg of Na_2O_2; D: sampling; E: adding 8 mg of Na_2O_2; F: sampling; G: sampling; H: equilibrium log a_{Na_2O} = -11.90.

end of the transient period, the cell potential decreases instantaneously and takes 86 hours to return to the equilibrium level of -148.7 mv. The solid electrolyte is kept away from the melt during Na_2O_2 addition, no EMF measurement is recorded at that time. The two samplings at 210 hour and 570 hour raise the cell EMF which returns subsequently to an equilibrium potential of -148 mv in 187 hours and 170 hours, respectively. Only one cell potential of -148.5 mv or log a_{Na_2O} = -11.19 is attained under pure oxygen atmosphere regardless of the type of disturbances, and the rate of EMF recovery in alumina crucible is much slower than that in platinum crucible.

The concentration of aluminum in sodium sulfate contained in an alumina crucible during the course of equilibration under oxygen atmosphere (Figure 5.26) is shown in Figure 5.27. The concentration of aluminum decreases as the cell potential decreases. As the EMF approaches equilibrium, the concentration of aluminum in sodium sulfate diminishes to a minute level.

5.1.4 Kinetic Study of Sulfur Trioxide Solubility

The kinetic study on the adsorption and desorption of SO_3 gas in liquid Na_2SO_4 contained in platinum crucibles is focused on three rate determining steps: (1) gas phase mass transfer; (2) gas-liquid chemical reaction; and (3) liquid phase mass transfer. The rate determining step is the
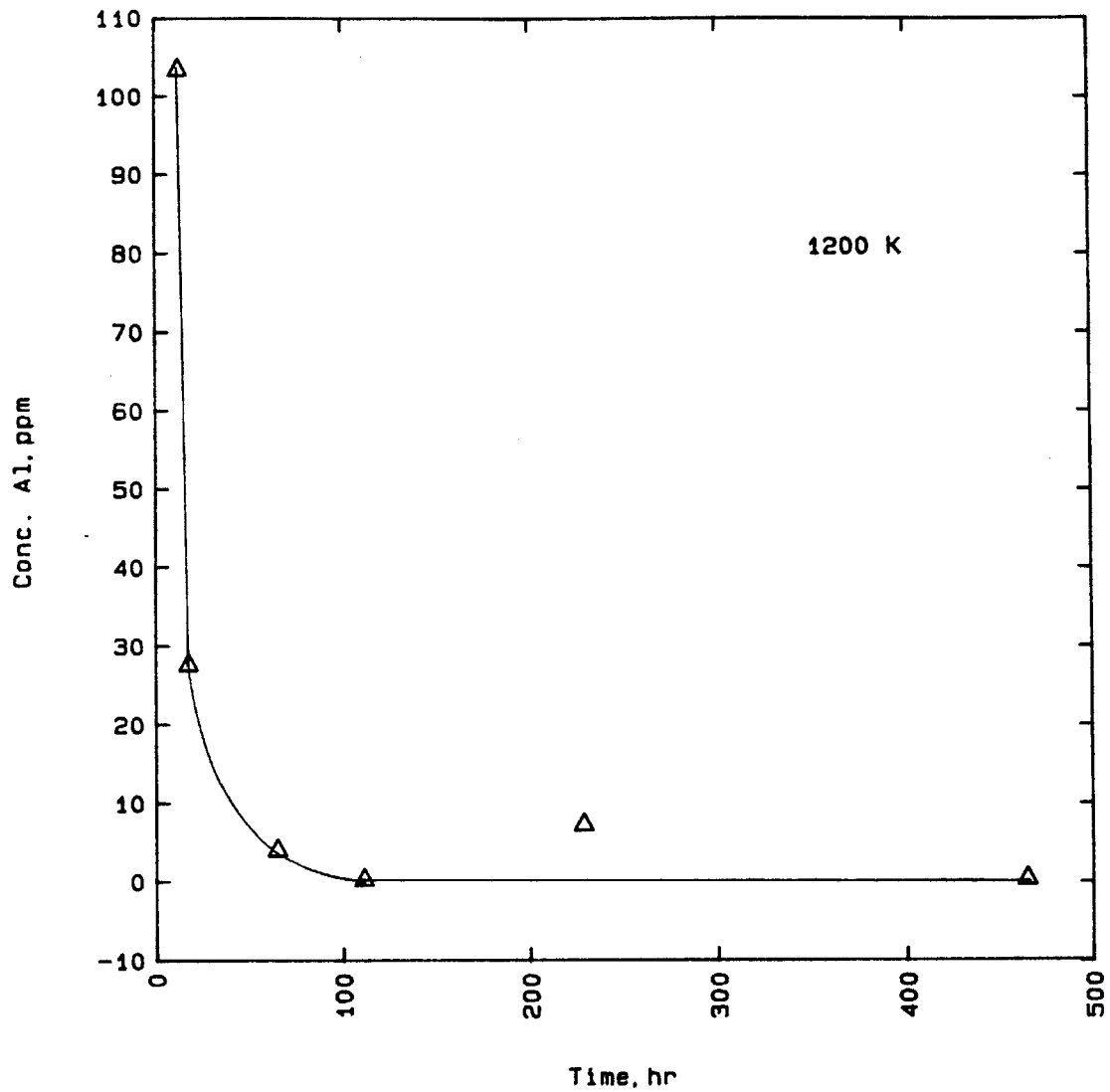
Figure 5.27 - Change of concentration of dissolved aluminum in Na_2SO_4 due to Na_2O_2 additions at 1200 K. Melt sampled periodically and analysed for aluminum at P_{O_2} = 1 atm with reference to the run depicted in Figure 5.26.

process which is slower than the others. The rate of this step will then be essentially the rate of the whole reaction as all preceding and succeeding steps are in equilibrium. Forty sets of the TGA experimental data in terms of weight change of liquid Na_2SO_4 in response to a step change in partial pressure of SO_3 at a constant temperature of 1160 K, 1200 K, 1224 K, or 1250 K are analyzed to determine the controlling step. Figure 5.28 illustrates, for example, the change in weight of the molten Na_2SO_4 caused by a step increase in P_{SO_3} from 0.0187 atm to 0.0735 atm at 1224 K.

The TGA experiment is conducted in such a way that, for example, in experiment TGA20-22, a step increase in P_{SO_3} from 0.0648 to 0.1158 atm at 1160 K is imposed. With O_2 and SO_2 reaction gases flowing respectively at 42.3 and 80.7 cc/min, the rate of SO_3 supplyed to the reaction chamber is 8766 mg/min. The maximum weight gain registered by the thermobalance is 0.29 mg/min. Therefore, starvation of SO_3 species does not exist. The rate of SO_3 absorption is not limited by the SO_3 supply in all of the TGA experiments.

The model of gas phase mass transfer control is represented by diffusion of SO_3 species through a gas boundary layer above the surface of the melt. The flux of SO_3 species in $mole \cdot cm^{-2} \cdot sec^{-1}$ is

$$J_{SO_3} = k_g (c_b^g - c_i^g) \qquad (5-55)$$

where $k_g = D_g / \delta_g$ $\qquad (5-56)$
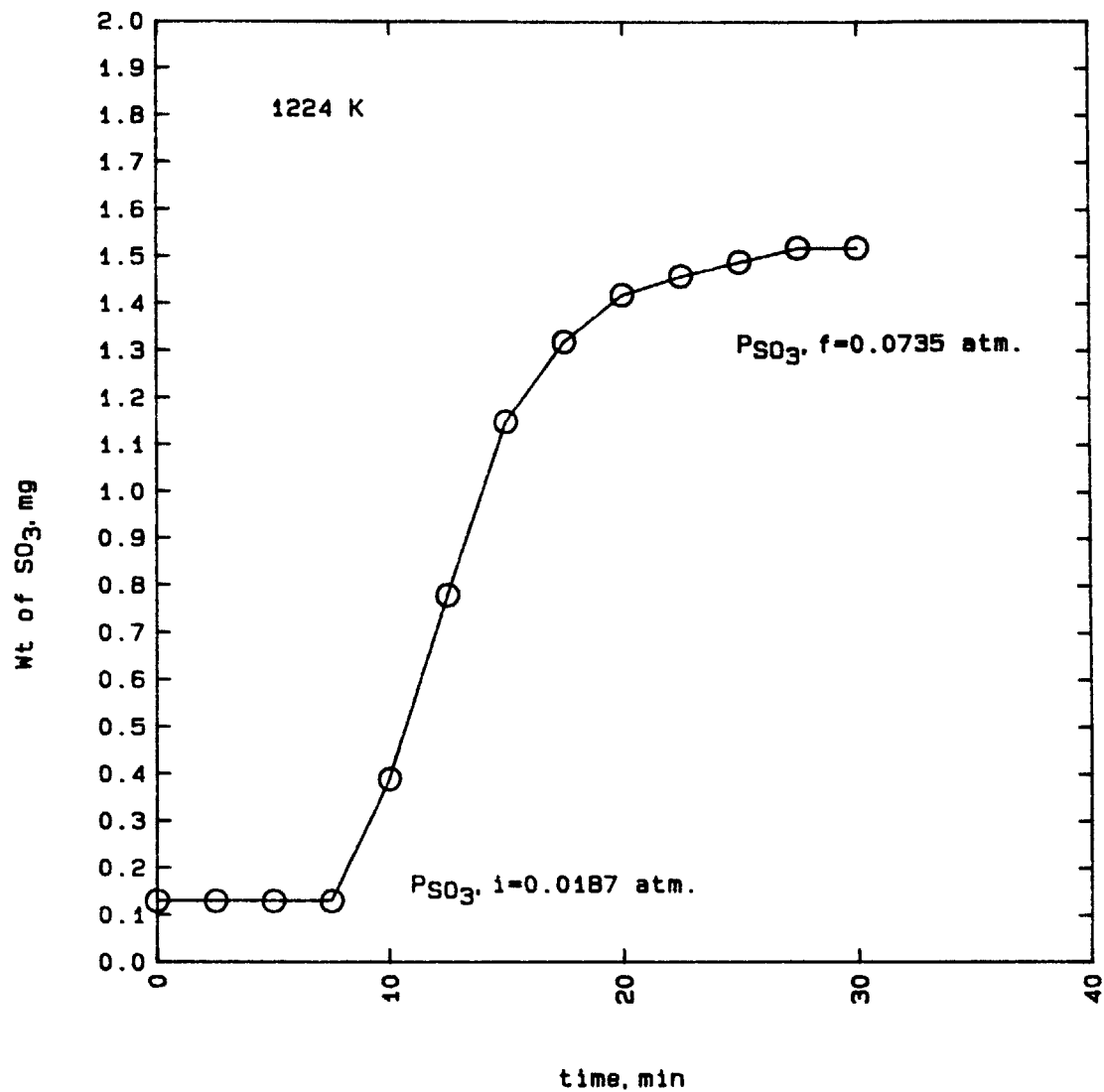
Figure 5.28 - Weight gain of sodium sulfate in response to a step increase in P_{SO_3} from 0.0187 atm to 0.0735 atm at 1224 K.

The symbols are explained in the nomenclature section of this document. The diffusion coefficient in gas is in the order of 10^{-1} cm^2sec^{-1}. The integrated form of equation (5-55) in terms of weights and slope, m, of the curves of the equilibrium solubility of SO_3 in Na_2SO_4 in Figure 5.1. is expressed as

$$\ln \left[(W_e - W_t) / (W_e - W_0) \right] = - k_{W1} t \qquad (5-57)$$

$$\text{where} \quad k_{W1} = (A \cdot k_g \cdot m) / (R \cdot T \cdot n_{Na_2SO_4}) \qquad (5-58)$$

The model of gas-liquid chemical reaction control is focused on the first order and second order chemical reaction with respect to concentration of SO_3 in liquid. The first order chemical reaction is represented by

$$J_{SO_3} = k_{c1} \cdot C_{SO_3} \qquad (5-59)$$

the integrated form of equation (5-59) is

$$\ln (W_t / W_0) = k_{W2} \cdot t \qquad (5-60)$$

$$\text{where} \quad k_{W2} = (k_{c1} \cdot A) / V \qquad (5-61)$$

The second order chemical reaction is represented by

$$J_{SO_3} = k_{c2} \cdot C_{SO_3}^2 \qquad (5-62)$$

- 153 -

the integrated form of equation (5-62) is

$$[(1/W_0) - (1/W_t)] = k_{W3} \cdot t \qquad (5-63)$$

$$\text{where } k_{W3} = (k_{c2} \cdot A) / (V^2 \cdot M_{SO_3}) \qquad (5-64)$$

The model of liquid phase mass transfer control is described as diffusion of SO_3 species across a liquid boundary layer at the surface of liquid melt. The flux of SO_3 is expressed as

$$J_{SO_3} = k_1 (c_b^1 - c_i^1) \qquad (5-65)$$

$$\text{where } k_1 = D_1 / \delta_1 \qquad (5-66)$$

The diffusion coefficient in liquid is in the order of 10^{-5} $cm^2 sec^{-1}$. The integrated form of equation (5-65) in terms of weights is expressed as

$$\ln [(W_e - W_t) / (W_e - W_0)] = - k_{W4} t \qquad (5-67)$$

$$\text{where } k_{W4} = (A \cdot k_1) / V \qquad (5-68)$$

The kinetic runs are analyzed by plotting TGA data according to the integrated equations (5-57), (5-60), (5-63), and (5-67) versus time in each model. For example, Figure 5.29 is a plot of the TGA data in accordance with the

- 154 -
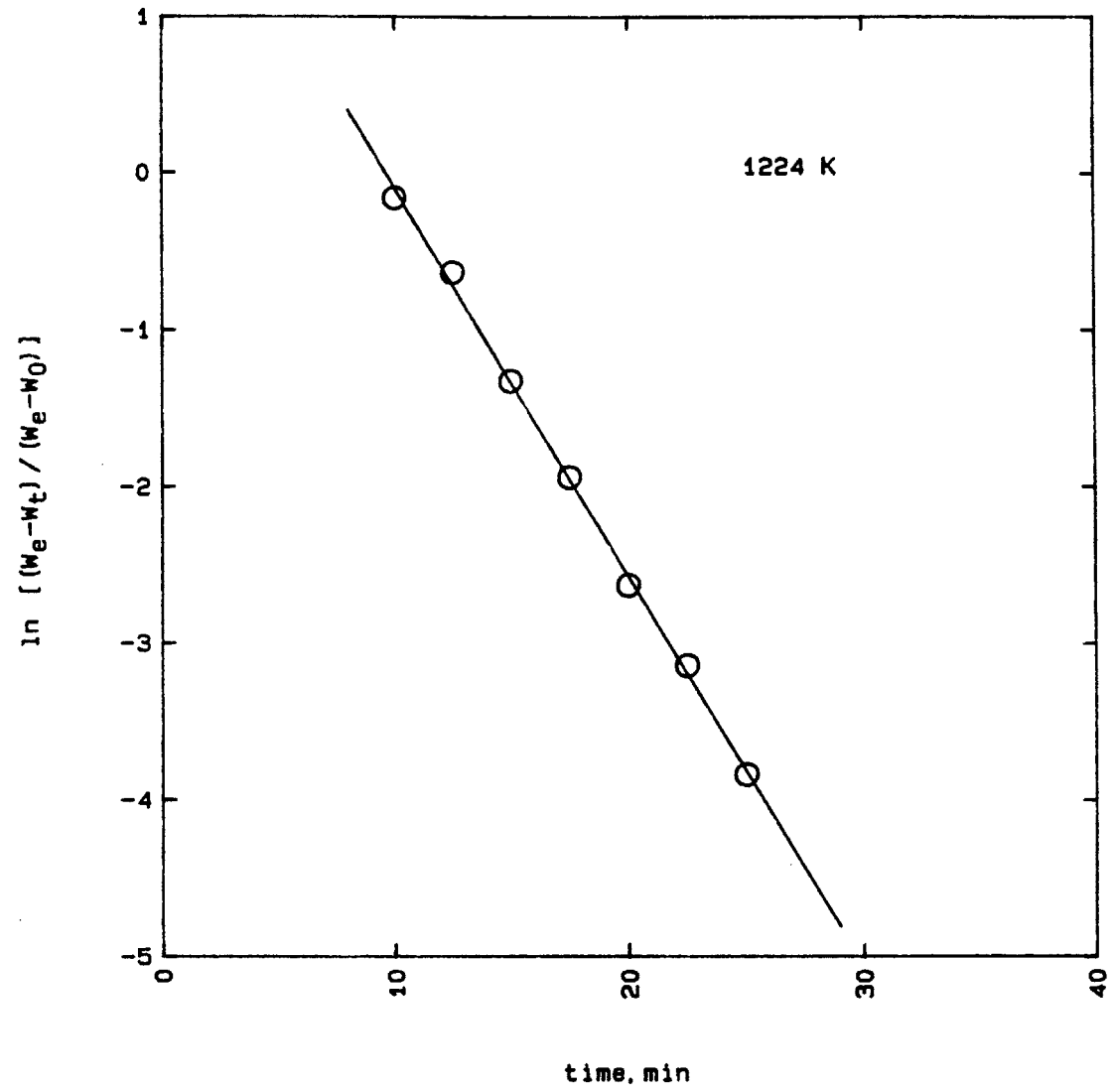
Figure 5.29 — Analysis of kinetic data according to the liquid phase mass transfer model at 1224 K.

liquid phase mass transfer model. The rate constants of both SO_3 absorption and desorption and correlation coefficients of least-square linear regression are tabulated in Table 5-4. The model with the best correlation for a given set of experimental data is indicated with a '+' in the Table. The experimental data exhibit essentially linear relationships in all plots, the correlation coefficients are greater than 0.9 in most cases. Mixed control is therefore not the control mechanism. The diffusion control model in either gas or liquid phase, in general, has the best correlation among the models in the process of SO_3 adsorption and desorption. Some of the SO_3 desorption runs, however, show a better fit with either of the two chemical reaction models.

The activation enthalpy for the kinetic process at 1160 K, 1200 K, 1224 K, and 1250 K is evaluated. A multilinear regression program is employed to investigate the relationship among rate constants (k_g, k_{c1}, k_{c2}, k_l), temperature (T), and change in partial pressure of SO_3 (ΔP) in each model. The rate constants calculated according to equations (5-58), (5-61), (5-64), and (5-68) are based on $n_{Na_2SO_4}$, A, V, and R being 0.0141 mole, 4.5 cm^2, 4.49 cm^3, and 82.057 cm$^3 \cdot$atm$\cdot$K$^{-1} \cdot$mole^{-1}, respectively. The relation being focused on is:

$$\ln k = a + b/T + c \cdot \ln \Delta P_{SO_3} \qquad (5-69)$$

Table 5-4

Rate constants and correlation coefficients in kinetic models
of absorption and desorption of SO_3 in/from liquid Na_2SO_4 contained in platinum crucibles

Expt. No.	T,K	ΔP,atm	$k_{W1} \times 10^3$,sec^{-1} or $k_{W4} \times 10^3$,sec^{-1}	cor. coef.	$k_{W2} \times 10^4$,sec^{-1}	cor.coef.	$k_{W3} \times 10^4$,sec^{-1}	cor.coef.
TGA19-02	1160	0.0247	3.58 +	0.993	1.83	0.952	0.255	0.945
TGA19-03	1160	0.0157	3.95	0.966	12.72 +	0.967	15.32	0.933
TGA19-04	1160	0.0036	4.29	0.946	6.91 +	0.960	6.54	0.932
TGA19-05	1160	0.0154	5.19 +	0.951	8.31	0.944	9.17	0.911
TGA19-07	1160	0.0126	3.12	0.941	5.36 +	0.955	5.48	0.921
TGA20-22	1160	0.0510	4.04 +	0.983	1.37	0.918	0.221	0.907
TGA20-23	1160	−0.0970	2.60 +	0.992	−4.38	0.952	−0.708	0.968
TGA20-25	1160	0.0316	3.36 +	0.989	11.89	0.806	18.82	0.659
TGA20-26	1160	0.0500	4.13 +	0.980	9.54	0.843	6.53	0.730
TGA20-27	1160	−0.0592	1.59	0.962	−8.48 +	0.987	−9.32	0.975
TGA06-01	1200	0.0247	2.98 +	0.973	2.49	0.898	0.989	0.873
TGA06-02	1200	0.0288	2.85 +	0.992	1.83	0.848	0.494	0.831
TGA06-07	1200	−0.0449	3.25 +	0.994	−2.74	0.923	−0.688	0.938
TGA06-08	1200	0.0352	3.95 +	0.993	2.81	0.887	0.681	0.868
TGA19-13	1200	0.0202	3.85 +	0.988	6.36	0.918	7.56	0.884
TGA19-15	1200	−0.0563	2.85 +	0.990	−2.17	0.969	−0.308	0.975
TGA19-16	1200	0.0660	4.60 +	0.997	2.68	0.888	0.360	0.874
TGA20-02	1200	0.0296	3.77 +	0.987	8.13	0.930	6.96	0.893
TGA20-03	1200	0.0274	4.29 +	0.973	9.80	0.929	12.98	0.881
TGA20-05	1200	−0.0187	1.95	0.979	−7.55 +	0.990	−11.98	0.988
TGA20-07	1200	0.0492	2.73 +	0.998	5.37	0.767	4.81	0.668
TGA20-08	1200	−0.0230	2.98	0.953	−6.53	0.990	−8.79 +	0.996
TGA20-09	1200	−0.0561	3.86	0.957	−13.44 +	0.990	−13.17	0.981
TGA20-10	1200	0.0173	6.58 +	0.978	10.17	0.951	12.77	0.927
TGA20-12	1200	−0.0176	4.60	0.982	−14.27	0.991	−27.57 +	0.992
TGA20-13	1200	0.0399	3.01 +	0.998	7.34	0.796	8.73	0.688
TGA20-29	1224	0.0548	4.14 +	0.999	14.25	0.841	20.09	0.757
TGA20-31	1224	0.0260	4.53 +	0.974	5.04	0.962	3.82	0.948
TGA20-33	1224	−0.0317	4.07	0.981	−4.85	0.972	−3.81 +	0.982
TGA20-34	1224	0.0531	2.79 +	0.964	6.74	0.953	5.19	0.904
TGA20-35	1224	−0.0432	3.76	0.978	−9.66	0.981	−11.65 +	0.994
TGA20-36	1224	0.0292	4.32 +	0.995	4.24	0.884	2.58	0.857
TGA06-04	1250	−0.0426	3.99 +	0.991	−1.62	0.877	−0.462	0.887
TGA06-05	1250	0.0381	4.25 +	0.983	2.82	0.972	0.748	0.966
TGA06-06	1250	−0.0498	3.85 +	0.991	−3.22	0.952	−0.970	0.961
TGA20-15	1250	−0.0373	4.35	0.970	−12.53 +	0.996	−21.74 +	0.996
TGA20-16	1250	0.0577	5.88 +	0.978	11.68	0.901	11.88	0.850
TGA20-17	1250	−0.0457	3.71 +	0.987	−7.32	0.970	−8.43	0.986
TGA20-18	1250	0.0390	4.83 +	0.982	9.24	0.907	10.34	0.856
TGA20-19	1250	−0.0339	4.51	0.958	−13.01 +	0.995	−26.60	0.987

+ the best correlation among the models

The value of $-b \cdot R$ indicates the activation enthalpy, ΔH^*, for the process. The results of the regressions and the activation enthalpy are listed in Table 5-5 for SO_3 adsorption and in Table 5-6 for SO_3 desorption. The small activation enthalpies in each cases indicate chemical reaction controls at the gas/liquid interface and at the bulk liquid are very unlikely to be the rate determining steps. Since negative activation enthalpies do not represent the physical behavior of the kinetic process, the liquid phase mass transfer control is the only reasonable model. The activation enthalpies of SO_3 absorption and desorption are 6.7 Kcal and 20.8 Kcal, respectively.

The boundary layer thickness of gas diffusion is calculated with the assumption that the equilibrium solubility of SO_3 in Figure 5.1 is approximated by linear relationships. m is thus a constant with values of 14.45, 20.32, 30.28, and 35.54 at 1160 K, 1200 K, 1224 K, and 1250 K, respectively. With the diffusion coefficient in gas, D_g, in the order of 10^{-1} $cm^2 \cdot sec^{-1}$, the gas boundary layer thickness is determined to vary from 1.01 cm to 3.40 cm by using equation (5-56). The gas boundary layer thickness is thus too large for a Na_2SO_4 melt with a depth of 1.2 cm surrounding by a 1.6 cm high platinum crucible wall. The gas phase mass transfer control is therefore eliminated.

Table 5-5

Activation Enthalpy of SO_3 Adsorption

$$\ln k = a + b/T + c \ln \Delta P_{SO_3}$$

kinetic model	a	b($\times 10^{-3}$)	c($\times 10^2$)	ΔH^*,Kcal
gas phase diffusion	−11.86	10.43	−8.46	−20.7
1st order reaction	−4.83	−3.87	−16.9	7.69
2nd order reaction	7.11	−13.80	−67.6	27.0
liquid phase diffusion	−3.03	−3.36	−8.79	6.7

Table 5-6

Activation Enthalpy of SO_3 Desorption

$$\ln k = a + b/T + c \ln \Delta P_{SO_3}$$

kinetic model	a	b($\times 10^{-3}$)	c($\times 10^2$)	ΔH^*,Kcal
gas phase diffusion	−6.53	3.89	−4.64	−7.72
1st order reaction	−12.5	3.94	−57.0	−7.83
2nd order reaction	−9.09	1.45	−188.0	−2.8
liquid phase diffusion	2.91	−10.5	−0.53	20.8

With the diffusion coefficient in liquid being in the order of 10^{-5} $cm^2 \cdot sec^{-1}$, the liquid boundary layer thickness is calculated to vary from 1.52×10^{-3} cm to 6.29×10^{-3} cm. Moore [105] stated that the boundary layer thickness is in the order of 10^{-3} cm for diffusion control. The liquid mass transfer is therefore a reasonable model to describe the process of adsorption/desorption of SO_3 gas in/from molten sodium sulfate.

5.2 Solubility of Alumina in Sodium Sulfate

Thermogravimetric analyses (TGA) and electrochemical (EMF) experiments are conducted to study the solubility of alumina in molten sodium sulfate at 1160 K and 1200 K. During the TGA experiments, solubility measurements are taken from the weight change of sodium sulfate contained in an alumina crucible under a controlled atmosphere of SO_3. During the EMF experiments, samples are extracted from the melt during equilibration under a partial pressure of SO_3. The concentration of aluminum in the sodium sulfate is then determined by the DC plasma arc elemental emission spectroscopy. The TGA results will be reported prior to the EMF results. The measurements from this study will be compared with other studies in the literature. The kinetics of Al_2O_3 solubility in sodium sulfate will be shown subsequently.

5.2.1 Thermogravimetric Results

Three thermogravimetric experiments were performed with pure sodium sulfate contained in alumina crucibles. Two of them are conducted at 1160 K, and the third experiment at 1200 K. The experimental data are tabulated in Appendix I. Figure 5.30 shows the equilibrium solubility of sulfur trioxide in terms of mole fractions of SO_3 in molten sodium sulfate using alumina crucibles. The partial pressure of sulfur trioxide was increased sequentially from 0.0202 to 0.1093 atm at 1160 K and from 0.0129 to 0.0662 atm at 1200 K. The corresponding maximum solubilities at 1160 K and 1200 K are 0.1875 and 0.0632 mole fraction of SO_3, respectively. The TGA experiments show that the solubility of sulfur trioxide increases in a non-linear fashion with an increase in partial pressure of SO_3. The SO_3 gas becomes less soluble in molten sodium sulfate at higher temperatures. Two independent experiments (TGA17 and TGA18) are conducted at 1160 K, their results have an excellent agreement with each other.

The comparisons between the solubilities of SO_3 in platinum and alumina crucibles at 1160 K and 1200 K are shown in Figures 5.31 and 5.32, respectively. Sulfur trioxide is found to have very small solubility in platinum crucibles in comparison with that in alumina crucibles. The solubilities of SO_3 in platinum crucibles are only approximately 3 and 5 percent of those in alumina crucibles at 1160 K and 1200 K, respectively. Therefore, the presence
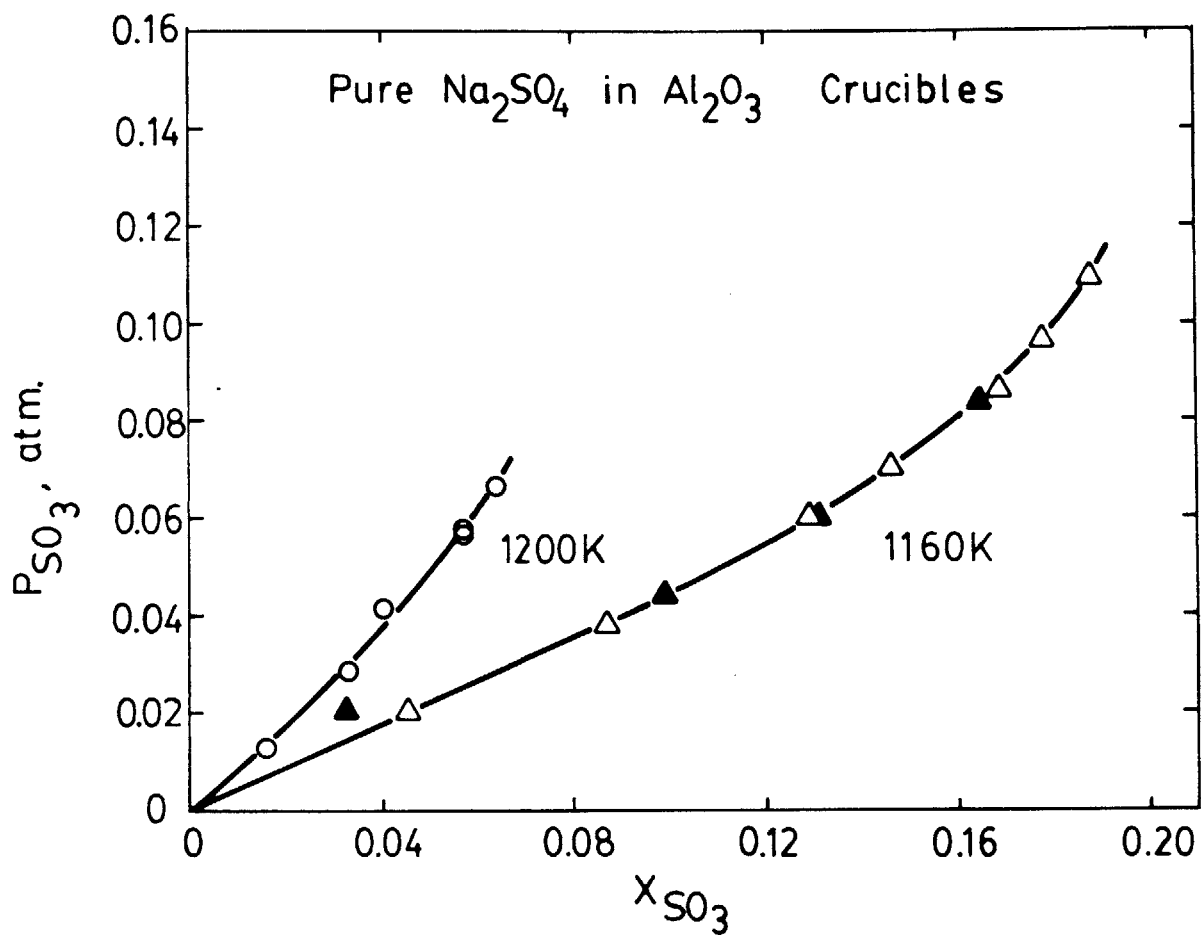
Figure 5.30 - Comparison of solubility of sulfur trioxide in sodium sulfate contained in Al_2O_3 crucibles at 1200 K and 1160 K. Each type of symbol represents an individual run.
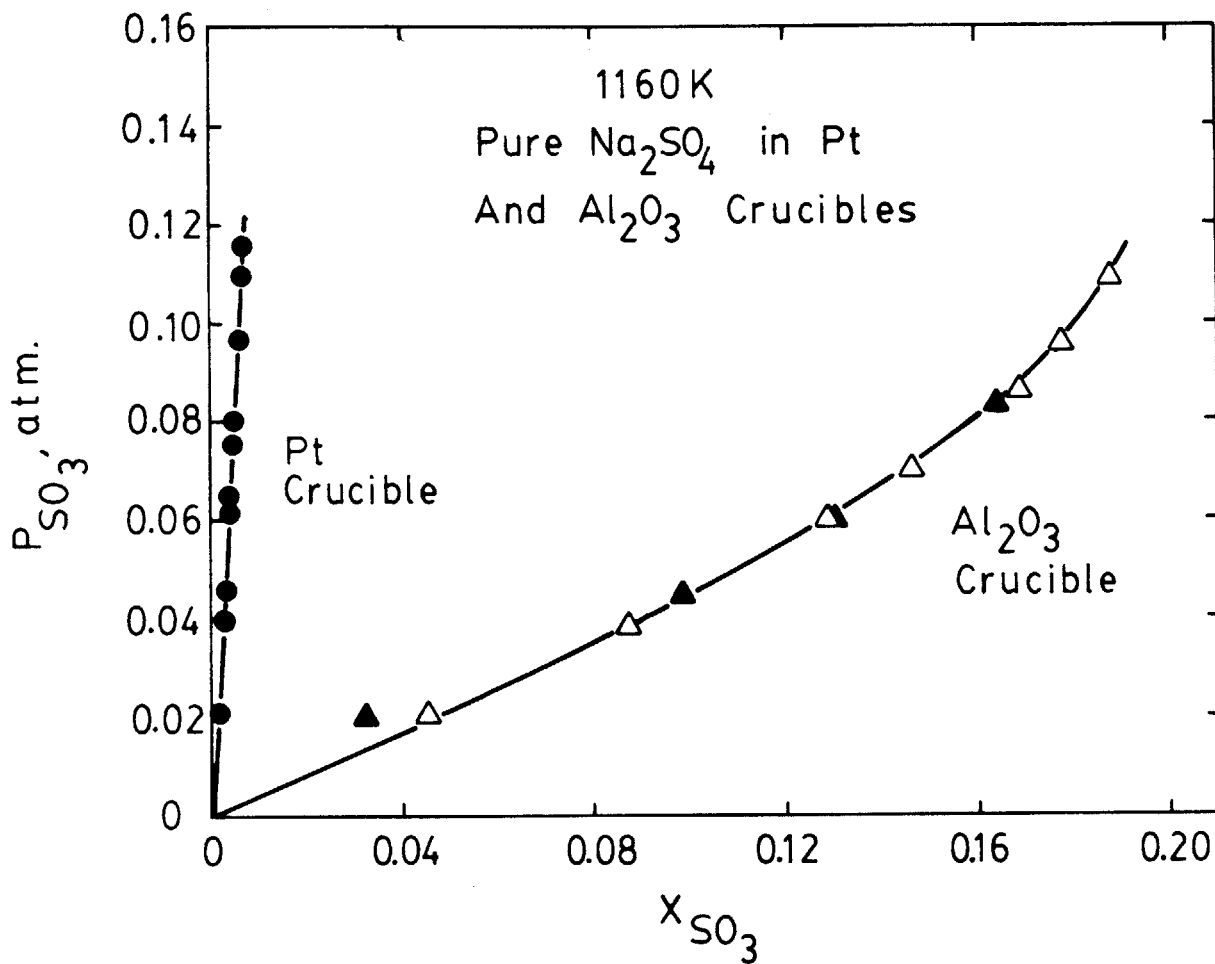
Figure 5.31 - Comparison of solubility of sulfur trioxide in sodium sulfate contained in Pt and Al_2O_3 crucibles at 1160 K. Each type of symbol represents an individual run.
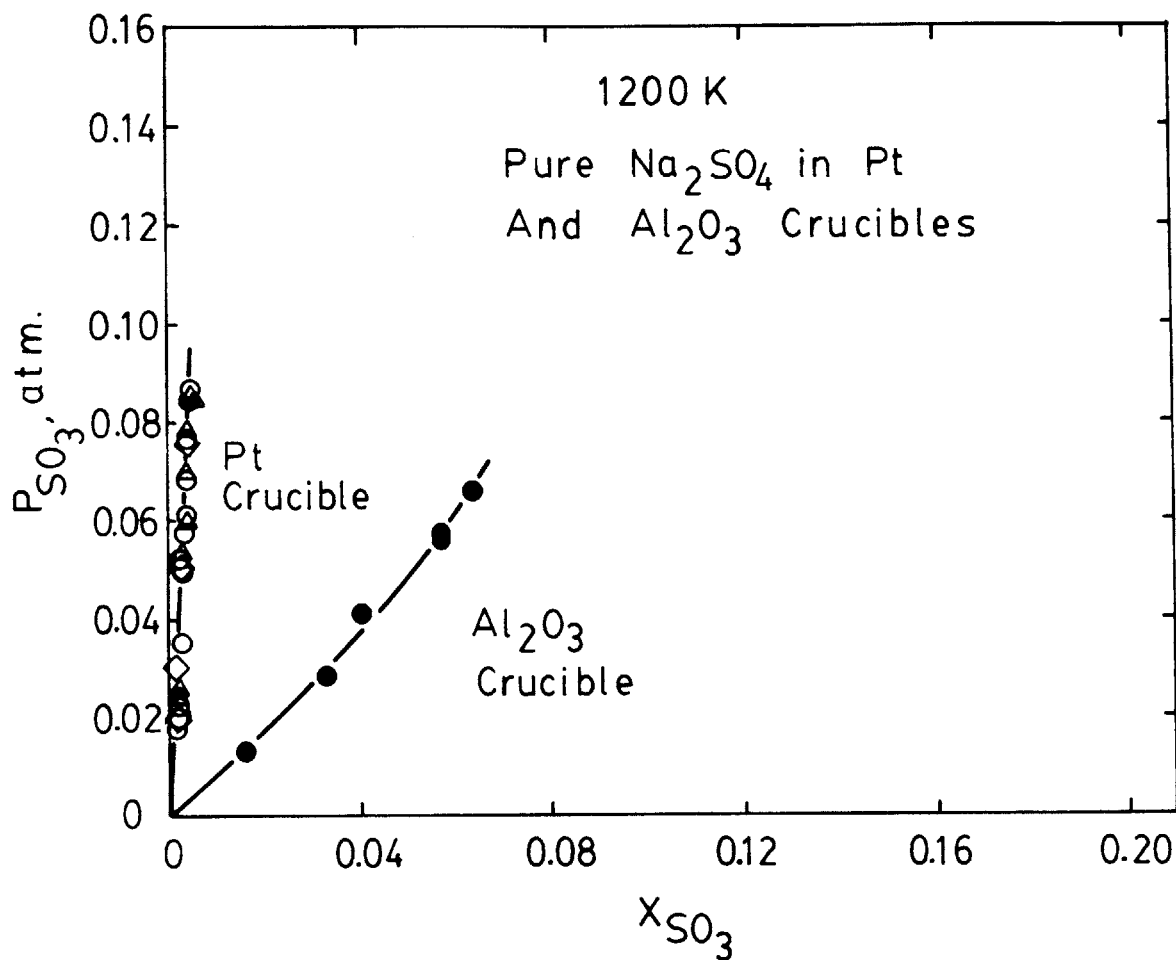
Figure 5.32 - Comparison of solubility of sulfur trioxide in sodium sulfate contained in Pt and Al_2O_3 crucibles at 1200 K. Each type of symbol represents an individual run.

of aluminum oxide causes an enormous SO_3 solubility in sodium sulfate.

Chemical analysis of the quenched samples taken after the thermogravimetric experiments using alumina crucibles confirms the dissolution of alumina in the melt and quantifies the extent of alumina solubility in molten sodium sulfate. The amount of aluminum dissolved in the melt analyzed by atomic absorption is compared with the amount of SO_3 absorbed in the melt recorded by the thermobalance. The ratios of one half of the moles of dissolved aluminum to one third of the moles of absorbed SO_3 gas are determined to be very closely equal to one. The results are listed in Table 5-7. It is therefore concluded that the absorbed SO_3 reacts almost entirely with the aluminum oxide to form aluminum sulfate in alumina crucibles. The amount of SO_3 reacts only with the molten Na_2SO_4 is comparatively small as it is also verified by the TGA results using platinum crucibles. The reaction between alumina and sulfur trioxide is thus written as

$$Al_2O_3(s) + 3[SO_3] = [Al_2(SO_4)_3] \qquad (5\text{-}70)$$
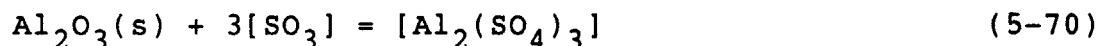
where brackets signify that the species is in solution. These results prove the existence of acidic fluxing at the experimental conditions as it is postulated in the acidic-basic fluxing model.

Table 5-7

Relationship Between Dissolved Alumina
And Absorbed Sulfur Trioxide In Sodium Sulfate

Expt.No.	T, K	P_{SO_3}, atm	$\dfrac{n_{Al(dissolved)}/2}{n_{SO_3(absorbed)}/3}$
TGA17-04	1160	0.08349	0.971
TGA17-04	1160	0.08349	0.998
TGA18-07	1160	0.10933	0.889

The solubilities of alumina in molten sodium sulfate at 1160 K and 1200 K are determined by converting the solubility data of sulfur trioxide using alumina crucibles. The amounts of absorbed SO_3 reacting with the alumina are calculated by taking the difference between the solubility data using alumina crucibles and those using platinum crucibles at the same temperature and partial pressure of SO_3. The thermogravimetric data are therefore converted in terms of concentrations of aluminum in parts per millions by weight (C_{Al}, ppm) according to the chemical reaction (5-70). The results are listed in Table 5-8 and presented in Figure 5.33. The results show that the solubility of alumina in the molten sodium sulfate increases with an increase in the partial pressure of SO_3. The amount of alumina dissolved in the sulfate decreases with an increase in temperature. One can therefore conclude that the reaction (5-70) between sulfur trioxide and alumina is an exothermic reaction according to the Principle of Le Chatelier. These results can be represented by the following linear relationships

$$\log C_{Al}, ppm = 5.258 + 0.873 \log P_{SO_3} \quad \text{at 1160 K} \quad (5-71)$$
and
$$\log C_{Al}, ppm = 4.936 + 0.884 \log P_{SO_3} \quad \text{at 1200 K} \quad (5-72)$$

The equation at 1200 K can be expressed in terms of the activity of sodium oxide in sodium sulfate by means of the reaction
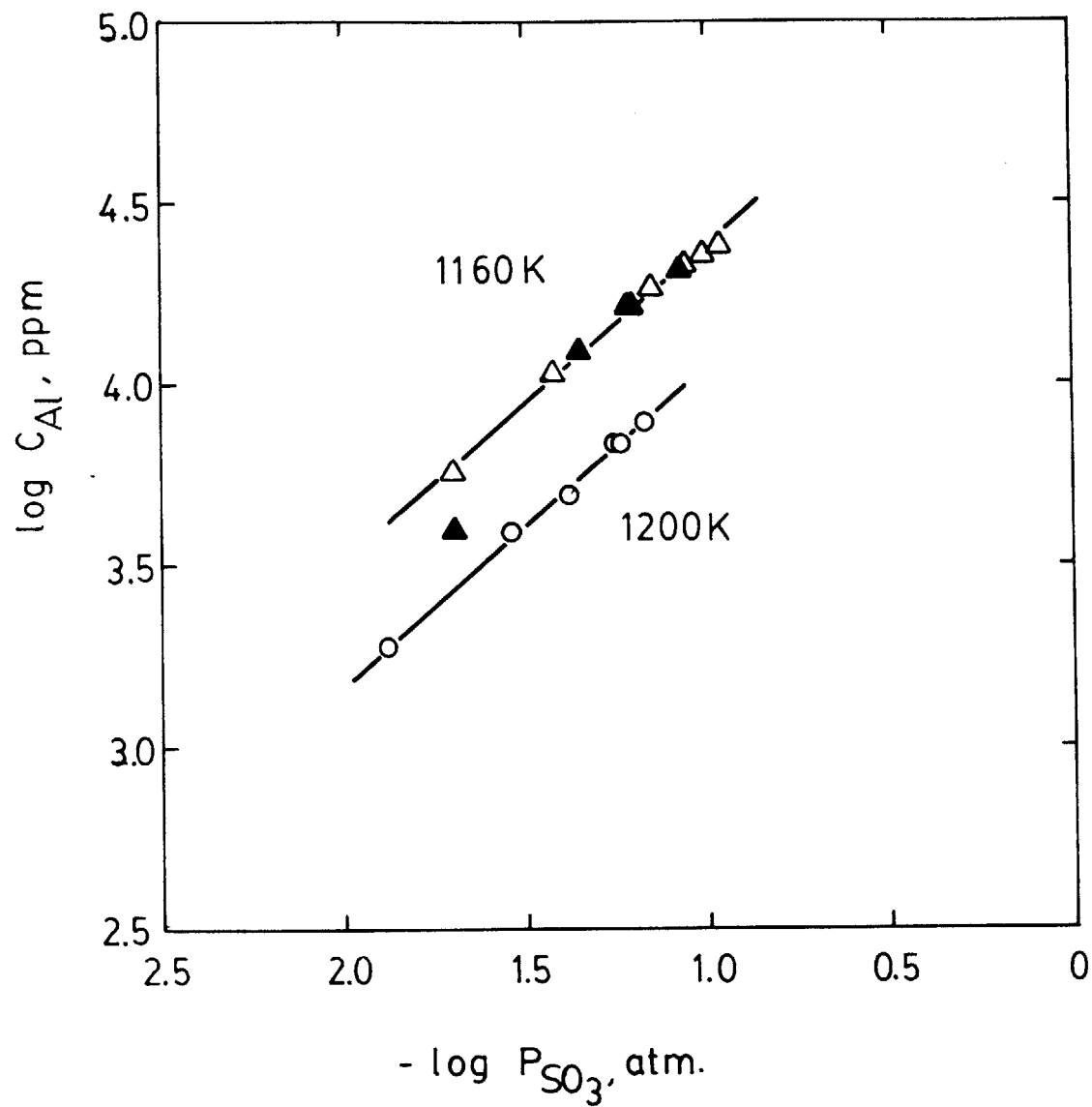
Figure 5.33 - Solubility of alumina in sodium sulfate at 1160 K and 1200 K obtained from TGA experiments.

Table 5-8

Equilibrium Solubility of Alumina in Sodium Sulfate

(1) Thermogravimetric Data

Exp. No.	gas mixtures	Equil. time,hr	T,K	$\log P_{SO_3}$	$\log C_{Al}$,ppm
TGA17-01	SO_2+O_2	46.25	1160	-1.6929	3.594
TGA17-02	SO_2+O_2	121.83	1160	-1.3556	4.092
TGA17-03	SO_2+O_2	71.41	1160	-1.2211	4.217
TGA17-04	SO_2+O_2	92.00	1160	-1.0784	4.317
TGA18-01	SO_2+O_2	98.75	1160	-1.6936	3.745
TGA18-02	SO_2+O_2	68.08	1160	-1.4206	4.036
TGA18-03	SO_2+O_2	104.91	1160	-1.2226	4.209
TGA18-04	SO_2+O_2	62.00	1160	-1.1532	4.266
TGA18-05	SO_2+O_2	94.25	1160	-1.0628	4.329
TGA18-06	SO_2+O_2	59.75	1160	-1.0159	4.351
TGA18-07	SO_2+O_2	36.00	1160	-0.9613	4.375
TGA26-04	SO_2+O_2	81.83	1200	-1.8864	3.272
TGA26-05	SO_2+O_2	41.16	1200	-1.5421	3.599
TGA26-06	SO_2+O_2	27.50	1200	-1.3867	3.684
TGA26-07	SO_2+O_2	66.17	1200	-1.2406	3.836
TGA26-08	SO_2+O_2	27.50	1200	-1.2496	3.836
TGA26-09	SO_2+O_2	44.08	1200	-1.1790	3.884

(2) Electrochemical Data

Exp. No.	gas mixtures	Equil. time,hr	T,K	EMF,mv	$\log a_{Na_2O}$	$\log P_{SO_3}$	$\log C_{Al}$,ppm
EMF4-2E	SO_2+O_2	138.45	1201.3627	381.8884	-15.673	-1.5068	3.904
EMF4-1C	SO_2+O_2	89.66	1200.0544	332.6086	-15.252	-2.0140	3.285
EMF3-2C	$4.9\%SO_2-Ar+O_2$	92.87	1200.3122	202.3254	-14.676	-2.4988	2.503
EMF3-3B	$4.9\%SO_2-Ar+O_2$	94.16	1200.2295	211.2805	-14.248	-2.9453	1.956
EMF3-1C	$4.9\%SO_2-Ar+O_2$	88.23	1202.2792	163.0249	-13.804	-3.4775	1.127
EMF5-1G	$0.93\%SO_2-Ar+O_2$	291.67	1200.9104	24.6008	-12.651	-4.5337	-0.433

$$Na_2SO_4(l) = Na_2O(l) + SO_3(g) \tag{5-73}$$
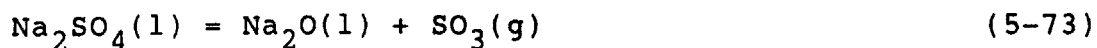
The value of log K for the reaction (5-73) is determined to be -17.187 at 1200 K in this study. Since the activity of sodium sulfate is unity in pure sodium sulfate, the partial pressure of SO_3 is related to the activity of Na_2O by

$$\log P_{SO_3} = -17.187 - \log a_{Na_2O}(l) \tag{5-74}$$

The relationship at 1200 K is then written as

$$\log C_{Al}, ppm = -10.25 - 0.884 \log a_{Na_2O}(l) \tag{5-75}$$

A thermogravimetric experiment with 2.2144 grams of sodium sulfate contained in an alumina crucible is conducted at low partial pressures of SO_3 in the range of 6.78×10^{-5} to 7.83×10^{-4} atm; however, no weight change is detected by the thermobalance. Gas mixtures of 0.93%SO_2-Ar and oxygen are employed to produce the desired low partial pressures of SO_3.

5.2.2 Electrochemical Results

Solubilities of alumina in sodium sulfate are investigated by analyzing samples taken from molten sodium sulfate contained in an alumina crucible at 1200 K. Cell potential and temperature are monitored during the process of equilibration at a controlled pressure of SO_3. The

molten sodium sulfate is brought to equilibrium with aluminum oxide under six different partial pressures of SO_3 ranging from 2.9×10^{-5} atm to 3.1×10^{-2} atm at 1200 K. Sixty particles of tabular alumina (ALCOA T-61, 6 to 8 mesh) are added to the sodium sulfate to reduce the time of equilibration. The total weight of the tabular alumina is 3 g, and the total increase in surface area of alumina is estimated to be 20 cm^2. High partial pressures of SO_3 in the range of 3.1×10^{-2} atm to 9.7×10^{-3} atm are produced by mixing pure O_2 and SO_2; whereas, partial pressures of SO_3 less than 3.5×10^{-3} atm are attained by using either O_2 and 4.9%SO_2-Ar or O_2 and 0.93%SO_2-Ar gas mixtures.

The equilibrium solubility of alumina in molten sodium sulfate determined during the electrochemical experiments are listed in Table 5-8 and presented in Figure 5.34. The equilibrium solubility of alumina in sodium sulfate increases with an increase in partial pressure of SO_3 or an decrease in activity of Na_2O. The slope of the line in the log-log plot of Figure 5.34 has a value of 3/2. The relationship is:

$$\log C_{Al}, \text{ppm} = 6.287 \pm 0.069 + 1.5 \pm 0.02 \log P_{SO_3} \qquad (5-76)$$

The standard deviation of $\log C_{Al}$,ppm and the coefficient of correlation are ± 0.056 and 0.9995, respectively. In accordance with the relationship at 1200 K shown in Table 5-2, the relation (5-76) can be rewritten in terms of the activity of sodium oxide as
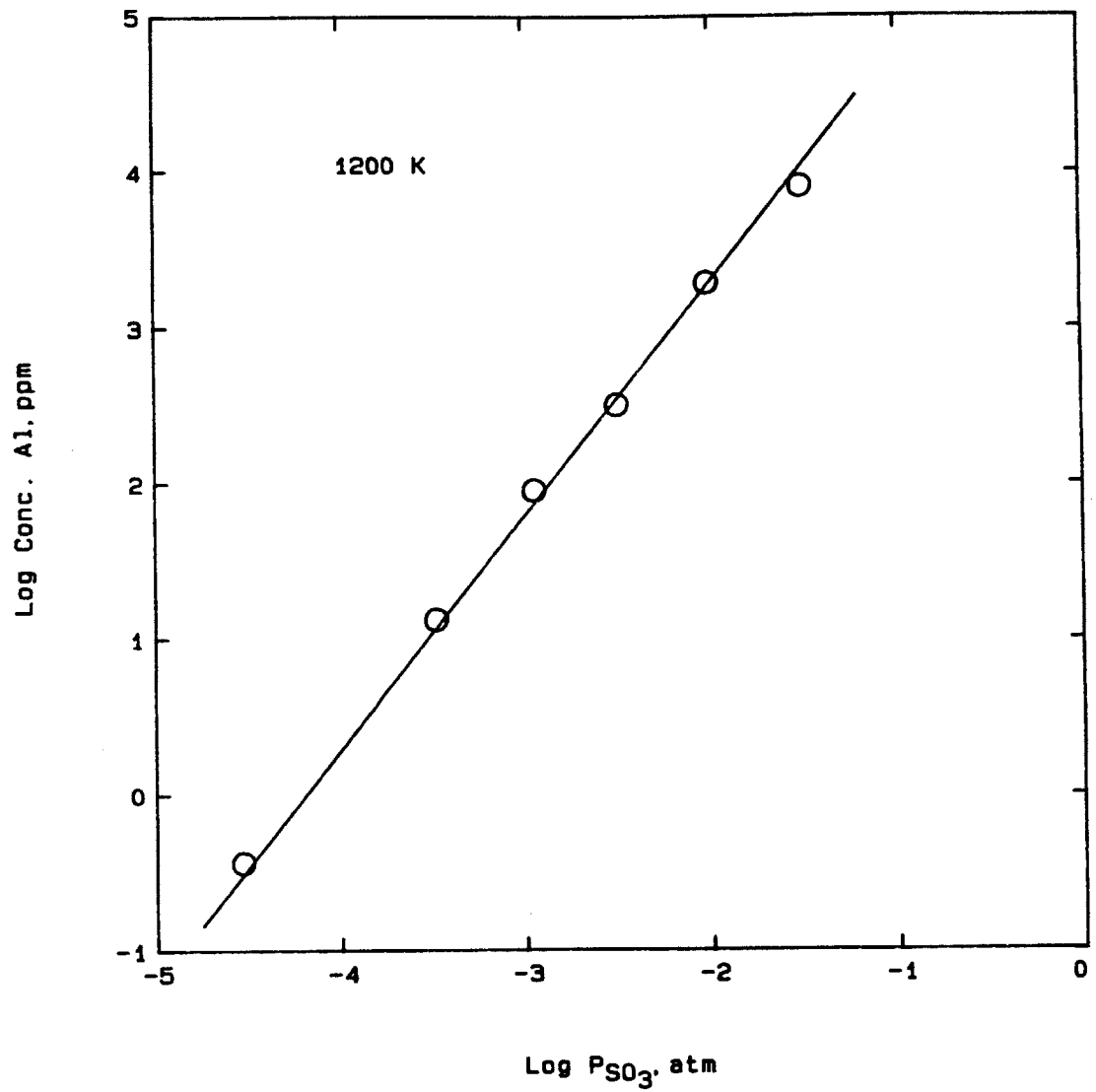
Figure 5.34 — Solubility of alumina in sodium sulfate at 1200 K obtained from EMF experiments.

$$\log C_{Al}, ppm = -19.49 \pm 0.07 - 1.5 \pm 0.02 \log a_{Na_2O(l)} \quad (5\text{-}77)$$

Efforts are made to identify whether the cell potentials are affected by the amount of dissolved aluminum during equilibrations under constant flowrates of SO_2 and O_2 reaction gases. Experimental conditions of partial pressure of SO_3, temperature, and EMF recorded every 15 minutes during the process of equilibration in alumina crucibles are incorporated to compute the standard Gibbs free energy of formation of sodium sulfate. For example, Figure 5.35 illustrates that the $\Delta G_f^o(Na_2SO_4(l))$ during the equilibration of sample EMF4-1B shows a sole dependence on temperature under a constant reaction gas ratio of SO_2 to O_2. The cell EMF is affected by the fluctuation in temperature which, in turn, influences the partial pressure of SO_3 and the activity of Na_2O. The dissolved aluminum concentration therefore plays no part in the slight change in cell potential while alumina dissolution is taken place.

Furthermore, the activity of sodium oxide in sodium sulfate contained in alumina crucibles at equilibrium Al_2O_3 solubility is compared with the electrochemical measurements taken in platinum crucible. Since platinum is an inert material, the activity measurements obtained with a platinum crucible represent the genuine thermodynamic properties of pure sodium sulfate as they are shown in Figure 5.18. The activities of sodium oxide at equilibrium Al_2O_3 solubility taken from alumina crucibles at 1200 K are compared with
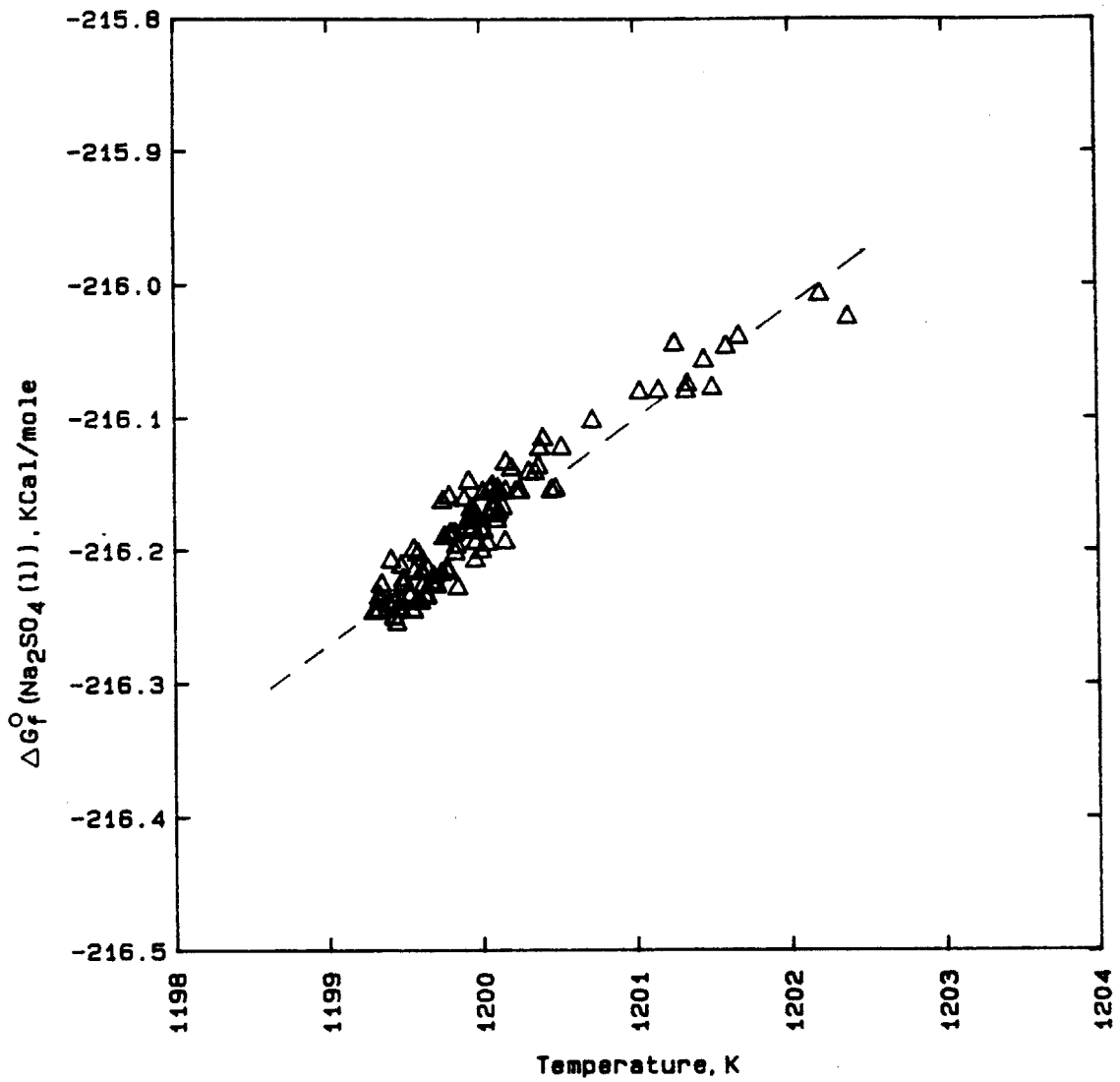
Figure 5.35 - Free energy of formation of sodium sulfate of EMF data taken during Al_2O_3 dissolution.

those measured with platinum crucibles in Figure 5.36. The thermodynamic properties of the six samples taken from alumina crucibles at 1200 K have excellent agreement with those measured with platinum crucibles, even though there are more than 8000 parts per million of aluminum in sodium sulfate at log P_{SO_3} = -1.51. Thus, the concentration of aluminum in sodium sulfate does not affect the thermodynamic properties of sodium sulfate.

The fused quartz solid electrolyte is inspected for possible attacks by either the working or the reference melt after each EMF experiments. The solid electrolyte remains intact after the experiments, no apparent attack is noted.

5.2.3 Kinetic Study of Alumina Solubility

During the EMF experiments, samples of the melt are periodically obtained to examine the aluminum concentration in the sodium sulfate until equilibrium concentration is achieved. The changes in aluminum concentration in the sodium sulfate with time and the experimental conditions before sampling in all the runs are listed in Table 5-9. The equilibrium concentrations of dissolved aluminum sulfate are achieved after spending 88.23, 92.87, 94.16, 89.66, 138.45, and 291.67 hours in the six equilibrations. The time for equilibrating alumina with sodium sulfate is thus found to be at least 88 hours. For example, in run EMF3-2, the solubility of alumina in sodium sulfate under a partial
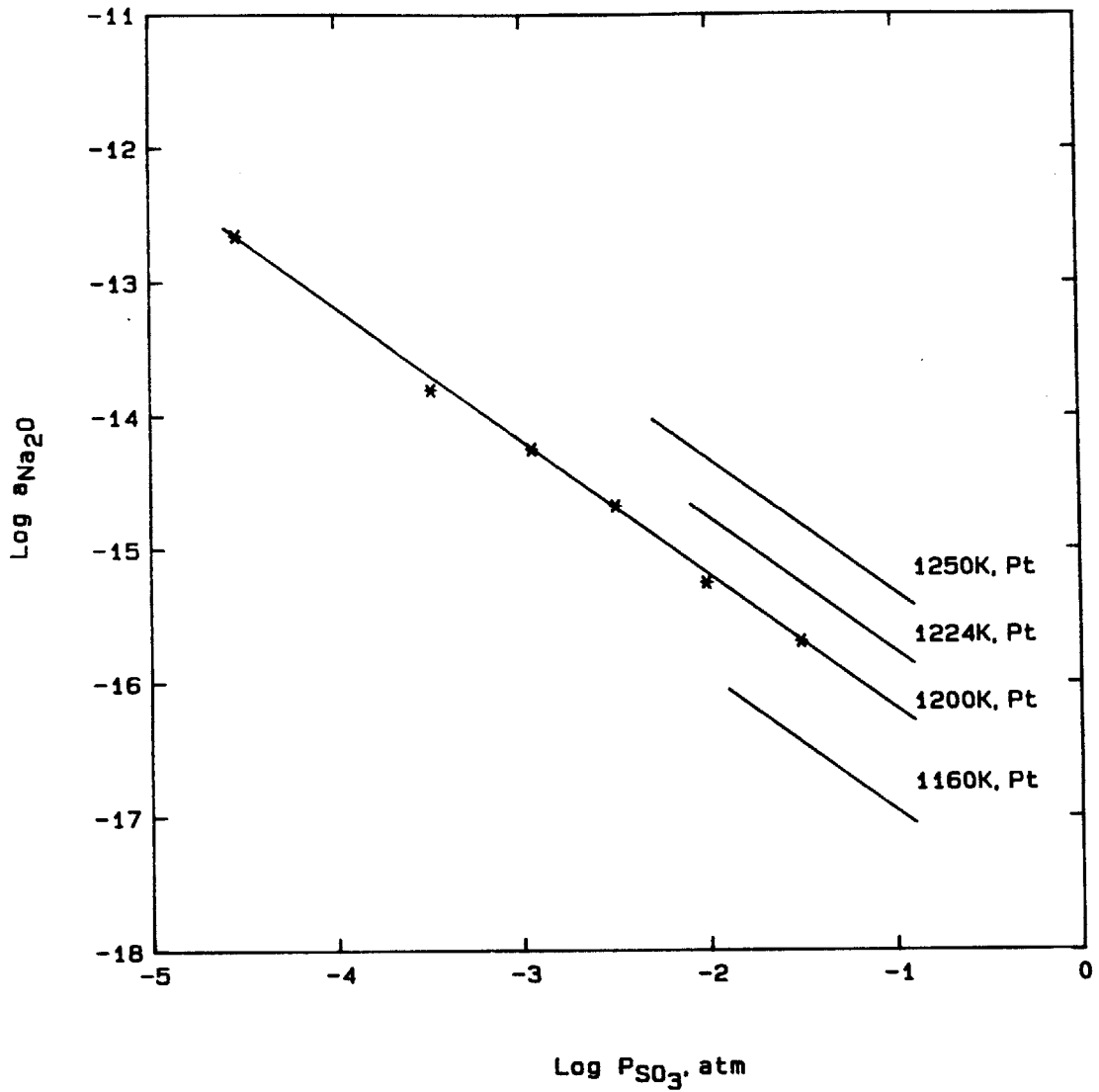
Figure 5.36 - Comparison of the thermodynamic properties of sodium sulfate at equilibrium alumina solubility with those obtained from platinum crucibles at 1200 K.

Table 5-9

Sampling Conditions of Sodium Sulfate in Alumina Crucible

Sample	equil. time,hr	T,K	EMF.mv	P_{SO_3},atm	C_{Al},ppm
SO_3 Absorption:					
EMF3-1A	16.71	1202.19	160.5212	0.000329	3.45
EMF3-1B	50.21	1202.40	157.5354	0.000328	11.62
EMF3-1C	88.23	1202.27	163.0249	0.000328	13.39
SO_3 Absorption:					
EMF3-2A	43.30	1202.23	206.1755	0.00311	252.1
EMF3-2B	70.59	1199.48	201.9812	0.00318	311.4
EMF3-2C	92.87	1200.31	202.3254	0.00316	318.4
SO_3 Desorption:					
EMF3-3A	68.17	1200.69	211.3269	0.00112	111.1
EMF3-3B	94.16	1200.23	211.2805	0.00113	90.3
SO_3 Absorption:					
EMF4-1A	42.28	1200.98	331.7883	0.00962	1536.
EMF4-1B	66.66	1200.72	331.1767	0.00963	1813.
EMF4-1C	89.66	1200.05	332.6086	0.00967	1925.
SO_3 Absorption:					
EMF4-2A	46.77	1200.66	382.9443	0.0307	6361.
EMF4-2B	69.61	1199.91	384.2810	0.0309	7024.
EMF4-2C	90.90	1201.30	383.7414	0.0306	7483.
EMF4-2D	114.23	1200.96	382.6684	0.0309	7849.
EMF4-2E	138.45	1201.36	381.8884	0.0308	8011.
SO_3 Absorption:					
EMF5-1A	33.25	1199.56	37.5732	0.0000288	0
EMF5-1B	59.46	1201.75	31.7932	0.0000267	0
EMF5-1C	96.72	1201.04	28.0456	0.0000292	0
EMF5-1D	143.13	1198.43	28.4045	0.0000269	0.1925
EMF5-1E	190.19	1198.41	28.7964	0.0000269	0.3140
EMF5-1F	265.96	1200.39	25.3491	0.0000293	0.3688
EMF5-1G	291.67	1200.91	24.6008	0.0000292	0.3689

pressure of 0.00316 atm, shown in Figure 5.37, reaches equilibrium in approximately 100 hours. In fact, the equilibration at low partial pressure of SO_3 of 2.92×10^{-5} atm requires more than 290 hours to reach total equilibrium. Therefore, the dissolution of alumina in molten sodium sulfate is an extremely slow process.

The changes in cell potential due to a step decrease in partial pressure of SO_3 from 0.0658 atm to 0.0185 atm and a step increase in partial pressure of SO_3 from 0.0178 atm to 0.0658 atm at 1200 K are illustrated in Figure 5.38 and 5.39, respectively. The EMF reaches 95 percent of its final value in approximately 40 minutes during SO_3 desorption and in about 25 minutes during SO_3 absorption. The kinetics of SO_3 desorption is slower than that of SO_3 absorption. It is therefore evident that the cell potentials are found to remain relatively stable as the dissolution of alumina is being taken place as they are shown in Table 5-9. Thus, the equilibrium between the molten sodium sulfate and the gas phase is found to proceed at a much faster pace than the equilibrium among alumina, sodium sulfate, and SO_3 gas.

A similar result is also noted during the TGA experiments with pure Na_2SO_4 when a platinum crucible is replaced with an alumina crucible at 1200 K. The time to reach a constant weight level after a step change in partial pressure of SO_3 increases more than 100 times when an alumina crucible is employed. The equilibration time with a platinum crucible is less than one hour.
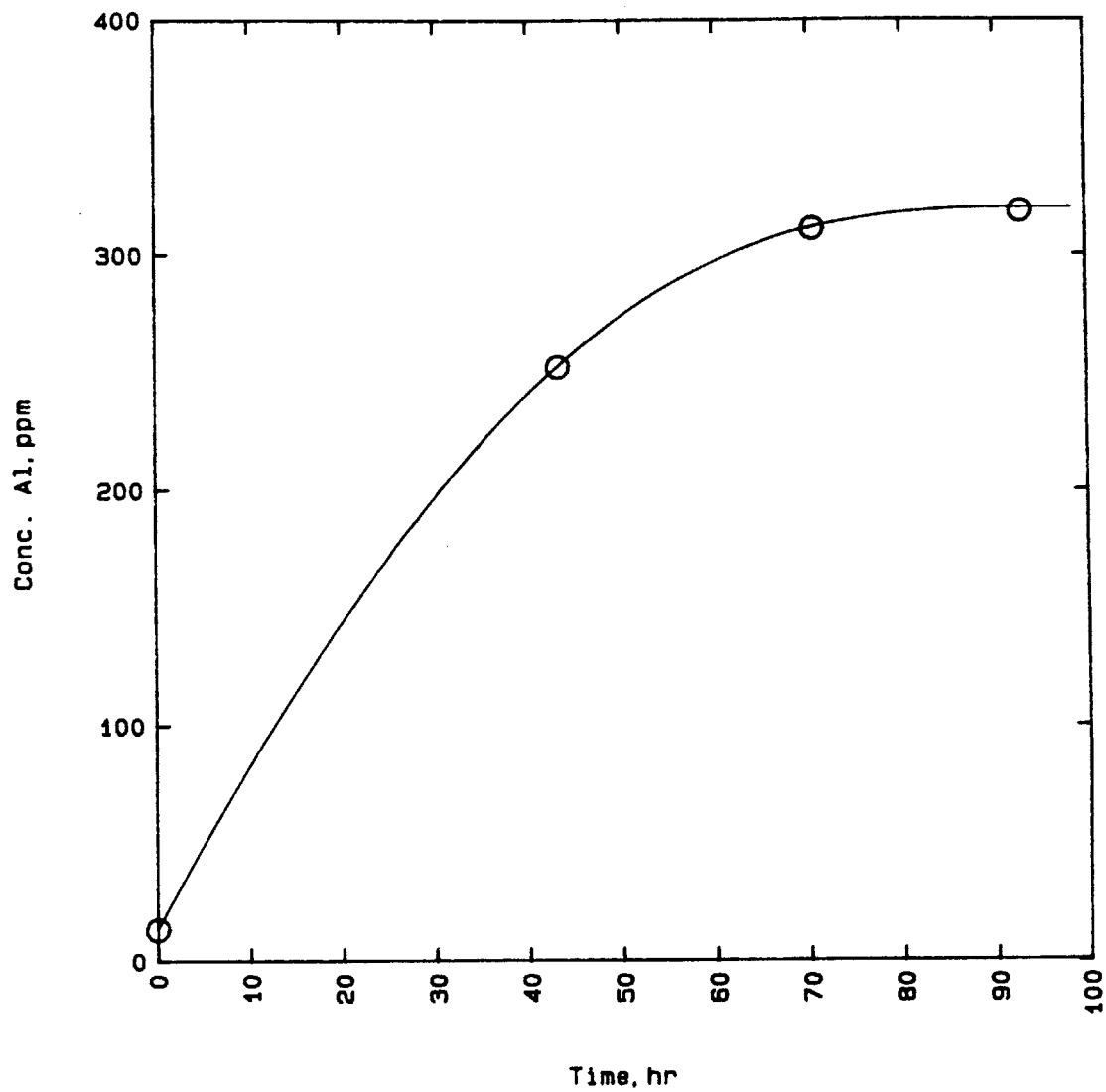
Figure 5.37 – Rate change of aluminum concentration in sodium sulfate equilibrated at partial pressure of SO_3 = 0.00316 atm at 1200 K.
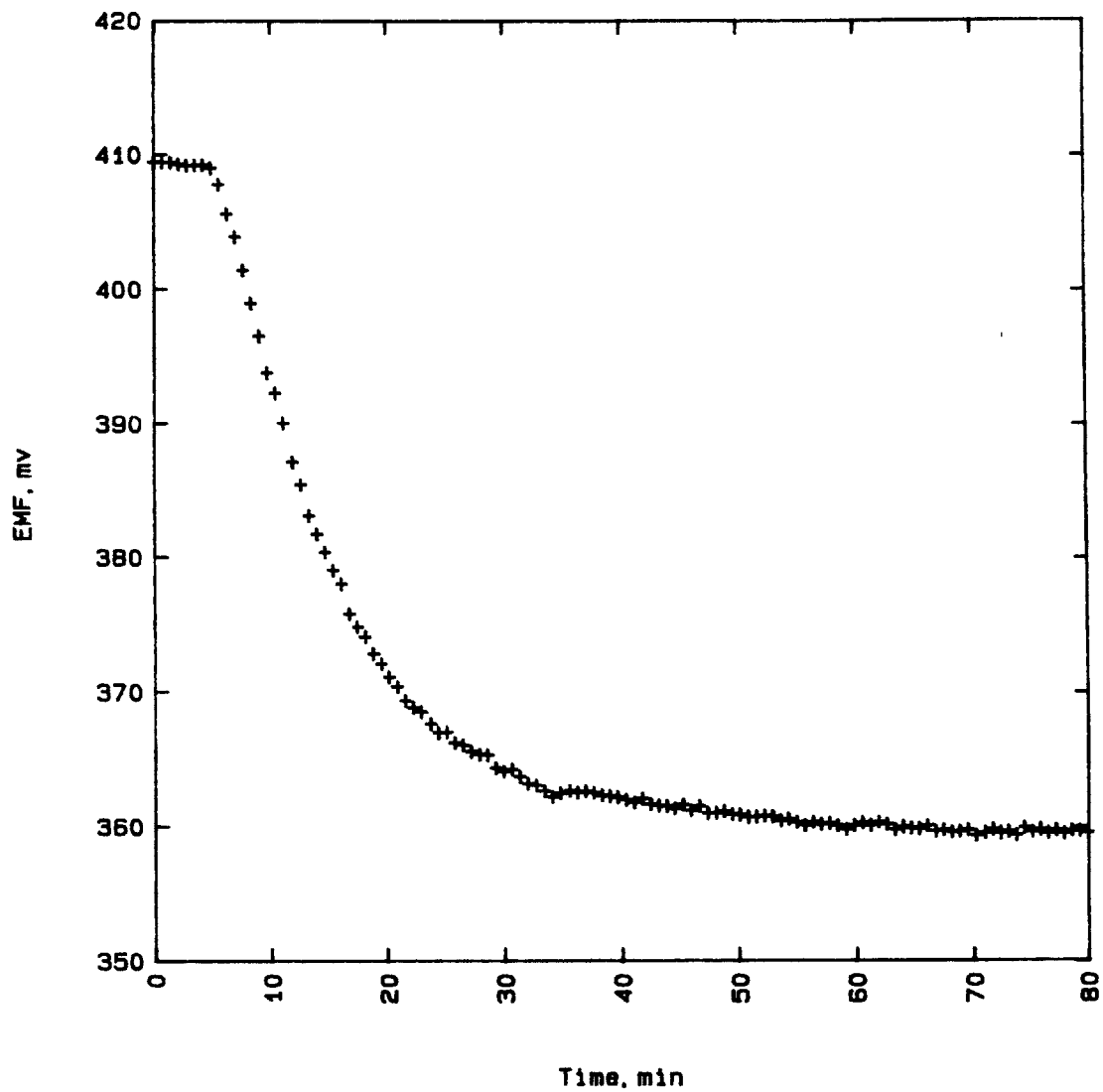
Figure 5.38 – Rate change of cell potential in sodium sulfate contained in alumina crucible in response to a step decrease in P_{SO_3} from 0.0658 atm to 0.0185 atm at 1200 K.
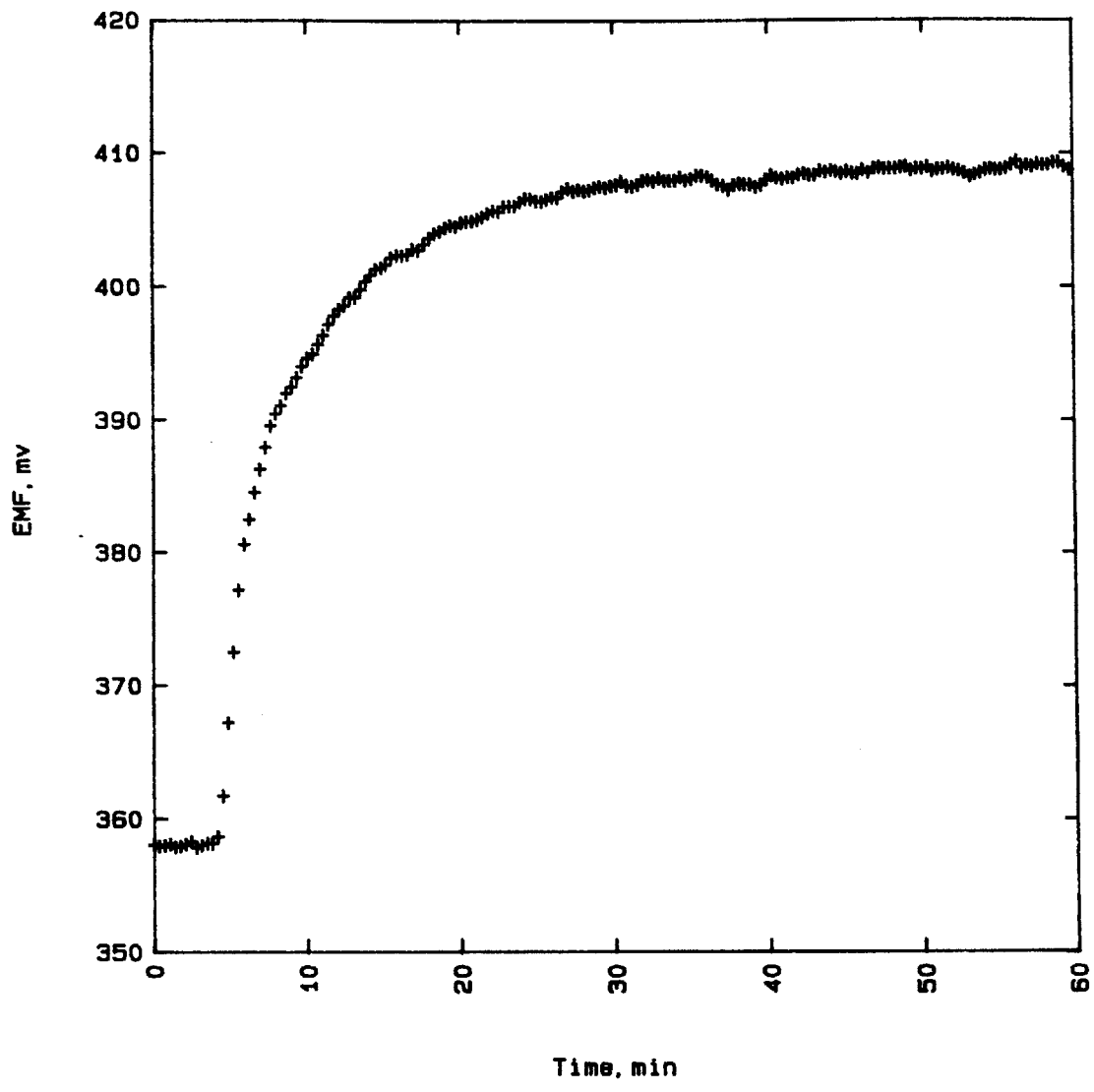
Figure 5.39 - Rate change of cell potential in sodium sulfate contained in alumina crucible in response to a step increase in P_{SO_3} from 0.0178 atm to 0.0658 atm at 1200 K.

5.3 Cobalt Sulfate-Sodium Sulfate System

Thermogravimetric analyses and electrochemical measurements have been conducted with various compositions of molten cobalt sulfate-sodium sulfate in alumina crucibles to investigate the solubility of SO_3 gas in the molten salt and the thermodynamic properties of the sulfate system. Alumina solubilities in Na_2SO_4-$CoSO_4$ melts are determined by atomic absorption on samples taken from TGA experiments. The techniques of DTA, sampling, and EDX are also performed to identify possible phase transformations.

5.3.1 Thermogravimetric Results

The equilibrium solubilities of SO_3 in 20, 30, 40, and 50 mole percent (m/o) $CoSO_4$-Na_2SO_4 melts contained in alumina crucibles at 1100 K are shown in Figure 5.40 in terms of mole fraction of SO_3 dissolved in the sulfate melt. Two independent experiments are completed with 20 m/o $CoSO_4$-Na_2SO_4 melts, and their results show good agreements with each other. The solubility of SO_3 in $CoSO_4$-Na_2SO_4 molten salt is determined to increase with an increase in partial pressure of SO_3 and with a decrease in concentration of $CoSO_4$ in the melt. The SO_3 solubility in pure Na_2SO_4 contained in alumina crucible at 1160 K presented in Figure 5.40 confirms the general pattern of the SO_3 solubility in sulfate melts.
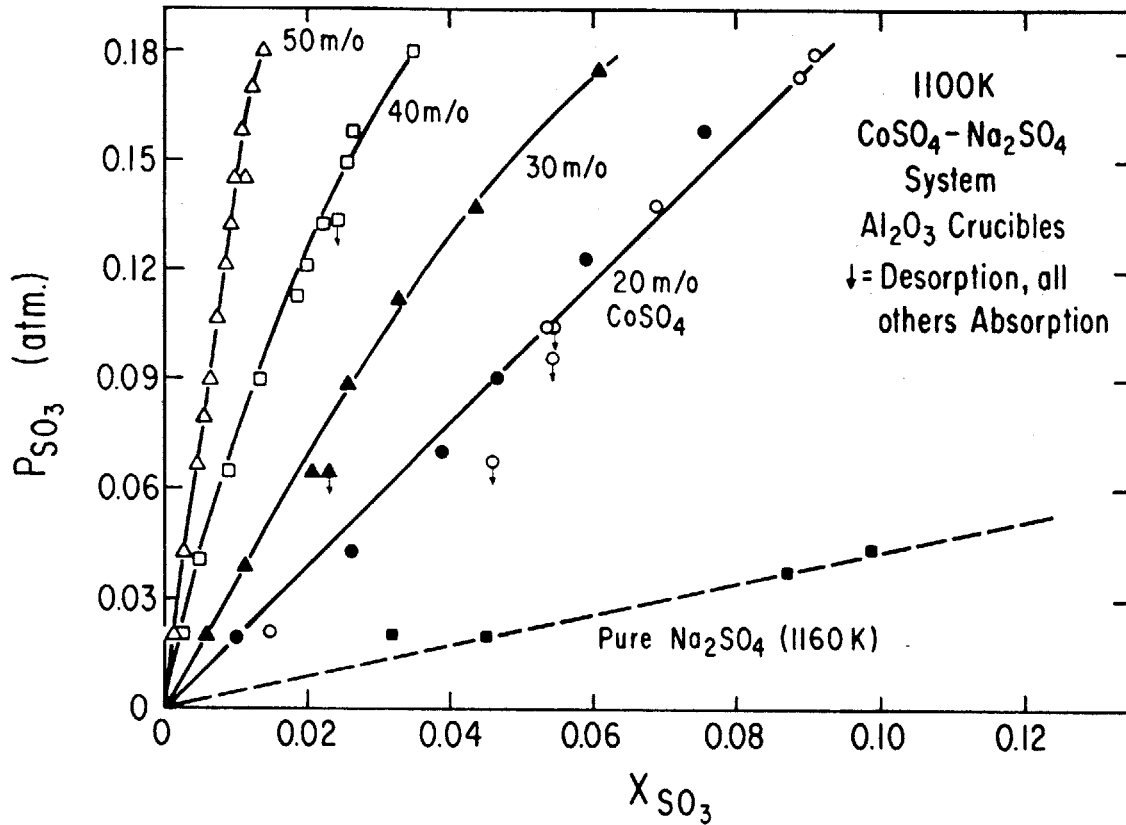
Figure 5.40 – Solubility of SO_3 in $CoSO_4$– Na_2SO_4 contained in alumina crucibles at 1100 K.

The temperature dependence of SO_3 solubility in $CoSO_4$-Na_2SO_4 melts is illustrated in Figure 5.41 by the results of 20 m/o $CoSO_4$-Na_2SO_4 melt equilibrated at 1100 K and 1160 K. The solubility of SO_3 in the sulfate melt is found to increase with a decrease in temperature. The TGA experimental data are tabulated in Appendix L.

Linear correlations are found among the solubility data taken at 1100 K. The log of mole fraction of dissolved SO_3, $\log(X_{SO_3})$, behaves linearly with the mole percent of $CoSO_4$ in Na_2SO_4 at a constant partial pressure of SO_3. The relationships are shown in Figure 5.42 and the numerical value in Table 5-10. The relationships between mole fraction of dissolved SO_3 and melt composition at 1100 K are depicted in Figure 5.43.

5.3.2 Alumina Solubility in Co-Na Sulfate

Quenched samples taken after equilibrations in TGA experiments are analyzed by atomic absorption techniques to determine the solubility of alumina in the sulfate melts. The samples are extracted from sulfate melts of 20, 30, 40, and 50 mole fraction of $CoSO_4$-Na_2SO_4 equilibrated at 1100 K. One sample is obtained from a melt of 20 mole fraction of $CoSO_4$-Na_2SO_4 exposed at 1160 K. The Al_2O_3 solubility analyzed by atomic absorption and the SO_3 solubility measured by the thermobalance in the same $CoSO_4$-Na_2SO_4 melt at various experimental conditions are listed in Table 5-11.
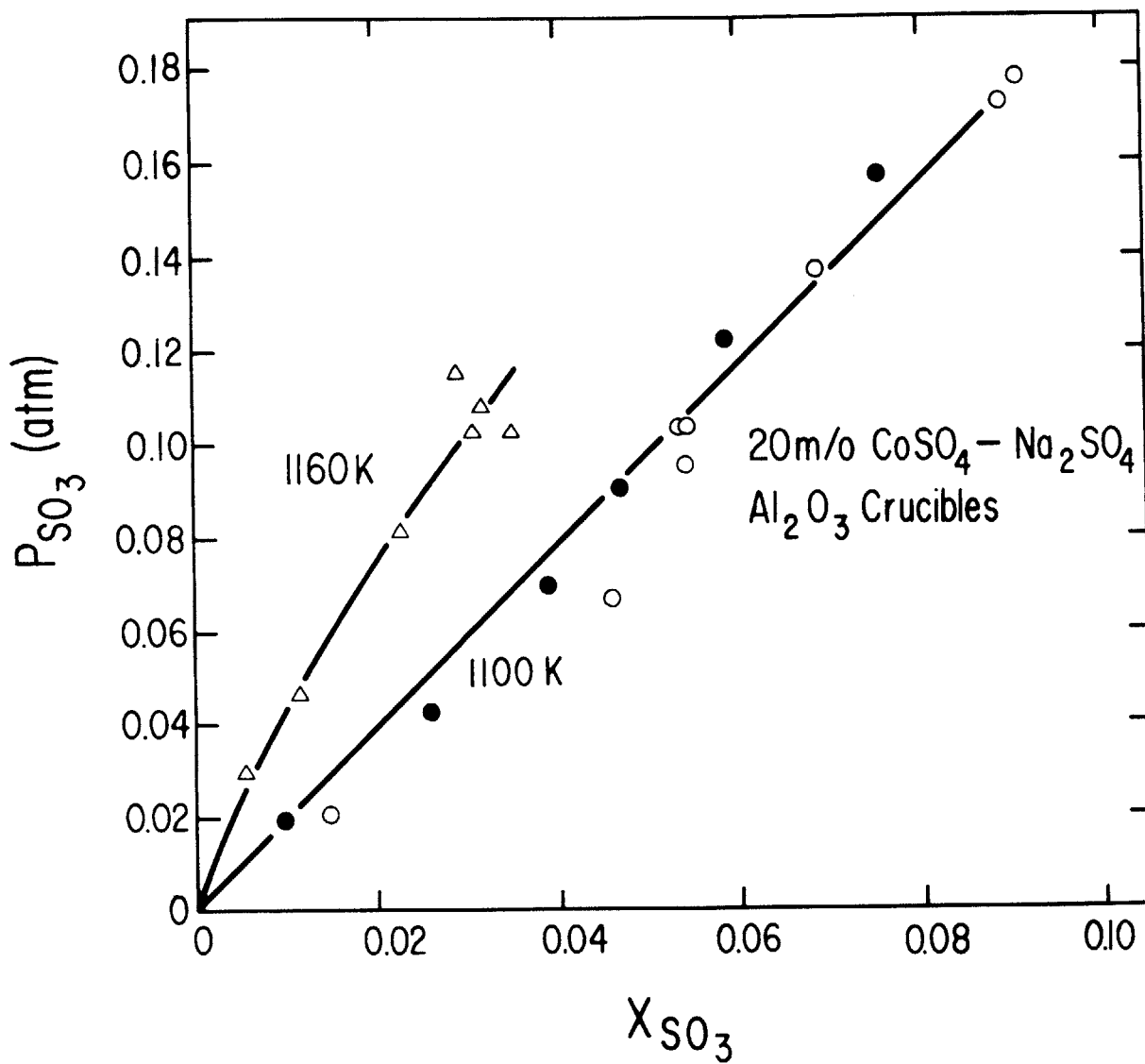
Figure 5.41 - Solubility of SO_3 in 20 m/o $CoSO_4$-Na_2SO_4 at 1160 K and 1100 K.
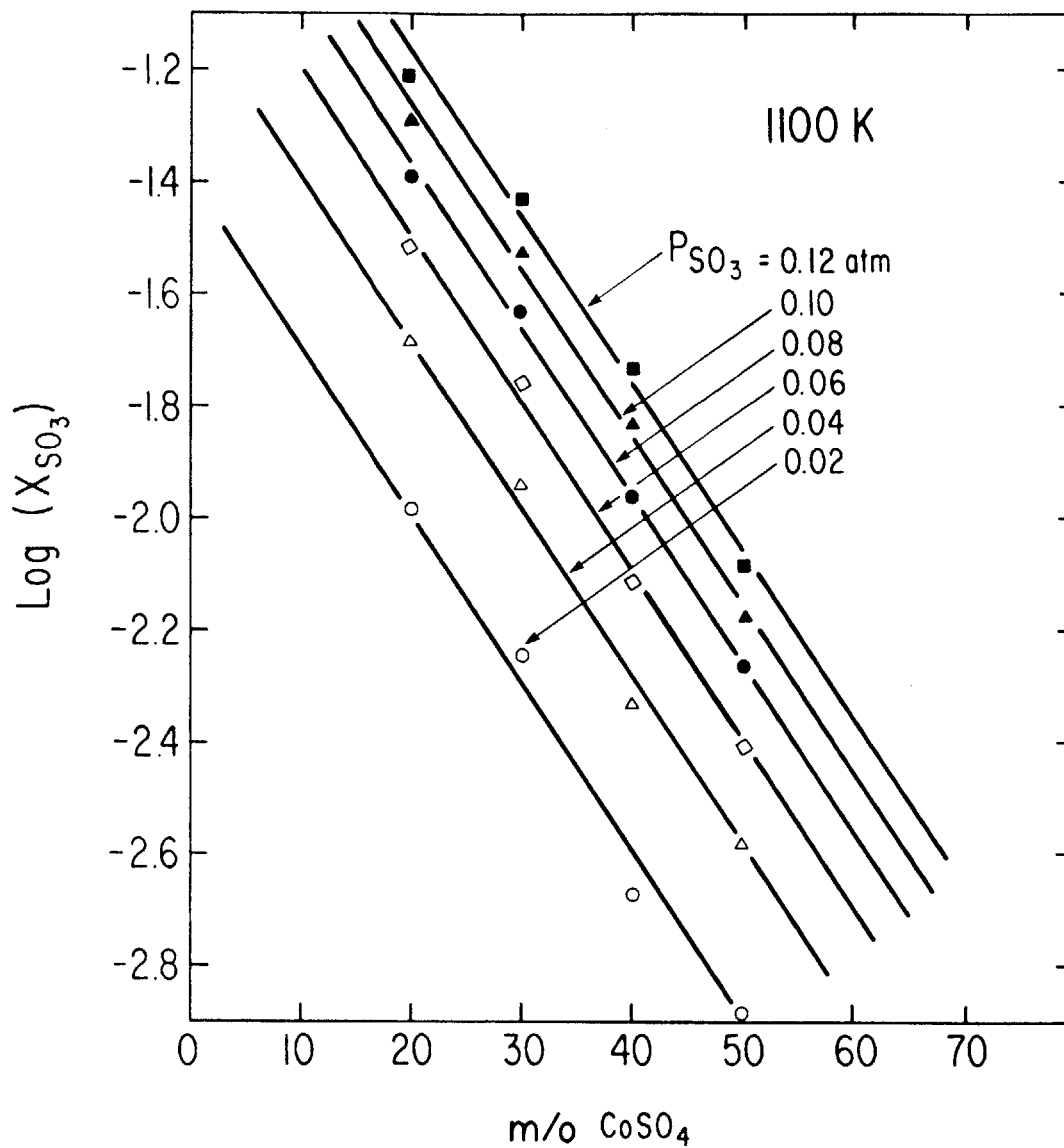
Figure 5.42 - Linear correlations of SO_3 solubility in $CoSO_4-Na_2SO_4$ at 1100 K.
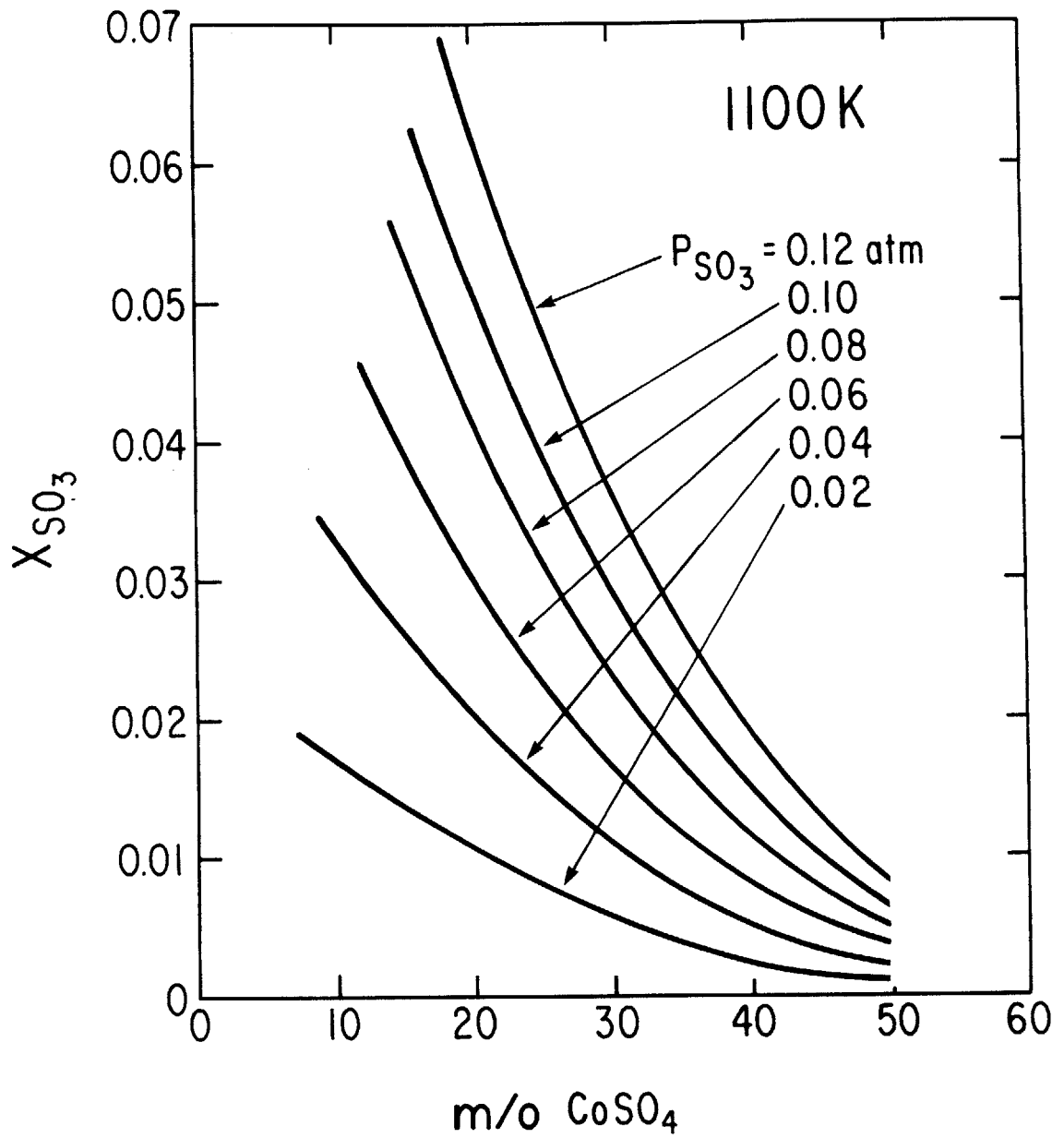
Figure 5.43 - Composition dependence of SO_3 solubility in $CoSO_4$-Na_2SO_4 at 1100 K.

Table 5-10

Relationships of SO_3 Solubility in $CoSO_4$-Na_2SO_4 Melts

$$\log X_{SO_3} = C \text{ m/o } CoSO_4 + D \text{ at constant } P_{SO_3}$$

P_{SO_3}, atm	C	D
0.02	−0.0313	−1.353
0.04	−0.0308	−1.059
0.06	−0.0303	−0.888
0.08	−0.0296	−0.776
0.10	−0.0296	−0.673
0.12	−0.0292	−0.596

Table 5-11

Comparison of absorbed SO_3 and dissolved Al

in $CoSO_4$-Na_2SO_4 melts

m/o $CoSO_4$	T, K	P_{SO_3}, atm	absorbed $n_{SO_3}/3$	dissolved $n_{Al}/2$
20	1160	0.1159	0.000143	0.000172
20	1100	0.0960	0.000266	0.000269
30	1100	0.1373	0.000213	0.000207
40	1100	0.1367	0.000181	0.000192
50	1100	0.1446	0.000052	0.000038

In combination with the solubilities of $Al_2O_3(s)$ and $SO_3(g)$ in pure Na_2SO_4 listed in Table 5-7, one half of the number of moles of aluminum dissolved in the Co-Na sulfate is compared with one third of the number of moles of sulfur trioxide gas absorbed in the melt in Figure 5.44. The ratio of the two mole fractions is approximately equal to unity at all sulfate compositions above liquidus temperatures. The SO_3 gas absorbed in the Co-Na sulfate therefore reacts almost entirely with the alumina crucible to form aluminum sulfate at the acidic experimental conditions according to reaction (5-70). There is probably a very small extent of reaction between the SO_3 gas and the molten $CoSO_4-Na_2SO_4$ only. The molten salt acts as a medium to faciliate the gas and solid species to react together.

With the knowledge of alumina solubility in $CoSO_4-Na_2SO_4$ melts, isobars of partial pressure of SO_3 is determined in the $CoSO_4-Na_2SO_4-Al_2(SO_4)_3$ system. As it is shown in the ternary phase diagram at 1100 K in Figure 5.45, the concentration of aluminum sulfate present in the $CoSO_4-Na_2SO_4$ melt is small. The molten salt is essentially a binary system of cobalt sulfate and sodium sulfate.

5.3.3 Electrochemical Results

This section will focus on the results obtained from electrochemical measurements with the fused silica solid electrolyte and the subsequent thermodynamic calculations.
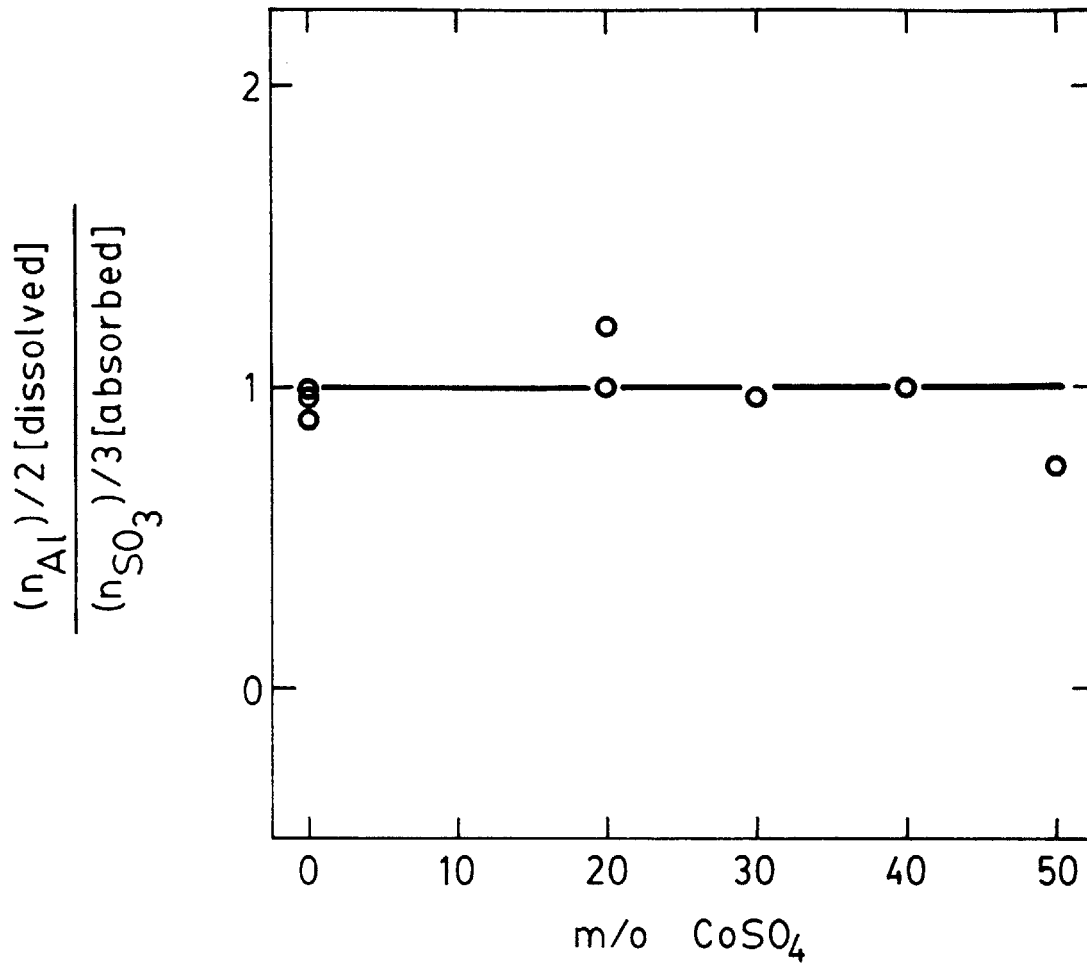
Figure 5.44 – Comparison of the amount of dissolved aluminum and that of absorbed SO_3 in $CoSO_4$-Na_2SO_4 melts.
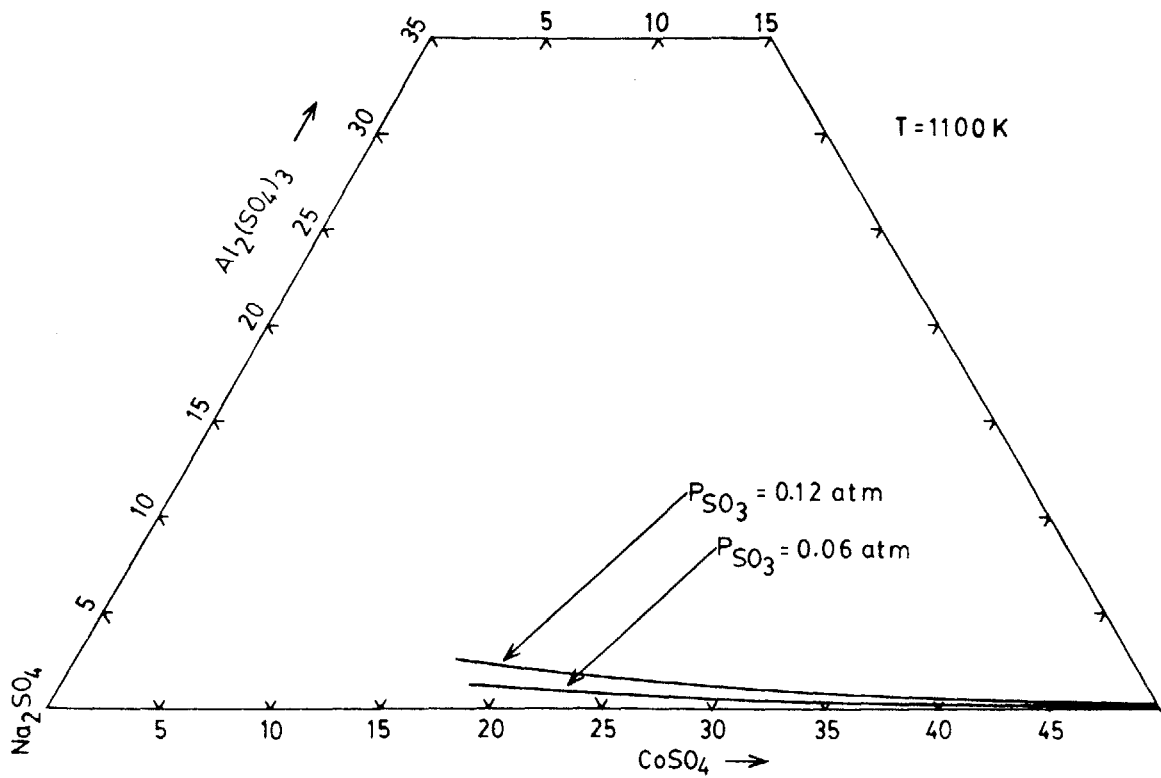
Figure 5.45 – Concentration of $Al_2(SO_4)_3$ in $CoSO_4$-Na_2SO_4 melts at 1100 K.

Because of a change in thermodynamic behavior of the Co-Na sulfate melts at approximately 1100 K, thermodynamic properties of the sulfate system are calculated based on the experimental data at temperatures above 1100 K.

Electrochemical measurements are performed on 80.00, 70.02, 59.96, 49.60, and 39.76 mole percent of Na_2SO_4-$CoSO_4$ melts contained in alumina crucibles from 900 K to 1300 K. The experiments are conducted at different temperatures with a constant inlet gas flowrate ratio of O_2 to SO_2 being 19.34. The experimental results in terms of activity of sodium oxide at different partial pressures of SO_3 and temperatures are listed in Appendix M. The equilibrium cell potentials at various temperatures shown in Figure 5.46 demonstrate linear relationships with a similar slope at temperatures above 1100 K. Below that temperature, the cell potential in general follows another type of linear relation with a different slope.

The breaks in the cell potential in 80.00, 70.02, 59.96, 49.60, and 39.76 mole percent of Na_2SO_4-$CoSO_4$ melts occur at 1090 K, 1076 K, 1110 K, 1120 K, and 1125 K, respectively. They are shown in the liquid field of the phase diagram in Figure 5.47. The EMF breaks are further tested by conducting two independent experiments on 80 mole percent of Na_2SO_4-$CoSO_4$ at different inlet gas flowrate ratio of O_2 to SO_2. The same EMF break at 1090 K is recorded, illustrated in Figure 5.48, at both ratios of inlet O_2/SO_2 of 19.345 and 0.562. The change in the
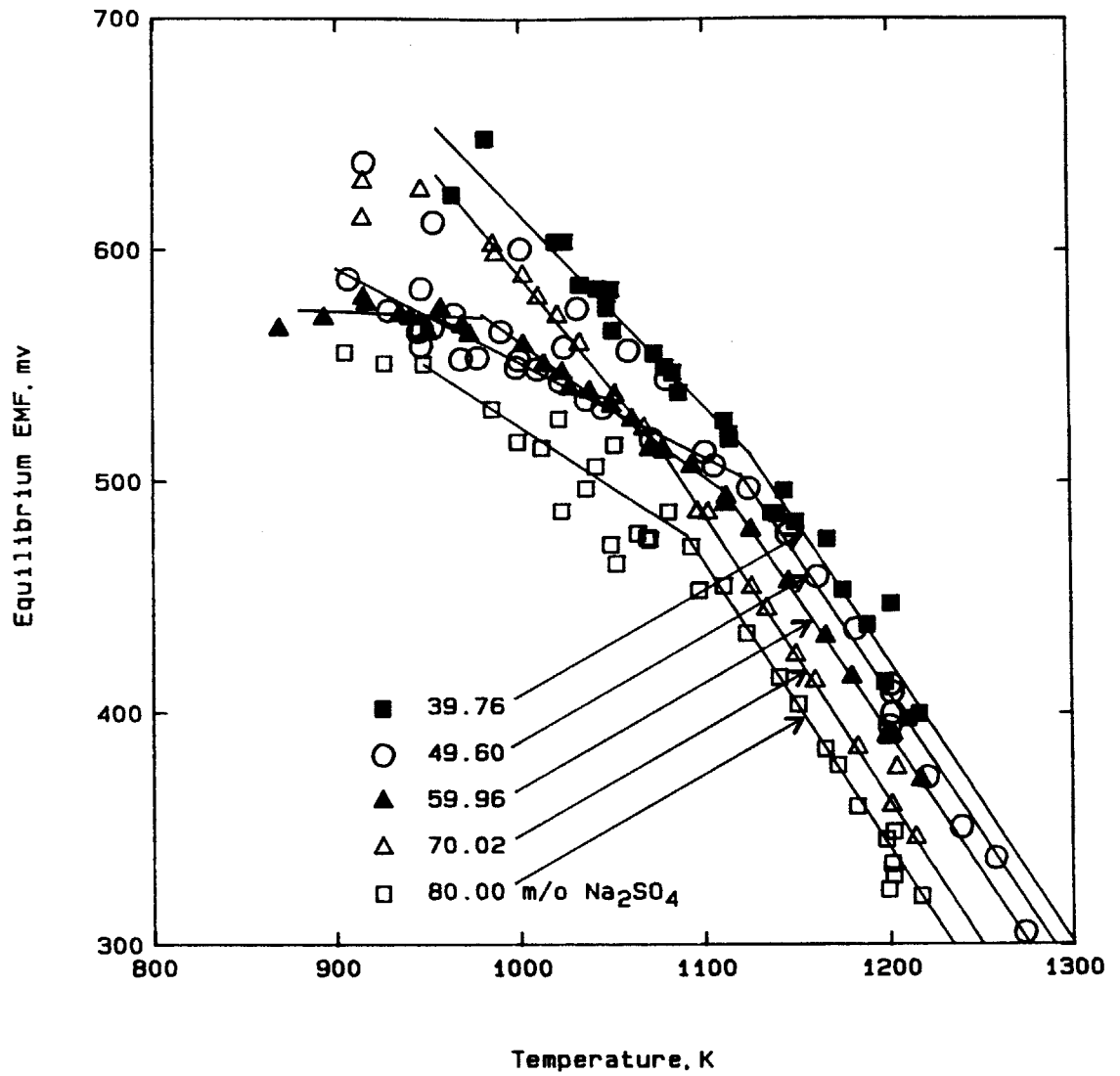
Figure 5.46 – Electrochemical results of $CoSO_4$-Na_2SO_4 melts at a constant inlet gas ratio.
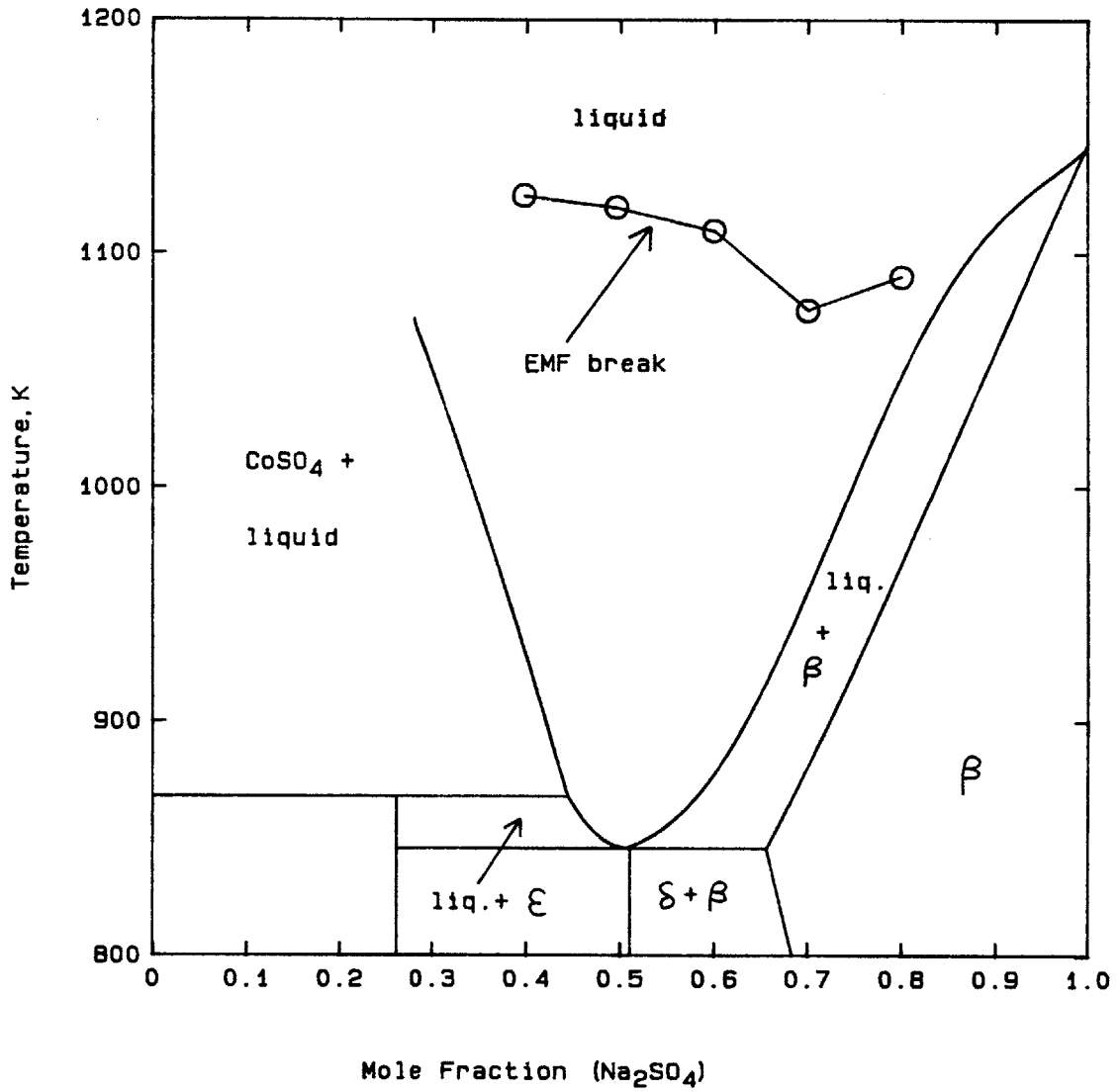
Figure 5.47 - Breaks in cell potential of $CoSO_4$-Na_2SO_4 melts.
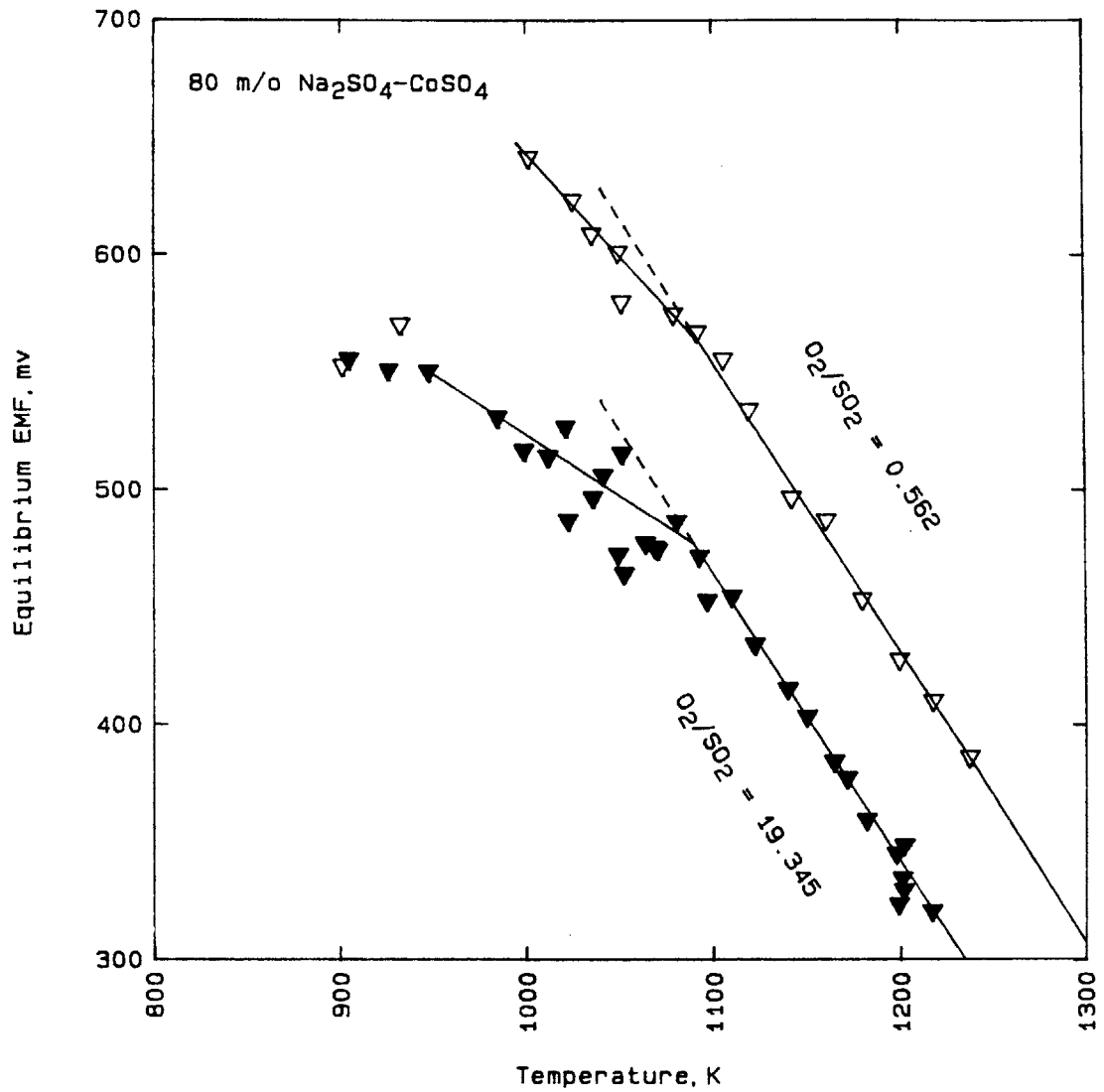
Figure 5.48 - Electrochemical results of 80 m/o Na_2SO_4-$CoSO_4$ at two inlet gas ratios.

thermodynamic properties of the Na_2SO_4-$CoSO_4$ melt is therefore not a function of the variables in the gas phase.

The activity of sodium oxide calculated from the Nernst equation is extrapolated to a constant pressure of SO_3 of 0.02 atm. The reaction of importance is

$$Na_2O(l) + SO_3(g) = Na_2SO_4(l) \qquad (5-78)$$
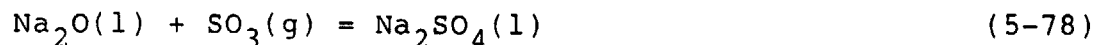
The equilibrium constant is

$$K = a_{Na_2SO_4(l)} / (a_{Na_2O(l)} \cdot P_{SO_3}) \qquad (5-79)$$

Since K and $a_{Na_2SO_4(l)}$ are constants at a constant temperature, the relationship of $a_{Na_2O(l)}$ and P_{SO_3} at their original condition, I, and those at partial pressure of SO_3 of 0.02, II, is:

$$\log a_{Na_2O(l)}^{I} + \log P_{SO_3}^{I}$$
$$= \log a_{Na_2O(l)}^{II} + \log P_{SO_3}^{II} \qquad (5-80)$$

or

$$\log a_{Na_2O(l)}^{II} = \log a_{Na_2O(l)}^{I} + \log (P_{SO_3}^{I}/P_{SO_3}^{II}) \quad (5-81)$$

The activities of sodium oxide in molten Na_2SO_4-$CoSO_4$ at the constant partial pressure of SO_3 of 0.02 atm calculated from equation (5-81) are presented in Figure 5.49, and those at high temperatures above 1100 K are shown in Figure 5.50. The linear relations with standard deviations and coefficients of correlation found at high temperatures are
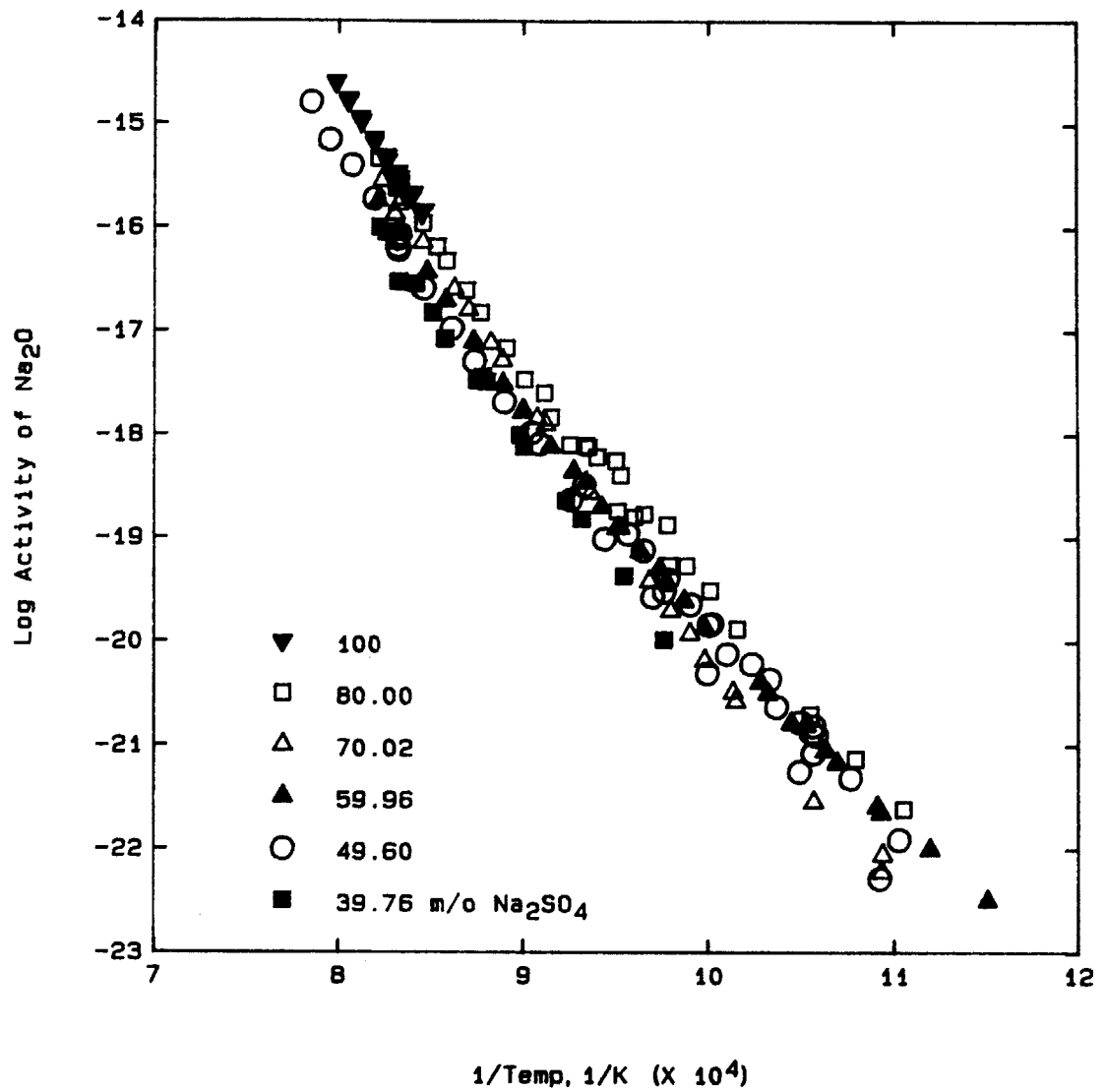
Figure 5.49 – Activity of sodium oxide in $CoSO_4$-Na_2SO_4.
melts at P_{SO_3} = 0.02 atm.
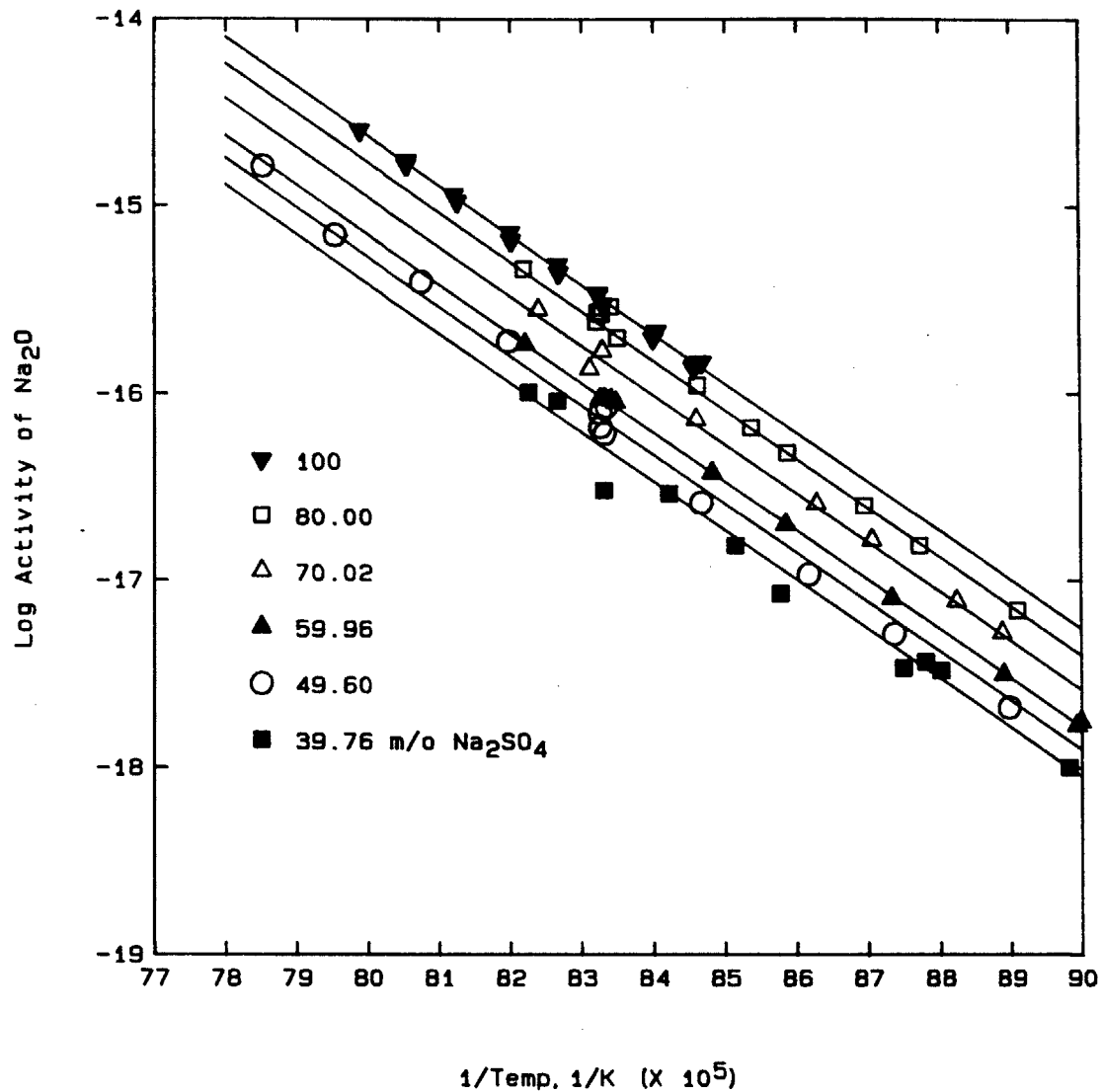
Figure 5.50 - Activity of sodium oxide in $CoSO_4-Na_2SO_4$ melts at P_{SO_3} = 0.02 atm. at high temperatures.

listed in Table 5-12.

The activity of sodium sulfate in the Na_2SO_4-$CoSO_4$ melt
is calculated from the activity of sodium oxide in the Co-Na
sulfate and that in the pure sodium sulfate under the same
pressure of SO_3 of 0.02 atm. Based on the facts that the
equilibrium constant K in equation (5-79) is the same in
Co-Na sulfate mixture and in pure sodium sulfate at a
constant temperature and the activity of Na_2SO_4 in pure
sodium sulfate is unity, the activity of Na_2SO_4 in Co-Na
sulfate is thus derived by equating the equilibrium
constants in Co-Na sulfate and in pure sodium sulfate under
the same P_{SO_3}. The final relationship becomes:

$$\log a_{Na_2SO_4(1)}{}^m = \log a_{Na_2O(1)}{}^m - \log a_{Na_2O(1)}{}^p \qquad (5\text{-}82)$$

where the superscipts of m and p denote Co-Na sulfate
mixture and in pure sodium sulfate, respectively.
Physically, the activity of sodium sulfate is the
perpendicular distance of the line of the Co-Na sulfate away
from the line of pure Na_2SO_4 in the Na_2O activity diagram in
Figure 5.50. The activity of sodium sulfate shown in Figure
5.51 reveals constant Na_2SO_4 activities at all compositions
at high temperatures above the temperature breaks; below
those temperatures, the Na_2SO_4 activity tends to increase
with decreasing temperature. The behavior of solution at
high temperatures is thus athermal with zero heat of mixing.

Table 5-12

Activity of Sodium Oxide at High Temperatures in $CoSO_4$-Na_2SO_4 melts at P_{SO_3} = 0.02 atm.

$$\log a_{Na_2O} = c + d/T$$

m/o Na_2SO_4	c	d	$S(\log a_{Na_2O})$	γ
100.	6.458 ± 0.266	-26352 ± 322	0.0207	0.998
80.00	6.316 ± 0.377	-26352 ± 442	0.0385	0.998
70.02	6.132 ± 0.615	-26352 ± 719	0.0471	0.997
59.96	5.932 ± 0.153	-26352 ± 178	0.0164	0.9997
49.60	5.813 ± 0.449	-26352 ± 538	0.0548	0.998
39.76	5.669 ± 0.412	-26352 ± 466	0.0819	0.998

where $S(\log a_{Na_2O})$ is the standard deviation of $\log a_{Na_2O}$

γ is the correlation coefficient
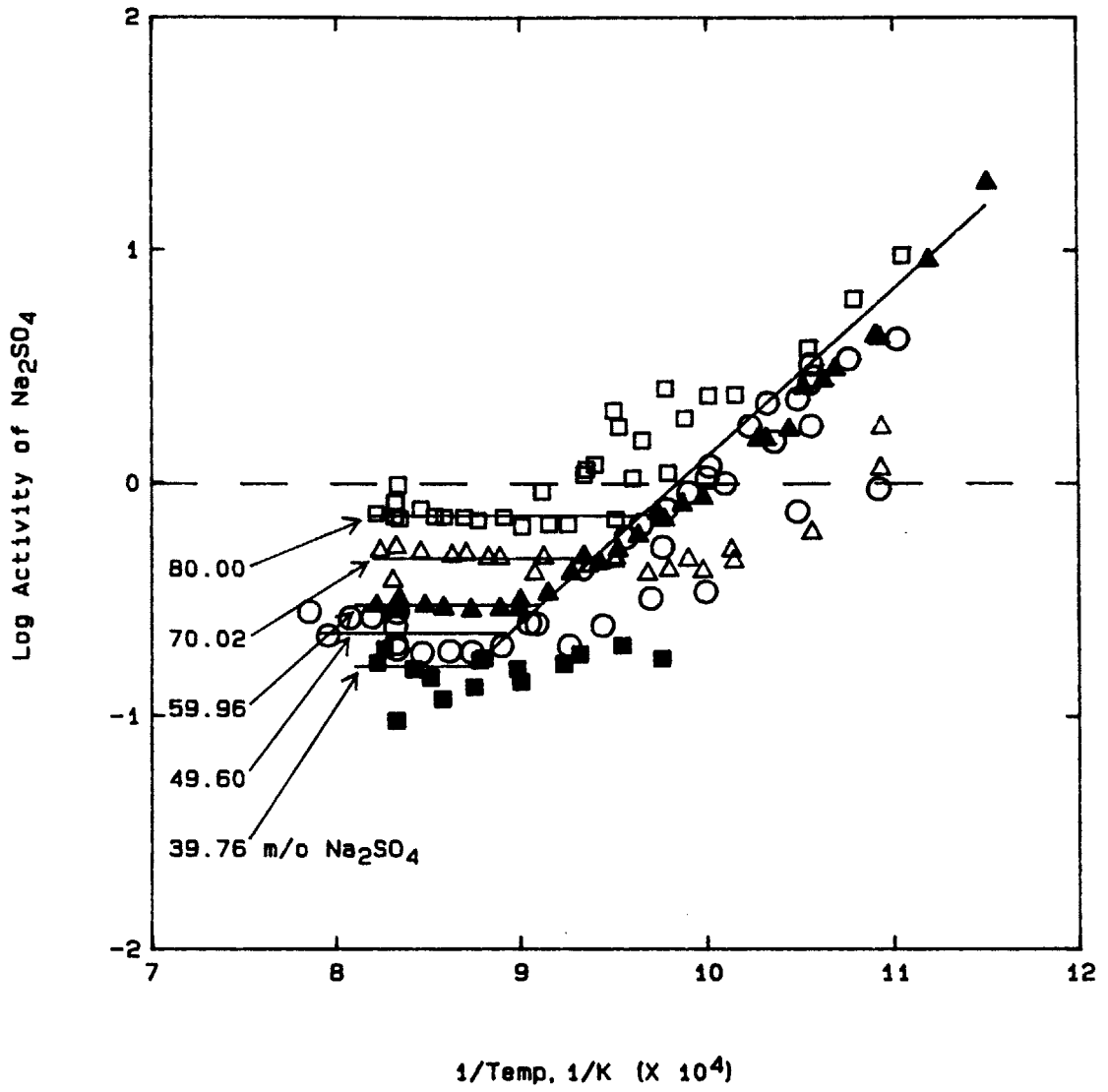
Figure 5.51 - Activity of sodium sulfate in $CoSO_4$-Na_2SO_4.

The alpha function of sodium sulfate shown in Figure 5.52 does not stay constant at all compositions; thus, the liquid solution of Na_2SO_4-$CoSO_4$ is not a regular solution.

Due to the inconsistent behavior of liquid Na_2SO_4-$CoSO_4$ at low temperatures, the following thermodynamic calculations are based on the experimental data at high temperatures above the EMF breaks. The activity of cobalt sulfate is calculated by means of the Gibbs-Duhem equation:

$$\log \gamma_2 = - \int \begin{array}{l} \log \gamma_1 \text{ at } X_2 = X_2 \\ (X_1/X_2) \, \partial \log \gamma_1 \\ \log \gamma_1 \text{ at } X_2 = 1 \end{array} \qquad (5\text{-}83)$$

where 1 and 2 represent species Na_2SO_4 and $CoSO_4$, respectively. The integration is performed to evaluate the area under the straight line in Figure 5.53.

The activities of Na_2SO_4 and $CoSO_4$ are illustrated in Figure 5.54. Both activities demonstrate a fair degree of negative deviation from ideality, so compound formation is favored in the sulfate system. Figure 5.55 shows the integral Gibbs free energy of mixing, G^M, integral Gibbs free energy of ideal mixing, G^{ID}, and excess Gibbs free energy of mixing evaluated according to the following equations:

$$G^M = RT (X_1 \ln a_1 + X_2 \ln a_2) \qquad (5\text{-}84)$$
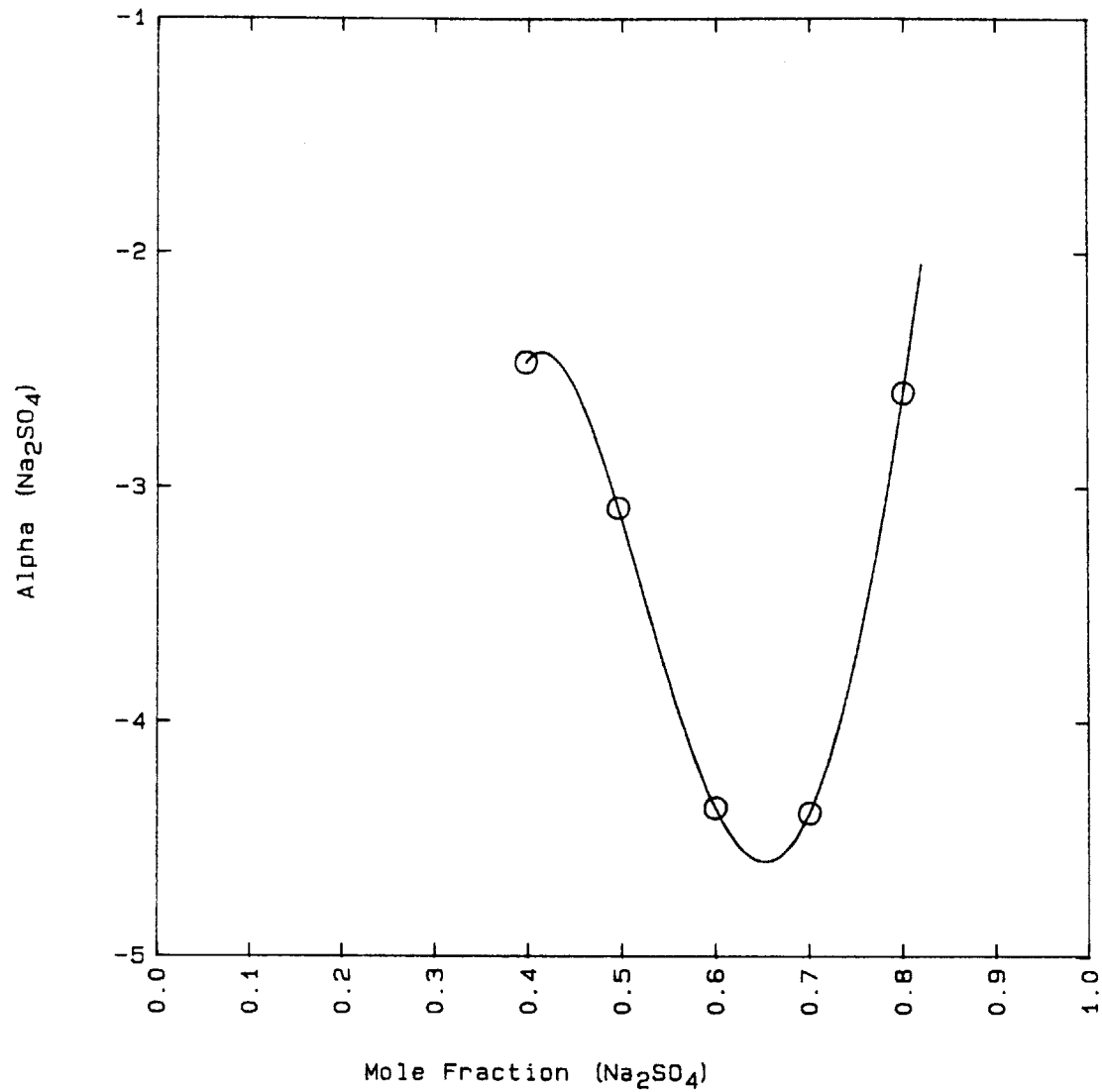
Figure 5.52 – Alpha function of Na_2SO_4 in $CoSO_4$–Na_2SO_4 melts.
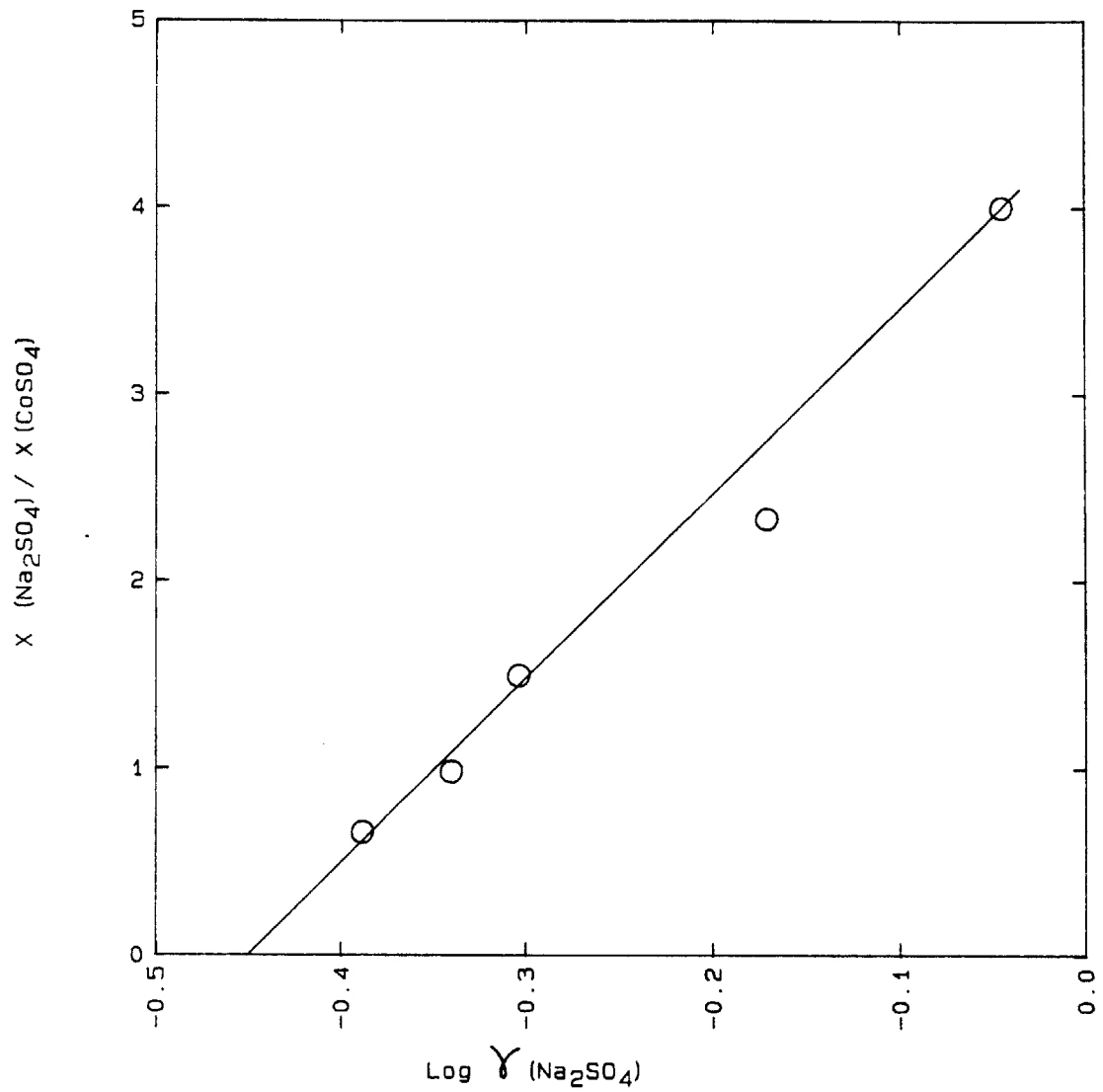
Figure 5.53 - Gibbs-Duhem integration for the activity of $CoSO_4$ in $CoSO_4-Na_2SO_4$ melts.
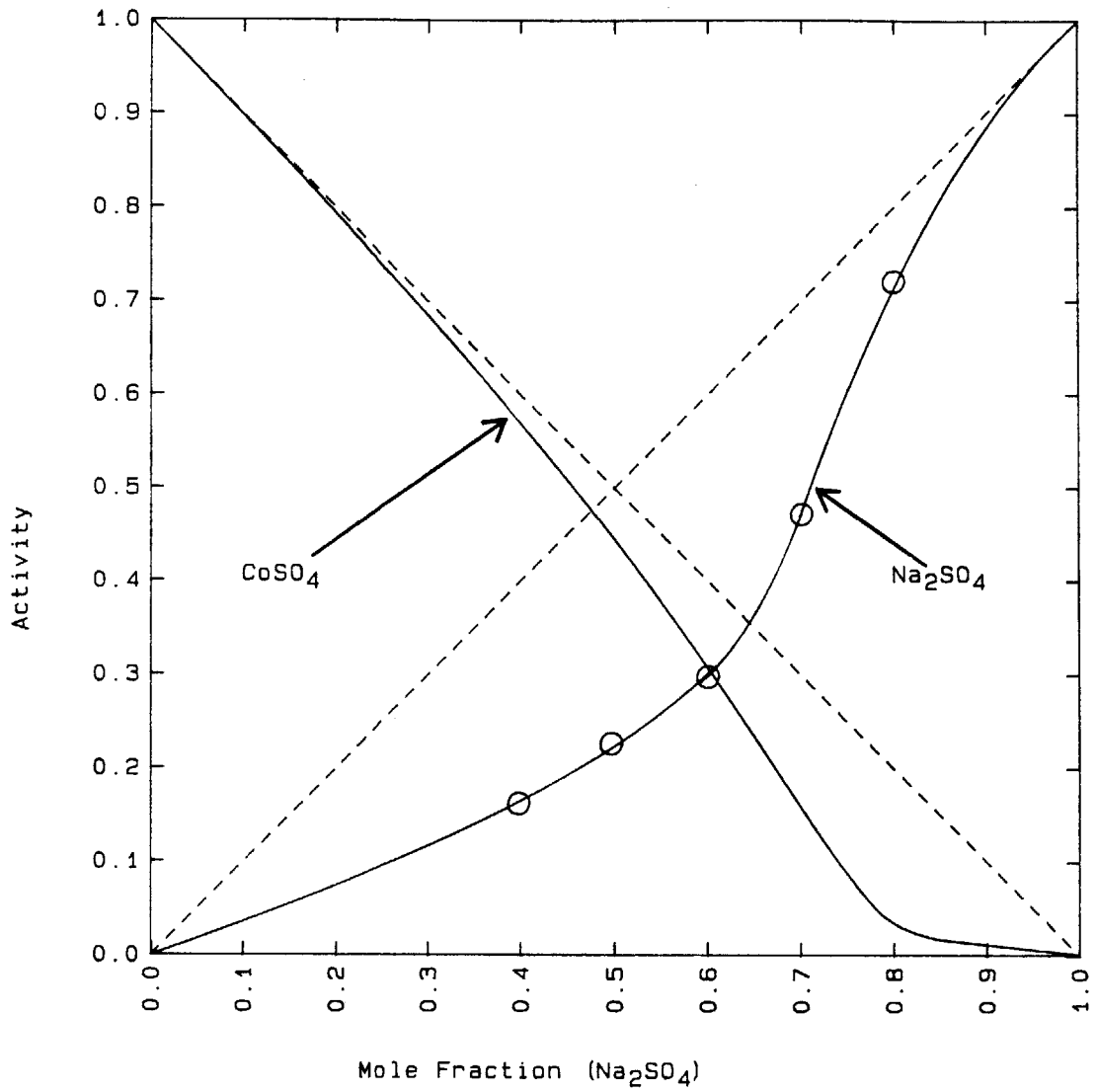
Figure 5.54 - Activities of $CoSO_4$ and Na_2SO_4.
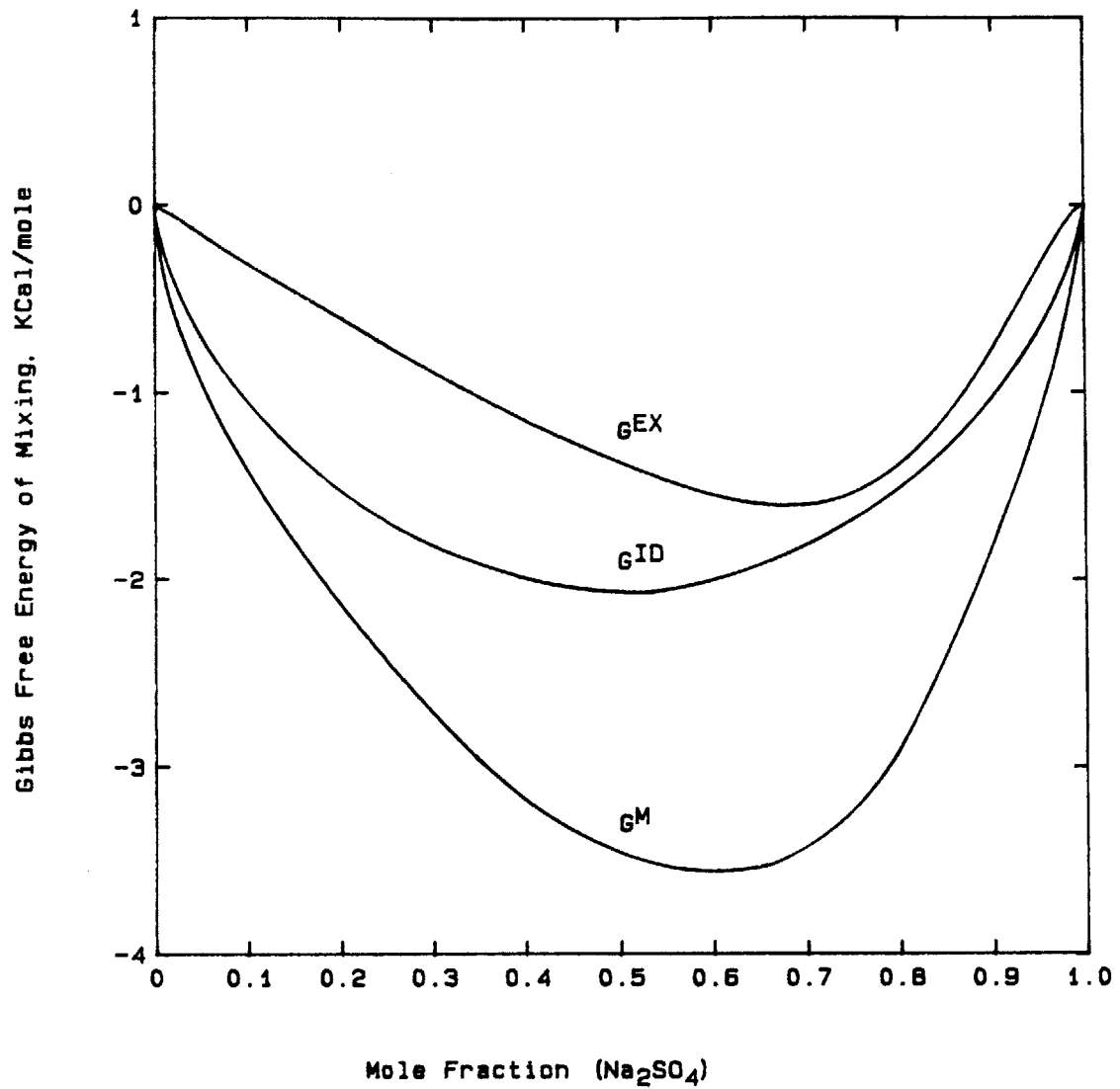
Figure 5.55 – Free energies of mixing of $CoSO_4$ and Na_2SO_4 at 1500 K.

$$G^{ID} = RT \; (X_1 \; \ln X_1 + X_2 \; \ln X_2) \tag{5-85}$$

$$G^{EX} = G^M - G^{ID} \tag{5-86}$$

where 1 and 2 denote species Na_2SO_4 and $CoSO_4$, respectively.

The thermodynamic properties of cobalt sulfate is further calculated according the equilibrium reaction at melting:

$$CoSO_4(s) = CoSO_4(l) \tag{5-87}$$

Since the activity of $CoSO_4(s)$ in respect to solid cobalt sulfate is unity, the molar Gibbs free energy of melting in terms of activity is equal to:

$$\Delta G_m = - \; RT \; \ln a_{CoSO_4(l)} \tag{5-88}$$

The activities of $CoSO_4$ at liquidus temperatures is presented in Figure 5.56, and the relationship is:

$$\ln a_{CoSO_4(l)} = 0.9926 - 1443/T \tag{5-89}$$

By means of $\Delta G_m = \Delta H_m - \Delta S_m \cdot T$ and equation (5-88), the following melting properties of cobalt sulfate are known.

$$\Delta G_{m,CoSO_4} = 2.868 - 1.972 \times 10^{-3} \; T \qquad [Kcal/mole] \tag{5-90}$$

The melting point of pure cobalt sulfate is determined to be

- 208 -
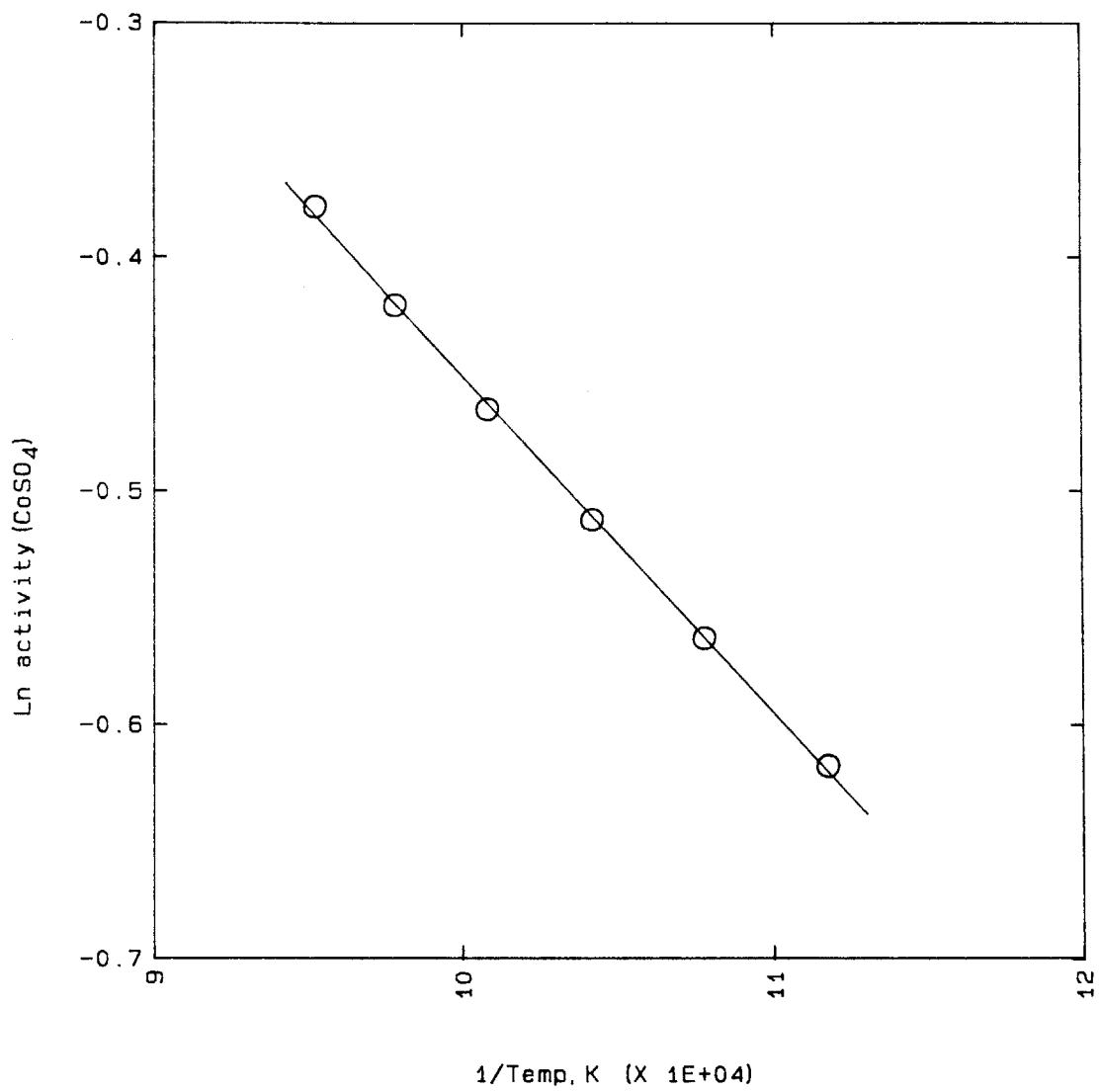
Figure 5.56 - Activity of $CoSO_4$ at liquidus temperature.

1454 K when ΔG_m is set to zero.

The standard Gibbs free energy of formation of liquid cobalt sulfate is obtained from the standard Gibbs free energy of melting found by this study and the standard Gibbs free energy of formation of solid cobalt sulfate taken from JANAF Tables [104] according to the following relationship:

$$\Delta G^o_f(CoSO_4(l)) = \Delta G_m + \Delta G^o_f(CoSO_4(s)) \qquad (5-91)$$

The $\Delta G^o_f(CoSO_4(s))$ in JANAF Tables [104] is $-223.2098 + 0.09743$ T in Kcal/mole in the range of 800 K to 1200 K; thus, the standard Gibbs free energy of formation of liquid cobalt sulfate is

$$\Delta G^o_f(CoSO_4(l)) = -220.3420 + 0.09546 \text{ T [Kcal/mol]} \qquad (5-92)$$

The standard Gibbs free energies of formation are shown in Figure 5.57.

The behavior of the activity of sodium oxide in the Co-Na sulfate as a function of partial pressure of sulfur trioxide at 1200 K is exhibited in Figure 5.58. The relationships between log a_{Na_2O} and log P_{SO_3} for 100, 80.00, 70.02, 59.96, and 50.01 mole percent of Na_2SO_4-$CoSO_4$ are tabulated with standard deviations and coefficients of correlation in Table 5-13. The log of the activity of sodium oxide in the Co-Na sulfate melt increases with an increase in the concentration of sodium sulfate in the Co-Na
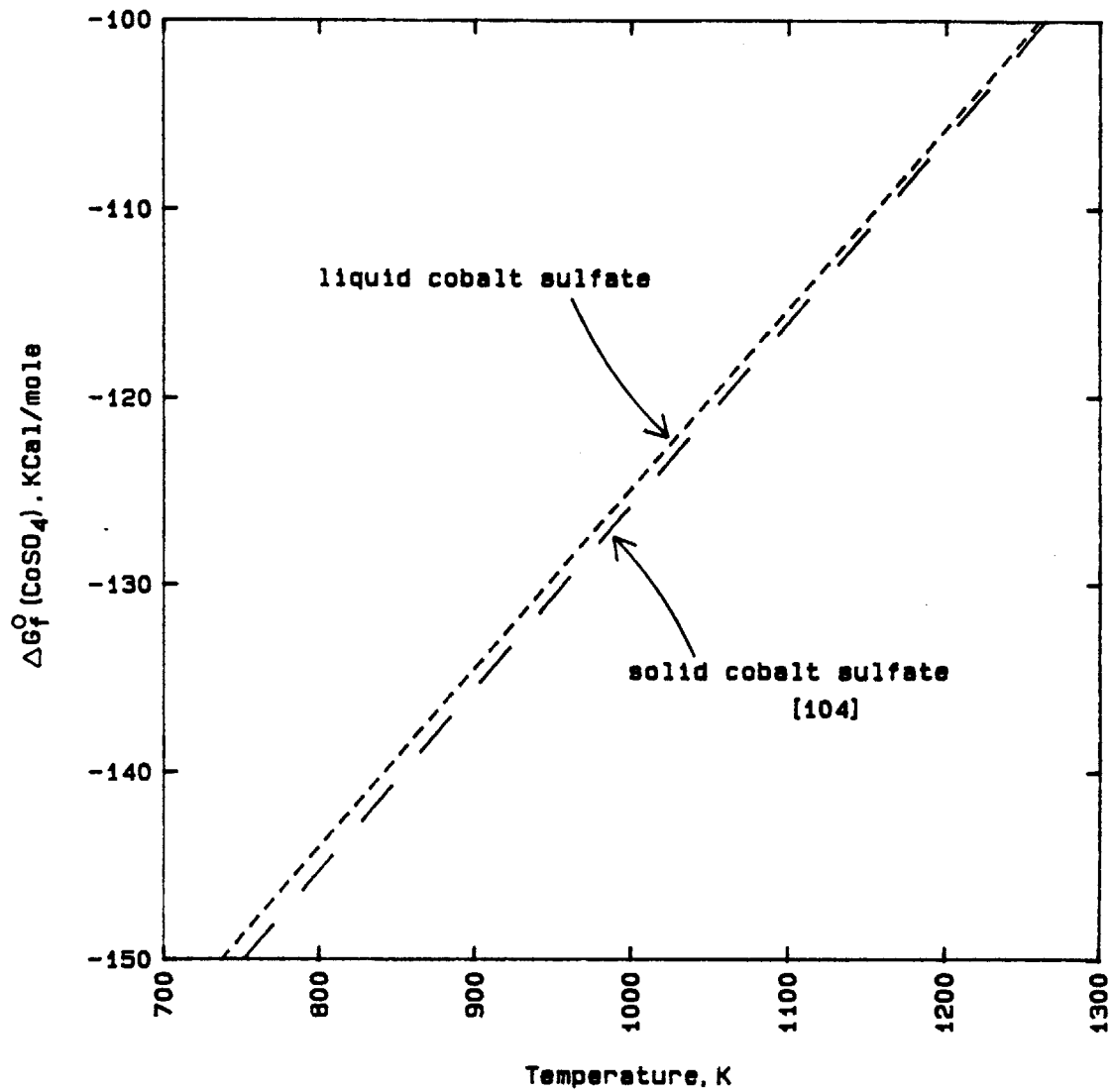
Figure 5.57 - Standard free energy of formation of liquid CoSO$_4$ and solid CoSO$_4$.
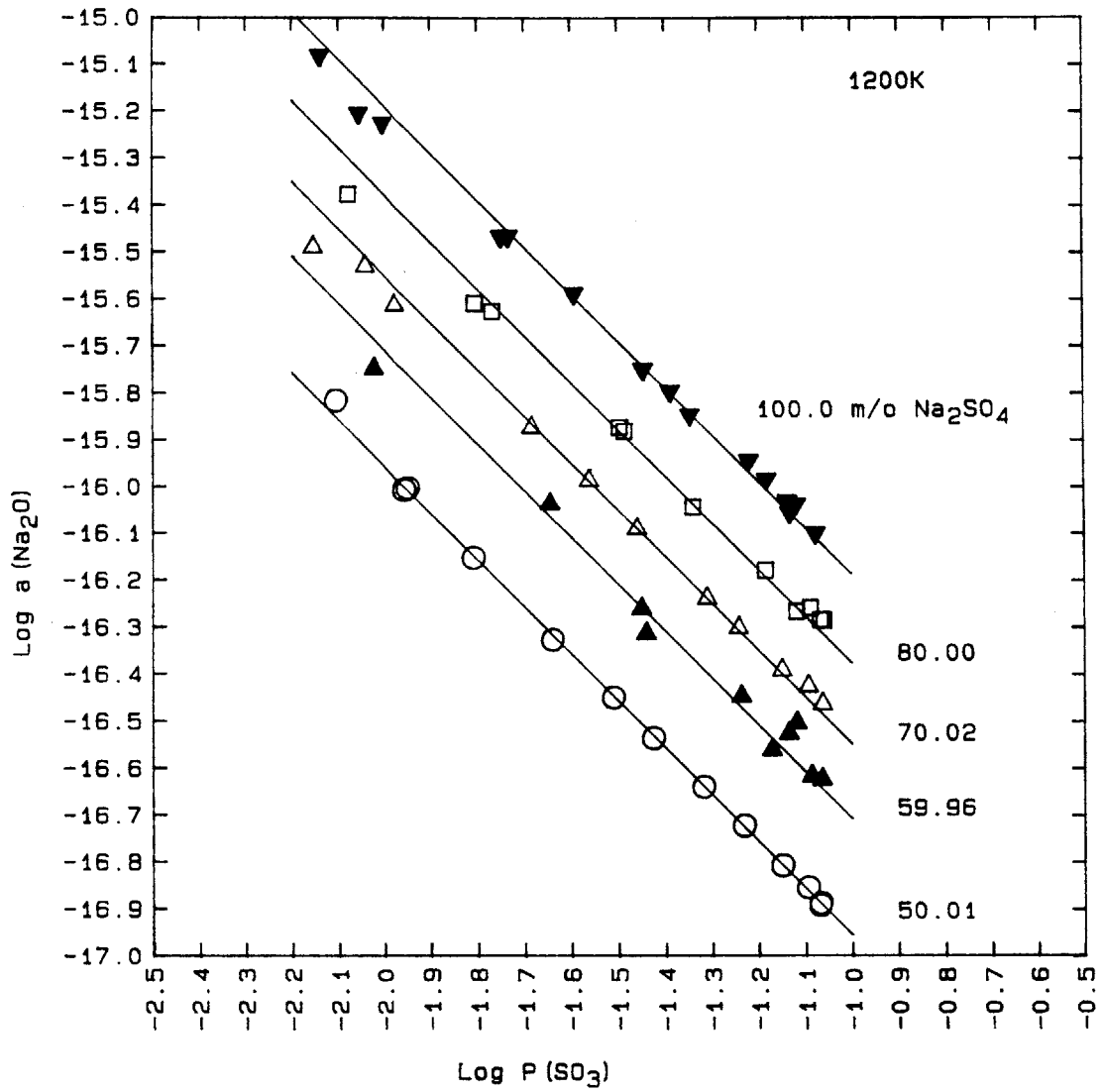
Figure 5.58 - SO_3 pressure dependence of activity of Na_2O in $CoSO_4$-Na_2SO_4 melts at 1200 K.

Table 5-13

Relationships Between Sodium Oxide and Sulfur Trioxide
in Cobalt Sulfate-Sodium Sulfate Melts at 1200 K

$$\log a_{Na_2O(1)} = \log a_{Na_2SO_4} - \log K - c \cdot \log P_{SO_3}$$

m/o Na_2SO_4	$\log a_{Na_2SO_4} - \log K$	c	$S(\log a_{Na_2O})$	γ
100.00	-17.187 ± 0.015	1.0 ± 0.010	0.014	0.9992
80.00	-17.376 ± 0.021	1.0 ± 0.014	0.016	0.998
70.02	-17.548 ± 0.022	1.0 ± 0.013	0.017	0.999
59.96	-17.708 ± 0.055	1.0 ± 0.041	0.037	0.992
50.01	-17.956 ± 0.013	1.0 ± 0.008	0.011	0.9996

where $S(\log a_{Na_2O})$ is the standard deviation of $\log a_{Na_2O}$

γ is the correlation coefficient

sulfate melt and linearly with an decrease in the log of partial pressure of SO_3. The slope of the line equals to -1 in all cases.

With the knowledge of the activity of liquid cobalt sulfate and the $\Delta G_f^o(CoSO_4(l))$ from this study, the stability diagram of $Na_2SO_4-CoSO_4$ in equilibrium with Co_3O_4 and CoO is drawn in Figure 5.59 according to the four chemical equilibria:

$$1/3 \; Co_3O_4(s) + SO_3(g) = CoSO_4(s) + 1/6 \; O_2(g) \qquad (5-93)$$

$$1/3 \; Co_3O_4(s) + SO_3(g) = CoSO_4(l) + 1/6 \; O_2(g) \qquad (5-94)$$

$$CoO(s) + SO_3(g) = CoSO_4(s) \qquad (5-95)$$

$$CoO(s) + SO_3(g) = CoSO_4(l) \qquad (5-96)$$
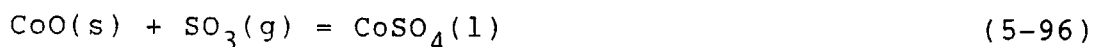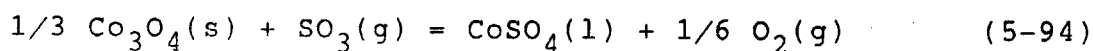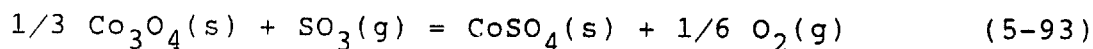
In view of the activities of $Co_3O_4(s)$, CoO(s), and $CoSO_4(s)$ are unity in respect to the solid state as the standard state, the equilibrum constants for the reactions (5-93) to (5-96) derived from $K=\exp(-\Delta G^o/RT)$ can be written respectively in terms of the partial pressure of SO_3 as follows:

$$\log P_{SO_3} = 6.119 + 1/6 \; \log P_{O_2} - 9083/T \qquad (5-97)$$

$$\log P_{SO_3} = 5.688 + 1/6 \; \log P_{O_2} + \log a_{CoSO_4(l)} - 8456/T \qquad (5-98)$$

$$\log P_{SO_3} = 9.013 - 12610/T \qquad (5-99)$$

$$\log P_{SO_3} = 8.582 + \log a_{CoSO_4(l)} - 11983/T \qquad (5-100)$$

The equations (5-97), (5-98), (5-99), and (5-100) are depicted respectively by the curves A, B, C, and D in the
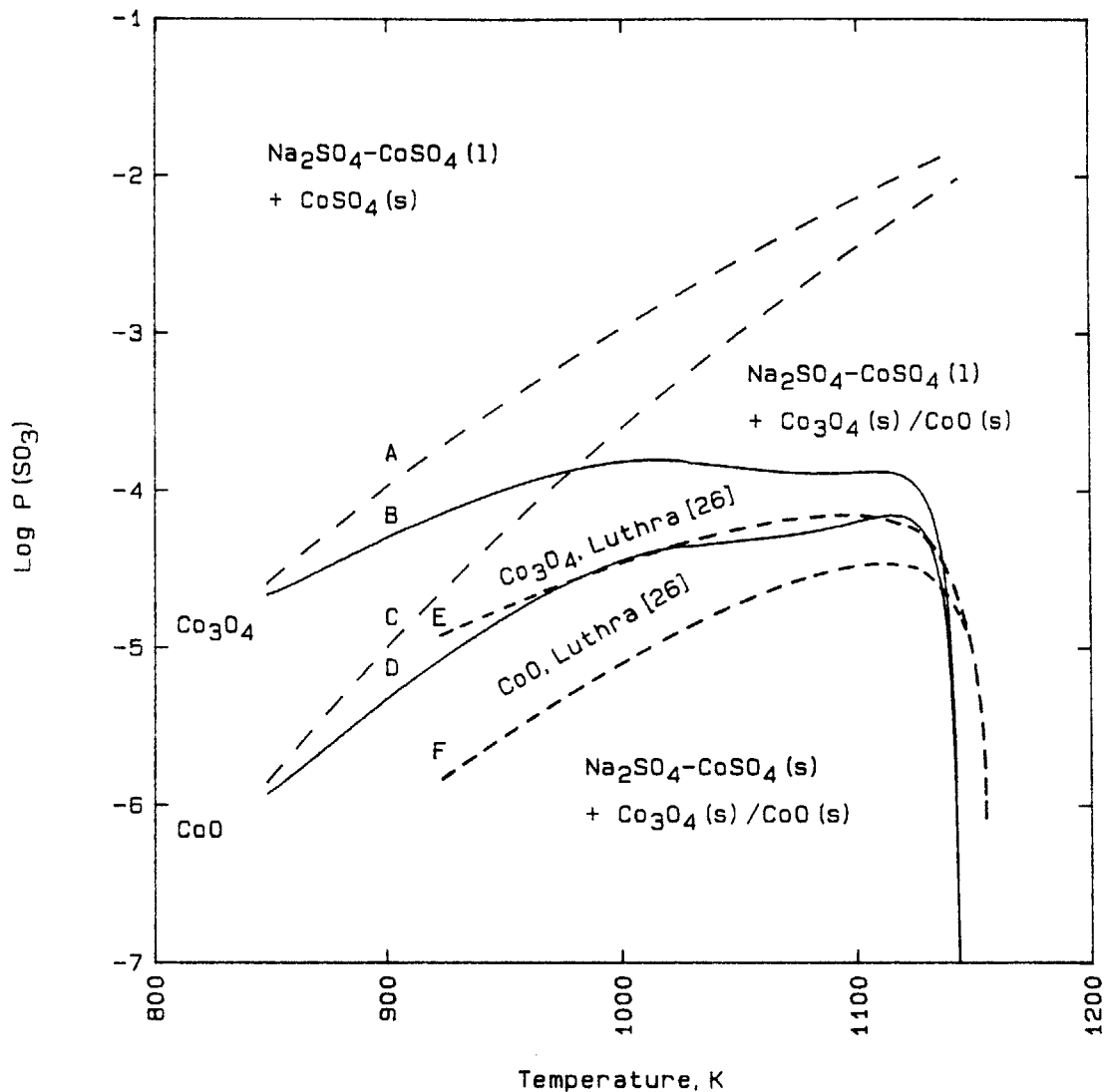
Figure 5.59 – Phase stability diagram of $CoSO_4$-Na_2SO_4 system and comparison with Luthra [26] at P_{O_2} = 1 atm. A and C: boundaries between $Co_3O_4(s)$/$CoO(s)$ and $CoSO_4(s)$ in equilibrium with liquid $CoSO_4$-Na_2SO_4, respectively; B and D: boundaries between liquid and solid $CoSO_4$-Na_2SO_4 in eqilibrium with $Co_3O_4(s)$/ $CoO(s)$, respectively; E and F: boundaries between liquid and solid $CoSO_4$-Na_2SO_4 in equilibrium with $Co_3O_4(s)$/$CoO(s)$, respectively [26].

- 215 -

stability diagram included in Figure 5.59. The partial pressure of oxygen is taken to be one atmosphere and the activity of $CoSO_4$ liquid equals to that at the liquidus at the Na_2SO_4 end of the $Na_2SO_4-CoSO_4$ phase diagram in Figure 2.4.

The isoactivity lines of SO_3 are determined for the equilibrium among liquid solution of $Na_2SO_4-CoSO_4$, solid Co_3O_4, SO_3 gas, and O_2 gas in reaction (5-94). The isobars of P_{SO_3} are calculated from equation (5-98) which is rewritten as:

$$T = \frac{-8456}{\log P_{SO_3} - 5.688 - \log a_{CoSO_4(l)} - 1/6 \log P_{O_2}} \quad (5-101)$$

The activity of $CoSO_4(l)$ is further related to the mole fraction of Na_2SO_4 according to the activity diagram in Figure 5.54. With the partial pressure of O_2 being one atmosphere, isobars of SO_3 in terms of $\log P_{SO_3}$ in the range of −4.50 to −2.5 with increment of 0.25 are illustrated on the phase diagram in Figure 5.60. Constant partial pressures of SO_3 are described across the two-phase regions of $CoSO_4$+liquid and Liquid+β at a constant temperature. Isobars of SO_3 are not drawn in the β region, because the exact behavior of P_{SO_3} across that region is not known. The isobars of SO_3 in the β region behaves in the same way governed by the Gibbs-Helmholtz equation as those in the β region in the $Na_2S_2O_7-Na_2SO_4$ system.
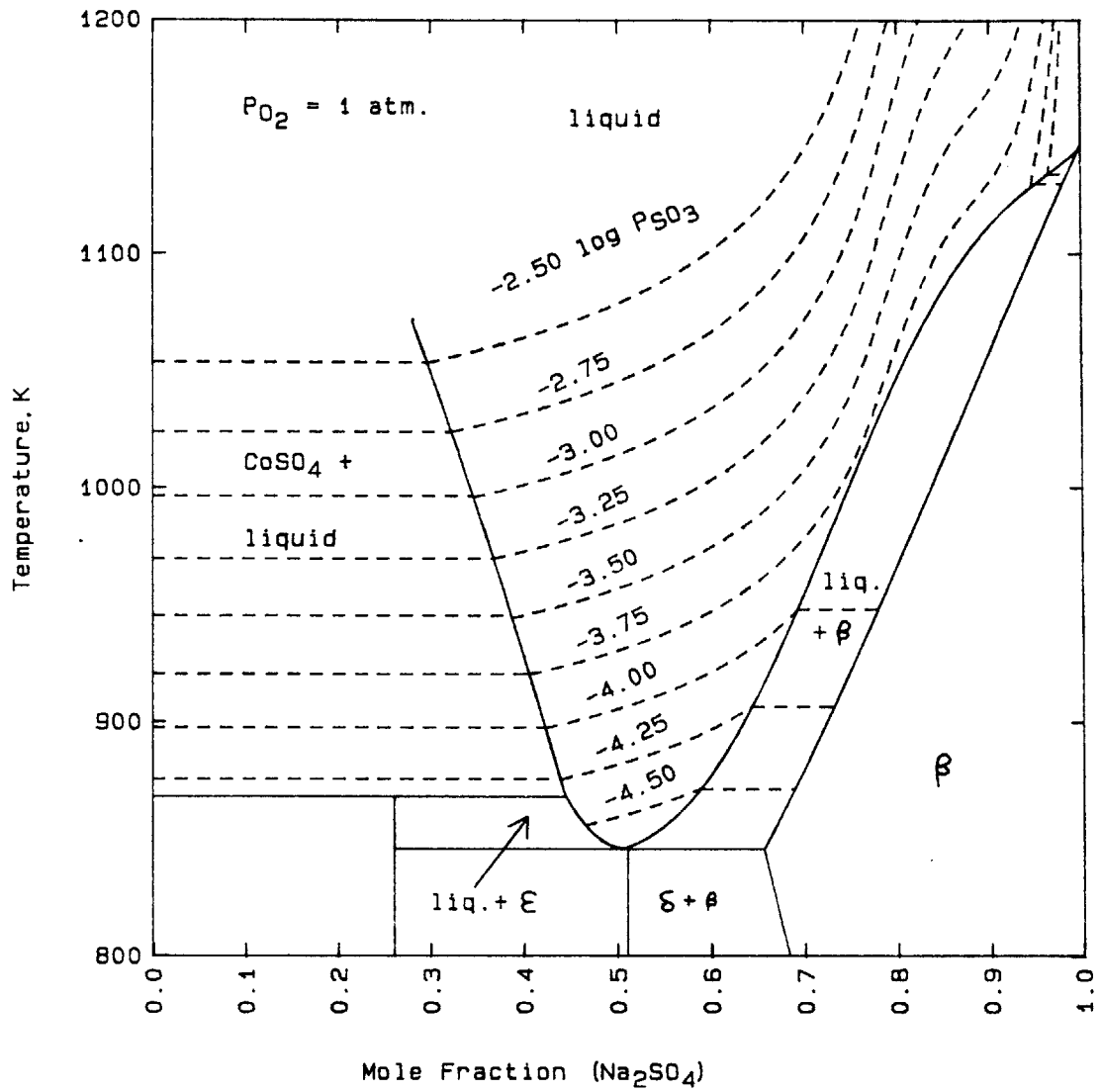
Figure 5.60 – Isoactivity lines of SO_3 in $CoSO_4$-Na_2SO_4 system.

5.3.4 Phase Determinations

Because the electrochemical measurements reveal discordant thermodynamic behaviors of the sulfate system at temperatures below the EMF breaks in the homogeneous liquid phase of the $CoSO_4-Na_2SO_4$ phase diagram reported by Bolshakov & Fedorov [25], differential thermal analysis (DTA) is conducted to investigate possible phase transformations taken place in the liquid phase. Samples are also extracted at different temperatures during equilibrations in electrochemical experiments. They are drawn into a fused silica tube with the aid of a syringe, and they are quenched in static air at room temperature. Lastly, the sample morphology is examined by optical microscopy and scanning electronic microscopy, and the samples are then quantitatively analyzed by energy dispersive analysis of X-ray spectroscopy (EDX).

5.3.4.1 Differential Thermal Analysis

The differential thermal analysis is performed on 80.00, 70.02, 59.96, 49.60, 39.76, and 29.98 mole percent of $Na_2SO_4-CoSO_4$ under static atmosphere in the temperature range of 298K to 1273K. The thermographs of heating only are presented in Figure 5.61. The DTA peaks are shown in their relative proportions and the baseline is normalized to be horizontal at low temperatures. Two to three distinct peaks are identified at each melt composition.
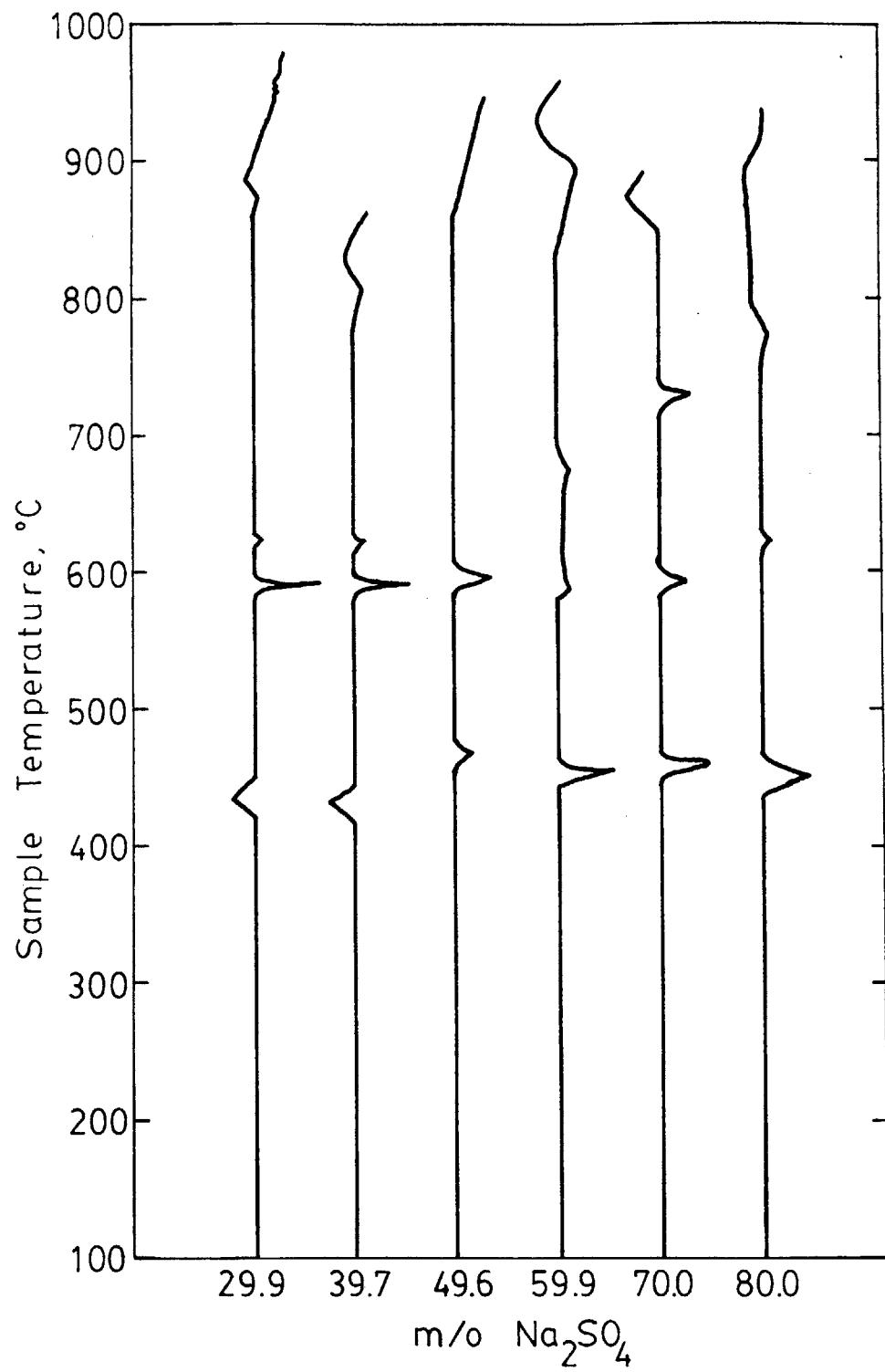
Figure 5.61 - DTA thermograph of $CoSO_4$-Na_2SO_4 melts.

Nevertheless, noticeable changes in the slope of the baseline are detected at 1144 K, 1080 K, 1132 K, 1166 K, 1120 K, and 1155 K on 29.98, 39.76, 49.69, 59.96, 70.02, and 80.00 mole percent of Na_2SO_4-$CoSO_4$, respectively.

The phase relationship of the EMF reference material, sodium tungstate, is also investigated by differential thermal analysis (DTA) to ensure that the EMF breaks are not a result of erroneous measurements by the electrochemical cell itself. Figure 5.62 shows the thermograph of heating Na_2O-54.98 m/o WO_3 reference material at a rate of 2°C per minute. Two sharp endothermic peaks are observed, one at 874K (601°C) and the other one at 904K (631°C).

5.3.4.2 Sampling

To further understand the nature of the $CoSO_4$-Na_2SO_4 melts, samples are extracted from the electrochemical experiments. Liquid samples which can be extracted from the $CoSO_4$-Na_2SO_4 represent samples of either the liquid phase or the two-phase neighboring the liquid phase. The temperatures at which liquid samples are taken are represented by open triangles in Figure 5.63. Filled triangles denote solid phase is encountered during sampling operation. No sample can be extracted in this case.
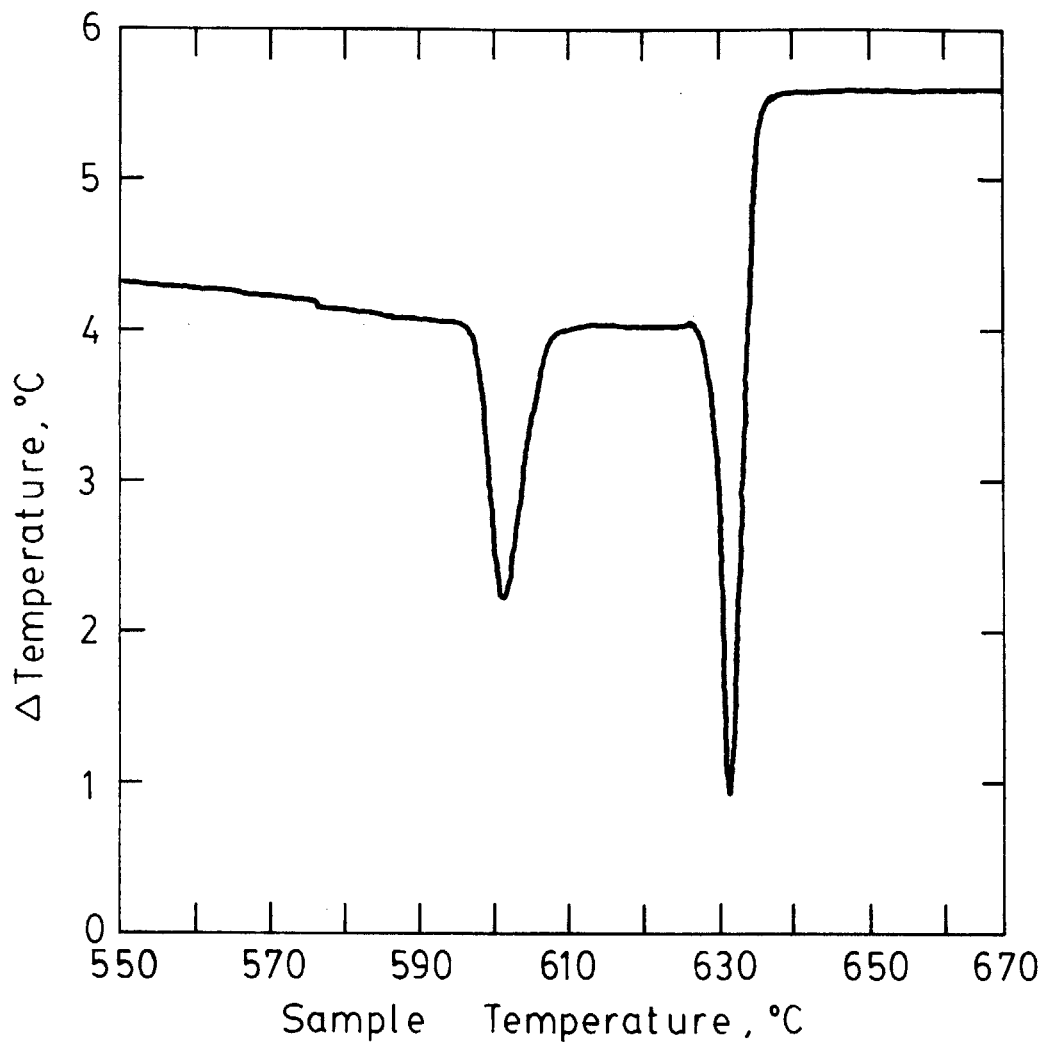
Figure 5.62 - DTA thermograph of Na_2O-WO_3 reference melt.
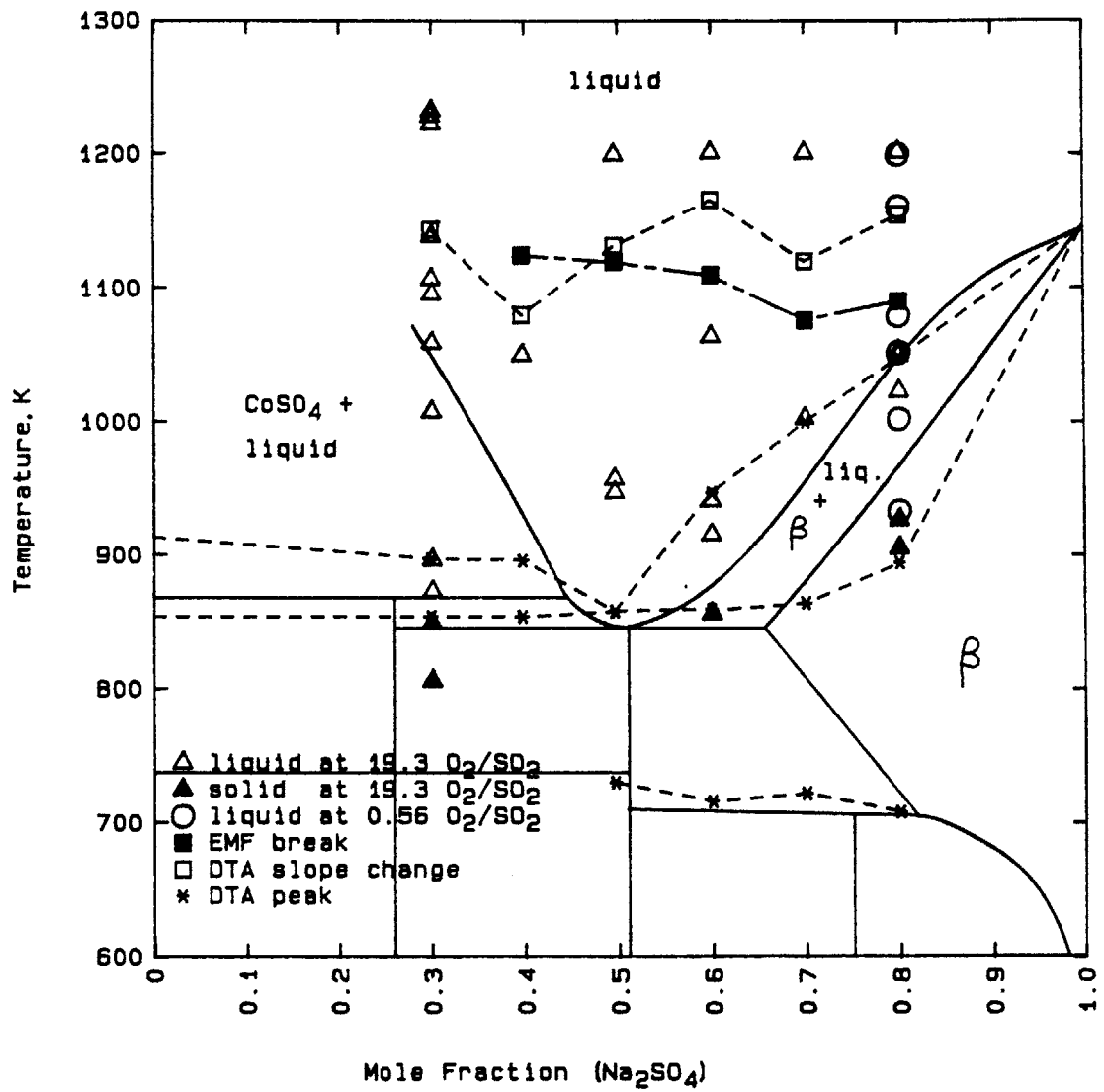
Figure 5.63 - Sample analysis and DTA results of $CoSO_4-Na_2SO_4$.

5.3.4.3 Morphology and EDX

Figure 5.64 describes the morphology of quenched samples taken from EMF experiments in relation to the phase diagram. Detail description of quenched samples and the expected morphology assuming no diffusion in solid and limited diffusion in liquid are found in Appendix N. The data and results of Energy Dispersive Analysis of X-Ray are displayed in Appendix O and P, respectively.
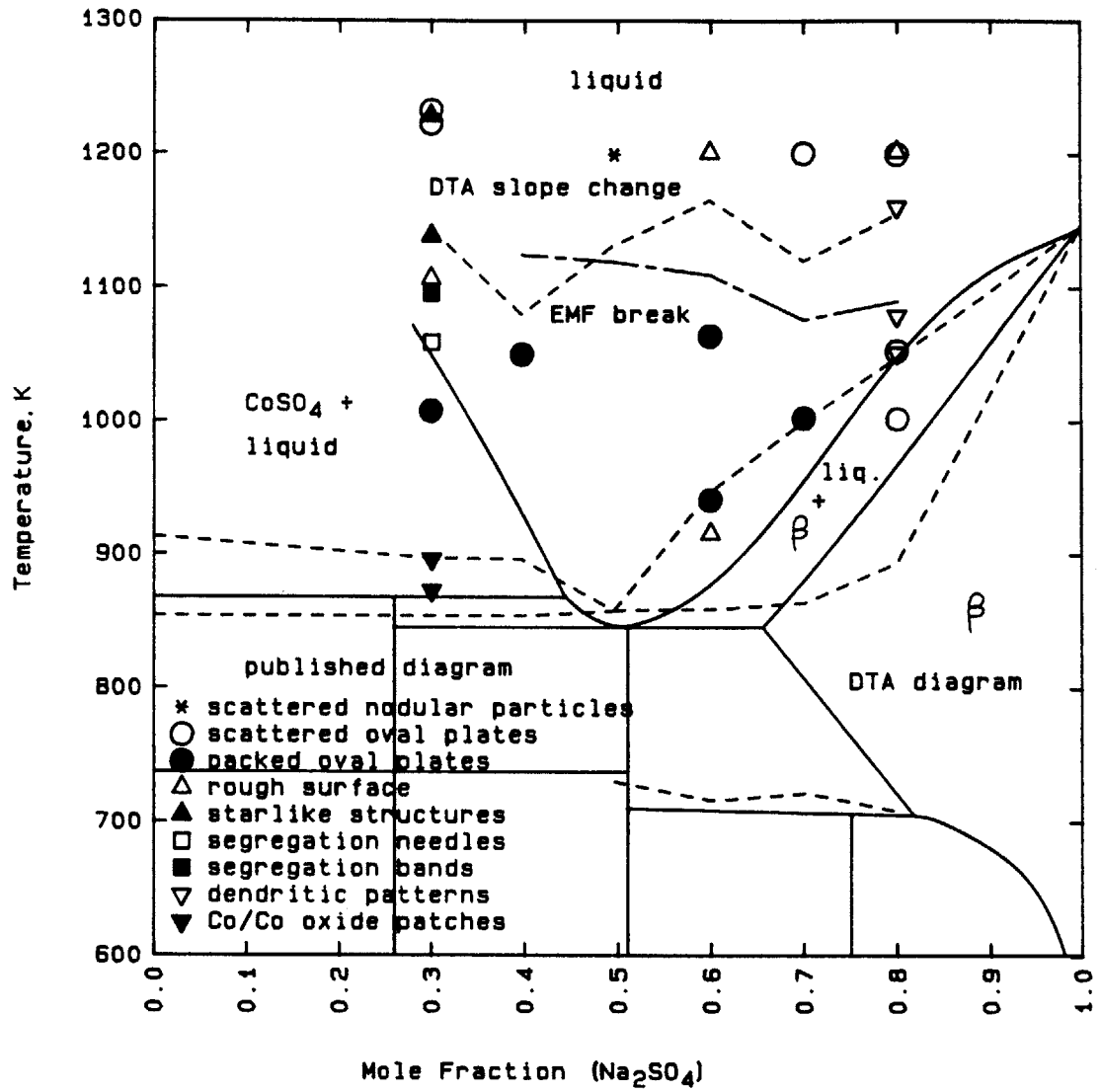
Figure 5.64 - Morphological study of $CoSO_4$-Na_2SO_4 samples.

CHAPTER SIX

DISCUSSION

The first section of this chapter discusses briefly the errors in the experimental variables of the thermogravimetric experiments and of the electrochemical experiments. The experimental results of the present study are then analyzed. The solubility of sulfur trioxide gas in molten sodium sulfate is discussed under the pseudo-binary of $Na_2S_2O_7$-Na_2SO_4. Thermodynamic properties of Na_2SO_4, performance of the solid electrolyte at basic conditions, and kinetics of SO_3 absorption/desorption are also included. The equilibrium solubility of Al_2O_3 solid in Na_2SO_4 at 1200 K is compared with other results in the literature. The system of $CoSO_4$-Na_2SO_4 is later analyzed for the thermodynamic properties and phase identifications. The final section of this chapter focuses on the implications of the findings of this study on the sodium sulfate induced hot corrosion.

6.1 Error Analysis

Error Analyses have been performed on the experimental variables measured in the thermogravimetric analysis and in the electrochemical experiments. Tables 6-1 and 6-2 summaried the errors found respectively in partial pressures of SO_3 and in mole fractions of SO_3 in the thermogravimetric

Table 6-1

Error Analysis in Partial Pressure of SO_3

Source of Error	Type of Error	Magnitude of Error	Resultant Error in log P_{SO_3}
1. Calibration of thermocouple [94]	systematic	±0.8K	
2. Calibraton of potentiometer	systematic	0.0K	
3. Measurement by thermocouple	random	±1.0K	
From eqn. (Q-1), subtotal 1,2,3		±1.3K	±0.0037
4. Measurement of the height of fluid in capillary flowmeters (a) oxygen (b) sulfur dioxide	random random	±0.05cm ±0.05cm	±0.0005 ±0.0005
5. Calibration of capillary flowmeters (a) oxygen (b) sulfur dioxide	systematic systematic	$\pm1.5\%$ flowrate $\pm1.5\%$ flowrate	±0.0062 ±0.0062
From eqn. (Q-1), subtotal 1,2,3,4,5			±0.0095
6. Published thermodynamic data	systematic	$\Delta G^o_{4-1}=\pm180$ cal/mol	±0.054

From eqn. (Q-1), Total error $= \pm0.055$

Table 6-2

Error Analysis in Mole Fraction of SO_3 or $Na_2S_2O_7$

Source of Error	Type of Error	Magnitude of Error	Resultant Error in log X_{SO_3} or log $X_{Na_2S_2O_7}$
1. Thermobalance wt.	random	$\pm 0.0005g$	± 0.00044
2. Temperature and pressure (from Table 6-1)	random/systematic	± 0.0095 log P_{SO_3}	± 0.0014
3. Melt composition $CoSO_4$-Na_2SO_4	systematic	$\pm 0.001g$	± 0.00088
4. Impurities in chemicals	systematic		± 0.00056
5. Absorption of moisture	systematic	$+0.0008g$	± 0.00040

From eqn. (Q-1), subtotal 1,2,3,4,5 = ± 0.0018

6. Published Thermodynamic data on P_{SO_3} (from Table 6-1)	systematic	± 0.054 of log P_{SO_3}	± 0.0081

From eqn. (Q-1), Total error = ± 0.0083

Table 6-3

Error Analysis in activity of $Na_2O(l)$

Source of Error	Type of Error	Magnitude of Error	Resultant Error in log $a_{Na_2O(l)}$
1.Temperature:			
a.Measurement by thermocouple	random	$\pm1.0K$	
b.Temperature measurement by Isaac	systematic	$\pm1.0K$	
c.Calibration of thermocouple [94]	systematic	$\pm0.8K$	
2.Cell Potential:			
a.Cell EMF measurement	random	$\pm1.0mv$	
b.Cell EMF measurement by Isaac	systematic	$\pm0.079mv$	
3.Oxygen Pressure:			
a.Measurement of height of fluid in flowmeters			
(1) oxygen	random	$\pm0.05cm$	
(2) sulfur dioxide	random	$\pm0.05cm$	
b.Flowmeter calibration			
(1)oxygen	systematic	$\pm1.5\%$ flowrate	
(2)sulfur dioxide	systematic	$\pm1.5\%$ flowrate	
c.Temperature fluctuation	random	±0.00013 log P_{O_2}	
d.Thermodynamic data for O_2 calculation	systematic	±180 cal/mol of ΔG°_{4-1}	

From eqn. (S-2), subtotal 7,8,9,10,11 = ±0.013

Source of Error	Type of Error	Magnitude of Error	Resultant Error in log $a_{Na_2O(l)}$
4.Melt Composition:			
a.Melt composition of $CoSO_4$-Na_2SO_4	random	$\pm$ 0.0029 of m/o Na_2SO_4	±0.0075
b.Composition of reference melt [94]	random	±0.01 of m/o WO_3	±0.0013
c.Impurties in $CoSO_4$-Na_2SO_4	systematic		±0.0073
d.Absorption of moisture by $CoSO_4$	systematic	$+0.0008g$	±0.0075
e.Impurties in reference melt [94]	systematic	±0.0135 of m/o WO_3	±0.002

From eqn. (Q-1), subtotal 1,2,3,4 = ±0.018

Source of Error	Type of Error	Magnitude of Error	Resultant Error in log $a_{Na_2O(l)}$
5.Published thermodynamic data of reference melt	systematic		±0.914 at 1200K

From eqn. (Q-1), Total error = ±0.914

analysis. Table 6-3 illustrated errors occurred in activities of Na_2O in the electrochemical experiments. Detailed discussion on the error analyses are shown in Appendixes Q, R, and S.

In the thermogravimetric analysis, the random and systematic errors in the partial pressure of SO_3 and in the mole fraction of SO_3 or mole fraction of $Na_2S_2O_7$ are calculated. The total error in P_{SO_3} is ±0.055 in log P_{SO_3}; however, the errors due to the TGA experiment are only ±0.0095 in log P_{SO_3}. On the other hand, the total error in X_{SO_3} or $X_{Na_2S_2O_7}$ is determined to be ±0.0083 in log X_{SO_3} (or $X_{Na_2S_2O_7}$); nevertheless, the errors due to the TGA experiment are found to be ±0.0018 in log X_{SO_3} (or $X_{Na_2S_2O_7}$). This shows that the experimental measurements are highly accurate. The TGA experimental results can be improved only if the accuracies of the published thermodynamic data are upgraded. In fact, the random errors in the TGA experiments are small as it is shown in Figure 5.30 that two independent TGA experiments (TGA17 and TGA18) of Na_2SO_4 at 1160 K exhibit excellent agreements with each other.

In the electrochemical experiment, the same conclusions are drawn for the measurements of the activity of Na_2O. The total random and systematic errors in a_{Na_2O} are determined to be ±0.914 in log a_{Na_2O}. The systematic error caused by the uncertainties in the published thermodynamic data of the reference melt amounts to ±0.914 in log a_{Na_2O}, while the

errors contributed by the EMF experiment is only ± 0.018 in log a_{Na_2O}. Therefore, the error bar of the electrochemical measurements is only equal to ± 0.018 in log a_{Na_2O}, and most of the total error is caused by the uncertainties in the published thermodynamic data of the reference melt.

6.2 Solubility of Sulfur Trioxide in Sodium Sulfate

This section of discussion is divided into four subsections which will be presented in the following sequence: (1) sodium pyrosulfate – sodium sulfate system; (2) thermodynamic properties of sodium sulfate; (3) performance of fused silica solid electrolyte at basic conditions; and (4) kinetic study of sulfur trioxide solubility.

6.2.1 Sodium Pyrosulfate – Sodium Sulfate System

The absorption of SO_3 gas by sodium sulfate is considered to be the conversion of sodium sulfate to sodium pyrosulfate according to the reaction

$$Na_2SO_4(l) + SO_3(g) = Na_2S_2O_7(l) \tag{6-1}$$
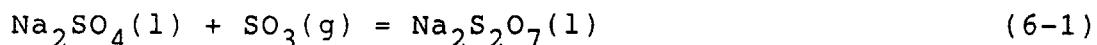
The SO_3 solubility results of this study have good agreements with those reported in the literature which includes Flood et al. [83], Coats et al. [84], and Kostin et

al. [85]. The results of Ingraham et al. [86] are discordant. The best relationship among all of the data is

$$\log K' = -(8.055\pm0.066) + (7946\pm53)/T \qquad (6-2)$$

The solution of $Na_2S_2O_7$ and Na_2SO_4 is determined that the activities of both species of the melt can be represented by their respective mole fractions in a dilution solution of $Na_2S_2O_7$ in Na_2SO_4, as the TGA results exhibit excellent comparisons with the solubility results calculated from an apparent equilibrium constant K' shown in Figure 5.3. In addition, all of the experimental data including those of Flood et al. [83], Coats et al. [84], and Kostin et al. [85] extrapolated to an isotherm of 1160 K by the Gibbs-Helmholtz equation is best correlated by a log K' value across the composition range at 1160 K (Figure 5.5). Therefore, the melt does not obey the regular solution models and it is analyzed to behave in such a way that the activities of the two components equal the mole fractions of the respective species.

The validity of extrapolating experimental data in the literature to an isotherm of 1160 K by means of the Gibbs-Helmholtz equation (5-8) is checked by the compressibility factor, Z, of the SO_3 gas. Based on the critical properties of SO_3: critical temperature $T_c = 491$ K and critical pressure $P_c = 83$ atm, the compressibility factor Z can be obtained from a generalized compressibility

chart [112] after the reduced pressure, $P_r = P/P_c$, and the reduced temperature, $T_r = T/T_c$ are evaluated. The Z factors are found to be approximately one at the experimental conditions listed in the literature and at the extrapolated conditions at 1160 K. The SO_3 gas is virtually an ideal gas at all of the conditions under considerations in this study. It is therefore evident that the extrapolation by the Gibbs-Helmholtz equation is valid.

A complete phase diagram of the $Na_2S_2O_7$-Na_2SO_4 binary system has been estimated and is shown in Figure 5.8. The liquidus line on the Na_2SO_4 side is determined by the molar Gibbs free energy of melting taken from the JANAF Tables [104] at temperatures above 900 K (627°C); below this temperature, the liquid phase boundary is extrapolated to the liquidus line of the partial phase diagram reported by Coats et al. [84]. If the molar Gibbs free energy of melting of Na_2SO_4 taken from the JANAF Tables [104] were employed down to 670 K (397°C), the liquidus line would have intersect the $Na_2S_2O_7$ + β region at $X_{Na_2SO_4}$ = 0.15. Nevertheless, the intersection was reported by Coats et al. [84] to be located at $X_{Na_2SO_4}$ = 0.052. The discrepancy could be caused by an uncertainty in the molar Gibbs free energy of melting as much as 1,000 cal reported by the JANAF tables [104] shown in Figure 5.6. The glass transition of $Na_2SO_4(l)$ at 800 K has little effect on the Gibbs free energy of melting due to the change in the enthalpy of melting listed in Table 5-1. This phase transformation can only account for 44 cal at 600 K. The partial phase diagram

reported by Coats et al. [84] is believed to be a good representation of the phases at mole fractions of Na_2SO_4 less than 0.11 and at temperatures below 743 K (470°C).

The isoactivity lines of SO_3 calculated under the ideal solution model have excellent agreements with the data reported by Coats et al. [84] at log P_{SO_3} = -2.2 depicted in Figure 5.7.

Coats et al. [84] have reported four phase fields in the $Na_2S_2O_7-Na_2SO_4$ system: liquid; liquid+$Na_2S_2O_7$(s); liquid+Na_2SO_4; and $Na_2S_2O_7$(s)+Na_2SO_4(s). One more phase field, β phase, is proposed in this study to maintain the equilibrium phase diagram compatible to the behavior of the SO_3 isobars, because the SO_3 isobars at log P_{SO_3} < 0.5 intersect the liquidus line two times. The β phase is estimated to have a maximum solubility of $Na_2S_2O_7$(s) in Na_2SO_4(s) at mole fraction of Na_2SO_4 = 0.9846 at the eutectic temperature of 396.8°C. The isoactivity lines of SO_3 in the β phase are governed by the Gibbs-Helmholtz equation. Thus, a maximum of partial pressure of SO_3 exists at approximately 800°C in the liquid+β phase region.

The stability diagram in Figure 5.11 showing the stable fields of $Na_2S_2O_7$(s), Na_2SO_4(s), and liquid in terms of temperature and partial pressure of SO_3 has the most practical engineering applications to predict and prevent the occurance of hot corrosion, since accelerated attacks only happen if a liquid phase of the molten salt is present. The diagram can readily provide information on whether a

liquid exists at a certain operating condition. The stability diagram has excellent agreements with the data reported by Coats et al. [84].

The solubility of SO_3 in Na_2SO_4 to form $Na_2S_2O_7$ is found to be small. The maximum solubility measured in this study is determined to be 0.00653 mole fraction of $Na_2S_2O_7$ under a SO_3 pressure of 0.1158 atm at 1160 K. It is evident that the compound Na_2SO_4 is relatively stable, and there is a limited compositional change in the presence of SO_3 gas. This agrees very well with the experimental results of Yurek and Deeter [90] that molten sodium sulfate remains virtually stoichiometric under P_{SO_3} ranging from 10^{-9} to 10^{-1} at 1200 K and 1250 K. This can be attributed to the fact that sodium pyrosulfate is not stable at moderate pressures of SO_3 gas. It has been determined from the tangents to the integral Gibbs free energy curve at $Na_2S_2O_7$ and Na_2SO_4 (Figure 5.16) that the equilibrium pressure of SO_3 over pure sodium pyrosulfate is equal to 15,837 atm. at 1160 K. On the other hand, it is found that the equilibrium partial pressure of SO_3 gas over the sodium sulfate at the stoichiometric composition is 5.6×10^{-6} atm at 1160 K.

The integral Gibbs free energy across the composition range between $Na_2S_2O_7$ and Na_2SO_4 has been fully determined by the analytical and numerical methods. The TGA data at 1160 K and 1200 K are shown to have excellent agreements with the theoretical G^M curve in Figures 5.12 and 5.13, respectively.

6.2.2 Thermodynamic Properties Of Sodium Sulfate

The validity of the measurements by the electrochemical cell of fused silica solid electrolyte is tested by comparing the thermodynamic properties of sodium sulfate reported by other investigators. Electrochemical measurements are taken by either varying partial pressure of SO_3 or temperature.

The thermodynamic relationships between $\log a_{Na_2O(l)}$ and $\log P_{SO_3}$ are determined with a platinum crucible. A slope of -1 is found in Figure 5.18 to agree with the theoretical equation (5-43) at 1160 K, 1200 K, 1224 K, and 1250 K. These results represent the sole properties of sodium sulfate in relation to the gaseous SO_3, because an inert crucible is employed. The activity of sodium oxide in molten pure sodium sulfate is therefore established to be a function of partial pressure of SO_3 in the gas phase at a constant temperature. At 1200 K, the log K for the reaction of (5-39) is found to be -17.187; while a value of -17.02 is obtained from the JANAF Tables [104] listed in Appendix T. The electrochemical results of this study therefore have a good agreement with the JANAF Table [104]. The Gibbs free energy for the reaction $Na_2O(l) + SO_3(g) = Na_2SO_4(l)$ is

$$\Delta G^{\circ}_{5-39} = -(120,080 \pm 686) + (21.39 \pm 0.57) \ T \ [cal/mol] \quad (6-3)$$

The thermodynamic properties of sodium sulfate at various temperatures are expressed in terms of the Gibbs free energy of formation of liquid sodium sulfate, $\Delta G_f^o(Na_2SO_4(l))$, both in Figures 5.21 and 5.23 for platinum and alumina crucibles, respectively. The electrochemical results obtained in platinum crucibles and alumina crucibles are in good agreement with the results of Liang & Elliott [66], Mittal [88], and the JANAF Tables [104], although the activity of Na_2O in the alumina crucibles (Figure 5.22) are more scattered than those in the platinum crucibles (Figure 5.20). The difference in the two studies is mainly a result of a slow reaction between sodium sulfate and aluminum oxide to form aluminum sulfate.

The free energies of formation of sodium sulfate are noted to have good agreements among the various sources in Table 5-3. The JANAF Tables [104] depict a better agreement with the results of this study than those of Liang & Elliott [66]. The maximum difference in $\Delta G_f^o(Na_2SO_4(l))$ between the results of this study and those of the JANAF Tables [104] is less than 3 Kilocalories at temperatures between 1160 K and 1260 K. Improved agreements are found at lower temperatures in the temperature range. The results from this study exhibit excellent agreements with those of Mittal [88] who performed EMF measurements with the same type of electrochemical cell in a platinum crucible. Thus, the EMF measurements of this study with the solid electrolyte of fused silica and the computerized data acquisition system are valid and reliable.

6.2.3 Performance of Fused Silica Solid Electrolyte at Basic Conditions

Additions of granular sodium peroxide to molten sodium sulfate under an atmosphere of oxygen have shown to increase instantaneously the activity of sodium oxide in sodium sulfate contained both in platinum and in alumina crucibles. However, Figures 5.24 to 5.26 show that a single equilibrium activity of sodium oxide in sodium sulfate is always maintained regardless of how the activity of sodium oxide is displaced under a stream of oxygen. The equilibrium values of $\log a_{Na_2O}$ at 1200 K recorded in platinum crucibles and in alumina crucibles are -12.25 and -11.19, respectively.

The activity of Na_2O has been demonstrated to be a function of the partial pressure of SO_3 in pure sodium sulfate in accordance with reaction (5-39). With reference to the Gibbs phase rule for the pseudo-binary system of Na_2O-SO_3 with two components and two phases, there are two degrees of freedom which may be selected among temperature, activity of Na_2O, and pressure of SO_3. The activity of Na_2O increases with a decrease in the pressure of SO_3. Under a stream of pure oxygen atmosphere, the activity of Na_2O is supposed to keep increasing due to the low partial pressure of SO_3 in the gas phase. The activity of Na_2O is also supposed to increase with an increase in the concentration of Na_2O from Na_2O_2 additions. Because of a single equilibrium cell potential is recorded in spite of efforts to increase the activity of Na_2O, the activity of sodium

oxide is not controlled by the pressure of SO_3 according to the equilibrium (5-39) at high a_{Na_2O} conditions. It is also important to note that the solid electrolyte of fused silica and the alumina crucible may not be inert in the presence of molten sodium sulfate at certain a_{Na_2O} conditions.

Based on the thermodynamic properties of Na_2O-SiO_2 melts at 1273 K to 1373 K measured with beta-alumina solid electrolyte by Neudorf and Elliott [106] and the phase diagram of Na_2O-SiO_2 reported by Kracek [107], the activity of Na_2O is extrapolated to the liquidus in satuation with either solid quartz or tridymite. The phase stability diagram of quartz/tridymite is shown in Figure 6.1. The liquidus line in the diagram seperates a homogeneous liquid phase from a two-phase of liquid plus solid quartz/tridymite. At activities of Na_2O above the liquidus line, silica will dissolved or become unstable; on the contrary, silica remains intact at conditions below the line. The attack of the electrolyte by the melts containing Na_2O is a result of the reaction

$$[Na_2O] + XSiO_2(s) = [Na_2O \cdot XSiO_2] \qquad (6-4)$$
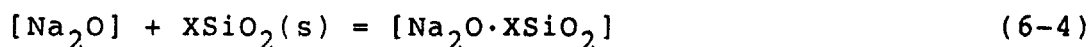
The log a_{Na_2O} on the liquidus in saturation with solid quartz/tridymite is found to be -10.7 at 1200 K from Figure 6.1. Mittal and Elliott [78] also estimated the stability of fused silica based on the measurements by Neudorf and Elliott [106] of Na_2O-SiO_2 binary system; nevertheless,
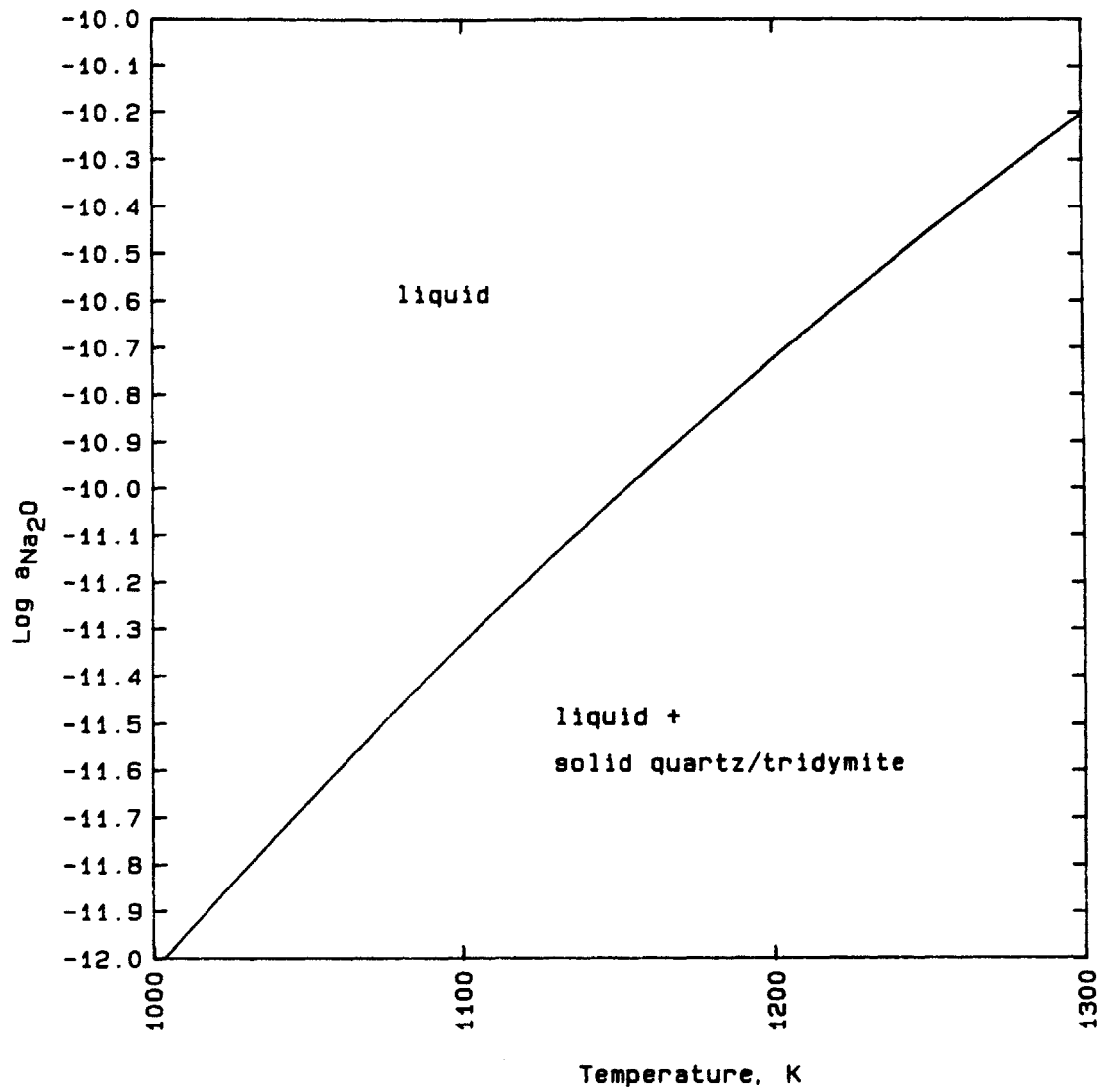
Figure 6.1 - Phase stability diagram of quartz/tridymite
[106].

their stability curve lies below that in Figure 6.1. The log a_{Na_2O} on the liquidus in saturation with solid quartz/tridymite is estimated by Mittal and Elliott [78] to be -11.2 at 1200 K. For the EMF measurements at 1200 K with platinum crucibles, the equilibrium log a_{Na_2O} stays at -12.25 which indicates experimentally the limit on the activity of Na_2O for intact silica, although the limit does not match very well with the two estimations based on the measurements with beta-alumina solid electrolyte by Neudorf and Elliott [106]. The difference in the values of activity of sodium oxide at the stability limit of silica might be caused by the intrinsic errors in measurements by two distinct solid electrolytes, as different thermodynamic properties of sodium sulfate have been reported by EMF measurements with beta-alumina and fused silica solid electroytes shown in Figure 5.21. Within experimental errors, the constant cell potential at high sodium oxide activity is therefore determined to be controlled by the stability of clear fused silica solid electrolyte in the Na_2SO_4 melt.

The EMF experimental results in alumina crucibles shown in Figures 5.25 and 5.26 at 1200 K demonstrate that Al_2O_3 does dissolve in liquid sodium sulfate; 103 ppm dissolved aluminum is detected after 12.5 hours of equilibration under 0.00225 atm of SO_3. When the gas input is switched to pure oxygen, the cell potential decreases (or the activity of Na_2O increases) simultaneously with the concentration of dissolved aluminum. The equilibrium activity of Na_2O always

- 240 -

maintains at log a_{Na_2O} = -11.19 regardless of how the EMF cell is disturbed, while the concentration of dissolved aluminum falls to a very low level of 0.25 ppm or log $C_{Al,ppm}$ = -0.587 at 1200 K. Because of a single equilibrium cell potential is again recorded in spite of efforts to increase the activity of Na_2O, the activity of sodium oxide is not controlled by the equilibrium (5-39) at high a_{Na_2O} conditions.

A similar explanation may also apply to the equilibration of sodium sulfate at 1200 K under a stream of oxygen in alumina crucibles. The silica solid electrolyte and the alumina crucible may be involved in reactions with molten sodium sulfate, the ternary system of Na_2O-Al_2O_3-SiO_2 is thus under considerations. DeYoung [94] reported the activity of Na_2O in the liquid phase of the Na_2O-Al_2O_3-SiO_2 system at 1323 K in Figure 6.2. The log activity of Na_2O on the liquidus line in saturation with tridymite at 1323 K varies from -10.7 at 0 m/o Al_2O_3 to -13.5 at 8 m/o Al_2O_3. DeYoung [94] also determined that the activity of Na_2O decreases with a decrease in temperature at a constant composition; thus, the log activities of Na_2O on the liquidus at 1200 K is slightly lower than those reported at 1323 K. Because the concentration of dissolved aluminum is determined to be very small at the final equilibrium potential in Figure 5.27, the equilibrium EMF corresponds to a melt composition located on the liquidus line close to the pseudo-binary of Na_2O-SiO_2. Therefore, a slightly smaller value of log a_{Na_2O} = -10.7 based on the data of DeYoung [94]
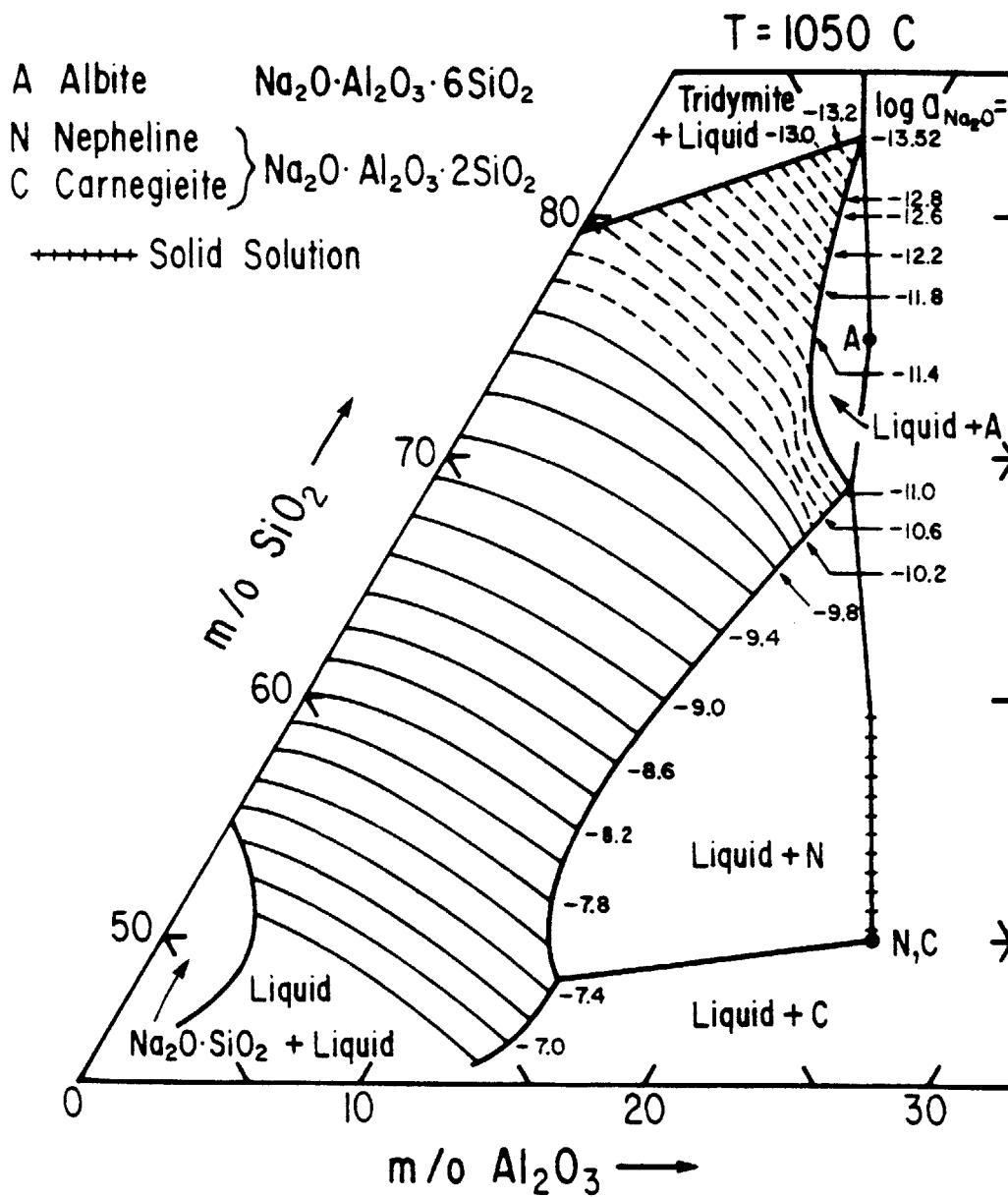
Figure 6.2 – Isoactivity lines of sodium oxide in $Na_2O-Al_2O_3-SiO_2$ system at 1050°C [94].

has a good agreement with the value of log a_{Na_2O} = -11.19 found experimentally in alumina crucibles. The stability of the fused silica solid electrolyte again governs the highest activity of Na_2O which can be maintained in the electrochemical cell.

6.2.4 Kinetic Study of Sulfur Trioxide Solubility

In view of the good correlations of TGA experimental data to the equation (5-67), low activation enthalpies (6.7 Kcal for SO_3 absorption and 20.8 Kcal for SO_3 desorption), and reasonable liquid boundary layer thickness ranging from 1.52×10^{-3} cm to 6.29×10^{-3} cm, the model of liquid phase mass transfer control is most likely to be the rate determining step in the absorption and desorption of SO_3 gas in and from liquid Na_2SO_4.

6.3 Solubility of Alumina in Sodium Sulfate

This section will be presented in three subsections: (1) Discussions and comparisons of the two results of equilibrium solubility of Al_2O_3 solid in sodium sulfate at 1200 K obtained from the TGA and EMF experiments with results of other investigators; (2) Kinetics of alumina dissolution in sodium sulfate in reference to the cell equilibration; (3) Effects of dissolved aluminum on the thermodynamic properties of sodium sulfate.

6.3.1 Equilibrium Alumina Solubility

The TGA and EMF results of the equilibrium solubility of alumina in molten sodium sulfate at 1200 K are compared in Figure 6.3. The two experimental results are slightly discordant. It is evident that higher solubility of alumina in sodium sulfate is reported by the EMF experiments in the range of partial pressure of SO_3 employed by the TGA experiments. In the plot of log C_{Al},ppm versus log P_{SO_3}, the EMF solubility results possess a slope of 3/2 while the TGA result exhibits a slope of 0.8849. The slope of 3/2 implies that the dissolution of alumina by acidic fluxing obeys the Temkin ideal ionic solution model. The same solution behavior in acidic fluxing was also observed by Stroud & Rapp [39] and Jose, Gupta, & Rapp [45].

The discrepancies between the two experimental results lie probably on the facts that (1) the reaction between alumina and sodium sulfate is very slow. Long time of equilibration is thus required to reach true equilibrium. (2) Difficulties in determining whether equilibrium is reached in the TGA experiment. Limited amount of sodium sulfate, 2 grams, is employed in the TGA experiments. Small weight change occuring in a very slow pace may cause errors in determining whether equilibrium is attained. (3) There are limitations on the thermobalance. The detection level in weight change by the thermobalance is limited by the sensitivity of the thermbalance of ± 0.1 mg. Therefore, as equilibrium is approached slowly, small change weight may
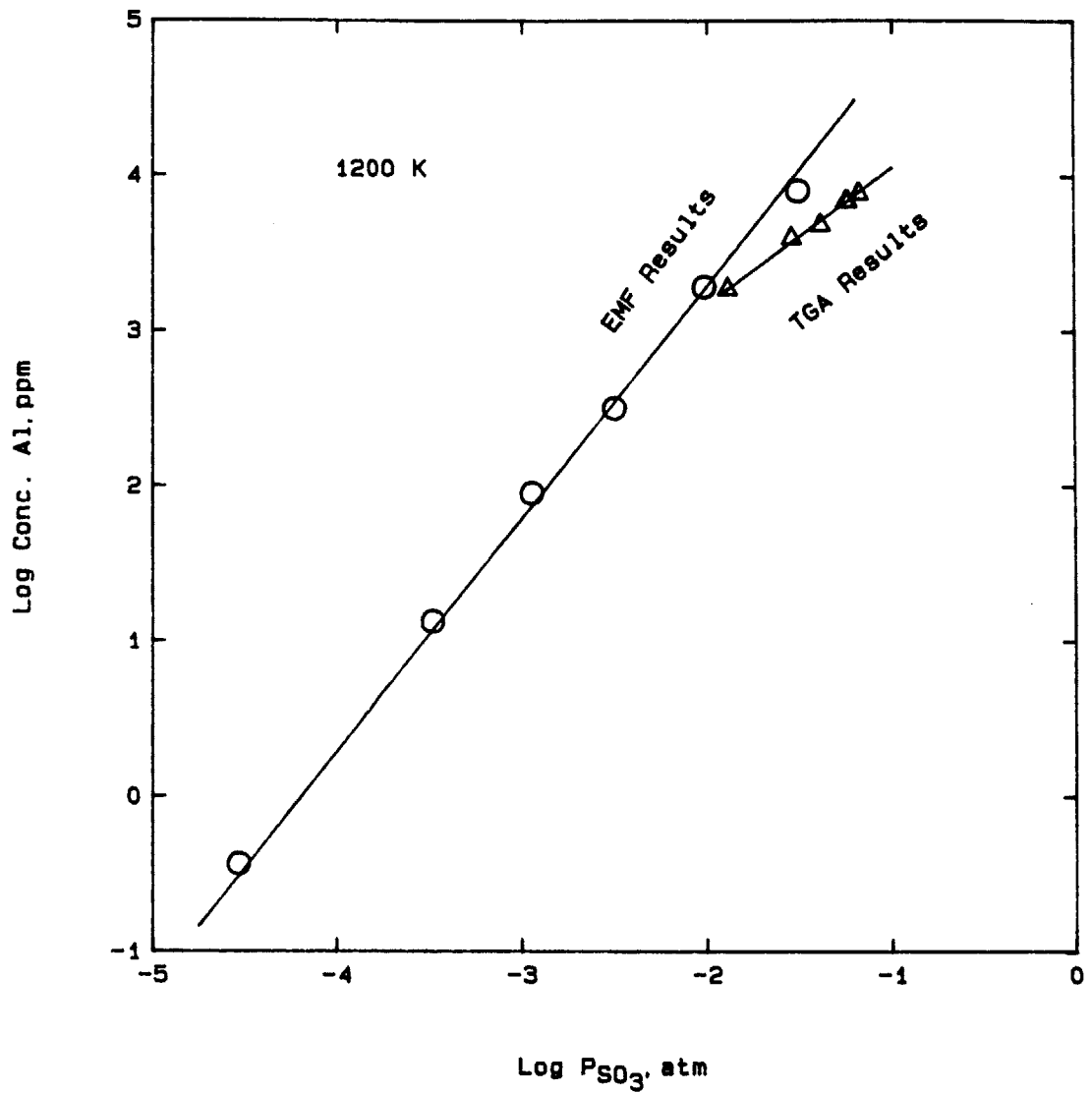
Figure 6.3 - Comparison of alumina solubility in sodium sulfate obtained from TGA and EMF experiments at 1200 K.

not be displayed by the TGA chart recorder. It has been confirmed by a TGA experiment that the thermobalance is not able to detect any weight change of 2 grams of sodium sulfate exposed to low partial pressure of SO_3 in the range of 6.78×10^{-5} atm to 7.83×10^{-4} atm. Whereas, samples taken from the EMF experiment under a partial pressure of SO_3 of 2.93×10^{-5} atm are determined to consist of 0.37 ppm of dissolved aluminum. On the other hand, the EMF solubility results are direct measurements of the aluminum concentration in samples taken from the melt. Chemical analysis by the DC plasma arc elemental emission spectrometer is very sensitive at low concentrations. The detection limit of the spectrometer is 0.002 mg Al per liter of solution. As a consequence, the Al_2O_3 solubility obtained from EMF experiments represent measurements with higher level of accuracy and reliability.

The Al_2O_3 solubility in molten sodium sulfate has been measured by several groups of researchers; however, the activity of Na_2O is not reported in the same basis. The activity of Na_2O is controlled by the partial pressure of SO_3 in accordance with the reaction

$$Na_2O(l) + SO_3(g) = Na_2SO_4(l) \qquad\qquad (6-5)$$
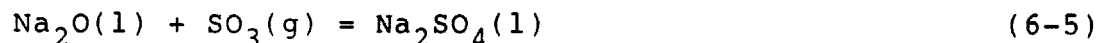
For unit activity of $Na_2SO_4(l)$, the relationships between activity of $Na_2O(l)$ and partial pressure of SO_3 at 1200 K pertaining to various studies are as follows:

This study: log K = -17.187   (6-6)

Liang & Elliott [66]: log K = -17.51   (6-7)

JANAF [108]:   log K = -17.02   (6-8)

Elliott, Yurek, McNallan, and Minh [40] did not have direct measurements of the activity of Na_2O in molten Na_2SO_4. Their Al_2O_3 solubility results were reported in terms of partial pressures of SO_3, the relationship derived from the JANAF Tables [104] in equation (6-8) is thus assumed to be appropriate. Nevertheless, measurements of Stroud and Rapp [39] and Jose, Gupta, and Rapp [45] are in terms of the activity of solid Na_2O according to the equilibrium:

$$Na_2SO_4(l) = Na_2O(s) + SO_2(g) + 1/2\ O_2(g) \qquad (6-9)$$
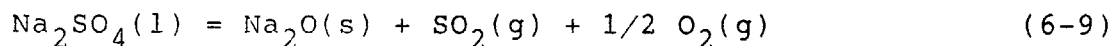
the equilibrium constant at 1200 K based on the data of the JANAF Tables [104] is log K = -16.11. With reference to the electrochemical measurements of this study with platinum crucibles, the Al_2O_3 solubilities results of other studies are shifted accordingly for comparison. The measurements of log a_{Na_2O} of Liang et al. [66], Elliott et al. [40], Stroud et al. [39], and Jose et al. [45] are adjusted by adding +0.323, -0.167, -1.077, and -1.077, respectively.

The Al_2O_3 solubility results of this study at 1200 K are compared with four other studies. In the first study, Elliott, Yurek, McNallan, and Minh [40] employed 14 grams of 120 mesh granular alumina and a rotating alumina rod to react with molten Na_2SO_4 contained in a platinum crucible.

The whole assembly was exposed to a controlled partial pressure of SO_3. Solubility data were obtained by chemical analysis of samples taken from the melt at 1200 K. Their measurements are compared with those of this study in Figure 6.4. Their data at 1200 K are depicted by the linear relation

$$\log C_{Al}, ppm = 4.724 + 0.818 \log P_{SO_3} \qquad (6-10)$$

or

$$\log C_{Al}, ppm = -9.198 - 0.818 \log a_{Na_2O(l)} \qquad (6-11)$$

An excellent agreement is found between the TGA solubility results and those of Elliott et al. [40] at 1200 K, although a slightly higher solubility measurements are reported by the TGA experiments. Both studies have a similar slope of 0.8 in Figure 6.4. Nevertheless, disagreements exist between the EMF solubility results and those of Elliott et al. [40]. The EMF solubility results exhibit a slope of 3/2 which is in agreement with the Temkin solution model of random ionic species. The disagreements with the EMF results might be attributed to the use of fine (120 mesh) granular alumina and the lack of equilibrium state in their experiments. In general, the measurements of Elliott et al. [40] and the two results of this study have reasonable agreements with each other.
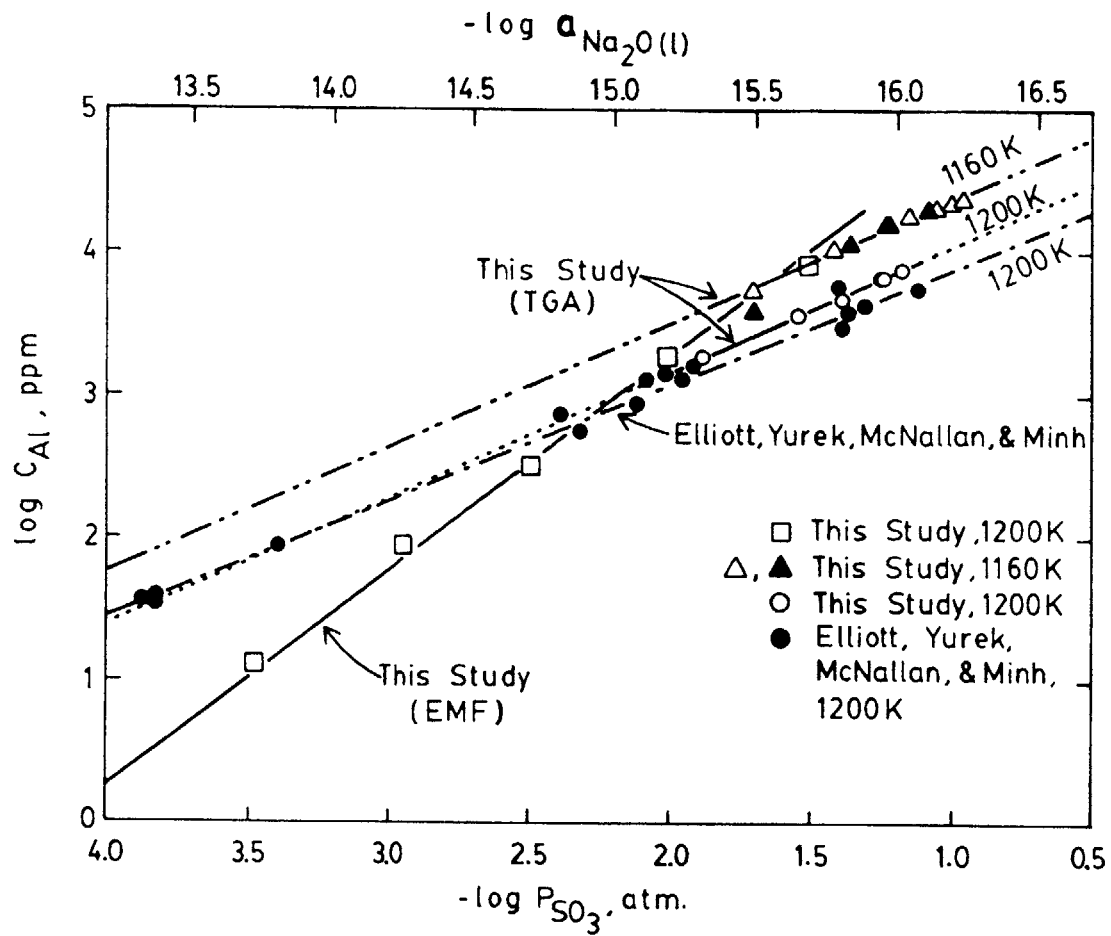
Figure 6.4 - Comparison of alumina solubility in sodium sulfate with results of Elliott et al.[40] at 1200 K.

In the second study, Stroud and Rapp [39] reported in 1978 a set of Al_2O_3 solubility both at the basic and acidic conditions at 1200 K in Figure 6.5. An electrochemical cell with mullite as the solid electrolyte was used to measure the activity of sodium oxide in sodium sulfate. Atomic absorption techniques were employed to determine the concentration of dissolved aluminum. The basicity of the melt was changed by adding either Na_2O_2 or $Na_2S_2O_7$. Their data agreed well with the behavior of an ideal ionic solution in such a way that the slope of data in acidic region and that in basic region were respectively 3/2 and -1/2 in a plot of log C_{Al},ppm versus -log a_{Na_2O}. The boundary between the basic and acidic dissolutions or the mininum in Al_2O_3 solubility was determined to be log a_{Na_2O} = -9.38 (or -8.3 in their scale). The acidic solubility results of Stroud and Rapp [39] are higher than those of this study by about one order of magnitude.

In the third study, Jose, Gupta, and Rapp [45] published a new set of Al_2O_3 solubility data in 1985 and declared that their previous study [39] was incorrect because of a reaction between Na_2SO_4 and the platinum electrode in the Na_2SO_4 melts. Their new results again consisted of a whole spectrum solubility data ranging from basic to acidic conditions with a slope of 3/2 on acidic regions and -1/2 on basic regions in a plot of log C_{Al},ppm versus -log a_{Na_2O}. The boundary between basic and acidic dissolutions was determined to be log a_{Na_2O} = -16.5 (or -15.4 on their scale) whereas the value of their previous

- 250 -
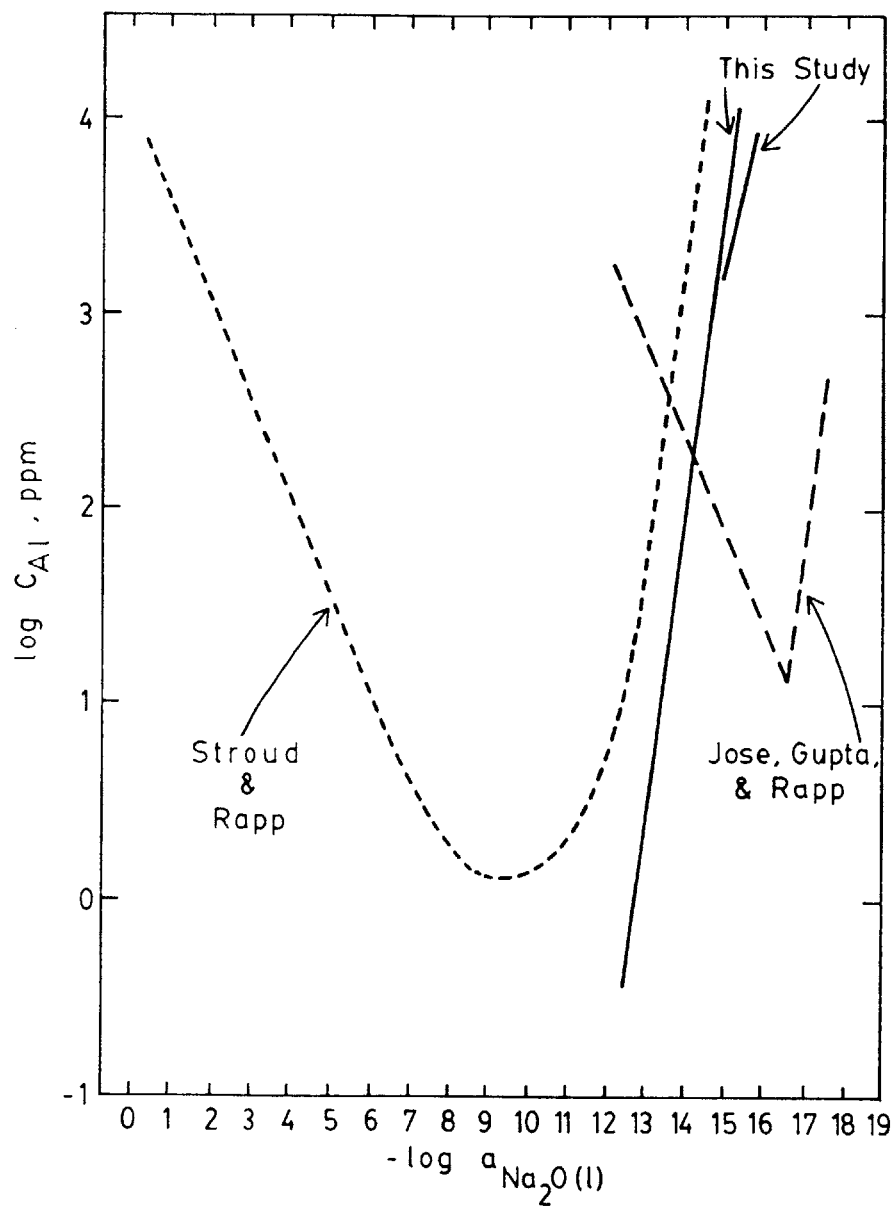
Figure 6.5 – Comparison of alumina solubility in sodium sulfate with results of Stroud and Rapp [39] and Jose, Gupta, and Rapp [45] at 1200 K.

study [39] was log a_{Na_2O} = -9.38 (-8.3 on their scale).
Their new data are displaced up and to the right from their
old results. The two results completely disagree with each
other in both measurements of aluminum concentration and
activities of sodium oxide.

In comparison between the solubility data of Jose et
al. [45] and the results of this study, a lot of
disagreements are noted. The acidic Al_2O_3 solubility
results of Jose et al. [45] are much less than those of this
study by more than 4 orders of magnitude at a given activity
of Na_2O. The disagreements are so serious that basic
dissolutions of alumina are reported by Jose et al. [45] in
the range acidic dissolution of alumina measured in this
study. The minimum in Al_2O_3 solubility claimed by Jose et
al. [45] corresponds to a very high Al_2O_3 solubility
measured both by the EMF and TGA experiments. The results
of Jose, Gupta, and Rapp [45] therefore have absolutely no
agreement with the results of this study.

The lack of agreement in the results of Jose et al.
[45] may be possibly caused by faulty EMF measurements on
the activity of Na_2O. Their electrochemical cell was a
complicated one consisted of a mullite electrolyte served as
a sodium probe and a CaO partially stablized zirconia
electrode served as a oxygen probe. Elliott [82] once
commented after observing electrochemical results from other
studies using mullite electrolyte that the use of the
electrochemical cell in studying the effects of additions of

oxides to the sodium sulfate is complicated by possible reactions with the mullite. As a matter of fact, Gupta and Rapp [41] who performed similar experiments with the same apparatus in molten sodium sulfate admitted that their cell EMF values exhibited a slight shift with time, presumably resulting from a slight attack of the mullite, zirconia, and alumina refractories. Consequently, their measurements on the activity of sodium oxide might be questionable.

On the contrary, during the TGA experiments of this study, molten sodium sulfate is only in contact with alumina while absorption or desorption of SO_3 is taken place. No chemical reaction with materials other than alumina is possible. The maximum weight increase of the sample has been tested to correspond to the calculated maximum partial pressure of SO_3; hence, internal equilibrium of the reaction gases is ensured. The measurements of partial pressures of SO_3 from the SO_2 and O_2 gas flowrates are properly justified. During the EMF experiments, sodium sulfate is in contact with an alumina crucible, alumina tablets, a platinum electrode, and a fused quartz solid electrode only. The platinum wire is found to remain inert in all EMF experiments of this study which are conducted at $\log a_{Na_2O}$ less than -11. Liang [108] reported that platinum is attacked by sodium sulfate to form sodium platinate, Na_2PtO_3, only if $\log a_{Na_2O}$ is higher than about -6. The solid electrolyte is determined to remain intact after the experiments. It has shown in section 6.2.3 that the EMF cell is operated in the SiO_2 stable region during Al_2O_3

solubility measurements. The Al_2O_3 solubility should not be affected by the presence of fused silica. The accuracy of our measurements is therefore firmly established.

In the fourth study, Liang [108] reported a few values on the solubility of alumina in Na_2SO_4 at 1200 K. Jose, Gupta, and Rapp [45] compared one solubility datum of Liang and Elliott [66] which showed a good agreement with their basic data at $\log a_{Na_2O(s)}$ = -14.57 (or -13.5 in Jose's scale). Nevertheless, none of the Al_2O_3 solubility data is presented in the report by Liang and Elliott [66]. All of the basic solubility data of Liang [108] were equilibrated under a SO_3 atmosphere of $\log P_{SO_3}$ = -8.779 which is equivalent to $\log a_{Na_2O}$ = -8.4 (or -8.73 in Liang's scale) Thus, the basic data of Liang [108] does not agree with those basic results of Jose et al. [45]. Jose et al. [45] probably compared the acidic dissolution data of Liang's sample 36-A [108] with their basic data and found that they agree with each other.

The acidic solubility data of Liang [108] were compared with the results of this study in Figure 6.6. The results from this study indicated reasonable agreements with the two acidic values (sample 36-A and sample 41-A) reported by Liang [108].

Liang [108] demonstrated that a base-acid titration curve was noted when basic oxide of Na_2O was added to Na_2SO_4 equilibrated under acidic atmospheres of $\log P_{SO_3}$ = -3.162 and -4.360 at 1200 K. An inflection point at $\log a_{Na_2O}$ =
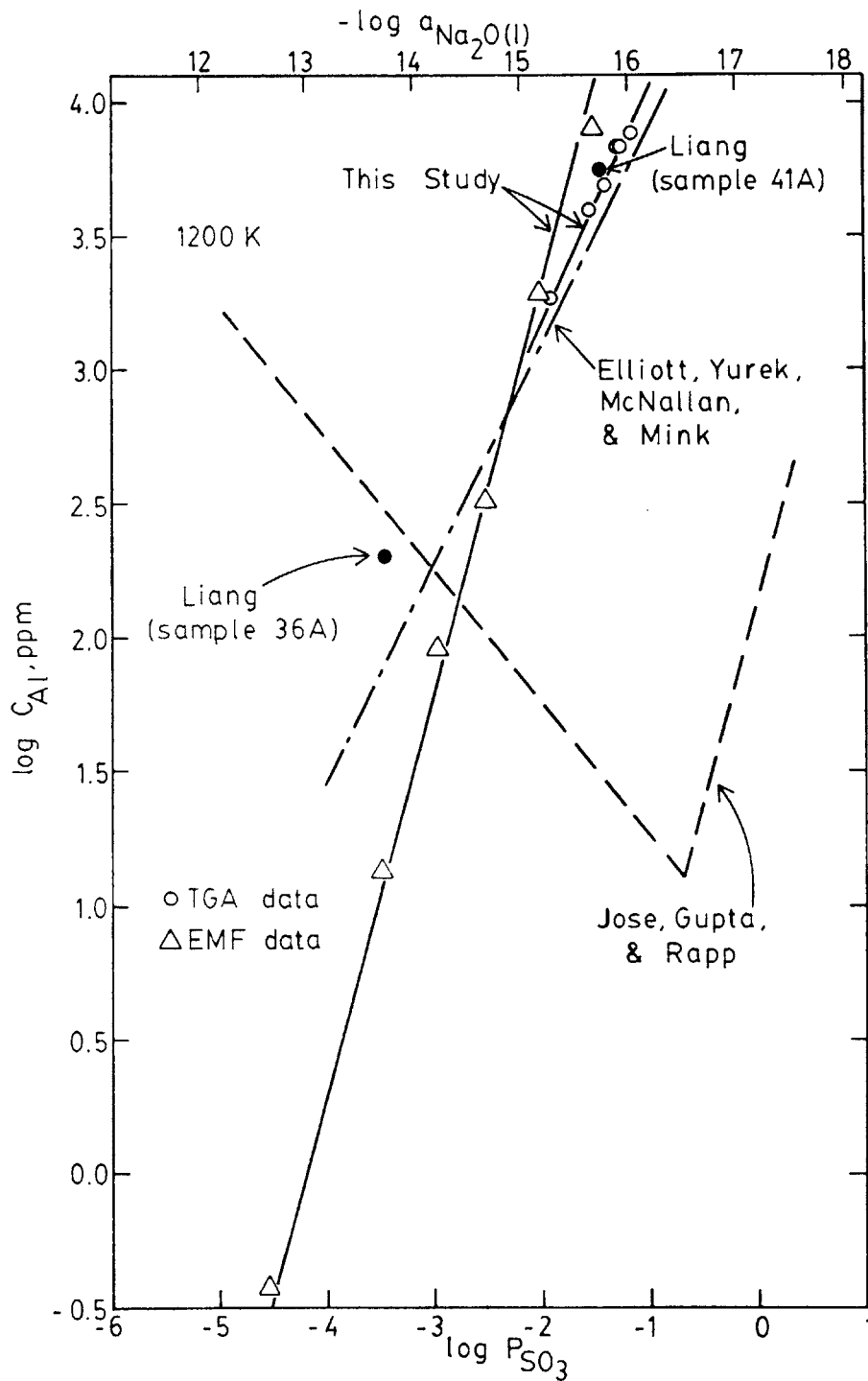
Figure 6.6 – Comparison of alumina solubility in sodium sulfate with other recent results at 1200 K.

-11.7 (or -12.09 in Liang's scale) is recorded to correspond to the neutralization of sodium aluminate. It is therefore infered that the boundary between basic and acidic dissolution of alumina is located at log a_{Na_2O} = -11.7 or log P_{SO_3} = -5.48.

The minimum of Al_2O_3 solubility is estimated from this study to be about log a_{Na_2O} = -12, although measurements on basic Al_2O_3 dissolution is not feasible with the fused silica cell. This result agrees very well with the titration result of Liang [108]. Nevertheless, Jose et al. reported the minimum of Al_2O_3 solubility at log a_{Na_2O} = -16.5 (or -15.4 in Jose's scale).

According to the stability diagram of Al-Na-O-S and Na-O-S systems at 1200 K (Figure 6.7) calculated from the thermodynamic data of the JANAF Tables [104] listed in Appendix T, the boundary between basic and acidic Al_2O_3 dissolutions is supposed to locate in the middle of the stable region of Al_2O_3(s) where log $a_{Na_2O(l)}$ = -13.41. Thus, the boundary reported by Liang [108] and that inferred from the stability diagram agree reasonably well with our solubility results.
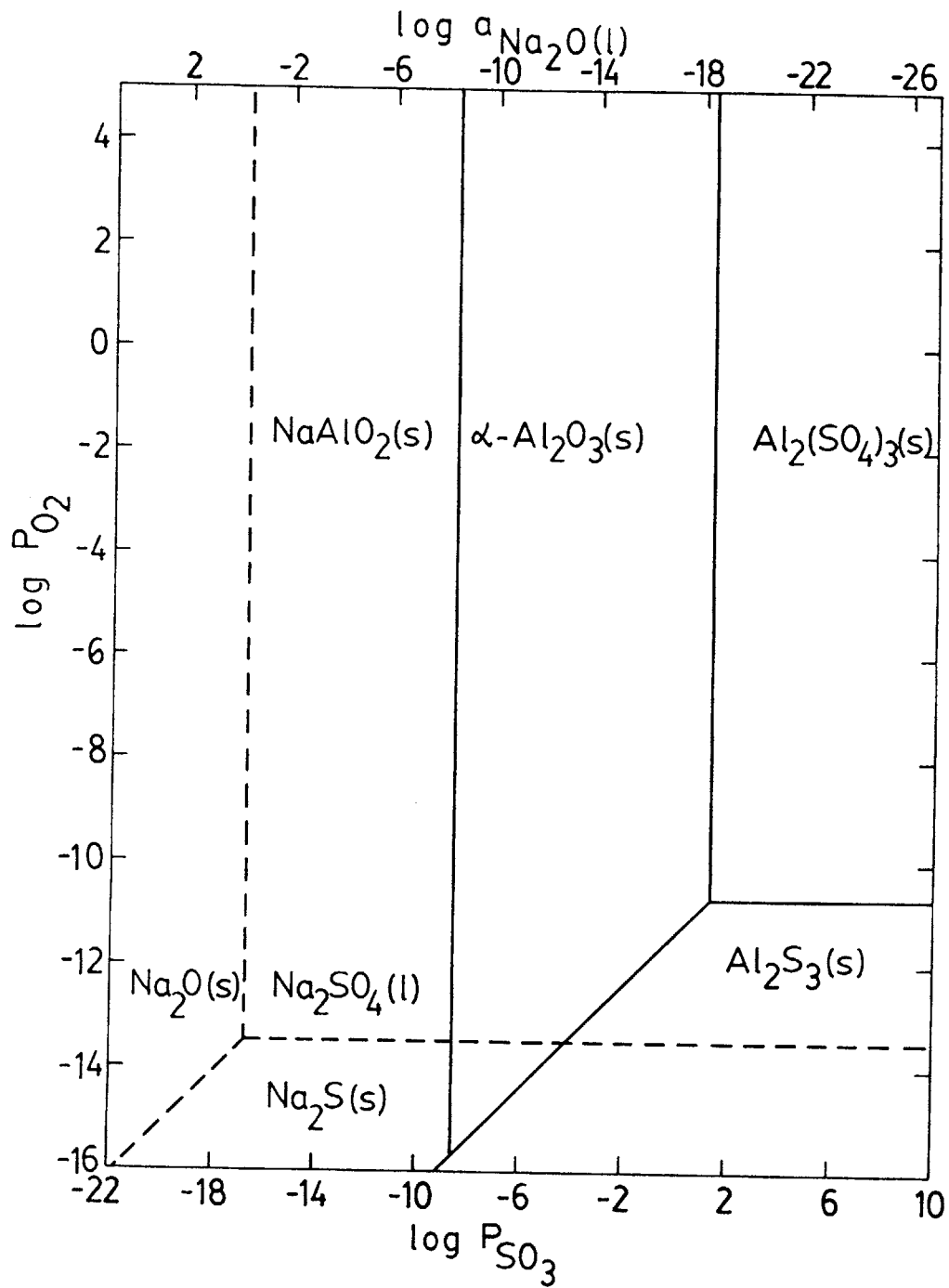
Figure 6.7 - Stability diagram of Al-Na-O-S and Na-O-S
system at 1200 K.

6.3.2 Kinetic Study of Alumina Solubility

The difference between the time to achieve equilibrium cell potentials and that to reach equilibrium concentration of aluminum in the sodium sulfate is tremendous. The time period for the former case is in the order of less than one hour; whereas, the latter case takes at least 88 hours. The cell potential reaches equilibrium at a much faster pace than the alumina achieves equilibrium with the sodium sulfate.

It is also noted during the TGA experiments with Na_2SO_4 that a much longer time is required to equilibrate with an alumina crucible than with a platinum crucible at 1200 K. The equilibration time with a platinum crucible is in the order of 40 minutes, while that with an alumina crucible is in the order of 80 hours.

The kinetics of SO_3 absorption/desorption in/from molten Na_2SO_4 is determined to be controlled by mass transfer across a liquid boundary layer. This process which is the slowest step takes less than one hour to reach equilibrium once a different partial pressure of SO_3 is imposed on the melt at 1200 K. With the presence of alumina equilibrated under a similar experimental condition, the equilibration time is increased more than 100 times. It is therefore evident that the steps of absorption of SO_3 gas and transport of dissolved SO_3 in molten Na_2SO_4 are not the limiting steps. The controlling step is the chemical reaction between dissolved SO_3 and solid Al_2O_3 to form

$Al_2(SO_4)_3$ or the chemical reaction between $Na_2S_2O_7$ and solid Al_2O_3 to form $Al_2(SO_4)_3$.

It is apparent with the employment of an alumina crucible that once a different partial pressure of SO_3 is imposed on the molten Na_2SO_4, the SO_3 gas reacts readily with the sodium sulfate to form sodium pyrosulfate in accordance with the reaction

$$Na_2SO_4(l) + SO_3(g) = Na_2S_2O_7(l) \qquad (6-12)$$
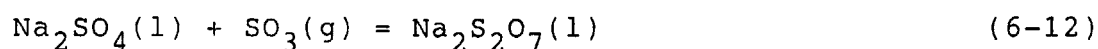
or the absorption of SO_3 may be regarded as an addition of SO_3 molecule to the molten Na_2SO_4. At the same time, the thermodynamic properties of sodium sulfate is affected by the dissolved SO_3. The activity of sodium oxide in the sodium sulfate is altered in accordance with the reaction

$$Na_2O(l) + SO_3(g) = Na_2SO_4(l) \qquad (6-13)$$
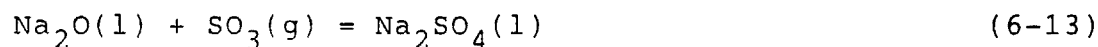
This equilibrium is the one detected by the electrochemical cell. This whole process reaches equilibrium in less than an hour.

Because of the presence of alumina, the formation of aluminum sulfate is also taken place according to the reactions

$$Al_2O_3(s) + 3[SO_3] = [Al_2(SO_4)_3] \qquad (6-14)$$
or

$$Al_2O_3(s) + 3[Na_2S_2O_7] = 3Na_2SO_4(l) + [Al_2(SO_4)_3] \quad (6-15)$$
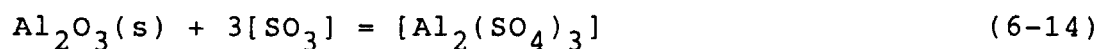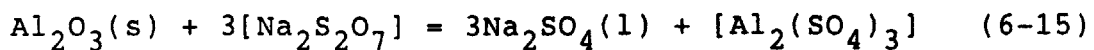
These reactions are likely to occur after the reactions between SO_3 and pure Na_2SO_4 have happened, because the formation of aluminum sulfate is a very slow reaction which can be inferred from the weight change in TGA experiments with alumina crucibles. The absorption of SO_3 after the first hour of equilibration is then contributed to the formation of aluminum sulfate in sodium sulfate. These reactions take more than one hundred hours to reach equilibrium.

It has been shown that the thermodynamic properties of the sodium sulfate remain unaffected by the presence of aluminum sulfate in the melts. Comparisons are made in terms of the standard Gibbs free energy of formation of sodium sulfate of EMF data taken every 15 minutes during the course of alumina equilibration shown in Figure 5.35. The entropy and enthalpy of formation remain relatively constant during the temperature fluctuation. The activity of sodium oxide at equilibrium concentrations of aluminum sulfate is also found to be same as the activity of sodium oxide in an inert platinum crucible under the same experimental condition shown in Figure 5.36. This indicates that the formation of aluminum sulfate does not affect the activity of sodium oxide in sodium sulfate. The concentration of aluminum sulfate is small in the melt; the sodium sulfate melt behaves as if it is pure sodium sulfate.

6.4 Cobalt Sulfate-Sodium Sulfate System

The thermodynamic properties of the $CoSO_4$-Na_2SO_4 system derived from the TGA and EMF experiments will be discussed first. Discussions on phase identifications by DTA, sampling, and SEM/EDX techniques will then be followed.

6.4.1 Thermodynamic Properties of Co-Na Sulfate

The thermogravimetric results indicate that the solubility of SO_3 gas in $CoSO_4$-Na_2SO_4 increases with an increase in partial pressure of SO_3, a decrease in temperature, and a decrease in mole fraction of $CoSO_4$. At the same time, it is found that the dissolved SO_3 reacts almost entirely with solid Al_2O_3 to form $Al_2(SO_4)_3$. The solubility of SO_3 is thus equilvalent to the Al_2O_3 dissolution. The molten $CoSO_4$-Na_2SO_4 acts as a medium to facilitate the formation of aluminum sulfate.

The thermodynamic properties of molten $CoSO_4$-Na_2SO_4 are evaluated based on the electrochemical results at temperatures above 1100 K due to the fact that, below this temperature, discordant solution behaviors are observed. The sulfate solution is determined to be athermal with zero heat of mixing. The activities of both $CoSO_4$ and Na_2SO_4 exhibit negative deviations from ideality, and the solution does not behave as a regular solution. This finding is contrary to the assumption made by Luthra and Shores [22,23,26,27,92] and that of Misra, Whittle, and Worrell

[91] in their estimations of the thermodynamic properties of the $CoSO_4$-Na_2SO_4 system. Luthra and Shores [22,23,26,27,92] treated the solution as a regular solution made up of sulfate molecules; while, Misra, Whittle, and Worrell [91] regarded the solution as a regular solution made up of ions.

The properties of $CoSO_4$ at melting obtained from this study are compared with those from other investigators in Table 6-4. The molar enthalpy and entropy of melting of $CoSO_4$ found by this study are slightly lower than those results reported by Lei and Elliott [107], Luthra et al.[23], and Misra et al.[91]. The ΔH_m determined by this study is approximately 3 Kcal lower than that reported by Lei and Elliott [107]. The ΔS_m found by this study is approximately 3 cal, 1.5 cal, and 4 cal lower than that reported by Lei and Elliott [107], Luthra et al. [23], and Misra et al. [91], respectively. The lack of agreement among different investigations may be due to the facts that Lei and Elliott [107] incorporated EMF data at temperatures below 1100 K (EMF break) in their thermodynamic calculations. Luthra et al. [23] and Misra et al. [91] evaluated the $CoSO_4$-Na_2SO_4 system under the assumption of regular solution which have been proved by this study to be an inappropriate model.

The melting point of $CoSO_4$ is estimated to be at 1453 K which is 195 degrees and 191 degrees higher than those reported by Lei and Elliott [107] and Barin et al.[106], respectively. Table 6-4 also shows that the standard

Table 6-4

Comparison of Properties of Cobalt Sulfate at Melting

	This Study	Lei & Elliott [107]	Barin et al. [106]	Luthra et al.[23]	Misra et al.[91]
$\Delta H_{m,CoSO_4}$ [Kcal/mole]	2.867	6.001	/	/	/
$\Delta S_{m,CoSO_4}$ [cal/mole·K]	1.972	4.768	/	3.5	6.0
$T_{m,CoSO_4}$ [K]	1453	1258	1262	/	/
$\Delta H^{\circ}_{f}(CoSO_4(l))$ [Kcal/mole]	−220.342	−216.517	/	/	/
$\Delta S^{\circ}_{f}(CoSO_4(l))$ [Kcal/mole·K]	−0.09546	−0.09178	/	/	/

enthalpy and entropy of formation of liquid $CoSO_4$ evaluated in this study agree well with those reported by Lei and Elliott [107].

In comparison with the molar enthalpy and entropy of melting of other sulfates [106] listed in Table 6-5, the two values found in this study are also slightly lower than those of other sulfates. For example, the ΔH_m and ΔS_m are 2.6 Kcal and 2.8 cal smaller than that of Na_2SO_4, respectively.

The conditions in terms of pressure of SO_3 and temperature at which liquid $CoSO_4$-Na_2SO_4 is stable are shown in Figure 5.59. This diagram is drawn based on the $CoSO_4$-Na_2SO_4 phase diagram (Figure 2.3) reported by Bolshakov and Fedorov [25]. The formation of liquid Na_2SO_4-$CoSO_4$ from an initially solid Na_2SO_4 occurs when the activity of $CoSO_4$ in Na_2SO_4-$CoSO_4$ solid solution becomes equal to or greater than that corresponding to the liquidus line. The minimum partial pressures of SO_3 to form a liquid Na_2SO_4-$CoSO_4$ in equilibrium with solid Co_3O_4 and solid CoO are represents by curves B and D, respectively. These two curves depict the intersections between the isoactivity lines of SO_3 and the liquidus line of the liquid+β phase in Figure 5.60. The chemical equilibria denoted respectively by the reactions (5-94) and (5-96) occur at the liquidus at the Na_2SO_4 end of the phase diagram where the activity of $CoSO_4(l)$ is depicted in Figure 5.54. Depending on either $Co_3O_4(s)$ or $CoO(s)$ is present, regions above curves B and D

Table 6-5

Properties of Other Sulfates at Melting [106]

Species	Melting pt.,K	ΔH_m,Kcal/mol	ΔS_m,cal/mol
Ag_2SO_4	933	4.3	4.609
$BaSO_4$	1623	9.7	5.977
$CaSO_4$.	1673	6.7	4.004
K_2SO_4	1342	8.8	6.557
$MgSO_4$	1400	3.5	2.500
Na_2SO_4	1157	5.5	4.754
$PbSO_4$	1139	4.1	3.600
Cs_2SO_4	1392	9.1	6.537

are the stable regions of liquid Na_2SO_4-$CoSO_4$; and below them, solid solution of Na_2SO_4-$CoSO_4$ is stable.

The solid $CoSO_4$ does not dissolve any appreciable amount of Na_2SO_4 shown in the phase diagram of Na_2SO_4-$CoSO_4$. The activity of $CoSO_4(s)$ with respect to pure solid cobalt sulfate as standard state at the liquidus line on the $CoSO_4$ end of the phase diagram should therefore be unity. The curves A and C denote the equilibra with $Co_3O_4(s)$ and $CoO(s)$ in reactions (5-93) and (5-95), respectively. Depending on whether $Co_3O_4(s)$ or $CoO(s)$ is present, areas above curve A and C solid $CoSO_4$ coexists with liquid solution of Na_2SO_4-$CoSO_4$; below them, the solid cobalt oxides exist in equilibrium with liquid Na_2SO_4-$CoSO_4$.

The boundaries between liquid and solid solutions of Na_2SO_4-$CoSO_4$ in equilibrium with $Co_3O_4(s)$ and $CoO(s)$ have been estimated by Luthra and Shores [22,23,26,27,92] with the assumption that the solution being a molecular regular solution. They are illustrated in curves E and F in Figure 5.59, respectively. Similar results have also been estimated by Misra, Whittle, and Worrell [91] with the assumption of ionic regular solution. In respect to the comparisons the stability of liquid $CoSO_4$-Na_2SO_4 between the curves B and E for equilibrium with Co_3O_4 and the curves D and F for equilibrium with CoO, the results estimated by Luthra [26] do not agree well with those of this study. Luthra [26] estimated that the transition from solid $CoSO_4$-Na_2SO_4 to liquid $CoSO_4$-Na_2SO_4 occurs at partial

pressures of SO_3 approximately one order of magnitude lower than those found in this study. Since Luthra [26] employed the regular solution model to estimate the thermodynamic properties of $CoSO_4$-Na_2SO_4, the results of this study derived from direct EMF measurements tend to be more reliable.

6.4.2 Differential Thermal Analysis

The phase diagram identified by the DTA peaks is compared with the one reported by Bolshakov & Fedorov [25] in Figure 5.63. The DTA phase diagram is represented by dotted lines; the published phase diagram by solid lines. The DTA phase diagram does not agree very well with the published one; however, they resemble each other. The region of $CoSO_4$+liquid is compressed, but the liquid+β phase occupies a larger area in the DTA phase diagram. Five DTA peaks have been identified at approximately 858 K and four DTA peaks are noted at about 710 K, the DTA results thus bear some agreements with the published phase diagram with respect to the two isotherms at 846 K and 705 K.

Conspicuous changes in the slope of the baseline are indicated in the DTA thermograph at temperature range of 1080 K to 1166 K in Figure 5.61. The EMF breaks occur in the range of 1076 K to 1125 K. The temperatures at which DTA slope changes and those of the EMF break are both presented in Figure 5.63 for comparison. Although the

temperatures at which the DTA baseline changes its slope do not coincide exactly with the temperatures of the EMF breaks, they are in close vicinity with each other. Since phase stability is later found to be dependent on the partial pressure of SO_3 in the gas phase, the DTA results which are conducted under an unknown partial pressure of SO_3 possibly bear some relationship to the EMF breaks.

Distinct DTA peak is not noted in the liquid region; heat of melting does not occur. It is therefore implies that presence of another phase in the liquid region is impossible. A noticeable change in the slope of baseline possibly indicates a change in the heat capacity of the sample. Second-order phase transition might be a possible cause for the EMF breaks.

The differential thermal analysis of the sodium tungstate reference material has recorded two sharp endothermic peaks at 874 K (601°C) and at 904 K (631°C) shown in Figure 5.62. Hoermann [109], Caillet [110], and Chang & Sachdev [111] have investigated the phase diagram of the $Na_2WO_4-WO_3$ system by various techniques. Caillet [110] who studied the system by DTA and X-ray diffraction reported a phase transformation at 590°C and a eutectic at 628°C in Figure 6.8. Hoermann [109] also reported α/β transformations at temperatures between 500°C to 600°C and a eutectic at 627°C and 56.5 mole percent WO_3. Chang & Sachdev [111] who employed only X-ray powder diffraction reported a eutectic point at 622°C and 56.3 mole percent
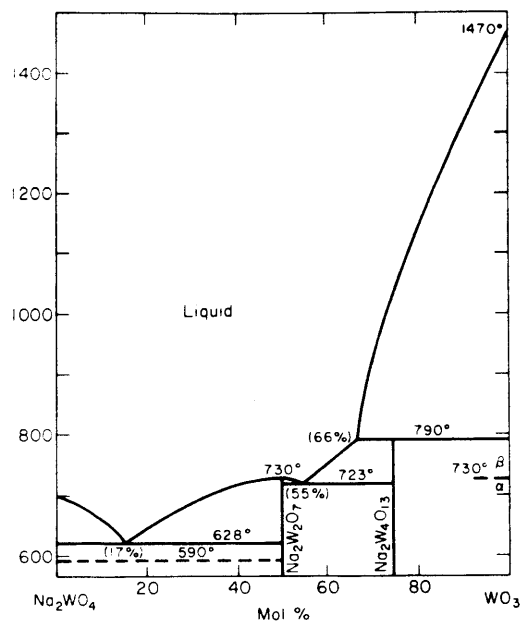
Figure 6.8 - Phase diagram of Na_2O-WO_3 system [110].

WO_3; however, they did not observe any phase transformation below the eutectice temperature. In this study, a distinct peak which is detected at 601°C in Figure 5.62 agrees very well with the phase transformation peak reported by Caillet [110]. The other peak found at 631°C also have excellent agreements with the eutectic point reported by Caillet [110] and Hoermann [109]. The secondary peak indicating the end of the transformation at the liquidus line is not observed; this also proves that the composition of the reference melt 54.98 m/o WO_3 is located closely to the eutectic composition of 56.3 m/o WO_3 reported by Chang & Sachdev [111]. It is therefore concluded that there are no changes in state in the WO_3-Na_2O reference melt to cause the obsecure changes in cell potentials.

6.4.3 Sampling

The results of sampling are summarized in Figure 5.63. Solid phases found respectively at 849 K and 856 K at 29.98 and 59.96 mole percent of Na_2SO_4 in Na_2SO_4-$CoSO_4$ system have excellent agreements with the DTA phase diagram. The two solid samples disagree with the published phase diagram in such a way that complete solid phases are encountered in the two-phase regions ε+liquid and β+liquid. Samples taken at 80.00 mole percent of Na_2SO_4, however, have good agreements with the published phase diagram. Solid phases are found in the β region.

The effect of the partial pressure of SO_3 on the phase diagram is also investigated by the technique of sampling. During the EMF equilibration under the initial gas flowrate ratio of O_2/SO_2 of 19.3, a solid phase is encounter at 926 K at 80.00 mole percent of Na_2SO_4-$CoSO_4$. On the contrary, a liquid sample is extracted under the O_2/SO_2 of 0.562 at 933 K at the same composition. The phase diagram is determined to be a function of the partial pressure of SO_3. Higher pressure of SO_3 tends to stablize the liquid field or the two-phase field neighboring the liquid to a lower temperature. The validity of the phase diagram of $CoSO_4$-Na_2SO_4 reported under an unspecified partial pressure of SO_3 by Bolshakov & Fedorov [25] is therefore questionable.

Liquid samples can be extracted at temperatures above and below either the EMF breaks and the DTA slope change in the liquid region of the published phase diagram. In addition, visible sign of DTA peak of the liquidus line is not detected at the temperatures of the EMF break; thus, first-order phase transition does not explain the EMF breaks.

6.4.4 Morphology and EDX

The results of the SEM analysis is included in Figure 5.64. For samples of compositions less than 50 m/o of Na_2SO_4 in Na_2SO_4-$CoSO_4$, quenched samples are supposed to

consist of $CoSO_4$ as the primary phase encased by ε in a matrix of eutectic of ε+δ or ε+β in accordance with the phase diagram. A variety of solidified forms is observed in these quenched samples; such as scattered oval plates, densely packed oval plates, dispersed starlike structures, segregation bands, segregation needles, coarse dendrites, and segregation patches. Nevertheless, the pure $CoSO_4$ phase is not found in any solidified form of the quenched samples, because Na is also detected by EDX.

Quenched samples of 30.04 m/o $Na_2SO_4-CoSO_4$ which are supposed to be equilibrated in the same two-phase region of $CoSO_4$+liquid manifest different morphologies at different temperatures. Equilibrium samples taken at 1007 K show either coarse dendrites or densely packed oval plates. Nevertheless, the two samples taken respectively at 896 K and 872 K consist of segregation patches of either cobalt or cobalt oxide only. Sodium and sulfur are not detected by EDX in the patches. These equilibrium samples tend to show an agreement with the phase boundary determined by the DTA results. The two-phase region of $CoSO_4$+liquid in the published phase diagram is therefore questionable.

For samples of compositions greater than 50 m/o $Na_2SO_4-CoSO_4$, quenched samples are supposed to consist of primary cored β phase encased by a matrix of ε+β or δ+β. A variety of morphologies are observed in these samples; such as circular ropy or plate-like areas in a smoother matrix, scattered oval plates in a grainy matrix, densely packed

oval plates, fine and coarse dendritic patterns, and rough grainy surfaces. These forms are probably the β phase surrounded by an eutectic matrix.

Quenched samples equlibrated in the β+liquid region are supposed to have scattered β phase in a matrix of either $\varepsilon+\beta$ or $\delta+\beta$ eutectic. The β is expected to have fine dendrites growing from coarse grains of β which are the original β phase in the liquid. The sample of 80.01 m/o Na_2SO_4-$CoSO_4$ at 1001 K is equilibrated in the two-phase region. It possesses scattered or clustered oval plates in a grainy matrix. The oval plates are probably the β phase; the matrix the eutectic. However, neither coarse nor fine dendrites are observed.

Distinguishable oval plates are observed in liquid samples quenched in air. If the oval plates were the primary phase solidified from the liquid, $CoSO_4$ would have been the phase on the $CoSO_4$ side while β would have been the phase on the Na_2SO_4 side. Since similar oval plates are observed on both sides of the phase diagram, the phase of the oval plates is uncertain. The EDX quantitative results cannot pinpoint a definite chemical composition of the oval plates that match any of the phase present in the published phase diagram. Nevertheless, sodium, cobalt and sulfur are all detected in the oval plates by EDX. The most probable formula may be $CoNaS_2$ with unknown oxygen quantity. The primary phase of pure $CoSO_4$ is not possible, because sodium is also detected by EDX in all of the oval plates. The

phase relationship of the oval plate cannot be determined at this time.

Oval plates are observed from quenched samples equilibrated at temperatures above and below the EMF breaks. In general, scattered oval plates are noted above the EMF breaks; densely packed oval plates below the EMF breaks. The density of the oval plates may be due to the difference in cooling rates. Higher cooling rate occurs in samples quenched from higher temperatures to room temperature, thus nucleation is slow and scattered oval plates are noted. On the contray, samples quenched from lower temperatures are packed with oval plates because of high rate of nucleation at low cooling rate.

As a conclusion, the abrupt changes in the EMF behavior of the $CoSO_4-Na_2SO_4$ system suggest phase transformations. The observations of oval plates with Na, Co and S in quenched samples might imply the presence of a compound which is in saturation with the liquid in the ternary system of Na_2O-SO_3-CoO. If a steep liquidus surface exists in the ternary system, differential thermal analysis might not show a distinct peak at the temperature of phase transformation, but indicates a change in the slope of the baseline. The existence of an unknown compound in the ternary at temperatures below 1100 K might be the explanation of obscure EMF behaviors. The validity of the published $CoSO_4-Na_2SO_4$ phase diagram is thus questionable.

6.5 Implications on Sodium Sulfate Induced Hot Corrosion

Hot corrosion is observed when a liquid phase of sulfate, mainly sodium sulfate, is present on the surface of a gas turbine blade at elevated temperatures. The corrosion dissolves the protective oxide coating, and then attacks the part itself. Gas turbine gases contain SO_3 at partial pressures of approximately 10^{-6} to 10^{-4} atm at 1200 K for a total pressure of one atmosphere depending on the fuel sulfur content [113]. From the quantitative study of Al_2O_3 dissolution by acidic fluxing (Figure 5.34), the concentration of aluminum in pure sodium sulfate equals 1.9 ppm at $P_{SO_3} = 10^{-4}$. The dissolution of aluminum oxide by pure sodium sulfate is therefore found to be small at the operating condition of a gas turbine which is contradictory to the observed accelerated attacks by hot corrosion. The mechanism of corrosion attack must be more complex than solely dissolving the protective coatings by pure sodium sulfate.

In the present study, it is demonstrated that the activity of sodium oxide determines the solubility of the protective aluminum oxide by either acidic or basic fluxing. Figure 5.58 has shown that additions of $CoSO_4$ to Na_2SO_4 decrease the activity of sodium oxide at a constant partial pressure of SO_3 at 1200 K. For example, when pure sodium sulfate is transformed to a 50/50 Na-Co sulfate by sulfidation of cobalt oxides in the protective coating, the acidity of the melt is increased by approximately an order

of magnitude whereas the concentration of dissolved aluminum in the sulfate is increased to more than 30 times. Severe acidic fluxing is then noted. At the same time, imperfections in the structure of the protective oxides, such as grain boundaries, will surely facilitate the oxide dissolution process because of the high interfacial energy at the grain boundaries. These structural imperfections are easily prone to corrosion attack by the fluxing mechanism. Catastrophic hot corrosion is therefore caused both by chemical factors which affect the activity of sodium oxide and by physical factors which relate to the structure of protective oxides.

The $CoSO_4$-Na_2SO_4 sulfate is known to form a liquid phase at temperatures below the melting point of sodium sulfate due to the existence of a low-temperature eutectic. At the same time, it is noted that the solubility of aluminum oxide, which is equilvalent to the solubility of SO_3 in the presence of alumina, increases with a decrease in temperature at a constant pressure of SO_3. Therefore, the addition of $CoSO_4$ in Na_2SO_4 induces severe corrosion attacks by dissolving more Al_2O_3 protective layer at a lower temperature.

The kinetics of SO_3 solubility in molten sodium sulfate is determined to be controlled by liquid phase mass transfer with a boundary layer thickness in the order of 10^{-3} cm. However, the kinetics of Al_2O_3 dissolution is likely controlled by chemical reactions between the dissolved SO_3

and Al_2O_3 solid. Thus, for a thin film of liquid Na_2SO_4 deposited on a turbine blade, the kinetic process that control the Al_2O_3 dissolution is governed solely by the chemical reaction to form aluminum sulfate.

The thermodynamic analyses of the $Na_2S_2O_7$-Na_2SO_4 system and the $CoSO_4$-Na_2SO_4 system and the equilibrium Al_2O_3 solubility measurements have provide valuable information on ways to prevent the accelerated material degradation of hot corrosion. Since the presence of a liquid phase is essential to cause hot corrosion, operating conditions at which either a solid Na_2SO_4 or a solid $Na_2S_2O_7$ is stable shown in the stability diagram in Figure 5.11 are important to get rid of the corrosion attacks by Na_2SO_4. In the later stage of the corrosion attack, when $CoSO_4$ mixes with the Na_2SO_4, gas turbines are advised to be operated below curve B and D in the stability diagram of the $CoSO_4$-Na_2SO_4 system shown in Figure 5.59 to maintain a $CoSO_4$-Na_2SO_4 solid. Even if a solid sulfate phase cannot be attained in the system, the activity of sodium oxide in the molten sulfate is suggested to maintain at the minimum of the Al_2O_3 solubility which is approximately at log a_{Na_2O} = -12 at 1200 K shown in the equilibrium Al_2O_3 solubility diagram in Figure 5.34. Therefore, the life time of a gas turbine can be prolonged.

CHAPTER SEVEN

SUMMARY AND CONCLUSION

This chapter presents a summary of the works of this investigation in the first section. The condensed conclusions of this study are included in the second section.

7.1 Summary Of The Study

The present investigation is focused on the chemical reactions involving Na_2SO_4 liquid, SO_3 gas, and Al_2O_3 solid; and the chemical reactions involving $CoSO_4-Na_2SO_4$ binary liquid, SO_3 gas, and Al_2O_3 solid. Two types of experimental techniques are employed in this study: (1) Thermogravimetric analysis; and (2) Electrochemical measurements. Other analytical analyses which includes DC plasma arc elemental emission spectrometry and differential thermal analysis are also performed. Either platinum or alumina crucibles are used in the two experiments. The thermogravimetric analysis makes use of a thermobalance to determine the weight change of the sulfate melt under a controlled partial pressure of SO_3 ranging from 0.18 atm to 0.003 atm at temperatures ranging from 1100 K to 1250 K. The electrochemical measurements measure the activity of sodium oxide in the sulfate melts under a controlled pressure of SO_3 ranging from 0.7 atm to 2.92×10^{-5} atm at temperatures 900 K to 1250 K by employing the following EMF

cell:

$$Pt, O_2(g) \quad | \quad Na^+ \quad | \quad Pt, O_2(g), SO_2(g)$$
$$Na_2O-WO_3(l) \quad | \quad fused \ silica \quad | \quad Na_2SO_4(l) \ or \ CoSO_4-Na_2SO_4(l)$$
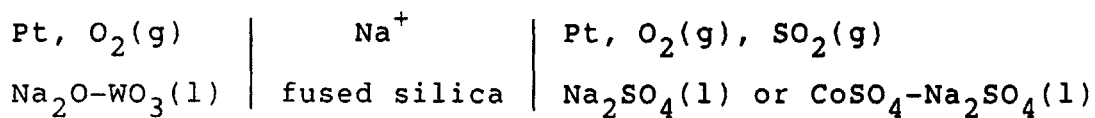
Samples are periodically extracted during EMF experiments with Na_2SO_4 in alumina crucibles to determine the Al_2O_3 solubility.

The solubility of SO_3 is observed to increase with an increase in partial pressure of SO_3, an decrease in temperature, and a decrease in $CoSO_4$ concentration in the sulfate melt. With the presence of alumina oxide in contact with the molten sodium sulfate or the Co-Na sulfate, more than 95 percent of the SO_3 dissolved in the sulfate melt reacts with solid aluminum oxide to form aluminum sulfate. The dissolved aluminum is determined to have no effect on the thermodynamic properties of the sulfate.

The solution of SO_3 gas in molten Na_2SO_4 is a much faster process than the solution of Al_2O_3 solid in molten Na_2SO_4. The difference in rate amounts to more than 100 times. An equilibration time of 100 hours is typical to reach equilibrium Al_2O_3 dissolution. The rate of SO_3 absorption is relatively faster than that of desorption. The solubility of SO_3 in liquid Na_2SO_4 is controlled by liquid phase mass transfer; whereas, the solubility of Al_2O_3 solid in Na_2SO_4 is controlled by the chemical reaction to form $Al_2(SO_4)_3$.

The thermodynamic properties of the $Na_2S_2O_7$-Na_2SO_4 binary system has been fully determined in accordance with the reaction

$$Na_2SO_4(l) + SO_3(g) = Na_2S_2O_7(l) \qquad (7-1)$$
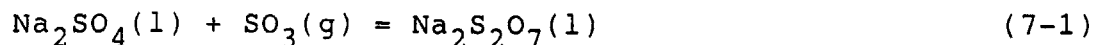
Results of other researchers are extrapolated to an isothermal of 1160 K by the Gibbs-Helmholtz equation, and the solution is found to behave in such a way that the activities of the two components equal to the mole fractions of the respective species. The equilibrium constant for reaction (7-1) is

$$\log K = -8.055 + 7946/T \qquad (7-2)$$

The phase diagram of the $Na_2S_2O_7$-Na_2SO_4 system mapped with isoactivity lines of SO_3 has been completely determined. A β phase is proposed to exist in the system due to the reaction

$$Na_2SO_4(s) + SO_3(g) = Na_2S_2O_7(s) \qquad (7-3)$$
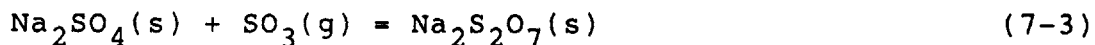
The standard Gibbs free energy of the reaction (7-3) between the solid species is estimated to be

$$\Delta G^\circ = -31129.46 + 31.79 \ T \ [cal/mol] \qquad (7-4)$$

A stability diagram of the liquid and solid phases has been

investigated. The log partial pressures of SO_3 in equilibrium with pure $Na_2S_2O_7$ and pure Na_2SO_4 are respectively determined to be 4.1997 and -8.97 at 1160 K; and 4.7895 and -8.59 at 1200 K.

The thermodynamic properties of Na_2SO_4 is evaluated according to the reaction

$$Na_2O(l) + SO_3(g) = Na_2SO_4(l) \qquad (7-5)$$
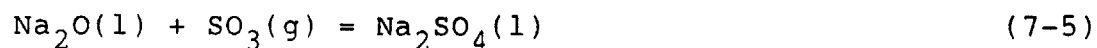
The standard Gibbs free energy for the reaction (7-5) is obtained to be

$$\Delta G° = -120080 + 21.3871 \ T \ [cal/mol] \qquad (7-6)$$

and the standard Gibbs free energy of formation of $Na_2SO_4(l)$ is

$$\Delta G_f^o(Na_2SO_4(l)) = -314.172 + 0.08195 \ T \ [Kcal/mol] \qquad (7-7)$$

The acidic fluxing of Al_2O_3 solid by molten Na_2SO_4 has been investigated by the TGA and EMF experiments. The two results from this study are slightly discordant. The results from the EMF experiments which obeys the Temkin ideal ionic solution model is determined to be more reliable. The dissolved aluminum concentration is measured to varies from 0.36 ppm to 8011 ppm at log P_{SO_3} = -4.5337 to -1.5068. The solubility results of alumina from this study

are in reasonable agreement with the results obtained by Elliott et al. [40] and Liang [108]; however, they disagree entirely with the results reported by Stroud and Rapp [39], and Jose, Gupta, and Rapp [45].

Measurements on the basic fluxing of Al_2O_3 are not possible with the present electrochemical cell because of the instability of silicon oxide in melts with high basicity. The maximum basicity that the electrolyte can be feasibly employed at 1200 K is recorded at about log a_{Na_2O} = -12. Above this value, the electrolyte is attacked by the reaction

$$[Na_2O] + XSiO_2(s) = [Na_2O \cdot XSiO_2] \qquad (7-8)$$
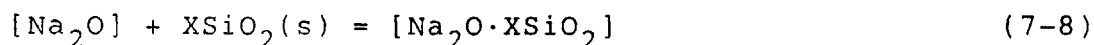
The electrochemical measurements show that the solution behavior of the $CoSO_4$-Na_2SO_4 system is athermal. The activities of $CoSO_4$ and Na_2SO_4 deviate negatively from ideality. The melting point of $CoSO_4$ is estimated to be 1454 K, and the standard Gibbs free energy of formation of liquid $CoSO_4$ is found to be

$$\Delta G_f^o(CoSO_4(l)) = -220.3420 + 0.09546 \ T \ [Kcal/mol] \qquad (7-9)$$

The activity of sodium oxide is observed to decrease with an increase in the partial pressure SO_3 and with an increase in $CoSO_4$ concentration. A stability diagram and a phase diagram mapped with P_{SO_3} isobars are also reported.

Electrochemical studies have revealed inconsistent thermodynamic behaviors in the liquid phase of the Co-Na sulfate at temperatures below 1100 K. With considerations from the results of DTA, SEM, EDX, and sampling techniques, the abrupt changes in EMF measurements might possibly be caused by the presence of an unknown compound in the ternary system of Na_2O-SO_3-CoO. Thus, the validity of the phase diagram reported by Bolshakov and Fedorov [25] is highly questionable.

7.2 Condensed Conclusion Of The Study

The physical chemistry of the reactions of $Na_2SO_4(l)$ and liquid $CoSO_4-Na_2SO_4$ mixtures with $SO_3(g)$ and $Al_2O_3(s)$ has been studied with thermogravimetric analysis and electrochemical measurement at 900 K to 1250 K. The conclusions are as follows:

(1) The thermodynamics and kinetics of the reaction of $SO_3(g)$ with $Na_2SO_4(l)$ have been studied. The thermodynamics have been evaluated under the binary system of $Na_2S_2O_7-Na_2SO_4$. The activities of the two species are found to be equal to the mole fractions of the respective components. The phase diagram is completed and the stability diagram is determined. The kinetics of SO_3 absorption/desorption is limited by liquid phase mass transfer.

(2) The slope of the equilibrium Al_2O_3 solubility in Na_2SO_4 at 1200 K is determined to be 3/2 in a log-log plot of Al concentration versus P_{SO_3}. The results differ significantly from those reported in earlier publications.

(3) The activities of the two components of the $CoSO_4$-Na_2SO_4 system exhibit negative deviation from ideality. The activity of Na_2O in the sulfate decreases with an increase in $CoSO_4$ concentration. The results of the study raise a question as to the validity of the published $CoSO_4$-Na_2SO_4 phase diagram.

(4) The solubilities of $SO_3(g)$ and $Al_2O_3(s)$ in sulfate melts increase with an increase in P_{SO_3}, a decrease in temperature, and a decrease in $CoSO_4$ concentration. The molar ratios of dissolved Al and absorbed SO_3 indicate the formation of $Al_2(SO_4)_3$. The kinetics of $SO_3(g)$ solution in molten sulfate are much faster than that of $Al_2O_3(s)$ dissolution.

CHAPTER EIGHT

RECOMMENDATION FOR FUTURE WORK

The present study has investigated the physical chemistry of molten sodium sulfate in reactions with aluminum oxide which is only one type of protective coatings found in high temperature applications. The outer layer of a turbine blade, however, consists of other oxides such as chromium oxide which provides protection to superalloys against hot corrosion. The literature is flooded with results of oxide solubility in Na_2SO_4 reported by a single research group; nevertheless, this study has shown that these results may be questionable. Precise quantitative measurements of the solubility of Cr_2O_3 and other oxides such as Fe_2O_3, CoO, and NiO in molten Na_2SO_4 are highly desirable to understand the fluxing mechanism and the protectiveness of different oxides.

With the understanding that the activity of sodium oxide in the sulfate melt is the determining factor of hot corrosion, electrochemical measurements of determining the basicity of the molten salt has proved to an important tool to understand the physico-chemical process of hot corrosion. This method of measurement is suggested to extend to investigations of the effects on the melt basicity by fuel impurities and alloying elements in superalloy which include Mo, Ta, Ti, and Mn. Mixed sulfates are often found in hot corrosion; therefore, electrochemical measurements on

$NiSO_4-Na_2SO_4$, and $FeSO_4-Na_2SO_4$ are also recommanded.

It is recognized that the present electrochemical cell with fused silica solid electrolyte provide good measurements on the activity of sodium oxide in sulfate melts; nevertheless, the application is limited to log a_{Na_2O} = -12 at 1200 K. A new electrochemical cell is thus suggested to be developed to eliminate this shortcoming so that electromotive force measurements can be possible at high basicity conditions.

APPENDIX A

SOURCES AND PURITIES OF MATERIALS

Sodium Sulfate (Na_2SO_4)
J.T.Baker   Lot No.015158

Insoluble matter	0.002%
Chloride	0.0003%
Phosphate	0.0002%
Calcium, Magnesium, and R_2O_3 ppt	<0.004%
Potassium	0.002%
Nitrogen Compound	3 ppm
Arsenic	<0.3 ppm
Heavy Metal	1 ppm
Iron	1 ppm

Cobaltous Sulfate ($CoSO_4 \cdot 7H_2O$)
MCB   Lot No.CX1825

Insoluble Matter	0.01%
Chloride	0.001%
Copper	0.002%
Iron	0.001%
Lead	0.002%
Nickel	0.1%
Nitrate	0.005%
Zinc	0.02%

Sodium Tungstate ($Na_2WO_4 \cdot 2H_2O$)
Mallinckrodt   Lot No.8112

Insoluble Matter	0.010%
Alkalinity (as Na_2CO_3)	0.20%
Arsenic	0.0005%
Chloride	0.005%
Heavy Metals and Iron	0.001%
Molybdenum	0.001%
Nitrogen Compound	0.001%
Sulfate	0.01%

Sodium Oxide (Na_2O)
Alfa-Ventron   Lot No.101773
    > 98%

Tungsten (VI) Oxide (WO_3)
Alfa-Ventron   Lot No.082478
     99.7%

Oxygen (O_2)
Union Carbide - Linde
     > 99.5%

Sulfur Dioxide, Anhydrous (SO_2)
Matheson
     > 99.98%

Argon (Ar)
Union Carbide - Linde
     > 99.997%

Sulfur Dioxide/Argon, Certified Grade
Matheson
     4.9% SO_2 balance Ar

Sulfur Dioxide/Argon, Certified Grade
Matheson
     0.93% SO_2 balance Ar

Sulfur Dioxide/Argon, Certified Grade
Matheson
     119 ppm SO_2 balance Ar

APPENDIX B

PREPARATION OF SODIUM TUNGSTATE MELT

The Na_2O-WO_3 reference melt with a composition of approximately 55 mole percent of WO_3 is prepared from sodium tungstate ($Na_2WO_4 \cdot 2H_2O$) and tungsten (VI) oxide (WO_3). Thirty grams of sodium tungstate contained in a platinum crucible are weighed and fused in air at 800°C with a muffle furnace (Lindberg model 51848) to remove the water. The crucible and its content are weighed again to determine the amount of Na_2WO_4 while they are still warm to avoid absorption of moisture from the air. A pre-weighed tungsten oxide of 4.7 gram is added to the Na_2WO_4, then the mixture is fused again at 800°C. The fused Na_2O-WO_3 and the crucible are weighed while still warm to determine the net amount of WO_3 added. The final composition of 54.9888 mole percent WO_3-Na_2O is determined based on the difference of the weighing of the crucible and its contents. The Na_2O-WO_3 is fused again in air at 800°C before it is quenched on a clean, cold stainless steel beaker. The solidified Na_2O-WO_3 is crushed and grounded into powders with a pestle and mortar. The reference melt is finally stored in a desiccator for future use.

APPENDIX C

WIRE METHOD OF THERMOCOUPLE CALIBRATION

1. The two leads of the thermocouple are bridged with a piece of gold wire 0.254 mm diameter by 10 mm length.

2. The thermocouple with the gold wire is heated with a programmable furnace at a rate of 0.5°C per minute.

3. The output voltage of the thermocouple is monitored continuously until the gold wire is melted off and an open circuit is detected.

4. The last recorded potential represented the voltage measured by the thermocouple at the melting point of gold.

APPENDIX D

PROGRAM FOR DATA ACQUISITION AND CONTROL
OF EMF EXPERIMENTS

```
100   REM  PROGRAM TO CONTROL AND RECORD DATA FROM EMF
      EQUILIBRIUM EXPERIMENT IN UNIT 1 AND RECORD EMF DATA
      FROM UNIT 2.
110   REM   PRESS "*" TO STOP PROGRAM EXECUTION
120   DIM WS(30),VS(900),TS(900)
130   HOME
140 IZ = 1: POKE  - 16368,0
150 D$ =  CHR$ (4):R$ =  CHR$ (13)
160 AP$ = "APPEND":WI$ = "WRITE"
170 P1$ = D$ + "PR 1":P0$ = D$ + "PR 0": PRINT P0$
180   HTAB 4: FLASH : PRINT "EQUILIBRIUM RUN ON UNIT 1 AND"
190   HTAB 4: PRINT "RECORD EMF DATA FROM UNIT 2": NORMAL
200   INPUT "HAVE YOU PUT DATAFILE DISK INTO DRIVE 1 ?";A$
210   IF A$ <  > "Y" THEN  GOTO 200
220   SLOT  = 4
230   BCDOUT,(DV) = 0,(D ) = 1
240   INPUT "HAVE YOU CONNECTED D/A TO TEMP CONTROLLER ?";B$:
      IF B$ <  > "Y" THEN 240
250   DAY TO DG,DH,DI,DJ
260   PRINT P1$: PRINT
270   PRINT "DATE  "DH"/"DI"/"DG: PRINT : PRINT P0$
280   INPUT "WRITE ON OLD DATAFILE FOR UNIT 1 ?";W0$: PRINT :
      PRINT P1$
290   IF W0$ <  > "Y" THEN 320
300   INPUT "OLD DATAFILE FOR UNIT 1 = ";FA$
310 A0$ = AP$: GOTO 340
320   INPUT "NEW DATAFILE FOR UNIT 1 = ";FA$
330 A0$ = WI$
340   INPUT "TOLERANCE ON TEMP (K)=";TTEMP
350   INPUT "TOLERANCE ON EMF IS (MV)=";TEMF
360   INPUT "MINUTES WITHIN TOLERANCE (MULTIPLE OF 5)=";EQT
370   INPUT "TOTAL AMOUNT OF TEMPERATURES WHERE EMF SHOULD BE
      TAKEN=";I
380 J = 0
390   INPUT "TARGET TEMPERATURE (K)=";WS(J)
400 J = J + 1
410   IF J < I THEN  GOTO 390
415   PRINT D$;"PREFIX,D1": PRINT D$;"PREFIX": INPUT R1$
417 F0$ = R1$ + FA$
419   PRINT D$;"OPEN ";F0$;",D1"
420 A1 = 79.484
430 B1 = 103.49
440 C1 =  - 0.7817
450 D1 = 0.0526
460 E1 =  - 8.739E - 3
470 F1 = 3.438E - 4
480   PRINT P0$: PRINT : PRINT
490   INPUT "HAVE YOU PUT DATAFILE DISK INTO DRIVE 2 ?";AN$
500   IF AN$ <  > "Y" THEN  GOTO 490
```

```
510    INPUT "WRITE ON OLD DATAFILE FOR UNIT 2 ? ";W2$: PRINT
       : PRINT P1$: PRINT
520    IF W2$ < > "Y" THEN 550
530    INPUT "OLD DATAFILE FOR UNIT 2 = ";FB$
540 A2$ = AP$: GOTO 570
550    INPUT "NEW DATAFILE FOR UNIT 2 = ";FB$
560 A2$ = WI$
570    INPUT "IDLE PERIOD (S) = ";SS
575    PRINT D$;"PREFIX,D2": PRINT D$;"PREFIX": INPUT R2$
577 F2$ = R2$ + FB$
580    PRINT D$;"OPEN ";F2$;",D2"
590    PRINT : PRINT "TIME<1>"; TAB( 12);"TEMP<1>,K"; TAB(
25);
       "EMF<1>,MV";
600    PRINT  TAB( 39);" ";"TIME<2>"; TAB( 12);"TEMP<2>,K";
       TAB( 25);"EMF<2>,MV"
610    _TIME TO HT,MT,ST
640 PH = HT
650 J = 0
660    GOSUB 1480: IF  PEEK ( - 16384) = 170 THEN 1440
670    IF TA > 1600 THEN  PRINT "TEMP IS TOO HIGN! PROGRAM
       ABORTED!": GOTO 1470
680    IF TA < 300 THEN  PRINT "TEMP IS TOO LOW! PROGRAM
       ABORTED!": GOTO 1470
690    IF  ABS (TA - WS(J)) < 10 OR  ABS (TA - WS(J)) = 10
       THEN 890
700    IF (TA + 10) < WS(J) THEN X = 1
710    IF (TA - 10) > WS(J) THEN X = 2
720    ON X GOTO 810,730
730    GOSUB 1640: PRINT
740    PRINT "DECREASE OF TEMP REQUIRED";
750    PRINT  TAB( 39);" ";HT":"MT":"ST; TAB( 12);TB;
       TAB( 25);VB
760    _BCDOUT,(DV) = X,(D ) = 1
770    _PAUSE = 4
780 X = 0
790    _BCDOUT,(DV) = X,(D ) = 1
800    _PAUSE = 600: GOTO 660
810    GOSUB 1640: PRINT
820    PRINT "INCREASE IN TEMP REQUIRED";
830    PRINT  TAB( 39);" ";HT":"MT":"ST; TAB( 12);TB;
       TAB( 25);VB
840    _BCDOUT,(DV) = X,(D ) = 1
850    _PAUSE = 5
860 X = 0
870    _BCDOUT,(DV) = X,(D ) = 1
880    _PAUSE = 600: GOTO 660
890 K = 0
900 L = 0
910 M = EQT / 5
920    GOSUB 1580
930    GOSUB 1480
940 TS(K) = TA
950    IF M > K THEN  GOTO 1070
960 B = K - M
970 C = TS(K) - TS(B)
```

```
980   IF C < 0 THEN C =  - C
990   IF C > TTEMP THEN  GOTO 1060
1000  D = VS(K) - VS(B)
1010  IF D < 0 THEN D =  - D
1020  IF D > TEMF THEN  GOTO 1060
1030  L = L + 1
1040  IF L < M THEN  GOTO 1070
1050  GOTO 1120
1060  L = 0
1070  GOSUB 1640
1075  PRINT D$;A0$;F0$
1076  PRINT HT;R$;MT;R$;ST;R$;TS(K);R$;VS(K)
1077  PRINT D$
1080  PRINT HT":"MT":"ST; TAB( 12);TS(K); TAB( 25);VS(K);
      TAB( 39);"   ";HT":"MT":"ST; TAB( 12);TB; TAB( 25);VB
1090  K = K + 1
1100  PAUSE = 258
1105  IF  PEEK ( - 16384) = 170 THEN 1440
1110  GOTO 920
1120  PRINT
1130  PRINT "THE EQUILIBRIUM TEMPERATURE AND EMF IS"
1140  B = K - M
1150  TF = 0
1160  VF = 0
1170  N = 1
1180  G = B + N
1190  TF = TF + TS(G)
1200  VF = VF + VS(G)
1210  N = N + 1
1220  IF G < K THEN  GOTO 1180
1230  TF = TF / M
1240  VF = VF / M:  TIME TO HT,MT,ST: GOSUB 1640
1245  PRINT D$;A0$;F0$
1246  PRINT HT;R$;MT;R$;ST;R$;TF;R$;VF
1247  PRINT D$
1250  PRINT HT":"MT":"ST; TAB( 12);TF; TAB( 25);VF;
1260  PRINT  TAB( 39);"   ";HT":"MT":"ST; TAB( 12);TB;
      TAB( 25);VB
1310  J = J + 1
1330  IF J < I THEN  GOTO 660
1400  GOSUB 1640
1410  PRINT  TAB( 39);"   ";HT":"MT":"ST; TAB( 12);TB;
      TAB( 25);VB
1420  PAUSE = SS
1430  IF  PEEK ( - 16384) <  > 170 THEN  GOTO 1400
1440  PRINT D$;"CLOSE ";F0$
1450  PRINT D$;"CLOSE ";F2$
1455  POKE  - 16368,0
1460  PRINT P0$
1470  END
1480  REM   SUBROUTINE TO DETERMINE TEMP FROM CHANNEL 0
1490  X0 = 0:Q0 = 0
1500  WRDEV,(DV) = 3,(W ) = 2,(D ) = 2
1510  ASUM,(TV) = Q0,(RT) = 10,(SW) = 1000,(C ) = 0,
      (D ) = 2
1520  X0 = Q0 / 1000
```

```
1530 V0 = 5 * 1E3 * (X0 - 2048) / (267.4 * 2048)
1540 T0 = A1 + V0 * (B1 + V0 * (C1 + V0 * (D1 + V0 * (E1
     + V0 * F1))))
1550  REM  ACTUAL READING ADJUSTMENT ON 11/21/86.
1560 TA = T0 + 2.5 + 273
1570  RETURN
1580 R = 0
1590  ASUM,(TV) = R,(RT) = 10,(SW) = 1000,(D ) = 0,
     (C ) = 0
1600 P = R / 1000
1610 VA = (P - 2048) * (2500 / 2048)
1620 VS(K) = VA - 4.7
1630  RETURN
1640  REM  SUBROUTINE TO DETERMINE AND RECORD TEMP _EMF
     FROM CHANNEL 2
1650 X2 = 0:Q2 = 0
1660  WRDEV,(DV) = 3,(W ) = 2,(D ) = 2
1670  ASUM,(TV)=Q2,(RT)=10,(C )=2,(D )=2,(SW)=1000
1680 X2 = Q2 / 1000
1690 V2 = 5 * 1E3 * (X2 - 2048) / (267.4 * 2048)
1700 T2 = A1 + V2 * (B1 + V2 * (C1 + V2 * (D1 + V2 *
     (E1 + V2 * F1))))
1710  REM  ACTUAL READING ADJUSTMENT ON 11/21/86.
1720 TB = T2 + 273 + 2.5
1730  REM  DETERMINE EMF FROM CHANNEL 2
1740 R = 0
1750  ASUM,(TV)=R,(RT)=10,(D )=0,(C )=2,(SW)=1000
1760 P = R / 1000
1770 V1 = (P - 2048) * (2500 / 2048)
1780  REM  REFERENCE CORRECTION
1790 VB = V1 - 4.25
1800  TIME TO HT,MT,ST
1810  IF HT < PH THEN 1840
1820 PH = HT
1830  GOTO 1870
1840  DAY TO DG,DH,DI,DJ: PRINT
1850  PRINT "DATE "DH"/"DI"/"DG: PRINT
1860 PH = HT
1870  PRINT D$;A2$;F2$
1880  PRINT HT;R$;MT;R$;ST;R$;TB;R$;VB
1890  PRINT D$
1900  RETURN
```

APPENDIX E

OPERATING INSTRUCTION ON
BECKMAN SPECTRASPAN V DC PLASMA ARC
ELEMENTAL EMISSION SPECTROMETER

TURNING ON THE SPECTROMETER

Check cooling water -- change it once a month.
Check electrodes and sleeves -- change them if necessary.
     replace graphite anodes daily (after 8-10 hr usage),
     replace tungsten cathode every 2-4 days or when the
     tip becomes dull.
Check pump and drain tubings -- change them if they appear
     cloudy or discolored.
Push 'PWR' button to turn power on.
Turn on other accessories : fan, printer, and pump.
Press 'ON LINE' on the printer.
Turn on Ar gas -- set sleeves pressure at 50 psi.
Check alignments of anode cooling block and sample tubes.
Push 'READY' to check if the electrodes are touching.
Press 'PLS'.
Push 'RUN' to establish a plasma.
Turn nebulizer pressure to 28 psi.
Push the pump tension rod up to engage the pump.
Turn on the pump motor -- samples are drawn up.

ADJUSTING PLASMA ARC

Turn the anode screw until no noise and vertical "Y" image
     are maintained.
Draw Li solution to obtain a red image/Na solution an
     orange image to increase visibility.
Turn the cathode screw to set tail flame at 45 degrees.
If the flame is not symmetrical, adjust electrode position:
     Take off pump tension.
     Turn off pump.
     Press 'PLS' again to turn off the plasma.
     Turn off nebulizer.
     Turn off Ar gas.
     Put in the special alignment tool on nebulizer tube.
     Align electrodes with eyeballs.

PEAKING

Check the atomic wavelength for the desired element.
Check input and output slit sizes (i.e. 50x300; 25x300 μ).
Draw peaking solution -- e.g. high standard solution.
Input the desired wavelength by turning the vertical and
     horizontal wavelength dial.
Set 'DIAG' switch up.
Set mode '1', time = 20, repeat = 0.
Reset the machine -- Turn 'AVG ONLY'.
                     Wait for 100 to show in digital
display.
                     Turn 'AVG ONLY' down.
                     Press 'RST'.
Adjust amphification by setting 'TIME' dial (6000 counts
     desired).
Adjust the plasma position with the vertical and horizontal
     knots to have the largest signal.
Adjust the wavelength dial to search the position with the
     largest number of counts.

PUTTING IN STANDARDS

Set mode to 'INT', time = 5, repeat = 5.
Push 'DH' and 'DL' to displace high and low standards.
Hit 'RST' button, then 'C' button to clear standard
     settings.
Press 'EH' to enter high standard.
Press 'EL' to enter low standard.
Draw high standard solution.
Press 'A/R' - auto range (only when start or change range)
              also enter high standard automatically.
     or press 'HI STD' to enter high standard.
Press 'data' -- print high standard.
Draw low standard solution.
Press 'LOW STD' to enter low standard.

SAMPLING AND STANDARD RESET

Set mode 'INT', time = 5, repeat = 5.
reset -- may be necessary.
Draw sampling solution for 25 seconds.
Press 'SMP' to analyze samples.
Check high and low standards periodically.
If standards drift off very much, reset standards:
     Draw high/low standard solution.
     Press 'SMP'.
     Press and hold 'DH'/'DL'.
     Press and release 'HI STD'/'LO STD' to reset hi/lo std.
     Release 'DH'/'DL' button after the cycle button light
     goes off.
Run samples and standards together to check drift.

TURNING OFF THE MACHINE

Draw deionized water.
Take the tubing away from the beaker.
Wait 25 seconds.
Take off pump tension.
Turn off the pump.
Press 'PLS' again to turn off the plasma.
Turn nebulizer pressure to zero.
Turn off and purge Ar gas.
Turn off powers of the accessaries -- fan, printer, and pump.
Hit 'PWR' to turn off main power only if the machine will be idle for a long period of time.

APPENDIX F

STANDARD SOLUTIONS
FOR
ANALYSIS OF ALUMINA SOLUBILITY

(1) Primary Standard Solutions
      0.9998 g Al/kg solution
     19.9995 g Na/kg solution

(2) Working Standard Solutions

0.0	mg Al + 1 g Na/kg solution
0.003033	mg Al + 1 g Na/kg solution
0.01029	mg Al + 1 g Na/kg solution
0.1026	mg Al + 1 g Na/kg solution
1.017	mg Al + 1 g Na/kg solution
10.018	mg Al + 1 g Na/kg solution
50.039	mg Al + 1 g Na/kg solution
100.015	mg Al + 1 g Na/kg solution
0.01001	mg Al + 10 g Na/kg solution
0.1004	mg Al + 10 g Na/kg solution

(3) Standard Solutions for Testing Matrix Effects

1	mg Al/liter solution
10	mg Al/liter solution
50	mg Al/liter solution
100	mg Al/liter solution
1	mg Al + 0.4 g Na/liter solution
10	mg Al + 0.4 g Na/liter solution
50	mg Al + 0.4 g Na/liter solution
100	mg Al + 0.4 g Na/liter solution
0.01	mg Al + 1 g Na/liter solution
0.1	mg Al + 1 g Na/liter solution
1	mg Al + 1 g Na/liter solution
10	mg Al + 1 g Na/liter solution
50	mg Al + 1 g Na/liter solution
100	mg Al + 1 g Na/liter solution
1	mg Al + 2 g Na/liter solution
10	mg Al + 2 g Na/liter solution
50	mg Al + 2 g Na/liter solution
100	mg Al + 2 g Na/liter solution

TGA EXPERIMENTAL DATA
OF
SODIUM SULFATE IN PLATINUM CRUCIBLES

Exp. No.	T,K	P_{SO_3},atm.	$X_{Na_2S_2O_7}$
TGA19A	1160	0.0206	0.001515
	1160	0.0453	0.002717
	1160	0.0610	0.003638
	1160	0.0646	0.004400
	1160	0.0799	0.004659
	1160	0.0968	0.005773
	1160	0.1094	0.006264
	1160	0.1158	0.006537
	1160	0.1099	0.006235
	1160	0.0751	0.004419
	1160	0.0391	0.002527
TGA20C	1160	0.0648	0.003470
	1160	0.1158	0.005876
	1160	0.0188	0.001290
	1160	0.0060	0.000513
	1160	0.0376	0.002259
	1160	0.0876	0.004592
	1160	0.0284	0.001619
TGA6A	1200	0.0246	0.000908
	1200	0.0535	0.002089
	1200	0.0699	0.002894
	1200	0.0788	0.003285
	1200	0.0852	0.003593
	1200	0.0703	0.003028
	1200	0.0254	0.001174
	1200	0.0606	0.002641
	1200	0.0862	0.003733
	1200	0.0533	0.002309
TGA19B	1200	0.0300	0.001501
	1200	0.0502	0.002309
	1200	0.0772	0.003114
	1200	0.0209	0.001302
	1200	0.0868	0.003411
TGA20A	1200	0.0199	0.000811
	1200	0.0495	0.001909
	1200	0.0769	0.002936
	1200	0.0869	0.003593
	1200	0.0682	0.002700
	1200	0.0351	0.001737

	1200	0.0843	0.003468
	1200	0.0613	0.002611
	1200	0.0052	0.000645
	1200	0.0225	0.001217
	1200	0.0352	0.001737
	1200	0.0176	0.000940
	1200	0.0576	0.002420
TGA20D	1224	0.0187	0.000415
	1224	0.0735	0.001850
	1224	0.0394	0.001185
	1224	0.0654	0.001953
	1224	0.0521	0.001539
	1224	0.0204	0.000730
	1224	0.0735	0.001985
	1224	0.0303	0.000758
	1224	0.0595	0.001835
TGA6B	1250	0.0382	0.000885
	1250	0.0502	0.001381
	1250	0.0604	0.001765
	1250	0.0178	0.000594
	1250	0.0559	0.001590
	1250	0.0061	0.000249
TGA20B	1250	0.0411	0.000901
	1250	0.0038	0.000155
	1250	0.0615	0.001530
	1250	0.0158	0.000456
	1250	0.0548	0.001368
	1250	0.0209	0.000562

RESULTS OF OTHER INVESTIGATORS EXTRAPOLATED TO 1160 K

1) Data of Flood & Forland [83]

Temp,K	P_{SO_3},atm	$X_{Na_2S_2O_7}$
1160.0	440.77481	0.961000
1160.0	202.70502	0.906100
1160.0	113.04771	0.872800
1160.0	73.68668	0.816200
1160.0	47.77848	0.733300
1160.0	35.80490	0.648000
1160.0	28.36905	0.593900

2) Data of Coats, Dear, & Penfold [84]

Temp,K	P_{SO_3},atm	$X_{Na_2S_2O_7}$
1160.0	90.66293	0.880000
1160.0	110.43289	0.885000
1160.0	159.00710	0.905000
1160.0	176.84602	0.921700
1160.0	190.63991	0.923300
1160.0	191.64180	0.930000
1160.0	241.49538	0.941200
1160.0	256.50018	0.942500
1160.0	278.08322	0.944200
1160.0	289.59882	0.945000

3) Data of Kostin, Pluzhnikov, & Ketov [85]

Temp,K	P_{SO_3},atm	$X_{Na_2S_2O_7}$
1160.0	419.36548	0.971400
1160.0	754.85767	0.982600
1160.0	300.37564	0.954000
1160.0	292.31192	0.951700
1160.0	150.51619	0.936900
1160.0	110.05844	0.916800
1160.0	208.99187	0.948000
1160.0	81.08189	0.895100
1160.0	153.87807	0.934200
1160.0	59.83411	0.857700

1160.0	113.89571	0.920800
1160.0	205.36761	0.958400
1160.0	44.45522	0.820100
1160.0	84.88431	0.898700
1160.0	151.98654	0.939400
1160.0	33.18145	0.768000
1160.0	63.49142	0.863500
1160.0	89.46231	0.914400
1160.0	113.26363	0.929400
1160.0	47.39788	0.846700
1160.0	66.74796	0.882800
1160.0	84.77871	0.908000
1160.0	35.96141	0.783100
1160.0	50.00706	0.813700
1160.0	63.82680	0.871100
1160.0	37.66356	0.810400
1160.0	48.11592	0.870300

APPENDIX I

TGA EXPERIMENTAL DATA
OF
SODIUM SULFATE IN ALUMINA CRUCIBLES

Expt. No.	T, K	P_{SO_3}, atm	X_{SO_3}
TGA17-01	1160	0.0203	0.0323
TGA17-02	1160	0.0441	0.0986
TGA17-03	1160	0.0601	0.1307
TGA17-04	1160	0.0835	0.1641
TGA18-01	1160	0.0203	0.0451
TGA18-02	1160	0.0380	0.0870
TGA18-03	1160	0.0599	0.1286
TGA18-04	1160	0.0703	0.1461
TGA18-05	1160	0.0865	0.1686
TGA18-06	1160	0.0964	0.1773
TGA18-07	1160	0.1093	0.1875
TGA26-04	1200	0.0130	0.0154
TGA26-05	1200	0.0287	0.0327
TGA26-06	1200	0.0411	0.0399
TGA26-07	1200	0.0575	0.0565
TGA26-08	1200	0.0563	0.0565
TGA26-09	1200	0.0662	0.0632

APPENDIX J

EMF EXPERIMENTAL DATA
OF
SODIUM SULFATE IN PLATINUM CRUCIBLES

Expt #	T, K	EMF, mv	P_{SO_3}, atm	log a_{Na_2O}
EMF9	1200.1694	397.3833	0.0450	-15.8456
EMF9	1200.7639	370.8452	0.0255	-15.5858
EMF9	1200.9272	406.1064	0.0604	-15.9434
EMF9	1200.4097	411.2749	0.0727	-16.0298
EMF9	1200.4583	395.1433	0.0836	-16.0998
EMF9	1200.2098	293.8994	0.0358	-15.7473
EMF9	1200.1985	376.4714	0.0738	-16.0548
EMF9	1200.7656	392.8472	0.0409	-15.7939
EMF9	1201.7433	411.7473	0.0761	-16.0362
EMF9	1201.2338	358.2317	0.0178	-15.4647
EMF9	1201.0640	409.2119	0.0658	-15.9830
EMF9	1201.6707	358.5930	0.0185	-15.4638
EMF9	1201.3645	314.0544	0.0072	-15.0800
EMF9	1200.8529	330.1628	0.0099	-15.2237
EMF9	1201.2386	328.3293	0.0088	-15.2029
EMF9	1224.3625	364.1704	0.0348	-15.2992
EMF9	1224.2903	380.5974	0.0526	-15.4785
EMF9	1223.8901	385.0066	0.0654	-15.5699
EMF9	1224.1769	346.8120	0.0232	-15.1373
EMF9	1224.0492	366.3676	0.0705	-15.6061
EMF9	1225.7939	383.9458	0.0591	-15.5150
EMF9	1224.8357	332.3735	0.0163	-15.0009
EMF9	1224.1987	329.5244	0.0163	-14.9839
EMF9	1223.9207	385.6035	0.0657	-15.5765
EMF9	1224.0934	346.8205	0.0233	-15.1383
EMF9	1223.1500	384.8869	0.0657	-15.5773
EMF9	1161.0367	408.6101	0.0247	-16.3573
EMF9	1162.3363	448.3684	0.0681	-16.7408
EMF9	1160.3972	459.9077	0.1058	-16.9555
EMF9	1159.8850	432.8606	0.0449	-16.6033
EMF9	1159.5986	455.7829	0.1146	-16.9853
EMF9	1159.9045	456.1992	0.0879	-16.8737
EMF9	1159.6003	387.8520	0.0733	-16.8084
EMF9	1161.2119	422.0976	0.0354	-16.4833
EMF9	1161.1211	453.2231	0.1137	-16.9477
EMF9	1161.0435	408.2768	0.0257	-16.3554
EMF9	1159.9194	448.1059	0.0701	-16.7697
EMF9	1159.2181	408.7212	0.0253	-16.3805
EMF9	1250.2084	314.0679	0.0196	-14.6073
EMF9	1250.7634	351.8962	0.0594	-15.0682
EMF9	1250.6685	347.0073	0.0414	-14.9227

EMF9	1251.5647	353.6980	0.0541	−15.0271
EMF9	1251.2163	273.7089	0.0078	−14.2517
EMF9	1251.4961	340.5034	0.0337	−14.8399
EMF9	1251.1786	277.7715	0.0378	−14.8927
EMF9	1250.7603	342.3369	0.0603	−15.0963
EMF9	1250.2786	327.5419	0.0248	−14.7260
EMF9	1250.9739	351.7058	0.0605	−15.0888
EMF9	1251.5416	317.6579	0.0201	−14.6246
EMF9	1251.3940	351.9536	0.0603	−15.0853
EMF9	1182.4384	354.7575	0.0123	−15.6349
EMF9	1230.6863	294.7856	0.0090	−14.6230
EMF9	1182.5311	356.4824	0.0123	−15.6486
EMF9	1209.4684	321.6716	0.0103	−15.0623
EMF9	1190.4419	345.3325	0.0117	−15.4658
EMF9	1219.4252	310.0517	0.0096	−14.8625
EMF9	1200.5277	333.1963	0.0109	−15.2538
EMF9	1241.5892	280.5254	0.0084	−14.3995
EMF9	1241.4076	361.4104	0.0645	−15.2629
EMF9	1181.8229	432.8484	0.0979	−16.5189
EMF9	1231.3735	374.2326	0.0691	−15.4722
EMF9	1180.9763	431.7754	0.0985	−16.5199
EMF9	1209.6233	398.3305	0.0804	−15.9073
EMF9	1189.7961	421.0527	0.0924	−16.3244
EMF9	1219.6288	387.4968	0.0749	−15.7073
EMF9	1201.4724	409.7209	0.0851	−16.0943
EMF9	1251.8812	350.7292	0.0601	−15.0698
EMF9	1201.4514	409.0812	0.0851	−16.0891

APPENDIX K

EMF EXPERIMENTAL DATA
OF
SODIUM SULFATE IN ALUMINA CRUCIBLES

Expt #	T,K	EMF,mv	P_{SO_3},atm	log a_{Na_2O}
$O_2/SO_2 = 25.5$				
EMF1	1196.1696	330.3761	0.00824	-15.1394
EMF1	1225.3425	295.1331	0.00683	-14.5498
EMF1	1161.0310	371.2814	0.0103	-15.8754
EMF1	1234.4880	282.7447	0.0643	-14.3598
EMF1	1202.2574	322.1490	0.00792	-15.0067
$O_2/SO_2 = 3.58$				
EMF1	1206.8420	386.2143	0.0395	-15.5402
EMF1	1187.7419	401.8661	0.0449	-15.8813
EMF1	1250.9832	333.6989	0.0295	-14.6602
EMF1	1170.8080	422.9444	0.0503	-16.2551
EMF1	1244.0845	345.2634	0.0309	-14.8208
$O_2/SO_2 = 5.02$				
EMF2	1211.5706	369.1538	0.0298	-15.4631
EMF2	1243.7146	331.9077	0.0241	-14.8230
EMF2	1257.5762	314.9674	0.0221	-14.5500
EMF2	1209.4032	372.0194	0.0303	-15.5104
EMF2	1224.2292	355.0898	0.0274	-15.2120
EMF2	1175.0801	409.8588	0.0380	-16.2187
$O_2/SO_2 = 22.7$				
EMF2	1218.7700	316.5937	0.00757	-14.9205
EMF2	1249.5203	279.7480	0.00621	-14.3139
EMF2	1200.7998	330.8741	0.00850	-15.2285
EMF2	1230.2813	296.2479	0.00703	-14.6362
EMF2	1181.0995	353.4672	0.00966	-15.6362
$O_2/SO_2 = 24.2$				
EMF2	1232.4200	290.3080	0.00623	-14.5653
EMF2	1199.0851	329.6931	0.00772	-15.2360
EMF2	1243.6171	275.0352	0.00580	-14.3315
EMF2	1211.4891	314.0074	0.00713	-14.9736
EMF2	1271.3512	237.8581	0.00486	-13.7754
EMF2	1223.7847	298.3952	0.00659	-14.7181
EMF2	1253.1899	259.8051	0.00546	-14.1175
EMF2	1204.6464	321.7634	0.00745	-15.1102
EMF2	1252.2231	260.9126	0.00549	-14.1355

TGA EXPERIMENTAL DATA
OF
COBALT SULFATE-SODIUM SULFATE

Expt.	T, K	P_{SO_3}, atm	X_{SO_3}
20 m/o $CoSO_4$-Na_2SO_4			
TGA11	1100	0.0205	0.01424
	1100	0.1038	0.05334
	1100	0.1374	0.06860
	1100	0.1741	0.08869
	1100	0.1794	0.09108
	1100	0.1046	0.05423
	1100	0.0670	0.04567
	1100	0.0960	0.05428
TGA16	1100	0.0191	0.00926
	1100	0.0426	0.02583
	1100	0.0695	0.03884
	1100	0.0909	0.04670
	1100	0.1231	0.05880
	1100	0.1581	0.07526
TGA16	1160	0.1030	0.03507
	1160	0.1029	0.03093
	1160	0.1085	0.03171
	1160	0.0297	0.00529
	1160	0.0468	0.01143
	1160	0.0814	0.02274
	1160	0.1159	0.02889
30 m/o $CoSO_4$-Na_2SO_4			
TGA12	1100	0.0204	0.00519
	1100	0.0395	0.01119
	1100	0.0644	0.02031
	1100	0.1762	0.06052
	1100	0.0649	0.02303
	1100	0.0884	0.02522
	1100	0.1126	0.03268
	1100	0.1373	0.04346
40 m/o $CoSO_4$-Na_2SO_4			
TGA13	1100	0.0201	0.00163
	1100	0.0402	0.00420
	1100	0.0647	0.00823
	1100	0.0894	0.01275
	1100	0.1130	0.01781

	1100	0.1209	0.01969
	1100	0.1323	0.02190
	1100	0.1332	0.02398
	1100	0.1490	0.02480
	1100	0.1574	0.02583
	1100	0.1703	0.02986
	1100	0.1794	0.03454

50 m/o $CoSO_4$-Na_2SO_4

TGA14	1100	0.0197	0.00105
	1100	0.0423	0.00247
	1100	0.0664	0.00442
	1100	0.0796	0.00536
	1100	0.0896	0.00611
	1100	0.1061	0.00706
	1100	0.1216	0.00844
	1100	0.1329	0.00902
	1100	0.1445	0.00969
	1100	0.1574	0.01082
	1100	0.1699	0.01230
	1100	0.1794	0.01383
	1100	0.1445	0.01110

EMF EXPERIMENTAL DATA
OF
COBALT SULFATE-SODIUM SULFATE

80.00 m/o Na_2SO_4-$CoSO_4$

Expt #	T,K	EMF,mv	P_{SO_3},atm	log a_{Na_2O}
EC3	1201.8096	348.7216	0.0115	-15.3710
EC3	1171.3630	377.5571	0.0119	-15.9555
EC3	1216.7402	320.8452	0.0089	-14.9783
EC3	1164.5266	384.6154	0.0121	-16.0961
EC3	1197.6543	345.3452	0.0097	-15.3853
EC3	1122.4017	434.3332	0.0158	-17.0585
EC3	1139.9980	415.3305	0.0142	-16.6634
EC3	1041.4650	506.4376	0.0253	-18.8994
EC3	1092.7461	471.4914	0.0189	-17.8004
EC3	1051.5129	515.8359	0.0249	-18.8318
EC3	1110.2214	454.6445	0.0177	-17.4046
EC3	1021.3869	527.0602	0.0289	-19.4287
EC3	1080.6171	486.6831	0.0211	-18.1159
EC3	1150.0968	403.6044	0.0137	-16.4354
EC3	948.1339	550.8151	0.0397	-21.0011
EC3	1069.0726	475.3571	0.0232	-18.1797
EC3	1012.0023	514.4247	0.0311	-19.4616
EC3	1181.8311	359.6457	0.0108	-15.6818
EC3	1070.4395	474.6227	0.0223	-18.1522
EC3	1035.9894	496.9589	0.0268	-18.8950
EC3	998.9582	517.0480	0.0319	-19.7111
EC3	1200.7922	334.8312	0.0098	-15.2634
EC3	1063.9087	477.3375	0.0231	-18.2750
EC3	1096.9755	452.8244	0.0191	-17.5697
EC3	984.8486	531.2436	0.0338	-20.1051
EC3	905.0777	555.8908	0.0429	-21.9446
EC3	1049.4921	472.3910	0.0229	-18.4453
EC3	1201.5234	329.7873	0.0090	-15.2123
EC3	1022.6713	487.1371	0.0276	-19.0133
EC3	926.6614	551.2509	0.0407	-21.4377
EC3	1052.5024	464.2648	0.0237	-18.3220
EC3	1198.9557	323.6972	0.0091	-15.1886
EC8	1198.8416	372.5053	0.0156	-15.6078
EC8	1200.3740	433.3439	0.0813	-16.2587
EC8	1199.5100	419.8564	0.0456	-16.0426
EC8	1199.6079	436.9707	0.0760	-16.2667
EC8	1199.5432	346.8449	0.0083	-15.3759
EC8	1200.1144	431.5812	0.0654	-16.1791
EC8	1199.7852	402.5969	0.0318	-15.8721
EC8	1199.4810	430.9624	0.0856	-16.2848
EC8	1199.9987	403.6979	0.0326	-15.8801

EC8	1199.7406	375.4704	0.0170	-15.6246
EC8	1199.6541	427.7043	0.0869	-16.2858
EC8	1179.7820	453.5051	0.1001	-16.7383
EC8	1236.6151	386.3237	0.0672	-15.5341
EC8	1142.1702	496.9609	0.1315	-17.5953
EC8	1217.3715	410.1970	0.0767	-15.9377
EC8	1051.4574	580.4094	0.2533	-19.7178
EC8	1079.3203	575.2275	0.2078	-19.2171
EC8	1160.7072	487.1623	0.1149	-17.2657
EC8	1091.8278	567.6396	0.1897	-18.9515
EC8	1119.6975	534.3449	0.1549	-18.2364
EC8	1001.7820	641.8596	0.3534	-21.2082
EC8	1106.1161	555.9111	0.1710	-18.6283
EC8	933.0568	570.8476	0.5243	-21.8624
EC8	1025.4474	623.6125	0.3026	-20.5867
EC8	901.3690	553.0937	0.6074	-22.3709
EC8	1035.9176	609.2205	0.2820	-20.2609
EC8	852.3122	712.9765	0.7267	-25.4491
EC8	1049.8064	601.4494	0.2560	-19.9445
EC8	829.2015	709.9284	0.7742	-26.0678

70.02 m/o Na_2SO_4-$CoSO_4$

Expt #	T,K	EMF,mv	P_{SO_3},atm	log a_{Na_2O}
EC5	1200.6050	359.9161	0.0102	-15.4764
EC5	1148.6381	424.8856	0.0143	-16.6403
EC5	1182.0619	384.7329	0.0115	-15.8939
EC5	1125.1343	454.0282	0.0166	-17.1999
EC5	1159.0674	413.5100	0.0134	-16.4128
EC5	1213.6647	345.8120	0.0094	-15.2180
EC5	1096.0012	486.6210	0.0199	-17.8944
EC5	1133.3110	444.5759	0.0158	-17.0087
EC5	1051.5549	536.4682	0.0268	-19.0298
EC5	1052.0205	537.4582	0.0267	-19.0319
EC5	1010.2345	579.4640	0.0329	-20.1410
EC5	1067.7856	522.7890	0.0245	-18.6471
EC5	987.1160	598.1772	0.0363	-20.7487
EC5	1203.1864	376.0714	0.0105	-15.5841
EC5	985.6591	602.3617	0.0349	-20.8181
EC5	1020.9808	571.3498	0.0299	-19.8730
EC5	946.6702	625.9677	0.0387	-21.8297
EC5	1033.0562	559.2788	0.0273	-19.5500
EC5	914.9284	629.4663	0.0421	-22.5441
EC5	1101.9182	486.0275	0.0185	-17.8051
EC5	914.5364	613.6288	0.0420	-22.3782
EC5	1002.3246	588.8266	0.0314	-20.3745
EC5	1200.3190	366.0238	0.0091	-15.5295
EC5	1200.5721	454.1269	0.0805	-16.4260
EC5	1200.8448	376.2863	0.0105	-15.6116
EC5	1200.5107	443.8395	0.0488	-16.2392

Expt #	T,K	EMF,mv	P_{SO_3},atm	log a_{Na_2O}
EC5	1200.4186	417.7438	0.0274	-15.9859
EC5	1201.1060	449.7043	0.0862	-16.4642
EC5	1200.4210	448.9853	0.0571	-16.3009
EC5	1201.0034	362.2983	0.0070	-15.4884
EC5	1200.9653	455.9579	0.0707	-16.3921
EC5	1200.5674	429.3576	0.0347	-16.0924
EC5	1200.4598	405.3488	0.0206	-15.8722

59.96 m/o Na_2SO_4-$CoSO_4$

Expt #	T,K	EMF,mv	P_{SO_3},atm	log a_{Na_2O}
EC2	1200.1825	389.9071	0.0102	-15.7328
EC2	1164.8424	432.8329	0.0129	-16.5103
EC2	1216.4949	370.7534	0.0092	-15.3947
EC2	1145.0510	456.4263	0.0146	-16.9627
EC2	1178.9709	415.1925	0.0117	-16.1898
EC2	1124.8892	478.6435	0.0166	-17.4237
EC2	957.4631	574.8151	0.0387	-21.0720
EC2	916.8396	577.0312	0.0433	-21.9260
EC2	935.5416	572.0353	0.0413	-21.4808
EC2	893.6810	570.6424	0.0455	-22.3612
EC2	969.2613	567.1820	0.0372	-20.7648
EC2	1061.2019	526.6726	0.0243	-18.7845
EC2	1023.3341	546.8939	0.0296	-19.5919
EC2	1078.4207	512.8714	0.0221	-18.3931
EC2	1002.0836	558.9038	0.0326	-20.0783
EC2	1038.2789	538.6532	0.0275	-19.2637
EC2	1093.2059	506.4209	0.0202	-18.1167
EC2	1111.1349	490.0566	0.0181	-17.7138
EC2	1198.9607	389.2392	0.0103	-15.7409
EC2	1111.8636	493.1564	0.0180	-17.7319
EC2	915.1899	579.4979	0.0435	-21.9884
EC2	1201.0597	390.8468	0.0102	-15.7310
EC2	941.0091	570.9323	0.0407	-21.3578
EC2	869.1539	565.8737	0.0473	-22.8707
EC2	1013.5047	550.3122	0.0310	-19.7931
EC2	1050.2233	532.5988	0.0258	-19.0132
EC2	973.0079	563.5168	0.0366	-20.6559
EC2	1027.3508	539.9469	0.0290	-19.4563
EC2	950.5013	564.5285	0.0395	-21.1001
EC2	1070.7474	513.8058	0.0230	-18.5169
EC2	1197.9375	389.9142	0.0104	-15.7580
EC2	1199.0010	390.1364	0.0035	-15.7470
EC2	1197.9108	473.3871	0.0817	-16.6173
EC2	1196.9530	472.4984	0.0672	-16.5611
EC2	1198.9298	447.0626	0.0354	-16.2606
EC2	1198.1245	470.1034	0.0860	-16.6239
EC2	1196.4548	449.8837	0.0362	-16.3133
EC2	1199.6532	465.1889	0.0579	-16.4470
EC2	1199.9526	469.7140	0.0731	-16.5265
EC2	1200.5682	424.6737	0.0226	-16.0358
EC2	1199.4542	431.0361	0.0760	-16.5040

50.01 m/o Na_2SO_4-$CoSO_4$

Expt #	T,K	EMF,mv	P_{SO_3},atm	log a_{Na_2O}
EC9	1198.7655	437.0817	0.0155	-16.1514
EC9	1200.1055	504.8417	0.0803	-16.8541
EC9	1199.9089	480.6413	0.0374	-16.5348
EC9	1199.4307	503.1547	0.0854	-16.8877
EC9	1200.1475	471.9060	0.0308	-16.4486
EC9	1199.7705	504.0092	0.0852	-16.8917
EC9	1200.2616	400.1775	0.0078	-15.8154
EC9	1200.1313	498.3720	0.0586	-16.7221
EC9	1199.9364	458.2902	0.0228	-16.3256
EC9	1199.8037	503.9299	0.0708	-16.8069
EC9	1200.3239	421.9560	0.0113	-16.0016
EC9	1200.5156	491.6838	0.0479	-16.6390
EC9	1200.5488	422.7324	0.0110	-16.0053

49.60 m/o Na_2SO_4-$CoSO_4$

Expt #	T,K	EMF,mv	P_{SO_3},atm	log a_{Na_2O}
EC1	1200.2249	412.3776	0.0102	-15.9211
EC1	1238.4252	350.7257	0.0080	-15.0007
EC1	1144.6377	477.2150	0.0147	-17.1511
EC1	1181.0895	436.2831	0.0116	-16.3450
EC1	1123.9501	497.2031	0.0167	-17.6027
EC1	1160.5444	458.7770	0.0132	-16.7881
EC1	1079.9542	544.4355	0.0219	-18.6649
EC1	1000.7672	600.5380	0.0328	-20.5210
EC1	1059.4541	556.7081	0.0246	-19.0974
EC1	915.6351	637.9135	0.0435	-22.6219
EC1	953.5835	612.1750	0.0392	-21.5431
EC1	1031.2112	573.3261	0.0285	-19.7185
EC1	1100.3763	512.7100	0.0194	-18.0716
EC1	1201.0077	408.8009	0.0102	-15.8822
EC1	1257.3505	337.3410	0.0071	-14.7030
EC1	1105.3674	506.9533	0.0188	-17.9481
EC1	1219.9302	372.2775	0.0090	-15.3706
EC1	953.1581	566.5460	0.0393	-21.0692
EC1	990.2120	564.8056	0.0344	-20.3510
EC1	907.0579	587.6624	0.0444	-22.2552
EC1	1024.4550	557.9376	0.0295	-19.6817
EC1	964.8801	572.4323	0.0378	-20.9033
EC1	1201.0262	399.9770	0.0102	-15.8080
EC1	1273.4250	305.2206	0.0064	-14.2928
EC1	1009.9510	548.7079	0.0315	-19.8385
EC1	968.3431	553.0518	0.0373	-20.6352
EC1	1045.5193	531.8228	0.0265	-19.0807
EC1	945.3695	565.1193	0.0402	-21.2082
EC1	1022.4596	543.1787	0.0297	-19.5700
EC1	999.9274	552.5504	0.0329	-20.0525

Expt #	T,K	EMF,mv	P_{SO_3},atm	log a_{Na_2O}
EC1	946.7335	558.8156	0.0401	−21.1139
EC1	998.4297	549.2783	0.0332	−20.0461
EC1	1036.4967	535.4008	0.0278	−19.2612
EC1	977.4063	553.5654	0.0361	−20.4709
EC1	1071.6543	518.2409	0.0229	−18.5450
EC1	929.0718	574.1657	0.0421	−21.6372
EC1	947.4382	565.8823	0.0400	−21.1752
EC1	1199.6976	394.2844	0.0102	−15.7750
EC1	946.8648	583.5727	0.0401	−21.3749

39.76 m/o Na_2SO_4-$CoSO_4$

Expt #	T,K	EMF,mv	P_{SO_3},atm	log a_{Na_2O}
EC4	1200.3417	447.1750	0.0099	−16.2115
EC4	1165.8391	475.0116	0.0124	−16.8624
EC4	1215.7247	399.5230	0.0089	−15.6411
EC4	1138.9301	486.0403	0.0147	−17.3029
EC4	1174.4686	452.9855	0.0113	−16.5664
EC4	1209.7908	397.5095	0.0090	−15.6891
EC4	1136.2085	486.4442	0.0145	−17.3420
EC4	1187.4165	438.0396	0.0113	−16.2855
EC4	1113.3459	520.5453	0.0182	−17.9595
EC4	1073.2535	555.4174	0.0227	−18.8699
EC4	1143.0195	496.0904	0.0148	−17.3385
EC4	1047.8359	575.0430	0.0248	−19.4588
EC4	1083.3075	547.0674	0.0204	−18.6383
EC4	1024.8002	603.7428	0.0279	−20.1257
EC4	1110.8257	526.2379	0.0173	−18.0458
EC4	1042.5756	583.4722	0.0251	−19.6265
EC4	981.7894	648.1977	0.0331	−21.3606
EC4	1050.0819	582.8684	0.0241	−19.4972
EC4	1196.9490	413.2980	0.0098	−15.9652
EC4	1050.9529	565.3439	0.0239	−19.3149
EC4	1086.4141	538.3900	0.0203	−18.5114
EC4	1033.1680	585.0412	0.0272	−19.7995
EC4	1149.0422	482.2775	0.0137	−17.1383
EC4	1078.8861	549.5873	0.0212	−18.7288
EC4	1113.5774	518.1705	0.0172	−17.9342
EC4	1019.8607	603.7619	0.0290	−20.2122
EC4	963.9250	623.9072	0.0365	−21.4594

Sample Analysis of $CoSO_4$-Na_2SO_4

(1) 29.98 m/o Na_2SO_4 (O_2/SO_2=19.3)

[The microstructure of quenched samples from liquid is
supposed to be pure cobalt sulfate encased by ε
in the eutectic of ε+β or ε+δ eutectic. At 863K, there are
33% cobalt sulfate and 67% liquid. The equilibrium phases
are: liquid until 1048K, liquid+cobalt sulfate until 863K,
liquid+ε until 840K.]

Sample	T,K phase	Descriptions
EC6B	1228.6663 liquid	Scattered starlike structures (d=90μm). The starlike structure seems to be the primary phase surrounded by a matrix of rough surface. However, it is not pure cobalt sulfate because Na is also detected. No ε phase is noted. The starlike structures possess a higher concentration of Co than in the matrix.
EC6A	1107.0152 liquid	Rough surface, no distinct structure is identified.
EC6C	1007.8597 $CoSO_4$+liq.	Densely packed oval plates (a=4.9μm, b=1.8μm)*. They are not cobalt sulfate because Na is detected. The primary phase of cobalt sulfate and ε are not found.

* a = longitudinal dimension of an oval plate.
  b = transverse dimension of an oval plate.

(2) 30.04 m/o Na_2SO_4 (O_2/SO_2=19.3)

[The microstructure of samples quenched from liquid is
supposed to be pure cobalt sulfate encased by ε
in the eutectic of ε+β or ε+δ eutectic. At 863K, there are
33% cobalt sulfate and 67% liquid. The equilibrium phases
are: liquid until 1048K, liquid+cobalt sulfate until 863K,
liquid+ε until 840K.]

Sample	T,K phase	Descriptions
EC7D	1232.6674 liquid	Scattered oval plates (a=10μm, b=6.3μm). The oval plates are encased completely by a thin layer of about 0.5μm in a rough matrix. If the oval plates are cobalt sulfate, the thin layer and the matrix will be the ε and eutectic, respectively. However, EDX reveals substantial Na in the oval plates. Oval plates have lower concentration of Co than matrix.
EC7A	1222.6066 liquid	Scattered oval plates (a=1.9μm, b=0.9μm), scattered nodular particles, d=9μm. Neither the oval plates nor the nodular particles are cobalt sulfate phase, since Na is detected. The ε phase is not apparent at the outer surface of the two sturctures. Both grains have lower concentration of Co than matrix.
EC7E	1138.9021 liquid	Starlike structures, d=50μm. The starlike structures are not pure cobalt sulfate. The ε phase is not observed. The structures possess lower concentration of Co than the matrix.
EC7B	1095.8928 liquid	Segregation bands, width=25μm. No pure cobalt sulfate and other primary phase are observed. The segregation bands have a much higher Co concentration than the matrix.
EC7C	1059.2004 liquid	Segregation needles, width=10μm, and nodular particles, d=2μm. No pure cobalt sulfate is observed. The segregation needles have a higher Co concentration than the matrix. The ε phase is not apparent at the outer surface of the two structures.
EC7F	1007.5302 $CoSO_4$+liq.	Coarse dendrites. No pure cobalt sulfate phase is detected. Co, Na, and S are found in the dendrites and the matrix. Dendrites have a higher concentration of Co than the matrix.

EC7G	896.6214 CoSO4+liq.	Segregation patches of Co or Co oxide. No pure cobalt sulfate phase is found. Only Co is essentially detected in the segregation patches.
EC7H	872.9635 CoSO4+liq.	Segregation patches of Co or Co oxide. No pure cobalt sulfate phase is found. Only Co is essentially detected in the segregation patches.

(3) 39.76 m/o Na_2SO_4 (O_2/SO_2=19.3)

[The microstructure of samples quenched from liquid is supposed to be pure cobalt sulfate encased by ε in the matrix of $\varepsilon+\beta$ or $\varepsilon+\delta$ eutectic. At 863K, there are 10% cobalt sulfate and 90% liquid. The equilibrium phases are: liquid until 923K, liquid+cobalt sulfate until 860K, liquid+ε until 840K. The EMF break locates at 1125K]

Sample	T,K phase	Descriptions
EC4A	1050.0819 liquid	Densely packed oval plates (a=2.3μm, b=0.7μm). Pure cobalt sulfate and ε is not detected, since Na is also detected in the oval plates.

(4) 49.60 m/o Na_2SO_4 (O_2/SO_2=19.3)

[The microstructure of samples quenched from liquid is supposed to be the $\varepsilon+\beta$ or $\varepsilon+\delta$ eutectic with small amount of ε. In the $\varepsilon+\beta$ eutectic, there are 37% ε and 63% β. The EMF break locates at 1120K.]

Sample	T,K phase	Descriptions
EC1B	1199.6069 liquid	Scattered nodular particles, d=4μm. The particle and the matrix might be either δ or ε; however, their EDX analyses do not correspond very well to those of δ and ε.

(5) 59.96 m/o Na_2SO_4 (O_2/SO_2=19.3)

[The microstructure of samples quenched from liquid is
supposed to be cored β in a matrix of ε+β or δ+β
eutectic. At 841K, there are 63% β and 37% liquid. The
equlibrium phases are: liquid until 873K, liquid+β
until 841K. The EMF break locates at 1110K.]

Sample	T,K phase	Descriptions
EC2B	1201.0597 liquid	Rough surface with circular ropy areas (d=100μm) in a smoother and darker matrix. No distinct plates is noted in the ropy areas.
EC2C	1064.0710 liquid	Densely packed oval plates (a=14μm, b=9μm) concentrated in lighter circular areas in a dark matrix. Diameter of the circular areas is about 100μm. Higher concentration of Co is detected in the dark matrix. The lighter areas of oval plates and dark matrix might be β and eutectic phases, respectively. However, moles ratios of of the two structures do not match with those of the expected phases.
EC2D	941.0091 liquid	Densely packed oval plates (a=1.9μm, b=0.6μm) concentrated in lighter circular areas (d=120μm) in a less ropy matrix. Cored striations are observed in the plates. The cored plates might be β while the matrix might be eutectic.
EC2A	915.1899 liquid	Rough surface with circular ropy areas (d=50 to 100μm) in a smoother and darker matrix. No distinct densely packed plate is noted in the ropy areas.

(6) 70.02 m/o Na_2SO_4 (O_2/SO_2=19.3)

[The microstructure of samples quenched from liquid is
supposed to be cored β phase in a matrix of δ+β
or ε+β eutectic. The equilibrium phases are:
liquid until 955K, liquid+β until 882K. The EMF break
locates at 1076K.]

Sample	T,K phase	Descriptions
EC5B	1200.6159 liquid	Scattered oval plates (a=2.7μm, b=1.7μm) in a grainy matrix. The oval plates is observed to have a layered morphology.
EC5A	1002.3246 liquid	Densely packed oval plates (a=1μm, b=0.6μm) are observed over the entire specimen. Matrix is not very apparent.

(7) 80.00 m/o Na_2SO_4 (O_2/SO_2=19.3)

[The microstructure of samples quenched from liquid is supposed to be cored β phase in a matrix of δ+β or ϵ+β eutectic. The β phase is supposed to occupy a larger portion of the sample than the eutectic. The equilibrium phases are: liquid until 1048K, liquid+β until 965K. The EMF break locates at 1090K.]

Sample	T,K phase	Descriptions
EC3B	1201.5234 liquid	Rough grainy surface. The surface might be made up of packed plates of less than 1μm in longitudinal dimension.
EC3D	1052.5024 liquid	Scattered oval plates (a=1.6μm, b=0.9μm) are observed in a grainy matrix.

(8) 80.01 m/o Na_2SO_4 (O_2/SO_2=0.562)

[The microstructure of samples quenched from liquid is supposed to be cored β phase in a matrix of δ+β or ϵ+β eutectic. The β phase is supposed to occupy a larger portion of the sample than the eutectic. The equilibrium phases are: liquid until 1048K, liquid+β until 965K. The EMF break locates at 1090K. Samples are equilibrated at a higher pressure of SO_3]

Sample	T,K phase	Descriptions
EC8A	1199.6540 liquid	Scattered oval plates (a=12μm, b=6μm) are noted in a grainy matrix. High Co concentration is detected in the oval plates than in the matrix. However, the eutectic matrix is supposed to possess a higher concentration of Co.
EC8D	1160.7072 liquid	Coarse dendrites. No plate-like structure or other phase is observed. The dendrites are likely to be the cored β phase surrounded by a eutectic matrix.
EC8C	1079.3202 liquid	Fine dendritic patterns. No plate-like sturcture or other phase is observed. The dendrites are likely to be the cored β phase surrounded by a eutectic matrix. The dentrite has a lower concentration of Co than the matrix, this observation is consistent with the phase diagram.
EC8B	1051.4574 liquid	Very coarse dendritic patterns. No plate-like structure or other phase is observed.
EC8E	1001.7820 β+liquid	Scattered/clustered oval particles (a=23μm, b=10μm) in a grainy matrix. The oval plates have a much higher concentration of Co then the matrix.

EDX DATA
OF
COBALT SULFATE-SODIUM SULFATE

(1) 29.98 m/o Na_2SO_4 (O_2/SO_2=19.3)

				Wt %		
	Sample	Na	Co	S	Si	Al
EC6B	starlike structures	21.68	35.84	40.55	1.07	0.86
EC6B	matrix	27.23	29.07	41.39	1.32	0.98
EC6C	oval plates	21.39	37.72	38.55	1.18	1.16

(2) 30.04 m/o Na_2SO_4 (O_2/SO_2=19.3)

				Wt %		
	Sample	Na	Co	S	Si	Al
EC7D	oval plates	16.63	36.66	44.70	1.16	0.85
EC7D	matrix	13.52	42.71	41.88	1.15	0.73
EC7A	oval plates	21.42	39.61	37.54	0.80	0.62
EC7A	nodular particles	20.73	35.84	40.93	1.37	1.15
EC7A	matrix	13.10	43.25	42.26	0.96	0.43
EC7A	matrix	17.87	38.72	41.73	1.10	0.59
EC7E	starlike structures	12.21	46.05	40.43	0.96	0.36
EC7E	matrix	9.78	48.41	40.63	0.84	0.34
EC7B	segregation bands	8.04	53.81	36.35	1.09	0.71
EC7B	matrix	17.41	40.17	40.51	1.16	0.74
EC7C	segregation needles	7.52	55.40	34.74	1.29	1.05
EC7C	matrix	12.31	46.21	39.42	1.19	0.88
EC7C	matrix	14.10	43.08	40.81	1.19	0.83
EC7F	overall analysis	21.09	40.09	36.57	1.21	1.05
EC7F	coarse dendrites	6.53	52.55	40.37	0.54	0.00
EC7F	matrix	23.93	38.69	35.43	1.07	0.87
EC7G	segregation patches	0.00	99.93	0.07	0.00	0.00
EC7G	matrix	14.20	44.15	39.81	1.15	0.69
EC7H	segregation patches	0.16	99.30	0.08	0.30	0.16
EC7H	matrix	11.30	50.25	35.80	1.34	1.30

(3) 39.76 m/o Na_2SO_4 (O_2/SO_2=19.3)

Sample		Na	Co	Wt % S	Si	Al
EC4A	oval plates	12.08	43.30	40.16	2.32	2.13
EC4A	matrix	7.31	59.90	28.43	2.63	1.74

(4) 49.60 m/o Na_2SO_4 (O_2/SO_2=19.3)

Sample		Na	Co	Wt % S	Si	Al
EC1B	nodular particles	19.02	35.46	43.85	/	1.66
EC1B	matrix	14.95	39.37	44.09	/	1.59

(5) 59.96 m/o Na_2SO_4 (O_2/SO_2=19.3)

Sample		Na	Co	Wt % S	Si	Al
EC2C	oval plates	17.39	35.69	45.98	/	0.93
EC2C	oval plates	20.63	34.42	44.06	/	0.89
EC2C	dark matrix	15.36	37.13	46.27	/	1.24
EC2D	oval plates	14.80	35.76	46.44	1.82	1.17
EC2D	oval plates	15.36	36.40	43.03	2.31	2.87
EC2D	matrix	19.52	35.15	43.27	/	2.06
EC2A	circular ropy area	14.91	41.12	42.45	/	1.49
EC2A	dark matrix	15.03	37.32	46.31	/	1.33
EC2A	transition zone	12.44	41.27	44.95	/	1.33

(6) 70.02 m/o Na_2SO_4 (O_2/SO_2=19.3)

Sample		Na	Co	Wt % S	Si	Al
EC5B	oval plates	10.59	37.22	48.78	2.27	1.12
EC5B	oval plates	10.27	41.82	44.51	1.38	1.98
EC5A	oval plates	18.47	21.86	50.51	3.54	5.59

(7) 80.00 m/o Na_2SO_4 $(O_2/SO_2=19.3)$

	Sample	Na	Co	Wt % S	Si	Al
EC3D	oval plates	7.29	59.84	28.49	2.63	1.72
EC3D	oval plates	17.57	29.59	42.30	1.29	9.27

(8) 80.01 m/o Na_2SO_4 $(O_2/SO_2=0.562)$

	Sample	Na	Co	Wt % S	Si	Al
EC8A	oval plates	14.62	38.48	44.86	1.11	0.94
EC8A	matrix	17.46	29.48	50.88	0.97	1.21
EC8D	dendrites	16.18	25.19	51.68	1.04	5.90
EC8C	dendrites	19.83	21.03	51.79	1.23	6.13
EC8C	matrix	18.22	24.32	52.11	1.32	4.03
EC8B	dendrites	24.11	23.38	48.40	1.08	3.03
EC8E	oval plates	9.05	47.80	41.06	1.23	0.87
EC8E	oval plates	7.07	49.17	42.42	0.87	0.47
EC8E	matrix	12.02	25.84	54.85	1.27	6.01

APPENDIX P

EDX Analysis of $CoSO_4-Na_2SO_4$

(1) 29.98 m/o Na_2SO_4 ($O_2/SO_2=19.3$)

Sample		moles ratios			
		Co/Na	S/Co	S/Na	(Na+Co)/S
EC6B	starlike structures	0.64	2.08	1.34	1.23
EC6B	matrix	0.42	2.62	1.09	1.29
EC6C	oval plates	0.70	1.88	1.32	1.29

(2) 30.04 m/o Na_2SO_4 ($O_2/SO_2=19.3$)

Sample		moles ratios			
		Co/Na	S/Co	S/Na	(Na+Co)/S
EC7D	oval plates	0.86	2.24	1.93	0.96
EC7D	matrix	1.23	1.80	2.22	1.00
EC7A	oval plates	0.72	1.74	1.26	1.37
EC7A	nodular particles	0.67	2.09	1.41	1.18
EC7A	matrix	1.28	1.79	2.31	0.99
EC7A	matrix	0.84	1.98	1.67	1.10
EC7E	starlike structures	1.47	1.61	2.37	1.04
EC7E	matrix	1.93	1.54	2.98	0.98
EC7B	segregation bands	2.61	1.24	3.24	1.11
EC7B	matrix	0.90	1.82	1.64	1.15
EC7C	segregation needles	2.87	1.13	3.24	1.19
EC7C	matrix	1.46	1.57	2.29	1.07
EC7C	matrix	1.19	1.74	2.07	1.05
EC7F	overall analysis	0.95	1.30	1.24	1.57
EC7F	coarse dendrites	3.14	1.41	4.44	0.93
EC7F	matrix	0.63	1.68	1.06	1.54
EC7G	segregation patches	Na=0,	Co=1.695,	S=0.00218	
EC7G	matrix	1.21	1.65	2.01	1.10
EC7H	segregation patches	Na=0.007,	Co=1.692,	S=0.002	
EC7H	matrix	1.73	1.31	2.27	1.20

(3) 39.76 m/o Na$_2$SO$_4$ (O$_2$/SO$_2$=19.3)

Sample		Co/Na	moles ratios S/Co	S/Na	(Na+Co)/S
EC4A	oval plates	1.39	1.70	2.38	1.01
EC4A	matrix	3.20	0.87	2.79	1.50

(4) 49.60 m/o Na$_2$SO$_4$ (O$_2$/SO$_2$=19.3)

Sample		Co/Na	moles ratios S/Co	S/Na	(Na+Co)/S
EC1B	nodular particles	0.72	2.27	1.65	1.04
EC1B	matrix	1.02	2.06	2.11	0.95

(5) 59.96 m/o Na$_2$SO$_4$ (O$_2$/SO$_2$=19.3)

Sample		Co/Na	moles ratios S/Co	S/Na	(Na+Co)/S
EC2B	circular area & matrix	0.58	2.49	1.46	1.08
EC2C	oval plates	0.80	2.37	1.89	0.94
EC2C	oval plates	0.65	2.35	1.53	1.08
EC2C	dark matrix	0.94	2.28	2.16	0.89
EC2D	oval plates	0.94	2.40	2.25	0.86
EC2D	oval plates	0.92	2.10	2.00	0.96
EC2D	matrix	0.70	2.26	1.58	1.07
EC2A	circular ropy area	1.07	1.89	2.04	1.01
EC2A	dark matrix	0.96	2.28	2.21	0.89
EC2A	transition zone	1.29	2.00	2.59	0.88

(6) 70.02 m/o Na$_2$SO$_4$ (O$_2$/SO$_2$=19.3)

Sample		Co/Na	moles ratios S/Co	S/Na	(Na+Co)/S
EC5B	oval plates	1.43	2.40	3.45	0.70
EC5B	oval plates	1.58	1.90	3.11	0.83
EC5A	oval plates	0.36	4.20	1.53	0.89

(7) 80.00 m/o Na_2SO_4 (O_2/SO_2=19.3)

Sample		moles ratios			
		Co/Na	S/Co	S/Na	(Na+Co)/S
EC3D	oval plates	3.20	0.87	2.80	1.50
EC3D	oval plates	0.65	2.60	1.73	0.96

(8) 80.01 m/o Na_2SO_4 (O_2/SO_2=0.562)

Sample		moles ratios			
		Co/Na	S/Co	S/Na	(Na+Co)/S
EC8A	oval plates	1.02	2.14	2.20	0.92
EC8A	matrix	0.65	3.17	2.09	0.79
EC8D	dendrites	0.60	3.77	2.29	0.70
EC8C	dendrites	0.41	4.53	1.87	0.75
EC8C	matrix	0.52	3.94	2.05	0.74
EC8B	dendrites	0.37	3.89	1.47	0.93
EC8E	oval plates	2.06	1.58	3.26	0.93
EC8E	oval plates	2.72	1.58	4.31	0.86
EC8E	matrix	0.84	3.90	3.27	0.56

Note:

Phase	moles ratios			
	Co/Na	S/Co	S/Na	(Na+Co)/S
ε	1.50	1.30	2.00	1.25
δ	0.50	2.00	1.00	1.50
γ	0.16	4.00	0.60	1.75
β of eutectic at 841K	0.25	3.00	0.75	1.66

where $\varepsilon = Na_2SO_4 \cdot 3CoSO_4$

$\delta = Na_2SO_4 \cdot CoSO_4$

$\gamma = 3Na_2SO_4 \cdot CoSO_4$

$\beta = 2Na_2SO_4 + CoSO_4$ at max. solubility at 841K

This appendix consists of a detailed discussion on the errors found in the calculated partial pressure of SO$_3$ in the thermogravimetric experiments. The summary of this discussion is listed in Table 6-1. According to the method outlined by Beers [115] and Baird [116], the summation of errors in quantity V due to quantities x, y . . . is given by

$$S_V = [(\partial V/\partial x)^2 \cdot (S_x)^2 + (\partial V/\partial y)^2 \cdot (S_y)^2 + \cdot \cdot \cdot]^{1/2} \quad (Q-1)$$

where S$_i$ is the standard deviation of the quantity i and can be replaced by the uncertainty in i. The above equation (Q-1) applies when the errors in the quantities, such as x, y, · · ·, are independent of each other.

In accordance with the reaction (4-1), the partial pressure of SO$_3$ is obtained by

$$\log P_{SO_3} = \log P_{SO_2} + \frac{1}{2} \log P_{O_2} - \frac{\Delta G^o_{4-1}}{2.303RT} \quad (Q-2)$$

The partial pressure of SO$_3$ is thus influenced by the uncertainties in temperature, O$_2$ flowrate, SO$_2$ flowrate, and published thermodynamic data on ΔG^o_{4-1}.

Q.1 ERRORS IN TEMPERATURE

The partial pressure of SO_3 is affected by the uncertainties in temperature which include (1) calibrations of thermocouple, (2) calibrations of potentiometer, and (3) measurements by thermocouple. DeYoung [94] has concluded that impurities in the gold wire can result an error of ± 0.08 mv in the calibration of thermocouple. This translates to a systematic error of ± 0.8K in temperature. The potentiometer used in the TGA experiments has been calibrated recently and checked periodically against other potentiometers in the laboratory; therefore, no systematic error is noted. Due the uncertainties in temperature fluctuation, thermal gradient, and positioning of the thermocouple, a random error of ± 1.0 K is estimated. Application of equation (Q-1) yields a total error of ± 1.3 K in temperature. Thus, an error of ± 0.0037 in log P_{SO_3} is found.

Q.2 ERRORS IN GAS PRESSURES

The uncertainties in the O_2 and SO_2 flowrates are resulted from the errors in (1) measuring the height of the fluid in the flowmeters and in (2) calibrating the flowmeters. The uncertainties in measurements of the height of the fluid in the capillary flowmeters which is determined to be ± 0.05 cm cause a random error of ± 0.0005 in log P_{SO_3} both in the O_2 flowmeter and in the SO_2 flowmeter. The uncertainties in the calibration of the capillary flowmeters

is estimated to $\pm1.5\%$ of the measured flowrates. A systematic error of ±0.0062 in log P_{SO_3} in both flowmeters is yielded by the calibrations. Consequently, the O_2 and SO_2 supplies cause a total error of ±0.0088 in log P_{SO_3} after applying equation (Q-1).

Q.3 ERRORS IN THERMODYNAMIC DATA

The thermodynamic data taken from the JANAF Tables [104] show that uncertainties of ±55 cal/mol and ±172 cal/mol are inherited in the standard free energies of formation of SO_2 and SO_3 gases, respectively. The ΔG°_{4-1} in equation (Q-2) thus possesses an uncertainty of ±180 cal/mol. Application of equation (Q-2) yields a systematic error of ±0.054 in log P_{SO_3} at 1200 K.

Q.4 SUMMARY OF ERRORS

As a conclusion, the total maximum error in log P_{SO_3} of ±0.055 is estimated. Most of the error is contributed by the uncertainties in the published thermodynamic data which account for an error in log P_{SO_3} of ±0.054 alone; while, an error in log P_{SO_3} of ±0.0095 which includes both random and systematic errors is resulted from the TGA experiment.

APPENDIX R

ERROR ANALYSIS IN MOLE FRACTION OF SO_3 OR $Na_2S_2O_7$

This appendix is focused on the errors in the calculation of the mole fraction of SO_3 or $Na_2S_2O_7$ obtained from the thermogravimetric experiments. The summary of the analysis is shown in Table 6-2. The accuracy of the mole fraction of SO_3 or $Na_2S_2O_7$ is affected by (1) weight measurement, (2) temperature, (3) gas pressures, (4) melt composition, and (5) thermodynamic data reported in the literature.

R.1 ERRORS IN WEIGHT, TEMPERATURE, AND GAS PRESSURES

The uncertainty in the weight measured by the thermobalance is estimated to be $\pm 0.0005g$ which is created by the convective effects of the gases in the reactor, the sensitivity of the balance, and the temperature fluctuations. This has caused a random error of ± 0.00044 in $\log X_{SO_3}$ or $\log X_{Na_2S_2O_7}$. The buoyancy effect have been taken into account by running a control experiment at different gas pressures encountered in actual experiments. At the same time, the thermobalance is calibrated before each experiment. Therefore, no systematic error in thermobalance measurement is noted.

The total errors in the pressure of SO_3 caused by uncertainties in temperature and gas pressures is noted in Table 6-1 to ± 0.0095 in $\log P_{SO_3}$. The slope of the maximum

solubility of SO_3^- in Na_2SO_4 contained in Al_2O_3 crucibles at 1160 K is evaluated graphically to be 0.15 in $\Delta X_{SO_3}/\Delta \log P_{SO_3}$; hence, an error of ± 0.0014 in $\log X_{SO_3}$ or $\log X_{Na_2S_2O_7}$ is produced.

R.2 ERRORS IN MELT COMPOSITION

The errors in X_{SO_3} due to uncertainties in melt composition are caused by the uncertainties in (1) weighing chemicals, (2) impurities in chemicals, and (3) absorption of moisture by chemicals.

The uncertainty in weighing is estimated to be ± 0.001g which yields a systematic error of ± 0.00088 in $\log X_{SO_3}$ or $\log X_{Na_2S_2O_7}$.

The purities of Na_2SO_4 and $CoSO_4$ listed in Appendix A are 99.991% and 99.859%, respectively. The impurities in Na_2SO_4 create an uncertainty of ± 0.0011 mole percent in both Na_2SO_4 and $CoSO_4$. Whereas, the impurities in $CoSO_4$ produce an uncertainty of ± 0.015 mole percent in both sulfates. A maximum systematic error of ± 0.00056 in $\log X_{SO_3}$ or $\log X_{Na_2S_2O_7}$ is produced by the impurities.

The absorption of moisture by $CoSO_4$ during weighing is estimated to be 0.0008g after the dehydration process of the $CoSO_4 \cdot 7H_2O$. This results a systematic error of ± 0.0004 in $\log X_{SO_3}$ or $\log X_{Na_2S_2O_7}$. Having dried with heat and vacuum, the sodium sulfate of anhydrous grade is noted to have no moisture pick-up during weighing.

R.3 ERRORS IN PUBLISHED THERMODYNAMIC DATA

With reference to Section O.3, an uncertainty in log P_{SO_3} of ±0.054 is caused by the published thermodynamic data. This creates a systematic error of ±0.0081 in log X_{SO_3} or log $X_{Na_2S_2O_7}$ based on the maximum SO_3 solubility results in alumina crucibles.

R.4 SUMMARY OF ERRORS

As a conclusion, an error of ±0.0018 in log X_{SO_3} or log $X_{Na_2S_2O_7}$ is a result of the TGA experiment alone. While, the thermodynamic data reported in the literature produce an error of ±0.0081 in log X_{SO_3} or log $X_{Na_2S_2O_7}$. The total error is calculated to be ±0.0083 in log X_{SO_3} or log $X_{Na_2S_2O_7}$. The TGA experiment is thus rated with high accuracy.

APPENDIX S

ERROR ANALYSIS IN ACTIVITY OF $Na_2O(l)$

This appendix is focused on the errors in the activity of sodium oxide measured in the electrochemical cell experiments. The analysis is summarized in Table 6-3. The calculation of the activity of $Na_2O(l)$ in the sulfate melt can be evaluated by equation (4-6) which may be rewritten as

$$\log a_{Na_2O,w} = a + \frac{b}{T} + \frac{1}{2} \log P_{O_2,w} - \frac{2FE}{2.303RT} \qquad (S-1)$$

where $a_{Na_2O,w}$ and $P_{O_2,w}$ are the activity of sodium oxide in the working melt and the partial pressure of oxygen above the working, respectively. The term $a + b/T$ represents the $\log a_{Na_2O}$ in the reference melt. The value of b for a 55 m/o WO_3-Na_2O is determined by Lin and Elliott [68] to be approximately -12,000. Applying equation (Q-1), the error in the activity of Na_2O can be calculated as follows:

$$S^2_{\log a_{Na_2O}} = (\frac{-b}{T^2} + \frac{2FE}{2.303RT^2})^2 S_T^2 + \frac{1}{2}^2 S^2_{\log P_{O_2}} + (\frac{-2F}{2.303RT})^2 S_E^2 \qquad (S-2)$$

Hence, the activity of sodium oxide is a function of temperature, cell potential, and log partial pressure of oxygen. The melt composition and the thermodynamic data reported in the literature also influence the activity of Na_2O.

S.1 ERRORS IN TEMPERATURE

Due the uncertainties in temperature fluctuation, thermal gradient, and positioning of the thermocouple, a random error of ±1.0 K is estimated in measurments by the thermocouple. The Cyborg ISAAC data-acquisition system operates with an accuracy of ±0.3 mv for each temperature sampling. Since an experimental point is an average of 1000 samplings, a systematic error of ±0.009 mv which is equilivalent ±1 K is noted. The other source of error is the impurities in the gold wire used in thermocouple calibration. This can produce a systematic error of ±0.8 K as it is shown by DeYoung [94]. Consequently, a total error in temperature amounts to ±1.6 K according to the equation (Q-1).

S.2 ERRORS IN CELL POTENTIAL

Because of temperature fluctuations in the electrochemical cell, the EMF measurement is estimated to have a random error of ±1.0 mv. The precision of the ISAAC system in cell EMF measurements is ±2.5 mv for each sampling. Each EMF experimental point represents an average of 1000 samplings. The systematic error caused by this uncertainty in sampling is ±0.079 mv. Application of the equation (Q-1) yields a total error of 1 mv in cell potential.

S.3 ERRORS IN OXYGEN PARTIAL PRESSURE

In accordance with the reaction (4-1), the partial pressure of O_2 can be evaluated by

$$\log P_{O_2} = 2 \log \left(\frac{P_{SO_3}}{P_{SO_2}} \right) + \frac{2\Delta G^{\circ}_{4-1}}{2.303RT} \qquad (S-3)$$

The partial pressure is affected by the uncertainties in (1) O_2 and SO_2 gas input, (2) temperature, and (3) thermodynmic data in the literature.

The uncertainty of ±0.05 cm in measuring the height of the fluid in capillary flowmeters causes uncertainties in $\log P_{O_2}$ of ±0.0011 and ±0.0012 in O_2 and SO_2 flowmeter, respectively. These uncertainties yield a total random error of ±0.0016 in $\log P_{O_2}$. The calibration of O_2 and SO_2 flowmeters is estimated to possess an uncertainty of $\pm1.5\%$ of the measured flowrates; thus, systematic errors of ±0.0036 in $\log P_{O_2}$ are noted in both flowmeters. the temperature fluctuation of ±1.0 K in the EMF cell creates a random error in $\log P_{O_2}$ of ±0.00013. Finally, the uncertainty in the standard free energy of reaction (4-1) is found to be ±180 cal/mol as it is shown in section O.3. The published thermodynamic data cause a systematic error of ±0.0054 in $\log P_{O_2}$. Applying equation (Q.1), the total error in $\log P_{O_2}$ is ±0.0076.

With the employment of equation (S-2) and the maximum cell potential of 0.4 v registered at 1200 K, the errors in temperature, cell potential, and pressure of oxygen produce an error of ± 0.013 in log a_{Na_2O}.

S.4 ERRORS IN MELT COMPOSITION

The melt composition is another source of error in the activity of Na_2O. The errors in melt composition include uncertainties in (1) the melt composition of the $CoSO_4-Na_2SO_4$, (2) composition of the reference melt, (3) impurities in the $CoSO_4$ and Na_2SO_4, (4) absorption of moisture by $CoSO_4$, and (5) impurities in reference melt.

An uncertainty in weighing of ± 0.001 g causes a random error of ± 0.0029 mole percent (m/o) of Na_2SO_4 in the $CoSO_4-Na_2SO_4$ melts. The EMF measurements of $CoSO_4-Na_2SO_4$ melts at different partial pressures of SO_3 has resulted the relationship

$$\log a_{Na_2O} = -18.643 + 0.01511 \text{ m/o } Na_2SO_4 \qquad (S-4)$$

The error in log a_{Na_2O} is thus equal to ± 0.0075. DeYoung [94] determined that a random error in log a_{Na_2O} of ± 0.0013 is resulted from an uncertainty of ± 0.01 m/o of WO_3 in the reference material.

The purities of $CoSO_4$ and Na_2SO_4 are respectively 99.859% and 99.991%. The impurities in $CoSO_4$ produce an uncertainty of ±0.015 mole percent in both $CoSO_4$ and Na_2SO_4. While, the impurities in Na_2SO_4 create an uncertainty of ±0.0011 mole percent in both sulfates. A maximum systematic error of ±0.0073 in log a_{Na_2O} is thus noted.

A maximum of 0.0008 g of moisture is estimated to be absorbed by $CoSO_4$ during weighing. According to the equation (S-4), a systematic error of ±0.0075 in log a_{Na_2O} is introduced by an uncertainty in mole percent of Na_2SO_4 of ±0.00046 in $CoSO_4$--Na_2SO_4 melts.

Lastly, there is an uncertainty of ±0.0135 mole percent of WO_3 due to the impurities in the reference melt as it is determined by DeYoung [94]. The error in log a_{Na_2O} amounts to ±0.002.

S.5 ERRORS IN THERMODYNAMIC DATA OF REFERENCE MELT

The partial molar free energy of mixing of Na_2O in the WO_3-Na_2O reference melt can be calculated from the following relationship given by Lin and Elliott [68]

$$G^M_{Na_2O} = 2FE + (2.303RT/2)\log P_{O_2} + \Delta G^o_f(Na_2S(s))$$
$$- \Delta G^o_f(Na_2O(l)) - (1/2) \Delta G^o_f(WS_2(s)) \qquad (S-5)$$

According to the JANAF Tables [104], the uncertainties in $\Delta G^o_f(Na_2S(s))$ and $\Delta G^o_f(Na_2O(l))$ are estimated to be ±4540 cal/mol and ±2000 cal/mol, respectively. Hager and Elliott

[117] reported an uncertainty of $\pm$ 300 cal/mol in $\Delta G_f^o(WS_2(s))$. Employing this with uncertainties in temperature (± 1.0 K) and cell potential ($\pm$ 1 mv) and applying equation (Q-1) to equation (S-5) results an error in $G_{Na_2O}^M$ of 5020 cal/mol. Therefore, a systematic error in log a_{Na_2O} of ± 0.914 is found at 1200 K.

S.6 <u>SUMMARY OF ERRORS</u>

Combining the errors in temperature, cell potential, oxygen pressure, and melt composition, an error of ± 0.018 in log a_{Na_2O} is caused by the electrochemical experiment alone. Nevertheless, the uncertainties in the published thermodynamic data of the reference melt produce an error of ± 0.914 in log a_{Na_2O} at 1200 K. Application of equation (Q-1) yields a total error of ± 0.914 in log a_{Na_2O}. Consequently, the error in the activity of Na_2O can only be reduced if the accuracy of the thermodynamic data are improved.

THERMODYNAMIC DATA AT 1200 K

Species	ΔG^o_f, Kcal/mole	Date of Record	Ref.
α-Al_2O_3(s)	-309.580	December 31,1979	[104]
Al_2S_3(s)	-121.685	December 31,1979	[104]
$Al_2(SO_4)_3$(s)*	-473.864	1977	[106]
$NaAlO_2$(s)	-206.962	March 31,1963	[104]
Na_2O(s)	-59.832	June 30,1968	[104]
Na_2O(l)	-58.089	June 30,1968	[104]
Na_2SO_4(l)	-213.903	June 30,1978	[104]
Na_2S(s)	-66.256	March 31,1978	[104]
SO_2(g)	-65.582	June 30,1961	[104]
SO_3(g)	-62.360	Sept 30,1965	[104]

* Extrapolated data.

BIBLIOGRAPHY

1. Hot Corrosion Problems Associated with Gas Turbines,
    ASTM Special Technical Publication No.421, American
    Society For Testing And Materials, Philadelphia, PA,
    1967.

2. A.B.Hart and A.J.B.Cutler: Editors, Deposition and
    Corrosion in Gas Turbines, John Wiley and Sons, New
    York, 1973.

3. J.F.Stringer: High Temperature Corrosion of Aerospace
    Alloys, Report No. AGARD-AG-200, Advisory Group For
    Aerospace Research and Development, North Atlantic
    Treaty Organization, 1975.

4. R.A.Rapp: Editor, High Temperature Corrosion, National
    Association of Corrosion Engineers, Houston, TX, 1983.

5. B.G.Markham: Trans. Inst. Mar. Eng., 1959, vol.71,
    pp.316-23.

6. W.T.Reid, R.C.Corey, and B.J.Cross: Trans. ASME, 1945,
    vol.67, pp.279-88.

7. E.L.Simons, G.V.Browning, and H.A.Liebhafsky:
    Corrosion, 1955, vol.11, pp.505t-14t.

8. P.A.Bergman: Corrosion, 1976, vol.23, pp.72-81.

9. A.U.Seybolt: Trans. TMS-AIME, 1968, vol.242,
    pp.1955-61.

10. J.Stringer, V.Nagarajan, and D.P.Whittle: in High
    Temperature Metal Halide Chemistry, D.L.Hildenbrand and
    D.D.Cubicciotti, eds., The Electrochemical Society,
    Princeton, NJ, 1978, pp.509-19.

11. G.J.Danek: Nav. Eng. J., 1965, vol.77, No.6,
    pp.859-69.

12. J.G.Tschinkel: Corrosion, 1972, vol.28, No.5,
    pp.161-69.

13. G.J.Santoro, S.A.Gokoglu, F.J.Kohl, C.A.Sterns, and
    D.A.Rosner: in High Temperature Corrosion in
    Energy Systems, M.F.Rothman, ed., TMS-AIME, Warrendale,
    PA, 1985, pp.417-34.

14. T.D.Brown: J. Inst. Fuel, 1966, vol.39, No. 308,
    pp.378-85.

15. Manual on Requirements, Handling, and Quality Control
    of Gas Turbine Fuel, ASTM Special Technical Publication

531, American Society For Testing And Materials, Philadelphia, PA, 1973.

16. J.Stringer: in Corrosion Problems in Energy Conversion and Generation, C.S.Tedmon, ed., The Electrochemical Society, Princeton, NJ, 1974, pp.79-101.

17. R.M.Schirmer and H.T.Quigg: in Hot Corrosion Problems Associated With Gas Turbines, ASTM Special Technical Publication No.421, American Society For Testing And Materials, Philadelphia, PA, 1967, pp.270-95.

18. M.A.DeCrescente and N.S.Bornstein: Corrosion, 1968, vol.24, No.5, pp.127-33.

19. F.J.Kohl, G.J.Santoro, C.A.Stearns, G.C.Frybury, and D.E.Rosner: J. Electrochem. Soc., 1979, vol.126, pp.1054-61.

20. A.U.Seybolt: in High-Temperature Metallic Corrosion of Sulfur And Its Compounds, Z.A.Foroulis, ed., The Electrochemical Society, Princeton, NJ, 1970, pp.160-69.

21. J.Stringer: High Temperature Corrosion, R.A.Rapp, ed., National Association of Corrosion Engineers, Houston, TX, 1983, pp.389-97.

22. D.A.Shores and K.L.Luthra: in Corrosion-Erosion Behavior of Materials, K.Natesan, ed., TMS-AIME, Warrendale, PA, 1980, pp.86-102.

23. K.L.Luthra and D.A.Shores: J. Electrochem. Soc., 1980, vol.127, No.10, pp.2202-10.

24. G.Calcagni and D.Marotta: Gazz. Chim. Ital., 1913, vol.43, pp.380-90.

25. K.A.Bolshakov and P.T.Fedorov: Zh. Obshch. Khim. (J. of General Chemistry, USSR), 1956, vol.26, pp.348-69.

26. K.L.Luthra: Metall. Trans. A, 1982, vol.13A, pp.1647-54.

27. K.L.Luthra: Metall. Trans. A, 1982, vol.13A, pp.1853-64.

28. R.L.Jones and S.T.Godomski: J. Electrochem. Soc., 1982, vol.129, No.7, pp.1613-18.

29. R.F.Reising: Corrosion, 1977, vol.33, pp.84-88.

30. R.A.Rapp and K.S.Goto: in Molten Salts, J.Braunstein and J.R. Selman, eds., The Electrochemical Society, Pennington, NJ, 1981, pp.159-77.

31. M.Kawakami, K.S.Goto, and R.A.Rapp: Trans. Iron Steel Inst. Japan, 1980, vol.20, pp.646-58.

32. N.S.Bornstein and M.A.DeCrescente: Trans. TMS-AIME, 1969, vol.245, pp.1947-52.

33. J.A.Goebel and F.S.Pettit: Metall. Trans., 1970, vol.1, pp.1943-54.

34. J.A.Goebel and F.S.Pettit: in Metal-Slag-Gas Reactions and Processes, Z.A.Foroulis and W.W.Smeltzer, eds., The Electrochemistry Society, Princeton, NJ, 1975, pp.693-710.

35. J.A.Goebel, F.S.Pettit, and G.W.Goward: Metall. Trans., 1973, vol.4, pp.261-78.

36. J.A.Goebel, E.J.Felten, and F.S.Pettit: in Corrosion Problems in Energy Conversion and Generation, C.S.Tedmon, Jr., ed., The Electrochemical Society, Princeton, NJ, 1974, pp.102-17.

37. W.W.Liang, H.K.Bowen, and J.F.Elliott: in Metal-Slag-Gas Reactions and Processes, Z.A.Foroulis and W.W.Smeltzer, eds., The Electrochemical Society, Princeton, NJ, 1976, pp.608-24.

38. W.W.Liang and J.F.Elliott: in Properties of High Temperature Alloys, Z.A.Foroulis and F.S.Pettit, eds., The Electrochemical Society, Princeton, NJ, 1976, pp.557-71.

39. W.P.Stroud and R.A.Rapp: in High Temperature Metal Halide Chemistry, D.L.Hildenbrand and D.D.Cubicciotti, eds., The Electrochemistry Society, Princeton, NJ, 1978, pp.574-94.

40. J.F.Elliott, G.J.Yurek, M.J.McNallan, and N.Q.Minh: Final Report on Combined Cycle Research Program (MIT-2295 T18-12), Energy Laboratory, Massachusetts Institute of Technology, Cambridge, MA, 1979.

41. D.K.Gupta and R.A.Rapp: J. Electrochem. Soc., 1980, vol.127, pp.2194-2202.

42. M.L.Deanhart and K.H.Stern: J. Electrochem. Soc., 1981, vol.128, pp.2577-82.

43. M.L.Deanhardt and K.H.Stern: J. Electrochem. Soc., 1982, vol.129, pp.2228-32.

44. Y.S.Zhang and R.A.Rapp: J. Electrochem. Soc., 1985, vol.132, pp.734-35.

45. P.D.Jose, D.K.Gupta, and R.A.Rapp: J. Electrochem. Soc., 1985, vol.132, pp.735-37.

46. Y.S.Zhang and R.A.Rapp: J. Electrochem. Soc., 1985, vol.132, pp.2498-2501.

47. Y.S.Zhang: J. Electrochem. Soc., 1986, vol.133, pp.655-57.

48. D.-Z.Shi and R.A.Rapp: J. Electrochem. Soc., 1986, vol.133, pp.849-50.

49. J.Stringer: in Behaviour of High Temperature Alloys in Aggressive Environments, I.Kirman, J.B.Marriott, M.Merz, P.R.Sahm, and D.P.Whittle, eds., The Metals Soc., London, 1980, pp.739-57.

50. J.Stringer and D.P.Whittle: in High-Temperature Materials in Gas Turbines, P.R.Sahm and M.O.Speidel, eds., Elsevier Scientific Publishing, New York, 1974, pp.284-314.

51. N.S.Bornstein: Written discussion in Hot Corrosion Problems Associated with Gas Turbines, ASTM Special Technical Publications 421, American Society For Testing And Materials, Philadelphia, PA, 1967, pp.221.

52. H.Flood, T.Forland, and K.Motzfeldt: Acta Chem. Scand., 1952, vol.6, pp.257-69.

53. H.Flood and N.C.Boye: Z. Elektrochem., 1962, vol.66, pp.184-89.

54. A.Rahmel: Electrochim. Acta, 1970, vol.15, pp.1267-72.

55. A.Rahmel: Werkst. Korros., 1968, vol.19, pp.750-56.

56. E.Tatar-Moisescu and A.Rahmel: Electrochim. Acta, 1975, vol.20, pp.479-84.

57. R.J.Labrie and V.A.Lamb: J. Electrochem. Soc., 1959, vol.106, pp.895-99.

58. F.J.Salzano and L.Newman: J. Electrochem. Soc., 1972, vol.119, pp.1273-78.

59. E.Erdoes and H.Altorfer: Electrochim. Acta, 1975, vol.20, pp.937-44.

60. G.Danner and M.Rey: Electrochim. Acta, 1961, vol.4, pp.274-87.

61. C.T.Brown, N.S.Bornstein, and M.A.DeCrescente: in High Temperature Metallic Corrosion of Sulfur and Its Compound, Z.A.Foroulis, ed., The Electrochemical Soc., Princeton, NJ, 1970, pp.170-86.

62. N.S.Bornstein, M.A.DeCrescente, and H.A.Roth: Metall. Trans., 1973, vol.4, pp.1799-1810.

63. D.A.Shores: Corrosion, 1975, vol.31, pp.434-40.

64. D.A.Shores and R.C.John: J. Appl. Electrochem., 1980, vol.10, pp.275-83.

65. D.A.Neudorf and J.F.Elliott: Metall. Trans. B, 1980, vol.11B, pp.607-14.

66. W.W.Liang and J.F.Elliott: J. Electrochem. Soc., 1978, vol.125, pp.572-74.

67. W.W.Liang and J.F.Elliott: J. Electrochem. Soc., 1976, vol.123, pp.617-20.

68. R.Y.Lin and J.F.Elliott: Metall. Trans. A, 1983, vol.14A, pp.1713-20.

69. D.H.DeYoung and J.F.Elliott: in Chemical Metallurgy - A Tribute to Carl Wagner, N.A.Gokcen, ed., TMS-AIME, Warrendale, PA, 1981, pp.51-67.

70. B.W.Burrows and G.J.Hills: Electrochim. Acta, 1970, vol.15, pp.445-58.

71. C.H.Liu: J. of Phys. Chem., 1962, vol.66, pp.164-66.

72. K.E.Johnson and H.A.Laitinen: J. Electrochem. Soc., 1963, vol.110, pp.314-18.

73. E.S.Woolner and D.G.Hill: J. of Phys. Chem., 1963, vol.67, pp.1571-73.

74. J.Guion: Inorg. Chem., 1967, vol.6, pp.1882-85.

75. F.A.Elrefaie and W.W.Smeltzer: J. Electrochem. Soc., 1981, vol.128, pp.1443-47.

76. G.W.Watt, R.E.Andresen, and R.A.Rapp: in Molten Salts, J.Braunstein and J.R.Selman, eds., The Electrochemical Society, Pennington, NJ, 1981, pp.81-109.

77. S.K.Mittal and J.F.Elliott: J. Electrochem. Soc., 1984, vol.131, pp.1194-99.

78. S.K.Mittal and J.F.Elliott: J. Electrochem. Soc., 1987, vol.134, pp.244-47.

79. M.J.Donachie, E.F.Bradley, R.A.Sprague, and F.P.Talboom: Source Book on Materials for Elevated-Temperature Applications, American Society For Metals, Metals Park, OH, 1979, pp.34-45.

80. R.M.Schirmer and H.T.Quigg: in Hot Corrosion Problems Associated with Gas Turbines, ASTM Special Technical Publication 421, American Society for Testing and Materials, Philadelphia, PA, 1967, pp.270-96.

81. C.E.Hussey, S.Y.Lee, and W.E.Young: in Manual on Requirements, Handling, and Quality Control of Gas Turbine Fuel, ASTM Special Technical Publication 531, American Society for Testing and Materials, Philadelphia, PA, 1973, pp.3-21.

82. J.F.Elliott: in Solid State Chemistry of Energy Conversion and Storage, Advances in Chemistry Series, No.163, J.B.Goodenough and M.S.Whittingham, eds., The American Chemical Society, 1977, pp.225-39.

83. H.Flood and T.Forland: Acta Chem. Scand., 1947, vol.1, pp.781-89.

84. A.W.Coats, D.J.A.Dear, and D.Penfold: J. Inst. Fuel, 1968, vol.41, pp.129-32.

85. L.P.Kostin, L.L.Pluzhnikov, and A.N.Ketov: Russ. J. Phys. Chem., 1975, vol.49, pp.1313-14.

86. T.R.Ingraham and M.C.B.Hotz: Can. Metall. Quart., 1968, vol.7, No.3, pp.139-51.

87. R.-Y.Lin: Sc.D. Thesis, Massachusetts Institute of Technology, Cambridge, MA, 1980.

88. S.K.Mittal: Sc.D. Thesis, Massachusetts Institute of Technology, Cambridge, MA, 1983.

89. R.E.Andresen: J. Electrochem. Soc., 1979, vol.126, pp.328-34.

90. G.J.Yurek and R.E.Deeter: J. Electrochem. Soc., 1981, vol.128, pp.2232-37.

91. A.K.Misra, D.P.Whittle, and W.L.Worrell: J. Electrochem. Soc., 1982, vol.129, pp.1840-45.

92. K.L.Luthra: in High Temperature Corrosion, R.A.Rapp, ed., National Association of Corrosion Engineers, Houston, TX, 1983, pp.507-12.

93. K.Sadakane, M.Kawakani, and K.S.Goto: Tetsu-to-Hagane, 1977, vol.3, pp.432-40.

94. D.H.DeYoung: Ph.D. Thesis, Massachsetts Institute of Technology, Cambridge, MA, 1981.

95. Y.S.Zhang and R.A.Rapp: Corrosion, 1987, vol.43, pp.348-52.

96. The International Practical Temperature Scale Of 1968, amended in 1975, London, HMSO, 1976, pp.29.

97. W.W.Wendlandt: Thermal Methods Of Analysis, 2nd edition, John Wiley & Sons, New York, 1974.

98. R.C.Mackenzie: Editor, Differential Thermal Analysis, vol. 1 and 2, Academic Press, New York, 1970 and 1972.

99. P.D.Garn: Thermoanalytical Methods Of Investigation, Academic Press, New York, 1965.

100. E.M.Barrall,II and R.J.Gritter: in Systematic Materials Analysis, J.H.Richardson and R.V.Petterson, eds., Academic Press, New York, vol.4 ,pp. 343-405.

101. M.I.Pope and M.D.Judd: Differential Thermal Analysis, Heyden & Son, London, 1977.

102. D.E.Etter, P.A.Tucker, and L.J.Wittenberg: in Thermal Analysis, R.F.Schwenker,Jr. and P.D.Garn, eds. Academic Press, New York, 1969, vol. 2, pp.829-50.

103. W.Gutt and A.J.Majumdar: in Differential Thermal Analysis, Volume 2, R.C.Mackenzie, ed., Academic Press, New York, 1972, pp.79-117.

104. JANAF Thermochemical Tables, Loose Leaf Edition, National Bureau of Standards, 1982.

105. J.J.Moore: Chemical Metallurgy, Butterworth, London, 1981, pp.120-23.

106. I.Barin, O.Knacke, and O.Kubaschewski: Thermochemical Properties of Inorganic Substances, Springer-Verlag Berlin Heidelberg, New York, 1973 and supplement 1977.

107. Y.-Q.Lei and J.F.Elliott: Report, Massachusetts Institute of Technology, Cambridge, MA, 1984.

108. W.W.Liang: Sc.D. Thesis, Massachusetts Institute of Technology, Cambridge, MA, 1976.

109. F.Hoermann: Z. anorg. u. allgem. Chem., 1928, vol.177, pp.167.

110. P.Caillet: Bull. Soc. Chim. Fr., 1967, No.12, pp.4750-55.

111. L.L.Y.Chang and S.Sachdev: J. Amer. Cer. Soc., 1976, vol.58, pp.267-70.

112. K.Wark: Thermodynamics, 3rd edition, McGraw-Hill, New York, 1977, pp.142-44.

113. K.H.Stern: NRL Memorandum Report 4772, Naval Research Laboratory, Washington, DC, March 1982.

114. J.Topping: Errors Of Observation And Their Treatment, 4th edition, Chapman and Hall, London, Great Britain, 1972.

115. Y.Beers: <u>Introduction To The Theory Of Error</u>, Addison-Wesley, Reading, MA, 1957.

116. D.C.Baird: <u>Experimentation: An Introduction To Measurement Theory And Experiment Design</u>, Prentice-Hall, New Jersey, 1962.

117. J.P.Hager and J.F.Elliott: <u>Trans. TMS-AIME</u>, 1967, vol.239, pp.513-20.

BIOGRAPHICAL NOTE

The author was born in Hong Kong on December 19, 1957. He was raised in Wanchai, Hong Kong. Upon graduation from Shing Kwong Church Primary School in 1970, he received his high school education from Rosaryhill School. Having finished high school in 1976, he came to the States and enrolled in the University of Hawaii at Manoa. His name was placed on the Dean's Honor List of the School of Engineering at the University of Hawaii in 1981. He had been a teaching assistant for a thermodynamic class in Mechanical Engineering for two semesters. He was granted the degree of Bachelor of Science in Mechanical Engineering in the summer of 1981. He then continued his education in the graduate program of Mechanical Engineering until January 1983. He received the degree of Master of Science in May 1983 from University of Hawaii. In the spring of 1983, he enrolled in the Department of Materials Science and Engineering at Massachusetts Institute of Technology and started the doctoral program in chemical/process metallurgy at the same time.

The author was married to Juliana in 1983 and his first child, Jake, was born in Boston in December 1987.